

# **Mechanochemical Synthesis of Multinary Sulfides**

vorgelegt von

**Eva Maria Heppke, B.Sc. M.Sc.**

an der Fakultät II - Mathematik und Naturwissenschaften  
der Technischen Universität Berlin

zur Erlangung des akademischen Grades

**Doktorin der Naturwissenschaften**

**Dr. rer. nat.**

genehmigte Dissertation

Promotionsausschuss:

Vorsitzende: Prof. Dr. Karola Rück-Braun

Gutachter: Prof. Dr. Martin Lerch

Gutachter: Prof. Dr. Hubert Huppertz

Tag der wissenschaftlichen Aussprache: 25.09.2020

Berlin 2021

## Acknowledgements

For the realisation of the present work I would like to express my gratitude to the following people.

First of all, I want to thank my supervisor Prof. Dr. Martin Lerch of the TU Berlin for giving me the possibility to work in his group, for the interesting topic and for his continuous and encouraging support during my doctoral work.

I also would like to thank Prof. Dr. Hubert Huppertz of the University of Innsbruck for the second review of this thesis and Prof. Dr. Karola Rück-Braun for taking over the chair of the doctoral committee.

Special thanks go to my cooperation partners for the successful collaboration that has resulted in the publications on which this thesis is based:

Oona Appelt and Dr. Ilias Efthimiopoulos of the GFZ Potsdam for WDX and Raman measurements and helpful comments.

Tim Küllmey and Prof. Dr. Beate Paulus of the FU Berlin for quantum-chemical calculations and general advice. Thanks also to Tim for the help with some  $\text{\LaTeX}$  problems.

J. Niklas Hausmann, Rodrigo Beltrán-Suito and Dr. Prashanth W. Menezes of the research group of Prof. Dr. Matthias Driess of the TU Berlin for using my materials for investigations according to their expertise.

Steffen Klenner, Dr. Oliver Janka and Prof. Dr. Rainer Pöttgen of the WWU Münster for magnetic and Mößbauer measurements and helpful comments.

For performing various measurements essential for this work I would like to thank:

Dr. Nina Genz of the research group of Prof. Dr. Thorsten Ressler of the TU Berlin for DTA- and UV/Vis measurements.

J. Niklas Hausmann and Rodrigo Beltrán-Suito of the research group of Prof. Dr. Matthias Driess and Dr. Stefan Berendts of the research group of Prof. Dr. Martin Lerch of the TU Berlin for EDX/SEM measurements. A big thanks also go to the Zentraleinrichtung für Elektronenmikroskopie (ZELMI) of the TU Berlin for the provision of the corresponding devices.

Leo Sagurna and Dr. Johannes Schmidt of the research group of Prof. Dr. Arne Thomas of the TU Berlin for the provision and support of UV/Vis measurements and XPS measurements.

Juana Krone and Astrid Müller-Klauke for combustion and ICP-OES analysis (both

TU Berlin).

Dr. Martin Mühlbauer of the MLZ Garching for Neutron diffraction measurements.

A big thanks go to Dr. Julia Kohl and Dr. Stephan Kohl (both TU Berlin) for the provision of the planetary ball mills, assistance with Schlenk technique and helping me with all kinds of questions.

I also want to thank the glassblowers of the TU Berlin, Wiebke Matthes and Ralf Reichert, for the preparation of reaction tubes and providing and melting of several ampoules.

Furthermore, I want to say thanks to the employees of the materials and chemicals counter of the Institute of Chemistry: Alex Billig, Barbara-Cornelia Fischer, Eric Neumann, Franziska Rau, Juana Krone and Luise Spreer.

Special thanks also go to Claudia Benzin and Andrea Rahmel for their organizational and administrative help.

Many thanks to the former and current members of the research group of Prof. Dr. Martin Lerch for the pleasant and friendly working atmosphere, constant discussions and help in various theoretical and practical aspects: Abdullah, Anna, Björn, Claudia, Dennis, Elisabeth, Ina, Gregor, Kevin, Matthias, Mirabbos, Nadine, Sevilay, Sophie, Stefan, Steven, Suliman and Tobias.

Particularly noteworthy at this point are Dr. Matthias Paun for the instruction in the skullmelting technique, Dr. Anna Ritscher for the introduction into mechanochemical synthesis and proofreading of this thesis, Dr. Steven Orthmann and Dr. Tobias Lüdtker for general assistance and helping me with all kinds of problems, Dr. Elisabeth Irran and Dr. Dennis Wiedemann for assistance with crystallographic issues, Dr. Stefan Berendts for high-temperature X-ray diffraction measurements and any technical support and Ina Speckmann for the good times when we shared an office.

A big thanks also go to my bachelor students Fatma D. Avci and Shamini Mahadevan for their support in sample preparation and structural evaluation.

Furthermore, I want to thank some people in particular for the unforgettable time at and outside the Institute: Alex, Chris, Ernesto, Frank, Jan, Mandy, Noah, Stefan, Vicky of the research group of Prof. Dr. Matthias Driess, Robert of the research group

of Prof. Dr. Martin Kaupp, Marc and Luise.

Finally, I would like to thank my parents Ilse and Gernot and my sisters Sabina and Christina and all my friends around Berlin and Austria for their continuous support and encouragement. Big thanks go to Pati for his engagement with L<sup>A</sup>T<sub>E</sub>X questions.

## Preface

This dissertation is a cumulative thesis in which the results are presented in form of published articles. The work summarized in this thesis was undertaken within *ca.* four years from February 2016 to June 2020 under the supervision of Prof. Dr. Martin Lerch at the Technical University of Berlin.

**Part I - Introduction** indicates some theoretical aspects of the material classes and the description of preparative and analyzing methods used in this work. **Part II - Publications** contains the following already published articles.

1. E. M. Heppke, T. Küllmey, I. Efthimiopoulos, F. D. Avci, O. Appelt, B. Paulus, M. Lerch. Experimental and theoretical investigations on the composition-dependent structural phase transition in  $\text{Cu}_2\text{Cd}_x\text{Zn}_{1-x}\text{SnS}_4$ . *Mat. Res. Express* **2019**, 6(12), 125525.
2. E. M. Heppke, S. Berendts, M. Lerch. Crystal structure of mechanochemically synthesized  $\text{Ag}_2\text{CdSnS}_4$ . *Z. Naturforsch. B* **2020**, 75(4), 393-402.
3. E. M. Heppke, M. Lerch.  $\text{Na}_2\text{MgSnS}_4$  – a new member of the  $\text{A}^{\text{I}}_2\text{B}^{\text{II}}\text{C}^{\text{IV}}\text{X}^{\text{VI}}_4$  family of compounds. *Z. Naturforsch. B* **2020**, 75(8), 721-726.
4. J. N. Hausmann, E. M. Heppke, R. Beltrán-Suito, J. Schmidt, M. Mühlbauer, M. Lerch, P. W. Menezes, M. Driess. Stannites—a new promising class of durable electrocatalysts for efficient water oxidation. *ChemCatChem* **2020**, 12(4), 1161-1168.
5. E. M. Heppke, S. Klenner, O. Janka, R. Pöttgen, M. Lerch. Mechanochemical Synthesis of  $\text{Cu}_2\text{MgSn}_3\text{S}_8$  and  $\text{Ag}_2\text{MgSn}_3\text{S}_8$ . *Z. Anorg. Allg. Chem.* **2020**, 646, 5-9.
6. E. M. Heppke, S. Mahadevan, M. Lerch. New compounds of the  $\text{Li}_2\text{MSn}_3\text{S}_8$  type. *Z. Naturforsch. B* **2020**, 75(6-7), 625-631.

The chronological order of each publication is in accordance with the published version. This means that some articles are constructed as follows *Introduction - Experimental Section - Results - Conclusions* and other ones in form of *Introduction - Results - Conclusions - Experimental Section*. As every article exhibits its own introduction some information is probably repeated over the whole thesis. The formatting of the publications thereby differs somewhat from the published versions. Figures and Tables

contained in the publications are numbered according to the respective chapter of this thesis. To ensure that Figures and Tables are indicated consistently throughout the thesis, Figures and Tables are not shown in bold in the text. In addition, sum formulas are presented in a consistent manner over the entire thesis. Referrals in the articles also have been adapted accordingly. Every article is concluded with a separate bibliography which is unified throughout the thesis.

In **Part III - Conclusion and Prospects** the results of each publication of Part II are summarized. Additionally, a short outlook on future work in this research area is given. Part I and III have their own bibliography, which is listed at the end of the thesis.

## Abstract

In the here-presented thesis the successful preparation and precise characterization of new and known compounds of the type  $A_2^I B^{II} C^{IV} S_4^{VI}$  and new compounds of the type  $A_2^I B^{II} C_3^{IV} S_8^{VI}$  using a newly developed mechanochemical synthesis approach is reported. The mechanochemical synthesis route consists of two steps, the milling in a high-energy planetary mill followed by annealing in  $H_2S$  atmosphere. This newly developed synthesis method is more environmentally friendly by requiring shorter reaction times, lower heating temperatures and shorter holding times. Moreover, the formation of secondary phases is suppressed compared to the commonly used solid state reaction preparing these materials.

Research data on the structural transition between the stannite- and kesterite-type structure in the solid solution series  $Cu_2Cd_xZn_{1-x}SnS_4$  could be expanded using highly crystalline and phase-pure bulk materials. The probable structure type for each composition could be determined by Rietveld refinement in four different models (ST, KS, DKS, partial DKS) and thus also the structural transition at a composition of  $x = 0.40$  localized. The radiographically obtained value is supported by Raman spectroscopic measurements, supplemented by quantum-chemical calculations at DFT level. The determined value agrees with earlier studies on off-stoichiometric and nanostructured/thin-film samples.

For mechanochemically prepared  $Ag_2CdSnS_4$  two further structure types than those mentioned in the literature could be indicated due to additionally observed reflections in the diffraction pattern. The low-temperature phase of mechanochemically synthesized  $Ag_2CdSnS_4$  could be refined in the wurtzkesterite-type structure with space group  $Pn$ , where an ordering of the cations on distinct positions is observed. At around 200 °C a first-order phase-transition from the wurtzkesterite-type to the wurtzstannite-type structure with space group  $Pmn2_1$  occurs.

Furthermore, a hitherto unknown  $A_2^I B^{II} C^{IV} S_4^{VI}$  compound with molecular formula  $Na_2MgSnS_4$  could be synthesized.  $Na_2MgSnS_4$  adopts a  $NaCrS_2$ -type structure in rhombohedral space group  $R\bar{3}m$ . Mg and Sn are thereby statistically distributed and form a  $CdCl_2$ -type structure together with S, whereas the Na ions are located on the remaining octahedral voids. In contrast to usual tetrahedral  $A_2^I B^{II} C^{IV} S_4^{VI}$  compounds, cations and anions in  $Na_2MgSnS_4$  are exhibiting an octahedral coordination.

In addition, further previously unknown compounds of the type  $A_2^I B^{II} C_3^{IV} S_8^{VI}$  could be synthesized. For the first time, Mg-containing thiospinels of this type, such as  $Cu_2MgSn_3S_8$  and  $Ag_2MgSn_3S_8$ , were produced. The substitution of monovalent Cu

and Ag with Li in these materials has also proved to be successful and resulted in the preparation of four hitherto unknown compounds with the empirical formula  $\text{Li}_2\text{M}\text{Sn}_3\text{S}_8$  with  $M = \text{Mg}, \text{Mn}, \text{Fe}, \text{Ni}$ . All newly prepared thiospinels of the type  $\text{A}_2^{\text{I}}\text{B}^{\text{II}}\text{C}_3^{\text{IV}}\text{X}_8^{\text{VI}}$  crystallize in space group  $Fd\bar{3}m$  where the monovalent cations are located on the tetrahedral sites and the divalent and tetravalent cations exhibit a statistical distribution on the octahedral sites.

## Kurzfassung

In der hier vorgestellten Arbeit ist die erfolgreiche Synthese und genaue Charakterisierung von neuen und bekannten Verbindungen vom Typ  $A_2^I B^{II} C^{IV} S_4^{VI}$  und neuen Verbindungen vom Typ  $A_2^I B^{II} C_3^{IV} S_8^{VI}$  unter Verwendung eines neu-entwickelten mechanochemischen Syntheseansatzes berichtet. Die mechanochemische Syntheseroute besteht aus zwei Schritten, dem Mahlen in einer Hochenergie Planetenkugelmühle gefolgt von Tempern in  $H_2S$ -Atmosphäre. Die neu-entwickelte Synthesemethode ist aufgrund kürzerer Reaktionszeiten, niedrigeren Aufheiztemperaturen und kürzeren Haltezeiten deutlich umweltfreundlicher. Außerdem ist, verglichen mit den üblicherweise verwendeten Festkörperreaktionen zur Herstellung dieser Materialien, die Bildung von Nebenphasen unterdrückt.

Forschungsdaten zum strukturellen Übergang zwischen der Stannit- und Kesterit-Struktur in der Mischkristallreihe  $Cu_2Cd_xZn_{1-x}SnS_4$  konnten unter Verwendung von hochkristallinen und phasenreinen bulk Materialien erweitert werden. Der wahrscheinliche Strukturtyp für jede Zusammensetzung konnte durch Rietveld-Verfeinerung in vier verschiedenen Modellen (ST, KS, DKS, teilweise DKS) bestimmt werden und so auch der strukturelle Übergang bei einer Zusammensetzung von  $x = 0.40$  lokalisiert werden. Der röntgenographisch erhaltene Wert wird durch ramanspektroskopische Messungen unterstützt, ergänzt durch quantenchemische Berechnungen auf DFT Niveau. Der ermittelte Wert stimmt mit dem früherer Studien an nicht-stöchiometrischen und nanostrukturierten/Dünnschicht-Proben überein.

Aufgrund zusätzlich erhaltener Reflexe im Beugungsdiagramm wurden für mechanochemisch hergestelltes  $Ag_2CdSnS_4$  zwei weitere Strukturtypen gefunden, die noch nicht in der Literatur erwähnt wurden. Die Niedrigtemperatur-Modifikation von mechanochemisch synthetisiertem  $Ag_2CdSnS_4$  konnte in der Wurtzkesterit-Struktur mit Raumgruppe  $Pn$  verfeinert werden, bei der eine Ordnung der Kationen auf eindeutigen Positionen zu beobachten ist. Bei ungefähr  $200\text{ °C}$  tritt ein Phasenübergang erster Ordnung von der Wurtzkesterit- zur Wurtzstannit-Struktur mit Raumgruppe  $Pmn2_1$  auf.

Desweiteren konnte eine bisher unbekannte  $A_2^I B^{II} C^{IV} S_4^{VI}$ -Verbindung mit molekularer Formel  $Na_2MgSnS_4$  synthetisiert werden.  $Na_2MgSnS_4$  kristallisiert in der  $NaCrS_2$ -Struktur in der rhomboedrischen Raumgruppe  $R\bar{3}m$ . Mg und Sn sind statistisch verteilt und bilden zusammen mit S eine  $CdCl_2$ -Struktur während die Na-Ionen auf den übrigen Oktaederlücken platziert sind. Im Gegensatz zu den üblichen tetraedrischen  $A_2^I B^{II} C^{IV} S_4^{VI}$ -Verbindungen weisen die Kationen und Anionen in  $Na_2MgSnS_4$  eine oktaedrische Koordination auf.

Darüber hinaus konnten weitere bisher unbekannte Verbindungen vom Typ  $A_2^I B^{II} C_3^{IV} S_8^{VI}$  synthetisiert werden. Zum ersten Mal wurden Mg-haltige Thiospinelle von diesem Typ, wie zum Beispiel  $Cu_2MgSn_3S_8$  und  $Ag_2MgSn_3S_8$ , hergestellt. Die Substitution von einwertigem Cu und Ag durch Li in diesen Materialien hat sich auch als erfolgreich erwiesen und führte zur Herstellung von vier bisher unbekanntem Verbindungen mit folgender empirischer Formel  $Li_2MSn_3S_8$  mit  $M = Mg, Mn, Fe, Ni$ . Alle neu hergestellten Thiospinelle vom Typ  $A_2^I B^{II} C_3^{IV} X_8^{VI}$  kristallisieren in der Raumgruppe  $Fd\bar{3}m$ , bei der sich die monovalenten Kationen auf den tetraedrischen Positionen befinden und die zwei- und vierwertigen Kationen eine statistische Verteilung auf den oktaedrischen Positionen aufweisen.

# Contents

<b>I. Introduction</b>	<b>1</b>
1. Motivation and aim of the thesis	2
<b>2. Diamondlike semiconductors</b>	<b>4</b>
2.1. Introductory remarks . . . . .	4
2.2. $A_2^I B^{II} C^{IV} S_4^{VI}$ compounds . . . . .	5
2.2.1. Crystal structure . . . . .	9
2.2.2. Compressed chalcopyrite-like structure . . . . .	19
<b>3. Spinel</b>	<b>22</b>
3.1. Introductory remarks . . . . .	22
3.2. Spinel structure . . . . .	23
<b>4. Methodology</b>	<b>28</b>
4.1. Preparative Methods . . . . .	28
4.1.1. Mechanochemical Synthesis . . . . .	28
4.1.2. $H_2S$ furnace . . . . .	30
4.2. X-ray diffraction . . . . .	32
4.2.1. Theoretical principles . . . . .	32
4.2.2. Rietveld refinement . . . . .	34
4.2.3. Crystallite size determination . . . . .	35
4.3. Raman spectroscopy . . . . .	36
4.4. Diffuse reflectance UV-Vis spectroscopy . . . . .	36
4.5. Electron microprobe analysis . . . . .	37
4.6. Inductively coupled plasma optical emission spectrometry . . . . .	39

<b>II. Publications</b>	<b>40</b>
<b>5. Publication 1</b>	<b>41</b>
5.1. Abstract . . . . .	43
5.2. Introduction . . . . .	43
5.3. Experimental and Theoretical Details . . . . .	46
5.3.1. Synthesis details . . . . .	46
5.3.2. Characterization details . . . . .	46
5.3.3. Computational details . . . . .	49
5.4. Results and Discussion . . . . .	52
5.4.1. XRD refinements . . . . .	52
5.4.2. DFT calculations . . . . .	55
5.4.3. Raman spectroscopic investigations . . . . .	57
5.4.4. Band gap . . . . .	58
5.4.5. The (D)KS $\rightarrow$ ST transition in $\text{Cu}_2\text{Cd}_x\text{Zn}_{1-x}\text{SnS}_4$ . . . . .	62
5.5. Conclusions . . . . .	64
5.6. Acknowledgements . . . . .	65
5.7. References . . . . .	65
<b>6. Publication 2</b>	<b>70</b>
<b>7. Publication 3</b>	<b>82</b>
<b>8. Publication 4</b>	<b>90</b>
8.1. Abstract . . . . .	92
8.2. Introduction . . . . .	92
8.3. Results and Discussion . . . . .	94
8.4. Conclusions . . . . .	101
8.5. Experimental Section . . . . .	101
8.6. Acknowledgements . . . . .	106
8.7. References . . . . .	106
<b>9. Publication 5</b>	<b>113</b>
9.1. Abstract . . . . .	115
9.2. Introduction . . . . .	115
9.3. Results and Discussion . . . . .	115
9.4. Conclusions . . . . .	123
9.5. Experimental Section . . . . .	124
9.6. Acknowledgements . . . . .	125

9.7. Bibliography . . . . .	125
<b>10. Publication 6</b>	<b>128</b>
<b>III. Conclusion and Prospects</b>	<b>137</b>
<b>11. Conclusion</b>	<b>138</b>
11.1. $A_2^I B^I C^{IV} S_4^{VI}$ compounds . . . . .	138
11.2. $A_2^I B^I C_3^{IV} S_8^{VI}$ compounds . . . . .	140
11.3. Outlook . . . . .	141
<b>A. Appendices</b>	<b>143</b>
A.1. Additional information, Supplementary material . . . . .	143
A.1.1. Chemicals . . . . .	143
A.1.2. Diffraction pattern of binary starting materials . . . . .	144
A.1.3. Software . . . . .	149
A.2. List of Publications . . . . .	150
A.3. List of Conference Contributions . . . . .	151
<b>List of Figures</b>	<b>152</b>
<b>List of Tables</b>	<b>156</b>
<b>Bibliography</b>	<b>158</b>

**Part I.**

# **Introduction**

# 1. Motivation and aim of the thesis

Semiconductors - possessing an intermediate position between electrical conductors and nonconductors - are important for electrical engineering, especially electronics, and have become an integral part of our everyday lives. They have acquired their greatest significance with the development of the transistor effect in 1947 [1, 2]. This is also specified as the starting point of modern electronics. Transistors are switches that control electrical voltages and currents and are considered to play an important role in integrated circuits. With the miniaturization of circuits, semiconducting technology has found its way into all areas of our lives, such as computers, entertainment and communication (DVDs, flatscreens, mobilephones), transportation (motor control in all vehicles), medicine and many others. Semiconductors also play a crucial role in renewable energy sources such as photovoltaic/solar cells [3], wind turbines [4] and for water splitting in photocatalysis [5].

A class of materials based on semiconductors with a wide variety of applications are diamondlike semiconductors including  $A_2^I B^{II} C^{IV} X_4^{VI}$  compounds [6–8]. The most prominent examples of this class of materials at the moment are  $Cu_2ZnSnS_4$  and  $Cu_2ZnSnSe_4$ , respectively. Both compounds are p-type semiconductors and exhibit ideal band gap values for solar energy conversion [9, 10]. Extensive research is being carried out on  $Cu_2ZnSnS_4$  in particular, as it is considered to be an alternative absorber material to cadmium telluride and copper indium gallium selenide ( $Cu(In,Ga)Se_2$ ) due to its contained earth abundant elements and non-toxicity [11, 12].

Anyone dealing with  $A_2^I B^{II} C^{IV} X_4^{VI}$  compounds on an experimental level will involuntarily come across  $A_2^I B^{II} C_3^{IV} X_8^{VI}$  compounds [13–15], another class of materials consisting of compounds with semiconducting properties. As only a few sulfidic (and none selenic) compounds of this type are known by now, its applicational potential is not yet fully exploited. However, due to the fact that most compounds crystallize in the spinel-type structure, this class of materials is interesting as potential candidates for electrodes/electrolytes in batteries [16–19].

With quaternary compounds and the resulting increased compositional flexibility, a greater ability to tune the physical properties may be achieved. In the past, studies

have focused more on binary and ternary compounds as quaternary compounds are more difficult to synthesize. Including a further cation can lead to the production of new materials with improved or even new properties and thus opening up new areas of application. Although, it is not always possible to produce improved materials or optimize properties, the information that can be obtained is essential to gain a deeper understanding of structure-property relationships. The determination of the crystal structure itself is an important part of understanding the specific properties of a compound. This knowledge can advance the development of next generations of semiconducting materials and is therefore indispensable for future research.

The focus of the work presented here is the development of new materials and the reproduction of known materials of the types  $A_2^I B^{II} C^{IV} S_4^{VI}$  and  $A_2^I B^{II} C_3^{IV} S_8^{VI}$ . The aim is to get a better understanding of the structural properties of these materials and a more precise insight into the relationships between the structure and the chemical as well the physical properties. Priority is thereby given to the determination of the crystal structures and the chemical compositions. In addition, physical properties such as optical and magnetic properties are also part of the investigations.

The synthesis method used in this thesis is based on the mechanochemical synthesis approach introduced by Ritscher et al. [20] for the preparation of  $Cu_2ZnSnS_4$  which has proved to be a suitable method for the production of phase-pure and highly crystalline sulfides of the type  $A_2^I B^{II} C^{IV} X_4^{VI}$  [21, 22].

## 2. Diamondlike semiconductors

### 2.1. Introductory remarks

In the last few years semiconductors with cubic or hexagonal diamond related structures of the type  $A_2^I B^II C^{IV} X_4^{VI}$  have attracted a lot of attention. These materials belong to the adamantine compound family which have long been the subject of a broad field of research as they consist of several compounds with interesting properties including Si or GaN [23].

Members of the adamantine compound family are characterized by tetrahedral bonding and form so-called tetrahedral structures [24, 25]. In normal tetrahedral structures the average number of valence electrons per atoms has to be four which implies four neighbouring atoms in the primary coordination sphere. This can also be expressed by the Grimm-Sommerfeld rule [26] - as an example for a compound with composition  $A_n B_m$  [24]:

$$\frac{ne_A + me_B + \dots}{n + m + \dots} = 4 \quad (2.1)$$

$A, B$	elements
$e_A, e_B$	valence electrons of element $A, B$
$n, m$	integers

The average valence number per anion thereby has to be eight. According to these two features, the number of cations in these compounds is equal to the number of anions. A deviation of that is allowed for defect tetrahedral structures with a smaller number of nearest atoms [25]. However, the defect tetrahedral structure compounds are not considered in this work. The bonding character itself within these materials can range from ionic to covalent but can also assume anything in between depending on the electronegativities. A larger difference of the electronegativities rather indicates a stronger ionic character [6, 27].

The Grimm-Sommerfeld rule was firstly introduced for binary compounds, however, can be extended to multinary more complex compounds. By now, multinary tetrahedral compounds including binary, ternary, quaternary with different general formulas are mentioned in the literature as diamond derived semiconductors forming tetrahedral

structures [6, 28]. This work focus only on quaternary diamondlike semiconductors of the type  $A_2^I B^{II} C^{IV} X_4^{VI}$ .

The wide range of compositional flexibility of the  $A_2^I B^{II} C^{IV} X_4^{VI}$  group is expressed by the large number of already known compounds, such as oxides, sulfides, selenides and tellurides [23, 24, 29–33]. Although some compounds belong to the  $A_2^I B^{II} C^{IV} X_4^{VI}$  compound family depending on their molecular formula not all of them form tetrahedral structures. Some  $A_2^I B^{II} C^{IV} X_4^{VI}$  compounds differ in their coordination spheres from tetrahedral structures and form tetrahedral framework structures. However, a relation to tetrahedral structures (such as the stannite-type structure) can occur, for example, with compounds that adopt the compressed chalcopyrite-like structure [34, 35]. A detailed description of the compressed chalcopyrite-like structure can be found in section **2.2.2 Compressed chalcopyrite-like structure.**

This work only focus on the preparation of sulfides of the type  $A_2^I B^{II} C^{IV} X_4^{VI}$ . A more detailed insight into this interesting group will be given in the following sections.

## 2.2. $A_2^I B^{II} C^{IV} S_4^{VI}$ compounds

Quaternary semiconductors with general formula  $A_2^I B^{II} C^{IV} S_4^{VI}$  are characterized as a class of materials with a stable structure and compositional flexibility. Due to that a lot of compounds with different physical properties were generated over the past few years which enables a wide applicational field for these compounds.

The first compounds of this type - which either adopt stannite- or wurtzstannite-type structure (hexagonal analogue of stannite-type structure) - were synthesized in the 1960s [36]. As natural occurring compounds,  $Cu_2FeSnS_4$  (mineral stannite) and  $Cu_2ZnSnS_4$  (mineral kesterite) were already discovered at that time [37, 38]. Since then a lot of new diamondlike compounds of this type have been synthesized exhibiting interesting properties.

The biggest group among them are  $A_2^I B^{II} C^{IV} S_4^{VI}$  with  $A = Cu$  [29, 39–41] whereas  $Cu_2ZnSnS_4$  has attracted the most attention in recent years as potential absorber for thin film solar cell applications due to its (nearly ideal) band gap and high absorption coefficient [42, 43]. Cu-compounds with a smaller tetravalent cation such as Si show a higher tendency for the formation of hexagonal diamond derived structures such as the wurtzstannite-/wurtzkesterite-type structure [29, 40]. For Cu compounds with Ge as tetravalent cation related structures of both aristotypes are realized [29, 39–41]. Sn-bearing Cu compounds favor cubic diamond derived structures such as the stannite-

and kesterite-type structure [29, 44].

Silver compounds are more difficult to synthesize and less stable compared to Cu compounds. Nonetheless, few  $A_2^I B^{II} C^{IV} S_4^{VI}$  with  $A = Ag$  are known so far [36, 45–51]. Considering the tetravalent cations, a similar preference as for Cu-bearing compounds appears for Ag-containing materials. Although, Sn-bearing compounds occur in the cubic as well as hexagonal diamond derived structures [36, 45–49]. Si-bearing Ag compounds exclusively crystallize in the wurtzkesterite-type structure [50, 51].

By composition, also one Au-bearing compound of the type  $A_2^I B^{II} C^{IV} S_4^{VI}$  is mentioned in the literature [52]. However, from a structural point of view,  $Au_2 Ba Sn S_4$  with an antiprismatic surrounding of barium and a twofold coordination of the independent gold atoms cannot be counted as a tetrahedral structure derived from cubic/hexagonal diamond structure but belong to tetrahedral framework structures.

The substitution with Na and Li also has proved to be successful and some Na- and several Li-bearing compounds were produced. Li compounds of the type  $A_2^I B^{II} C^{IV} S_4^{VI}$  mainly crystallize in hexagonal diamond/wurtzite related structures such as the wurtzstannite- and wurtzkesterite-type structure [51, 53–61].

Two Na-bearing compounds are described to crystallize in the tetragonal crystal system.  $Na_2 Zn Sn S_4$  adopts the kesterite-type structure in space group  $I\bar{4}$  with a severe compression along  $c$ -axis [62].  $Na_2 Ba Sn S_4$  crystallizes in space group  $I\bar{4}2d$ , but is exhibiting a higher coordination of Na, Ba and S. Analogous Ge-bearing compound ( $Na_2 Ba Ge S_4$ ) crystallizes in the trigonal crystal system in space group  $R\bar{3}c$  and shows also a higher coordination of Na, Ba and S [63].  $Na_2 Cd Sn S_4$  crystallizes in the monoclinic space group  $C2$  with tetrahedral coordination of all the contained atoms [53].

Inserting of  $NH_4^+$  representative as the divalent cation in  $A_2^I B^{II} C^{IV} S_4^{VI}$  compounds was also possible and led to the formation of a compressed chalcopyrite-like structure (space group  $I\bar{4}2m$ ) with an [4+4] (in total 8-fold) coordination of the divalent part [64]. Note that in this case instead of a tetravalent cation a trivalent was used.

As divalent cations are usually transition metals (group 4 period 7 to 12; group 12) as well as earth alkaline metals like Mg, Sr and Ba, even the rare earth element Eu and Pb mentioned for  $A_2^I B^{II} C^{IV} S_4^{VI}$  compounds. Compounds with bigger divalent cations thereby tend to adopt the compressed chalcopyrite-like structure [34, 35].

As described above,  $A_2^I B^{II} C^{IV} S_4^{VI}$  compounds contain Si, Ge and Sn as tetravalent cations.  $A_2^I B^{II} C^{IV} S_4^{VI}$  compounds containing Pb as tetravalent cation are not realized so far.

**Properties/Applications**

Due to their compositional flexibility a wide variety of physical properties have been realized for  $A_2^I B^{II} C^{IV} S_4^{VI}$  diamondlike materials. They are characterized as tunable semiconductors for solar cell applications and photovoltaics, as nonlinear optics, multiferroics and magnetic materials as well as photocatalysts. In the following abstracts some selected areas for the use of diamondlike semiconductors of the type  $A_2^I B^{II} C^{IV} X_4^{VI}$  are presented.

**Solar cells/Photovoltaics**

The usage of diamondlike semiconductors as absorbers in thin film solar cell technologies is in the focus of interest for many years. As a result, investigations on ternary chalcogenides of the type  $A^I B^{III} X_2$  are adequately accomplished with an efficiency of 22.6 % for Ga doped  $CuInS_2$  [65]. Quaternary diamondlike semiconductors of the type  $A_2^I B^{II} C^{IV} X_4^{VI}$  have been examined intensively in the last two decades. Thereby,  $Cu_2ZnSnS_4$  has attracted much attention with its high absorption coefficient, ideal band gap ( $E_g = 1.5$  eV) and non-toxic, earth-abundant elements. Up to now, an efficiency of 12.6 % was reached for selenium doped  $Cu_2ZnSnS_4$  [66] which is lower than the one of the compared chalcopyrite-based materials but still promising for the implementation as prospective absorber material. All in all, a band gap between 1.0 and 2.0 eV is suitable for application in solar cell technologies [67, 68]. Many other Cu- and Ag-bearing  $A_2^I B^{II} C^{IV} X_4^{VI}$  chalcogenides exhibit appropriate band gap values too which are consequently taken for further investigations as potential candidates for absorber layers in thin film solar cells.

**Nonlinear optics**

With the discovery of frequency doubling in a quartz crystal when being irradiated by a laser in the 1960s [69], the applicational field of nonlinear optics has come to start. It includes many physical phenomena resulting in a wide applicational area such as spectroscopy, laser medicine, optical communication and signal processing. Frequency doubling or, as it is also termed, second harmonic generation thereby holds an important role amongst second-order nonlinear optical materials. For such interactions noncentrosymmetric structures are indispensable. Frequency doubling occurs - as the description itself already says - when a material is illuminated and the frequency of the outgoing radiation is doubled. Diamondlike semiconductors on the basis of the chalcopyrite-type structure - in general sulfur-based materials - show second harmonic generation in the IR range [70–73] whereas oxide-based materials cover the UV/Vis

region [74–76, 76]. Due to the relatively low laser damage threshold depending on the narrow band gap of chalcopyrite-based materials, their application is limited [73]. Recently reported quaternary diamondlike semiconductors of the type  $A_2^I B^{II} C^{IV} S_4^{VI}$  with lithium as monovalent cation exhibit a wider band gap than the analogue Cu- or Ag-bearing compounds which makes them utterly interesting for second harmonic generation application [35, 55–57].

### **Multiferroics**

Multiferroics are materials that show simultaneously multiple ferroic ordering phenomena such as ferroelectricity, ferromagnetism and ferroelasticity [77]. The coupling between at least two of them offers interesting and new field of application. In recent years investigations were mainly done for oxidic materials like the perovskite family. However, Nernert et al. [78] showed that ternary and quaternary diamondlike semiconductors crystallizing in space group  $I\bar{4}2m$  or  $Pmn2_1$  are promising candidates for multiferroic properties. The spontaneous polarization - an indication for large coupling between the dielectric and the magnetic properties - was calculated for several Cu-bearing  $A_2^I B^{II} C^{IV} S_4^{VI}$  compounds showing high values comparable to that of  $BaTiO_3$ . Besides,  $Cu_2MnSnS_4$  is suggested to be a magnetic induced ferroelectric. Experimental studies still remain to be carried out as they would provide more accurate information.

### **Photocatalysts**

Photocatalysis is not considered to be the typical applicational field for diamondlike semiconductors. Nevertheless, some of them have been taken for investigations and even showed partly suitable properties. Tsuji et al. started their investigations with binary and ternary diamondlike semiconductors [79, 80] and expanded it to quaternary  $A_2^I B^{II} C^{IV} S_4^{VI}$  compounds [81]. Thereby,  $Cu_2ZnGeS_4$  and  $Ag_2ZnSnS_4$  using ruthenium or platinum as co-catalysator showed high activities.

### 2.2.1. Crystal structure

$A_2^I B^{II} C^{IV} X_4^{VI}$  compounds belong to the adamantine compound family and are structurally derived from cubic/hexagonal diamond structure [23, 25, 82].

In the cubic diamond structure [83] the carbon atoms form a cubic closest packing and occupy half of the tetrahedral voids which can be described as two overlapping face-centered cubic sublattices. Each carbon atom is hereby tetrahedrally surrounded by other carbon atoms.

In consideration of two conditions, multinary compounds with tetrahedral structures can be generated by substitution. The average number of valence electrons per atom has to be four and the total number of valence electrons per anion has to be eight. In the following section the substitution schema from cubic/hexagonal diamond to  $A_2^I B^{II} C^{IV} X_4^{VI}$  compounds is given which was formulated by [6]. Other substitution schemas leading to a big variety of feasible tetrahedral compounds with different molecular formulas are also possible. A general substitution approach is described by Mooser and Pearson [28], although not all known tetrahedral structures are thereby considered.

By replacing half of the atoms of group IV element (e. g. carbon) with group II and the other half with group VI elements binary compounds with general formula  $A^{II} X^{VI}$  are generated. These compounds crystallize in sphalerite-type structure, as an example ZnS (mineral sphalerite) can be given. A next substitution leads to ternary compounds of the type  $A^I B^{III} X_2^{VI}$  with chalcopyrite-type structure. As at this step two cations have to be distributed in an ordered manner through the structure the unit cell has to be doubled and at this point the transition from cubic to tetragonal crystal system occurs. Another substitution with group II and group IV elements leads to compounds with general formula  $A_2^I B^{II} C^{IV} X_4^{VI}$ , for these two tetragonal structures are proposed, the stannite- and kesterite-type structure [84].

Both structures are built of a cubic closest packing of sulfur anions. In the higher symmetric stannite-type structure (space group  $I\bar{4}2m$ ) the cations are distributed along the  $c$ -axis in form of Cu- and Fe/Sn-layers using  $Cu_2FeSnS_4$  (mineral stannite) [37] as an example (In general:  $A^I$ - and  $B^{II}/C^{IV}$ -layers). Fe is located on Wyckoff position  $2a$  with  $(0, 0, 0)$ , Sn occupies position  $2b$  with  $(0, 0, 1/2)$  and Cu is located on a superior position  $4d$  with  $(0, 1/2, 1/4)$ .

In the kesterite-type structure the Cu-layer of the stannite-type structure is formed by two kinds of cations. Using  $Cu_2ZnSnS_4$  (mineral kesterite) [85] as an example half of Cu in this particular layer is substituted with Zn. This leads to a splitting of the  $4d$  position of the stannite-type structure into two non-equivalent positions  $2c$  with  $(0, 1/2, 1/4)$  for Cu and  $2d$  with  $(0, 1/2, 3/4)$  for Zn in kesterite-type structure.

The remaining Cu is located on Wyckoff position  $2a$  with  $(0, 0, 0)$  whereas group IV element Sn remains on position  $2b$ . This results in an alternating stacking of Cu/Zn- and Cu/Sn-layers along  $c$ -axis for the kesterite-type structure (in general:  $A^I/B^{II}$ - and  $A^I/C^{IV}$ -layers).

In the Cu-Zn-layer of the kesterite-type structure partly and fully disorder between Cu and Zn can occur. For a fully disorder (both Wyckoff positions  $2c$  and  $2d$  are occupied half by Cu and half by Zn) the disordered kesterite-type structure has been proposed [86, 87] which has to be described in the higher symmetric space group  $I\bar{4}2m$ .

Derivatives of the hexagonal diamond structure can also be described by this kind of substitution schema.

Hexagonal diamond (lonsdaleite) [88] is a high-pressure polymorph of cubic diamond which can be synthesized by shock-wave loading of cubic diamond [89] or graphite [90]. The structure is built of a hexagonal closest packed arrangement with occupation of half of the tetrahedral voids. The major difference to the cubic diamond structure lies in their stacking sequences (cubic diamond: ABCABC..., hexagonal diamond: ABAB..).

The substitution of group IV element with group II and VI elements leads again to binary  $A^{II}B^{VI}$  compounds for which in the hexagonal crystal system the wurtzite-type structure named after its representative wurtzite is listed which is the high-temperature polymorph of ZnS [91]. The structurally analogue to the chalcopyrite-type structure derived from hexagonal diamond structure is the  $BeSiN_2$ -type structure [92] which marks the transition from hexagonal to orthorhombic crystal system. Substitution of the two cations in  $BeSiN_2$  with three different cations (group I, II, IV elements) leads to quaternary compounds of the type  $A_2^I B^{II} C^{IV} X_4^{VI}$ . For hexagonal diamond related  $A_2^I B^{II} C^{IV} X_4^{VI}$  compounds also two structure types are mentioned, the wurtzstannite- and wurtzkesterite-type structure [93, 94].

Both structure types are built of a hexagonal closest packing of sulfur anions but exhibit a different cation arrangement. Regarding the honeycomb set-up, an alternating stacking of Cu- and Cd/Ge-layers (in general:  $A^I$ - and  $B^{II}/C^{IV}$ -layers) is formed in the wurtzstannite-type structure (space group  $Pmn2_1$ ) using  $Cu_2CdGeS_4$  [36] as an example.

In the wurtzkesterite-type structure (space group  $Pn$ ) using  $Cu_2ZnSiS_4$  [95] as an example the cations are distributed in form of alternating Cu/Zn- and Cu/Si-layers (in general:  $A^I/B^{II}$ - and  $A^I/C^{IV}$ -layers) which leads to the monoclinic crystal system for wurtzkesterite-type compounds instead of the orthorhombic crystal system as realised in the wurtzstannite-type structure.

The substitution schema from cubic/hexagonal diamond to  $A_2^I B^{II} C^{IV} X_4^{VI}$  via  $A^{II} X^{VI}$  and  $A^I B^{III} X_2^{VI}$  compounds with indication of the structure types is summarized in Table 2.1. The crystal structures of the corresponding structure types are shown in Figures 2.1, 2.2 and 2.3.

**Table 2.1.:** Summarization of pronounced structure types derived from cubic/hexagonal diamond structure reaching  $A_2^I B^{II} C^{IV} X_4^{VI}$  compounds.

Composition	2 layer stacking	3 layer stacking
A	lonsdaleite	diamond
AX	wurtzite	sphalerite
ABX <sub>2</sub>	BeSiN <sub>2</sub>	chalcopyrite
A <sub>3</sub> BX <sub>4</sub>	enargit	famatinite
A <sub>2</sub> BCX <sub>4</sub>	wurtzstannite	stannite
	wurtzkesterite	kesterite

DIAMONDLIKE SEMICONDUCTORS

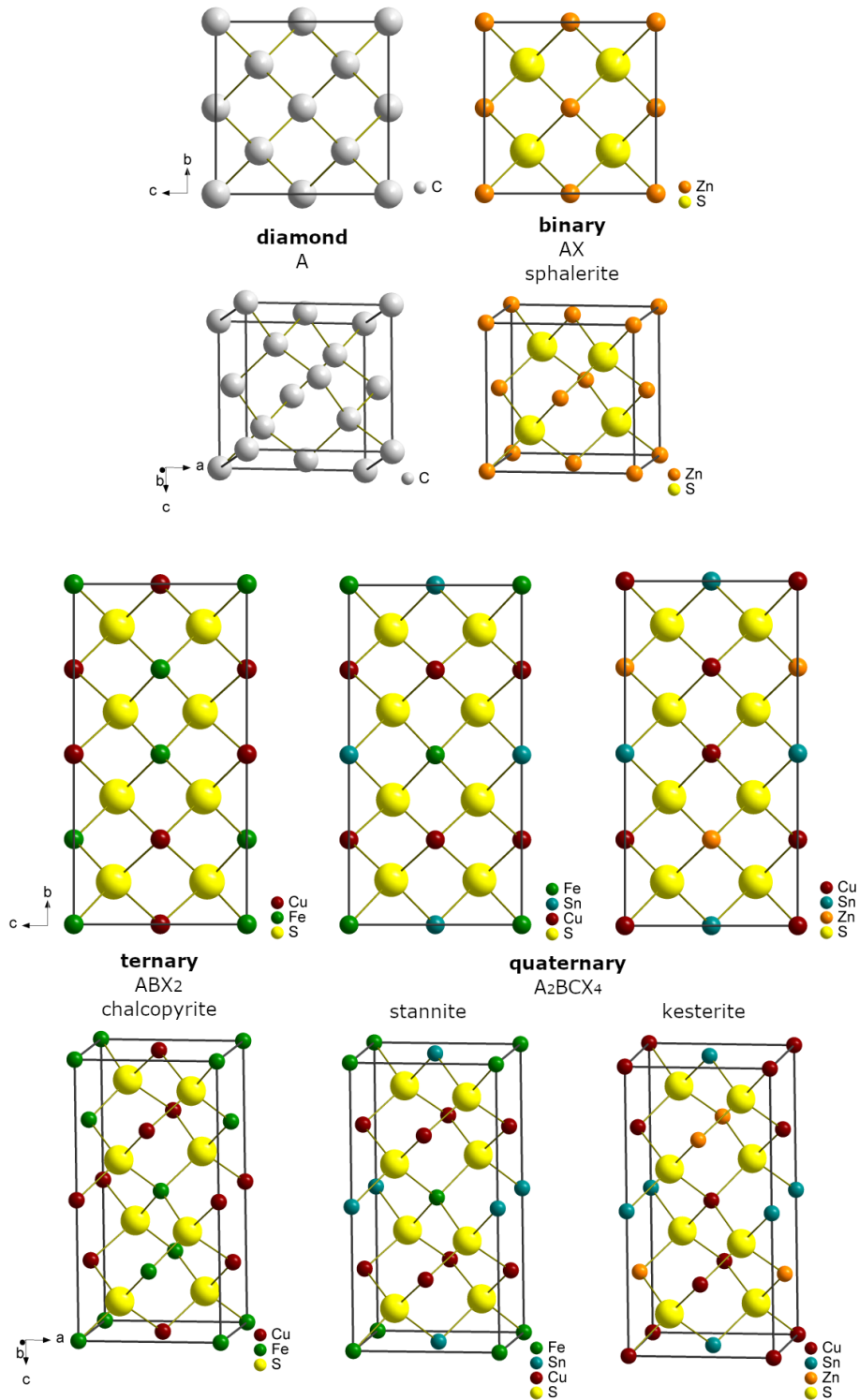
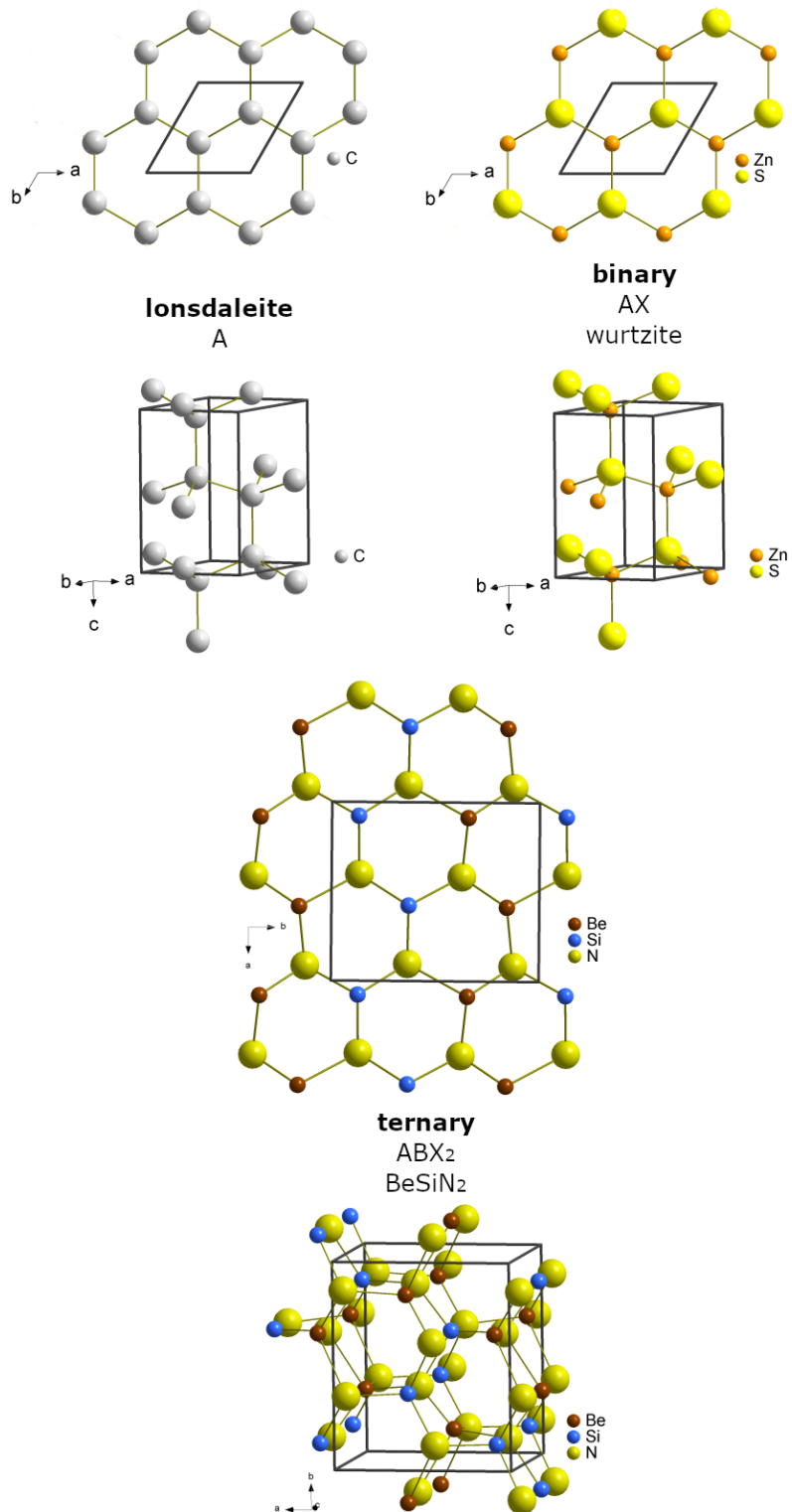
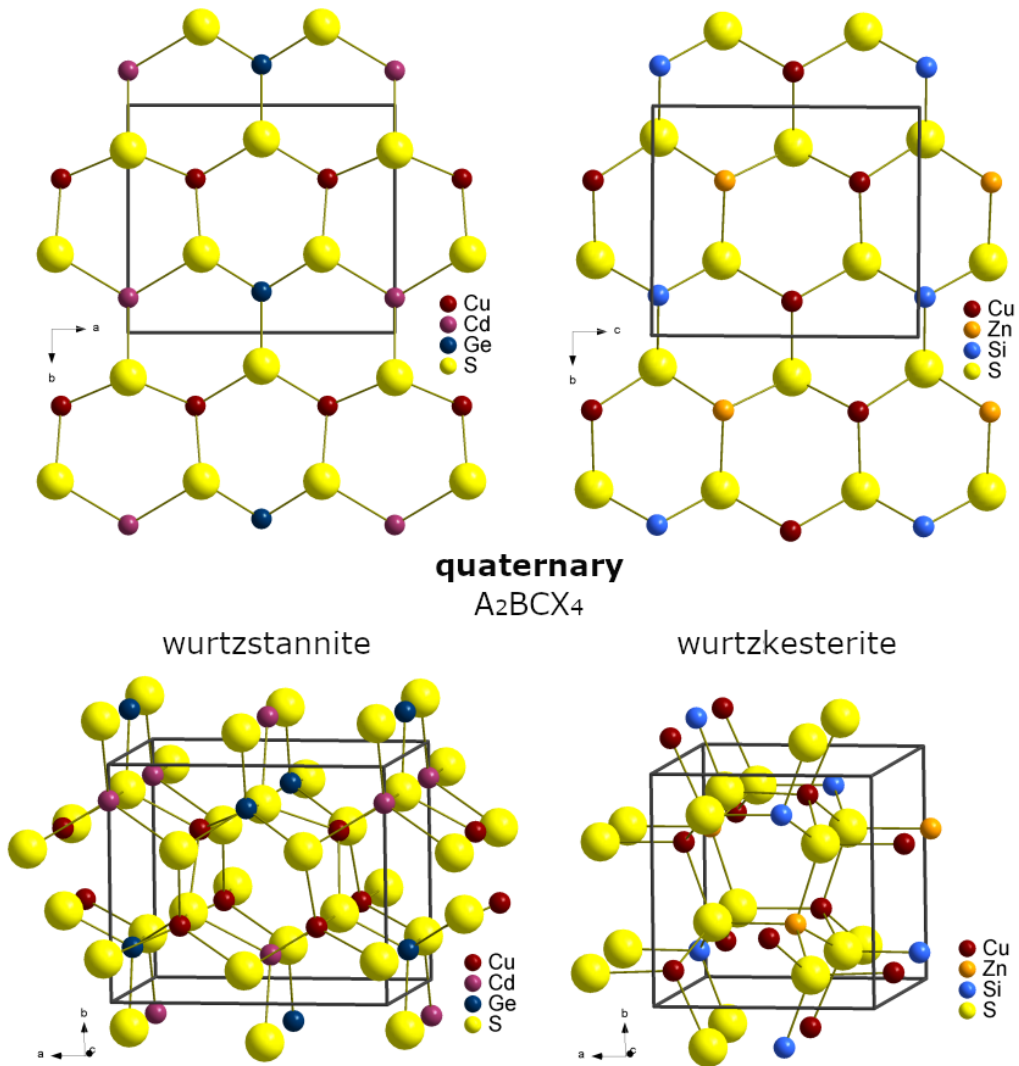


Figure 2.1.: Two- and threedimensional representation of the crystal structures of cubic diamond [96], sphalerite [97], chalcopyrite [98], stannite [37] and kesterite [85].



**Figure 2.2.:** Two- and threedimensional representation of the crystal structures of lonsdaleite [88], wurtzite [91] and BeSiN<sub>2</sub> [92].



**Figure 2.3.:** Two- and threedimensional representation of the crystal structures of wurtzstannite-type using  $Cu_2CdGeS_4$  [36] and wurtzkesterite-type structure using  $Cu_2ZnSiS_4$  [95] as example.

**Group-subgroup relation between cubic diamond and stannite-/kesterite-type structure**

The structural relation between cubic diamond and its derivative structures as the sphalerite-, stannite- or kesterite-type structures can be described using the Bärnighausen formalism [99, 100] and is presented in Figure 2.4.

Starting from space group  $Fd\bar{3}m$  for cubic diamond structure via *translationengleiche* transition with index 2 the sphalerite-type structure with space group  $F\bar{4}3m$  is reached. Half of the carbon atoms are substituted by zinc whereas the other half is replaced by sulfur, therefore Wyckoff position  $8a$  splits up into two fourfold positions  $4a$  (Zn) and  $4c$  (S). Due to the splitting of the Wyckoff position  $8a$  forced by substitution and therefore loss of the inversion center half of the symmetry is reduced. Data are taken from [96] for cubic diamond and from [97] for sphalerite-type ZnS. In the next step a *translationengleiche* transition with index 3 occurs and space group  $I\bar{4}m2$  is reached. At this step the transition from cubic to tetragonal crystal system takes place with the loss of the threefold spacediagonal axis. In the next symmetry reduction to space group  $P\bar{4}m2$  (*klassengleiche* transition with index 2) Wyckoff position  $2a$  splits up into two independent cation sites  $1a$  and  $1c$ . In the Bärnighausen tree  $\text{CaZnSe}_2$  is mentioned as an example for space group  $P\bar{4}m2$  with data taken from [101]. From  $P\bar{4}m2$  via *translationengleiche* transition with index 2 and doubling of the unit cell in  $c$ -axis the stannite-type structure with space group  $I\bar{4}2m$  is reached. Wyckoff position  $1a$  splits up into two twofold positions  $2a$  (Fe) and  $2b$  (Sn) whereas Wyckoff position  $1c$  changes to a fourfold position  $4d$  (Cu). The data for  $\text{Cu}_2\text{FeSnS}_4$  used here are taken from [37]. Another symmetry reduction leads to the kesterite-type structure with space group  $I\bar{4}$ . The fourfold position  $4d$  splits up into two positions  $2c$  and  $2d$ , so that kesterite-type structure is built up of 4 non-equivalent twofold cation positions with Cu1 on position  $2a$ , Cu2 on  $2c$ , Sn located on position  $2b$  and Zn on  $2d$  with data for  $\text{Cu}_2\text{ZnSnS}_4$  taken from [85].

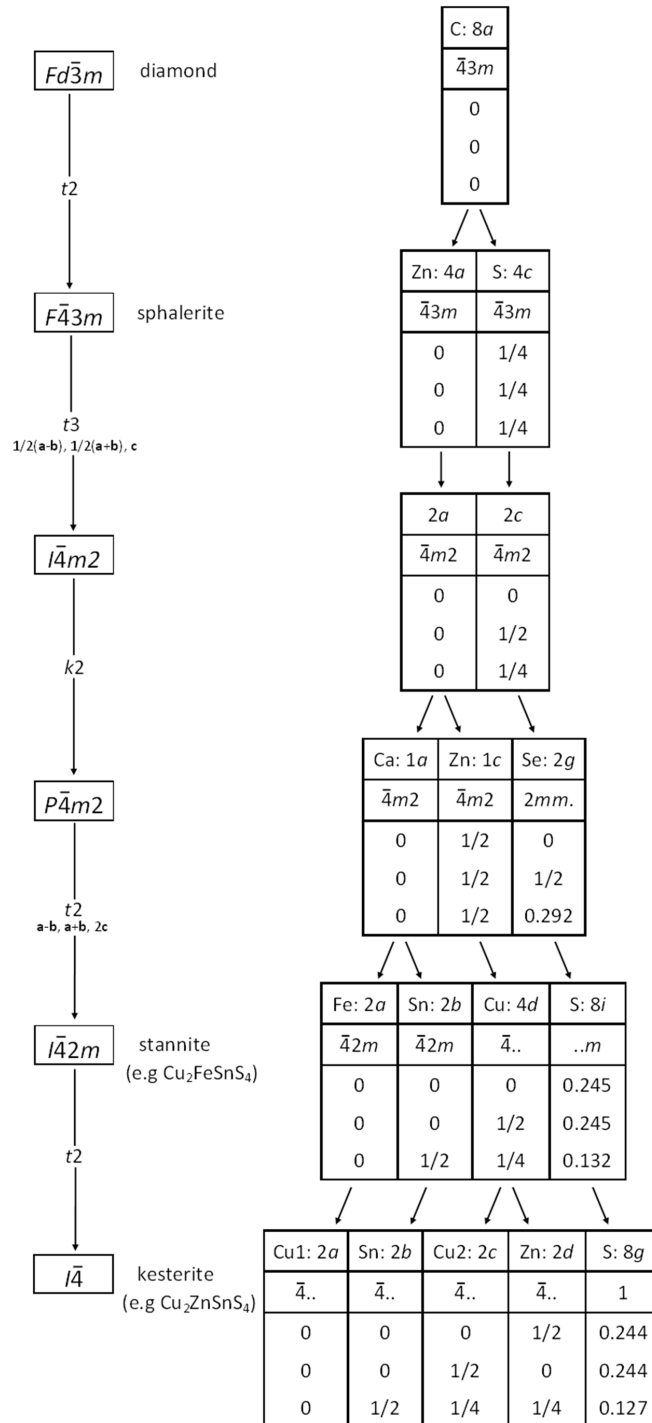


Figure 2.4.: Group-subgroup scheme for the grouptheoretical relation between cubic diamond and stannite-/kesterite-type structure.

### Group-subgroup relation between hexagonal diamond and wurtzstannite-/wurtzkesterite-type structure

Analogue to the group-subgroup relation between the cubic diamond and stannite-/kesterite-type structure a grouptheoretical relation [99, 100] between the hexagonal diamond and wurtzstannite-/wurtzkesterite-type structure can be given and is presented in Figure 2.5.

Starting from space group  $P6_3/mmc$  for hexagonal diamond structure (data from [88]) via *translationengleiche* transition with index 2 wurtzite-type structure is reached, a ZnS analogue to the sphalerite-type structure in the hexagonal crystal system in which Zn occupies half of the tetrahedral voids in a hexagonal closest packing of sulfur atoms. At this step of the symmetry reduction Wyckoff position  $4f$  splits up into two distinct atom positions  $2b$  with  $(1/3, 2/3, 0.000)$  for Zn and  $2b$  with  $(1/3, 2/3, 0.375)$  for S, data are taken from [91]. In the next symmetry reduction to  $Cmc2_1$  (data from [14]) a *translationengleiche* transition with index 3 occurs. At this step an origin shift is set which marks the transition from hexagonal to orthorhombic crystal system. From  $Cmc2_1$  via *klassengleiche* transition with index 2 we come to space group  $Pmc2_1$ . Due to the loss of the C-centered symmetry each anion and cation position splits up into two positions  $2a$  and  $2b$ . From  $Pmc2_1$  via *klassengleiche* transition with index 2 and doubling of the unit cell in  $a$ -axis the wurtzstannite-type structure with space group  $Pmn2_1$  is reached. Wyckoff position  $2a$  splits up into two independent and general positions  $2a$  and  $2a$  whereas position  $2b$  changes to a fourfold position  $4b$ . As an example for the wurtzstannite-type structure in the Bärnighausen tree  $Cu_2CdGeS_4$  (data from [36]) was taken in which Cu occupies the fourfold position  $4b$  with  $(0.274, 0.344, 0.141)$ , Cd is located on  $2a$  with  $(0, 0.152, 0.005)$  and Ge on  $2a$  with  $(0, 0.821, 0.510)$ . The same splitting is applied for the anion positions which makes the wurtzstannite-type structure built up of 3 independent sulfur atoms (Wyckoff positions  $2a$ ,  $2a$  and  $4b$ ). A direct subgroup to the wurtzstannite-type structure is the wurtzkesterite-type structure with space group  $Pn$  with a *translationengleiche* transition with index 2. Analogue to the symmetry reduction from stannite-type structure to kesterite-type structure the fourfold position  $4b$  splits up into two twofold positions  $(2a, 2a)$ . Therefore, in the wurtzkesterite-type structure 4 crystallographic independent cations on non-equivalent Wyckoff positions are present. Additionally, the wurtzkesterite-type structure contains 4 independent sulfur atoms which are generated by the same kind of splitting as the cation positions. As an example for the wurtzkesterite-type structure  $Cu_2ZnSiS_4$  is used in the Bärnighausen tree (and not its oxidic structure type) with data taken from [95].

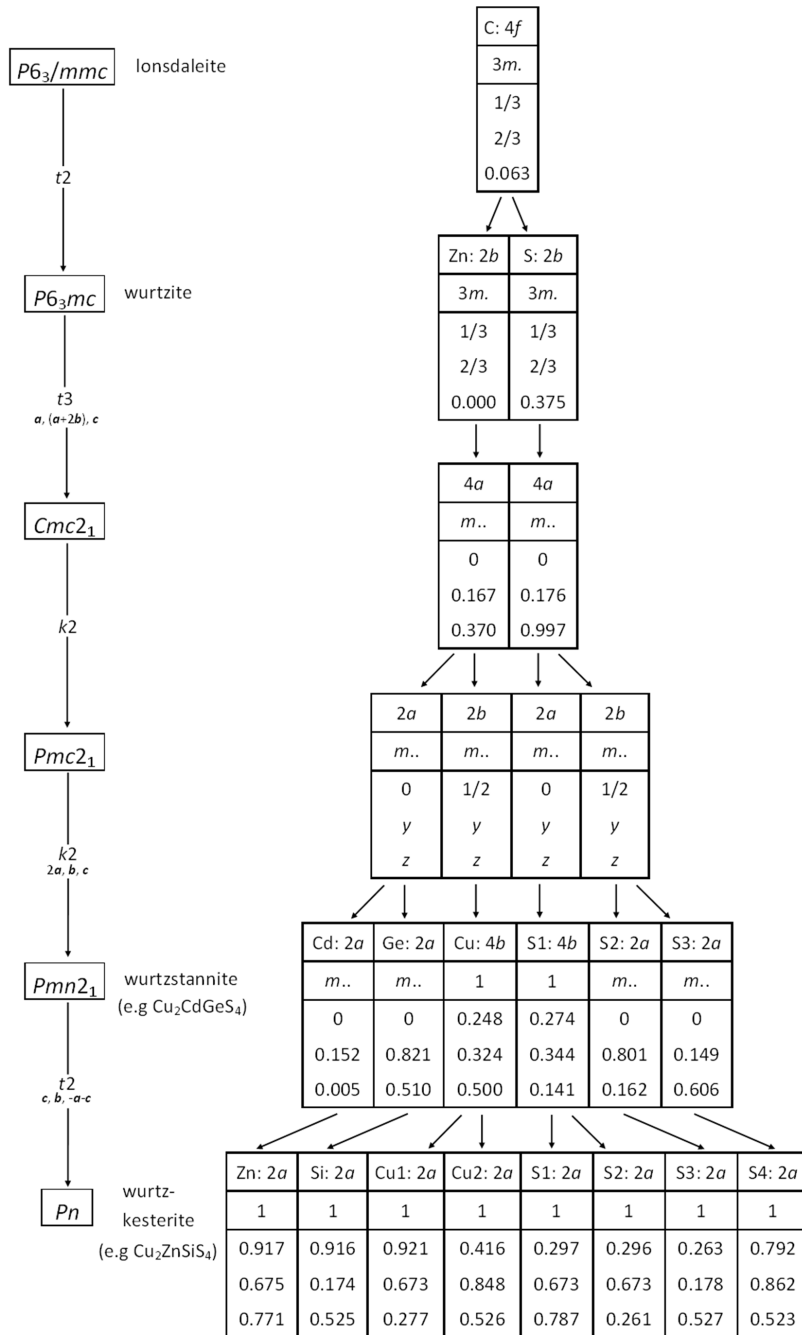


Figure 2.5.: Group-subgroup scheme for the grouptheoretical relation between hexagonal diamond and wurtzstannite-/wurtzkesterite-type structure.

### 2.2.2. Compressed chalcopyrite-like structure

As mentioned in the section before some quaternary compounds of the type  $A_2^I B^{II} C^{IV} X_4^{VI}$  with bigger divalent cations such as Ba, Eu, Pb adopt the compressed chalcopyrite-like structure [34, 35]. The compressed chalcopyrite-like structure belongs to space group  $I\bar{4}2m$  but cannot be considered as a tetrahedral structure anymore as the divalent cation as well as the sulfur anion exhibit higher coordination than in usual tetrahedral structures. Actually, it may be more accurate to name the compressed chalcopyrite-like structure compressed stannite-like structure as the same Wyckoff positions are occupied and the same cation distribution is present in the compressed chalcopyrite-like structure as in the stannite-type structure.

The deviation from sphalerite-type structure to the chalcopyrite-type structure implying the transition from cubic to tetragonal crystal system is associated with the occurrence of a small compression along  $c$ -axis. This compression is attributed inter alia to the difference of the radii of the by now two distinct contained cations (e.g.  $CuFeS_2$ ), so that the  $c$ -axis of the chalcopyrite-type structure is in fact a bit smaller than the doubled  $a$ -axis as it should be expected [102]. This circumstance also applies to compounds containing more than two different cations such as stannite- or kesterite-type compounds.

The incorporation of a bigger cation (such as Ba, Pb, Eu) as it is realized in compounds adopting the compressed chalcopyrite-like structure leads to a stronger compression along  $c$ -axis due to the larger difference of the cationic radii and consequently the formation of an 8-fold coordination of the divalent cation and a 5-fold coordination of the sulfur anion. In addition, the larger cations have a greater tendency for an 8-fold coordination instead of a tetrahedral one.

The  $c/a$ -relation or rather the term  $2-c/a$  is associated with this kind of tetragonal compression. For compounds exhibiting a small compression along  $c$ -axis (e.g.  $CuFeS_2$ ,  $Cu_2FeSnS_4$ ,  $Cu_2ZnSnS_4$  [84, 98]) the expression  $2-c/a$  attains a value close to zero. Compounds adopting the compressed chalcopyrite-like structure (e.g.  $Ag_2BaGeS_4$ ,  $Li_2PbGeS_4$ ,  $Li_2EuGeS_4$  [34, 35]) show a stronger compression which is expressed by values about 0.8 (closer to 1) for the term  $2-c/a$ .

The coordination polyhedra of the divalent cation in the compressed chalcopyrite-like structure can be described as a distorted dodecahedra which consists of two interpenetrating distorted tetrahedra (Figure 2.6) which share corners with 8 neighbouring  $BS_8$ -polyhedra. Sulfur in this structure type is surrounded by two monovalent, two divalent and one tetravalent atom in forms of a quadratic pyramide (Figure 2.6); the  $SM_5$ -polyhedra are edge-shared between themselves.

The occurrence of such a strong compression along the  $c$ -axis leading to a higher coordination of some ions should also be possible in space group  $I\bar{4}$ , however, has not been realized so far. For  $\text{Na}_2\text{ZnSnS}_4$  [62] - an example which crystallizes in the kesterite-type structure - a value of 0.59 for the term  $2-c/a$  is given which is still not sufficient to ensure an 8-fold coordination of the sodium atom on position  $2a$  and a 5-fold coordination of the sulfur atom.

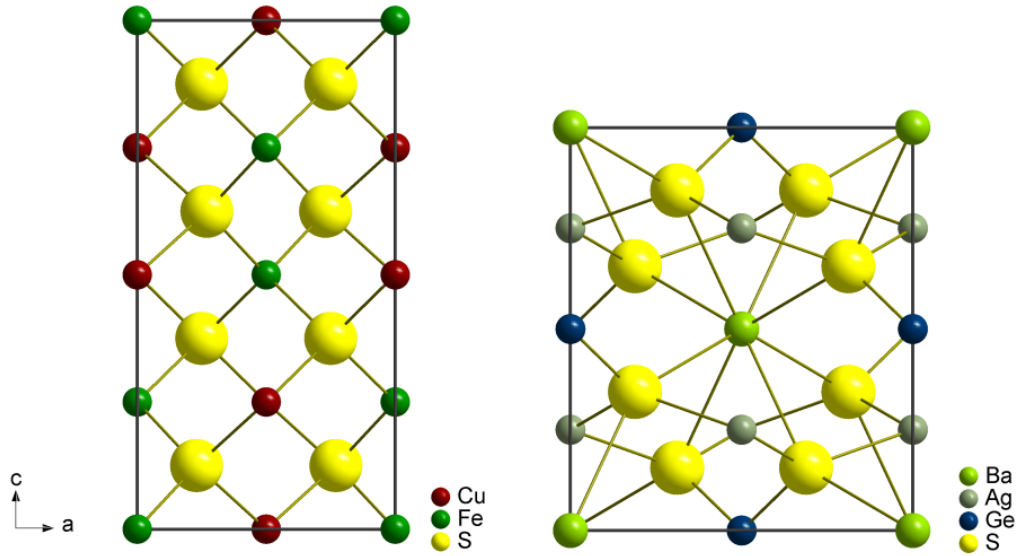


**Figure 2.6.:** Structural comparison of chalcopyrite-type  $\text{CuFeS}_2$  (left) [98] and compressed chalcopyrite-like  $\text{Ag}_2\text{BaGeS}_4$  (right) [34] with indication of the occurring bonds between cations and anions.

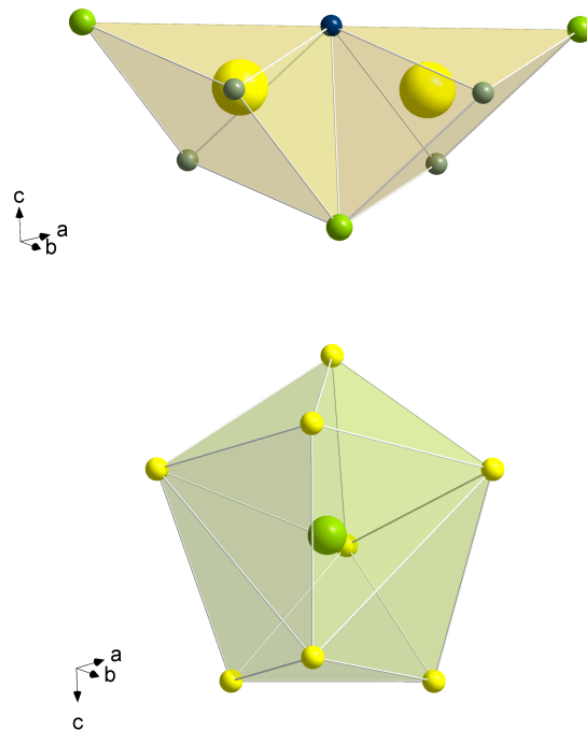


**Figure 2.7.:** Coordination polyhedra of two sulfur atoms in form of edge-sharing quadratic pyramids (top) and of the divalent  $\text{Ba}^{2+}$  cation in form of a distorted dodecahedra (bottom) in compressed chalcopyrite-type  $\text{Ag}_2\text{BaGeS}_4$  [34].

## 3. Spinels

### 3.1. Introductory remarks

Spinels are a big class of materials with general formula  $AB_2X_4$  forming various oxides, sulfides, selenides, tellurides and (pseudo)halides. Thereby, spinel compounds containing II-III, IV-II, II-I and VI-I cations are feasible [103]. Due to their manifold varied compositions and distinct cation distribution a big applicational field is provided for spinel compounds. Ferrit materials have currently the greatest technical significance among oxidic spinels. These are ferrimagnetic or antiferromagnetic materials [104] which have contributed advantages in electrical engineering and electronics.

For thiospinels also a wide range of physical phenomena is mentioned in the literature including supraconductivity [105, 106], metallic conductivity [107], semiconducting [108] and insulating [109] properties as well as multiferroic [110, 111] and varied magnetic properties [112, 113]. The field of application therefore include photocatalysis, optoelectronics and many others.

The focus of this work is on the preparation and characterization of quaternary thiospinels with general formula  $A_2^I B^{II} C_3^{IV} X_8^{VI}$ . Compared to  $A_2^I B^{II} C^{IV} X_4^{VI}$  compounds the biggest group among  $A_2^I B^{II} C_3^{IV} X_8^{VI}$  thiospinels are also Cu-bearing compounds [114–122]. A few Ag compounds of this type are also mentioned in the literature, even natural  $Ag_2 B^{II} C_3^{IV} X_8^{VI}$  compounds such as toyohaite ( $Ag_2 Fe Sn_3 S_8$ ) exist too [14, 123, 124]. One attempt producing a Na-containing  $A_2^I B^{II} C_3^{IV} X_8^{VI}$  compound is described in the literature as well, its crystal structure is not quite clarified though [125]. As divalent cations the following transition metals Fe, Mn, Co, Ni, Cd and Zn are mentioned. The biggest group regarding tetravalent cations are  $A_2^I B^{II} C_3^{IV} X_8^{VI}$  compounds with  $C = Sn$  [114–117, 119, 120]. The substitution of Sn by Ti was also quite successful and lead to the production of a few Ti contained compounds [118, 121]. By now, even one Zr-bearing  $A_2^I B^{II} C_3^{IV} X_8^{VI}$  compound is known [122].

As the majority of the tetrahedral and half of the octahedral voids are unoccupied, compounds adopting the spinel structure offer the possibility for ion transport and are therefore interesting materials for the use in batteries. Due to their structural stability and the cavities contained, spinel compounds can also be used as host lattices for

ion intercalation [126–128]. Especially lithium intercalation compounds are promising materials as cathodes in batteries [129].

## 3.2. Spinel structure

The spinel structure was first described independently by W. H. Bragg and S. Nikishawa and belongs to those crystal structures in which the tetrahedral as well as the octahedral voids are occupied by cations [130, 131].

The ideal spinel structure is built of a cubic closest packing of anions and in the normal spinels 1/8 of the tetrahedral voids are occupied by A-cations and 1/2 of the octahedral voids by B-cations. The following general formula  $A_T[B_2]_O X_4$  is given for normal spinels. The structure of a normal cubic spinel is shown in Figure 3.1 using the mineral spinel with general formula  $MgAl_2O_4$  [132] as an example. Hereby, 1/8 of the tetrahedral voids is occupied by Mg-cations and 1/2 of the octahedral voids by Al-cations. In inverse spinels half of the octahedral voids are occupied by half of the A- and half of the B-cations. The remaining B-cations occupy one eighth of the tetrahedral voids leading to a general formula of  $B_T[AB]_O X_4$  for inverse spinels.

For the normal and inverse distribution the term degree of inversion was introduced where  $x = 0$  equates to the normal and  $x = 1$  to the inverse spinel, generally indicated by  $(A_{1-x}B_x)[A_xB_{2-x}]X_4$ . Intermediate values for spinels with normal and inverse distribution of the cations simultaneously are also possible. Actually, the distribution in known compounds is mostly between the normal and inverse case. For example,  $MgFe_2O_4$  is with a degree of inversion of 0.9 at room-temperature close to the inverse configuration with just some Mg cations on the tetrahedral sites. With higher temperatures the degree of inversion decreases and more Mg cations are located on the tetrahedral voids [133]. The degree of inversion is always dependent on the temperature.

In general, the cation distribution in the spinel-type structure and therefore also the degree of inversion is attributed to the ionic radii, the electrostatic ratio of the lattice energy and the ligand stabilisation energy. The consideration of the ionic radii is for compounds forming spinel-type structures not sufficient as distortions lead to a shift of the anions in [111] direction which is accompanied by an expansion or reduction of the tetrahedral and octahedral voids, respectively. II-III spinels without distortion prefer the inverse configuration whereas the normal distribution is pronounced when a distortion occurs. The majority of II-III compounds form a normal distribution with the divalent cations located on the tetrahedral and the trivalent cations on the octahedral position (e. g.  $MgAl_2O_4$  [132],  $FeCr_2O_4$  [134],  $ZnFe_2O_4$  [135]). Only few II-III spinels including ferrites (e. g.  $NiFe_2O_4$  [136]) exhibit a cation distribution according

to the inverse configuration. For most IV-II spinels the normal distribution with the tetravalent cations on the tetrahedral and the divalent cations on the octahedral site is indicated (e. g.  $\text{GeMg}_2\text{O}_4$  [137]), however, also compounds are known exhibiting the inverse configuration (e. g.  $\text{TiMg}_2\text{O}_4$  [138]). Miscibility among spinel compounds has also been observed which probably influence the cationic distribution as well. In the  $\text{MgFe}_2\text{O}_4$ - $\text{MgAl}_2\text{O}_4$  solid solution series a transition from (nearly) inverse to normal spinel is obtained by the successive substitution of Fe with Al [139]. For spinel compounds containing transition metals the ligand field theory particularly has to be considered for the cationic distribution whether the tetrahedral or octahedral site is preferred.

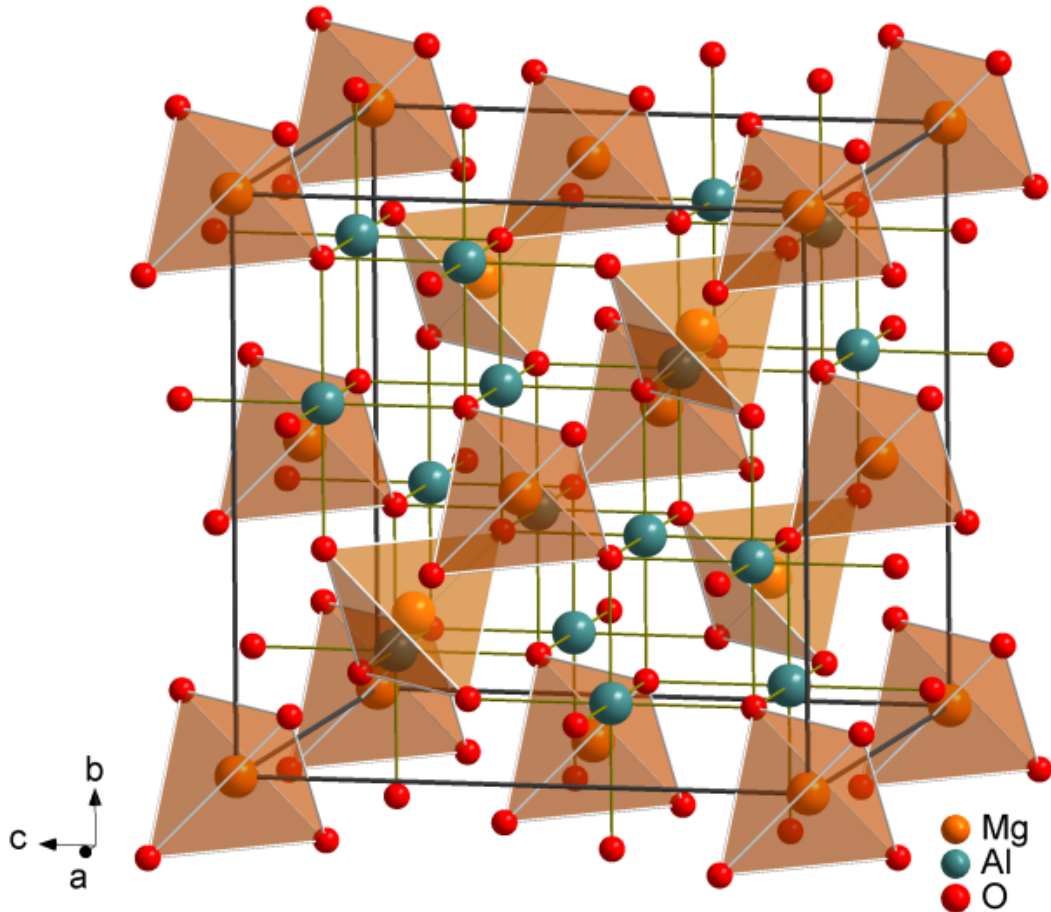


**Figure 3.1.:** Unit cell of  $\text{MgAl}_2\text{O}_4$  [132]; octahedral coordination of Al is presented by bonds between aluminium and oxygen; tetrahedral surrounding of Mg is indicated as  $\text{MgO}_4$ -tetrahedra.

The  $A_2^I B^II C_3^{IV} X_8^{VI}$  compounds considered in this thesis crystallize in a spinel-like structure where the A-cations are located on 1/8 of the tetrahedral voids and the B- and C-cations are statistically distributed on 1/2 of the octahedral voids. The statistical distribution of B- and C-cations at the octahedral site leads to the formation of a slightly distorted octahedra whereas for monovalent A-cations an ideal tetrahedra is formed.

### Deviations from the ideal spinel structure

The ideal spinel-type symmetry with space group  $Fd\bar{3}m$  can be lowered by certain effects such as rotation of the polyhedra, cation or magnetic ordering, removing individual atoms or occupation of unoccupied positions (interstitial sites). Transitions between the ideal spinel-type structure and distorted structures can be described using the Bärnighausen formalism [99, 100]. A relevant section - even though without the description of the corresponding Wyckoff positions - is presented in Figure 3.2 where some derived structures are explained with appropriate examples more detailed hereafter. Deviations within the cubic crystal system and from cubic to tetragonal and orthorhombic crystal system are thereby feasible.

For the formation of a tetragonal structure usually transition metals with Jahn-Teller distortion are contained. Jahn-Teller distortion is observed when the degenerated orbitals are occupied irregularly (*eg* for octahedral coordination and *t<sub>2</sub>* for tetrahedral coordination for high spin configuration) [140]. The distortion occurs to eliminate the degeneracy and achieve therefore a lower energy. The energetical lowering of the orbitals which are connected to the *xy*-plane leads to a compression or flattening of the polyhedra. When these orbitals have higher energy than the ones connected to the *z*-axis an elongation of the polyhedra is observed.

An elongation of the octahedra is realized in  $Mn_3O_4$  (hausmannite) which adopts a tetragonal spinel-type structure with a normal cation configuration in space group  $I4_1/amd$  [141]. The  $d^4$ -configuration (high spin) of  $Mn^{3+}$  tends to an octahedral surrounding, in this process only one of the *eg* orbitals is filled with an electron whereas the others are empty. This causes the lowering of the  $d_{z^2}$ -orbital which leads to a repulsion in *z*-direction forming an elongated octahedra. In the course of this symmetry reduction the loss of the 3-fold axis occurs expressed by a *translationengleiche* transition with index 3.  $CuCr_2O_4$  is an example exhibiting a flattening of the  $CuO_4$ -tetrahedra in space group  $I4_1/amd$  due to the irregular occupation of the *t<sub>2</sub>* orbitals with two fully and one half filled [142].

A further symmetry reduction leads to space groups *Imma* and *Fddd* among others.  $\text{Fe}_3\text{O}_4$  (magnetite) consists of divalent and trivalent iron cations whereas the trivalent exhibit  $d^5$ -configuration with no preference for tetrahedral or octahedral positions, however, the divalent iron cations ( $d^6$ -configuration) prefer the octahedral site leading to an inverse spinel configuration with mixed valent Fe cations on octahedral position [143]. Below 120 K an ordering between the di- and trivalent irons is observed resulting in an orthorhombic symmetry with space group *Imma* [144].

$\text{LiMn}_2\text{O}_4$  is known to crystallize in the ideal spinel-type [145] as well as in a tetragonal derived structure [146]. Additional reflections at lower temperature indicate an orthorhombic symmetry with space group *Fddd* [147]. The transition to the orthorhombic phase is not fully elucidated, however, could be due to a charge or polaron ordering.

For  $\text{LiFe}_5\text{O}_8$  two polymorphs are known where the high-temperature phase crystallizes in the ideal spinel-type structure exhibiting an inverse configuration with Fe on tetrahedral and Li and Fe statistically distributed on octahedral sites. The low-temperature phase shows an ordering of the octahedral site in space group  $P4_332$  forming a primitive cubic cell [148].

In the cubic polymorph of  $\text{AlV}_2\text{O}_4$  the di- and trivalent vanadium atoms are distributed on the octahedral site [149]. Around 700 K a phase transition to the rhombohedral space group  $R\bar{3}m$  occurs which is associated with an ordering of the mixed valent vanadium cations [150]. Another example to crystallize in space group  $R\bar{3}m$  is the thiospinel  $\text{CuTi}_2\text{S}_4$  [151].

$F\bar{4}3m$  as a direct subgroup to  $Fd\bar{3}m$  indicates the ordering of the tetrahedral site by splitting of the  $8a$  position into two non-equivalent positions  $4a$  and  $4d$ . As an example quaternary  $\text{LiFeCr}_4\text{O}_8$  can be described with Li and Fe on two crystallographically independent tetrahedrally coordinated positions [152].

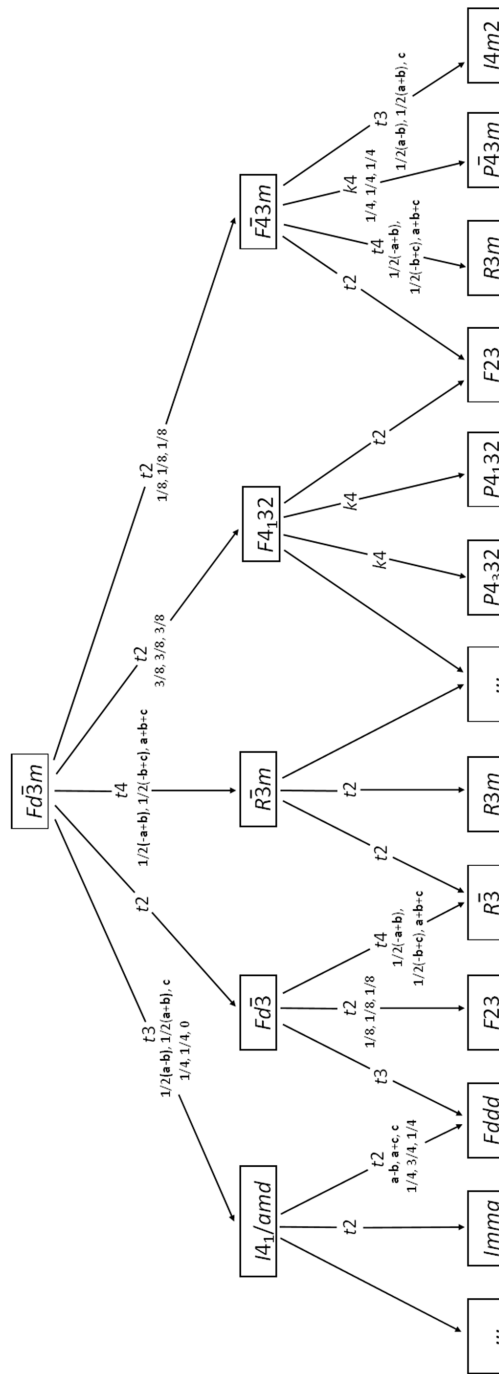


**Figure 3.2.:** Group-subgroup relations - without description of corresponding Wyckoff positions - between ideal spinel-type structure (space group  $Fd\bar{3}m$ ) and selected derived structures of known examples exhibiting specific distortions.

## 4. Methodology

### 4.1. Preparative Methods

All compounds reported in this thesis were prepared using the mechanochemical synthesis method. In the following section a detailed description of this synthesis approach is given including some historical aspects.

#### 4.1.1. Mechanochemical Synthesis

Benjamin and his colleagues from the Nickel Company developed 1966 a new synthesis method for materials which are difficult or impossible to synthesize by conventional techniques. Therefore they introduced the term mechanochemical milling which is a solid state powder process (starting from elemental powder mixtures) in which the materials are milled under material transfer to gain a homogenous powder [153]. Thereby, the particles are deformed due to the high energy impact force in the milling set-up and react together in form of cold welding. A big variety of materials were synthesized by now using this process including equilibrium and non-equilibrium phases such as supersaturated solid solutions, metastable, quasicrystalline, amorphous and nanostructured alloys [154]. Even though the disordering of ordered phases could be realized using this synthesis approach. The process of mechanical alloying is described in detail by Benjamin and his colleagues in several studies [153, 155, 156].

An expansion of the term mechanical alloying is the mechanochemical milling referred to as mechanochemical synthesis. Due to the mechanical energy generated by the grinding process, chemical reactions are induced and new materials can be synthesized.

The mechanochemical synthesis is highly complex and the understanding of its process remain an important issue so far. The successful outcome of a milling experiment is thereby influenced by several different parameters such as rotational speed, milling atmosphere, milling time, material and size of the grinding beaker, material, size and number of the grinding balls and the filling ratio of the grinding material also specified as the ball to powder ratio. Another significant parameter is the free volume, there has to be enough space in the grinding beaker in which the material is able to move.

Due to the repeated welding and fracturing of the powder particles a new surface is

created and therefore the contact area between the particles is increased. This leads to an increase of the reaction kinetics and allows reactions to occur which require usually high temperatures [154].

Two different types of reactions are thereby described [154, 157], which occur in mechanochemical synthesis processes. The gradual formation of a product with the grinding time is summarized in the gradual transformation type. The other reaction type is named the mechanically induced self-sustaining reaction (MSR) also known as the self-propagating combustion reaction. The reaction occurs after a certain time of milling (activation time) and implies thereby an increase of the temperature.

For mechanochemical synthesis as well as mechanical alloying the use of various milling types are mentioned in the literature which differ in their capacity, efficiency or maximum operating speed. The most commonly used milling type thereby is the planetary ball mill [157]. Planetary ball mills have their name from the planet-like movement of their grinding beakers. The utilized beakers are attached to a rotating support disk and rotate in opposite direction around their own axis (Figure 4.1). Due to that two opposite directed centrifugal forces are generated which have an effect on the content of the grinding beaker (sample and grinding balls). This results in the occurrence of the friction effect where the grinding balls run down inside the wall of the grinding beaker followed by the impact effect where the grinding balls hit the (opposing) inner wall of the grinding beaker (Figure 4.1). Furthermore, the ground material is influenced by the impact between the grinding balls [154].

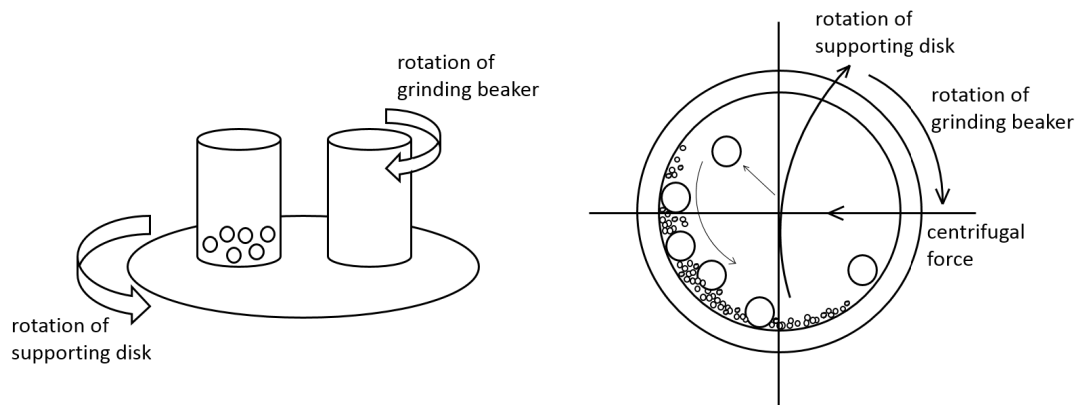


**Figure 4.1.:** Schematic illustration of milling set-up in planetary ball mills with two grinding beakers (left) and ball motion inside the grinding beakers according to [154] (right).

Mechanochemistry and especially mechanochemical synthesis has gained new interests as more economical and environmentally friendly synthesis techniques by reducing solvent consumption as well as reducing reaction temperature and time. Besides, mechanochemistry is not only suitable for the production of solids or inorganic compounds but also very promising for organic as well as organometallic synthesis by now [158–160].



**Figure 4.2.:** High energy Mill Pulverisette 6 (left) and 7 classic line (right).

Grinding beakers and balls provided by Fritsch (Idar-Oberstein, Germany) are available from different materials and sizes including agate, polypropylene, silicon nitride, sintered corundum, Fe-Cr-steel, tungsten carbide and zirconia. For this work various planetary ball mills were used as the PULVERISETTE 6 (classic line) and the PULVERISETTE 7 (classic and premium line). The PULVERISETTE 7 premium line was especially used for the preparation of the Li-bearing thiospinels. For each synthesis a 45 mL zirconia grinding beaker with six zirconia grinding balls with a diameter of 15 mm was used. The grinding beaker thereby was filled under Ar-atmosphere.

#### 4.1.2. H<sub>2</sub>S furnace

For the crystallization of the ground sulfidic powders two tube furnaces were used, a Gero furnace equipped with a SiO<sub>2</sub>-tube (diameter: 70 mm) and a HTM Reetz furnace with a Al<sub>2</sub>O<sub>3</sub>-tube (diameter: 38 mm). External heating controller (a Gero of the type 170595/7RU for the tube furnace with the SiO<sub>2</sub>-tube and an Eurotherm 3504 for the tube furnace with the Al<sub>2</sub>O<sub>3</sub>-tube) were connected to a Pt-Rh/Pt-thermocouple to set and control the reaction time and temperature. Excess H<sub>2</sub>S gas was introduced

## METHODOLOGY

---

into 20 % diluted sulfuric acid and subsequently into 15 % diluted sodium hydroxide to convert the harmful  $\text{H}_2\text{S}$  gas into nontoxic  $\text{Na}_2\text{SO}_3$ :

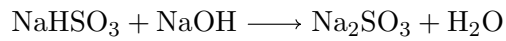
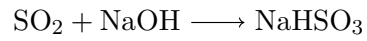
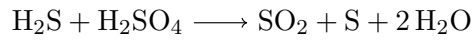


**Figure 4.3.:** Gero furnace with  $\text{H}_2\text{S}$  equipment used for the crystallization of the milled products.



**Figure 4.4.:** HTM Reetz furnace with  $\text{H}_2\text{S}$  equipment used for the crystallization of the milled products.

## 4.2. X-ray diffraction

### 4.2.1. Theoretical principles

X-ray diffraction is probably the most important analytical characterization method in solid-state chemistry.

In 1895, during experiments with a cathode ray tube, W. C. Röntgen discovered an invisible, hitherto unknown radiation with enormous penetration power [161]. The X-ray radiation named after its discoverer is an electromagnetic radiation with a wavelength of  $\lambda = 0.01 - 10$  nm. If X-ray radiation of a specific wavelength strikes matter, three types of secondary radiation are generated: scattered radiation, fluorescence radiation and Compton radiation. For X-ray crystal structure analysis only the scattered radiation is important.

Crystals are defined as three-dimensional, periodic arrays of atoms that can be considered as a three-dimensional (crystal) lattice. In order to observe diffraction phenomena, the wavelength of the applied electromagnetic radiation must be compatible with the distances of the scattering centers. The scattering centers in crystals are the electron shells of the atoms, which are arranged periodically in the crystal lattice. When X-rays hit a crystal lattice, each atom acts as a scattering center and thus becomes the starting point of a new spherical wave. Superposition of the individual spherical waves leads to interference phenomena, which either result in amplification of the intensity (constructive interference) or extinction of the intensity (destructive interference).

The diffraction conditions on crystals can be determined from the perspective of M. v. Laue or W. H. and W. L. Bragg. In Laue's approach crystals are described as a Bravais grid with punctiform scattering centers at the lattice sites. For constructive interference the diffraction conditions in all three spatial directions must be fulfilled simultaneously.

$$\begin{aligned}
 h\lambda &= a(\cos\alpha_n - \cos\alpha_0) \\
 k\lambda &= b(\cos\beta_n - \cos\beta_0) \\
 l\lambda &= c(\cos\gamma_n - \cos\gamma_0)
 \end{aligned}
 \tag{4.1}$$

$h, k, l$	integer indices
$\lambda$	wavelength of incident X-ray beam
$a, b, c$	base vectors
$\alpha_0, \beta_0, \gamma_0$	angles between the incident X-ray beam and the respective base vectors
$\alpha_n, \beta_n, \gamma_n$	angles between the diffracted beam and the base vectors

The equivalent approach is Bragg's law according to W. H. and W. L. Bragg which describes the atoms of a crystal as parallel lattice planes with constant spacing  $d$ . Constructive interference occurs only when the path length difference is an integer multiple value of the wavelength.

$$n\lambda = 2d_{hkl} \cdot \sin\theta \quad (4.2)$$

$n$	integer
$\lambda$	wavelength of incident X-ray beam
$d_{hkl}$	spacing between atomic layers (hkl)
$\theta$	diffraction angle

Both, the method according to M. v. Laue as well as Bragg's approach provide the same conditions for X-ray diffraction and are to an extent equivalent. The Laue symbols  $h, k$  and  $l$  are identical to the diffraction order  $n$  of the Bragg equation multiplied by the Miller indices of the reflecting lattice plane.

In addition to the position of the reflections of an X-ray structure analysis, the intensities of these are also important. A higher electron density leads in a higher scattering potential and depending on the intensity of the reflections the respective atomic species can be concluded.

For the X-ray powder diffraction measurements a PANalytical X'Pert Pro diffractometer (PANalytical, Almelo, Netherlands) and a Rigaku Smartlab 3 kW system (Rigaku, Tokyo, Japan) were used. Both diffractometers are operating in Bragg-Brentano geometry with a  $\theta/\theta$  arrangement and generate their radiation in a copper X-ray tube. Whereas the PANalytical diffractometer is not equipped with a monochromator and therefore the samples are hit by  $\text{CuK}_{\alpha 1}$ - ( $\lambda = 1.54064 \text{ \AA}$ ) and  $\text{CuK}_{\alpha 2}$ -radiation ( $\lambda = 1.54438 \text{ \AA}$ ) a Ge(111) crystal is used for monochromization of the beam in the Rigaku diffractometer ( $\lambda = 1.54060 \text{ \AA}$ ). The diffraction experiments carried out at the Rigaku Smartlab diffractometer were performed by Dr. Stefan Berendts of the TU Berlin.

### 4.2.2. Rietveld refinement

For evaluation of X-ray powder diffraction data a refinement according to H. Rietveld was provided. The Rietveld refinement [162, 163] is a mathematical approach based on the least squares method in which a theoretical diffraction pattern with a known crystal structure is fitted to an experimental diffraction pattern. The theoretical intensity is calculated for each point of the diffraction pattern and compared to the observed intensities. The refined parameters include structural parameters such as the unit cell, atom positions, site occupation and Debye-Waller factors, profile parameters which are based on the used mathematical function, asymmetry parameters, a set of background points and parameters depending on the measuring device (e. g. zero-shift, transparency, displacement).

For the quality of a refinement the accordance between theoretical and observed intensities is given in form of different residual values [164, 165].  $R_{exp}$  indicates the best possible solution for a refinement. Due to the signal to noise ratio an ideal value of zero cannot be reached.

$$R_{exp} = \sqrt{\frac{N - P + C}{\sum_{i=1}^N w_i (y_i(obs))^2}} \quad (4.3)$$

$N$	number of measured points
$P$	number of parameters
$C$	number of parameter linkings
$w_i$	weighting factor at points $i$
$y_i^{obs}$	observed intensity at point $i$

The mean deviation of the calculated intensities to the observed ones is indicated by  $R_p$  and including a weighting factor by  $R_{wp}$ .

$$R_p = \frac{\sum_{i=1}^N |y_i(obs) - y_i(calc)|}{\sum_{i=1}^N y_i(obs)} \quad (4.4)$$

$$R_{wp} = \sqrt{\frac{\sum_{i=1}^N w_i (y_i(obs) - y_i(calc))^2}{\sum_{i=1}^N w_i (y_i(obs))^2}} \quad (4.5)$$

$w_i$	weighting factor at points $i$
$y_i^{obs}$	observed intensity at point $i$
$y_i^{calc}$	calculated intensity at point $i$

$R_{Bragg}$  indicates the ratio of the observed and calculated intensities of  $n$  reflections which are present in the diffraction pattern.

$$R_{Bragg} = \sqrt{\frac{\sum_{n=1}^N (I_n(obs) - I_n(calc))}{\sum_{n=1}^N I_n(obs)}} \quad (4.6)$$

$I_n(obs)$	measured integral intensity of $n$ reflections
$I_n(calc)$	calculated integral intensity of $n$ reflections

The goodness of fit is specified by the quotient of  $R_{wp}$  and  $R_{exp}$ . Generally speaking, a value below 2 indicates a very good refinement.

$$S = \frac{R_{wp}}{R_{exp}} \quad (4.7)$$

Rietveld refinements of the here presented compounds were carried out using the program package FULLPROF [166]. As mathematical function the pseudo-Voigt function was used to adjust the observed reflections. Backgrounds were fitted using a manually set of multiple background points with refinable heights. For each refinement a suitable structural model from the ICSD was used.

#### 4.2.3. Crystallite size determination

The crystallite size was determined using the Scherrer equation [167]. For that, the full width at half maximum (FWHM) of selected reflections was calculated using the program Origin by applying a Pearson VII function.

$$\Delta(2\theta) = \frac{K\lambda}{L\cos\theta_0} \quad (4.8)$$

$\Delta(2\theta)$	full width at half maximum (FWHM)
$K$	Scherrer form factor (usually $\sim 1$ , in this work $K = 0.9$ )
$\lambda$	wavelength
$L$	mean crystallize size
$\theta_0$	diffraction angle

### 4.3. Raman spectroscopy

Raman spectroscopy is based on the Raman effect which was first experimentally observed by Sir C. V. Raman [168]. When monochromatic radiation hits a substance the radiation is inelastically scattered (Raman effect) after spectral decomposition in addition to the elastic scattering (Rayleigh scattering). The inelastic scattering is due to the change in the polarizability of a molecule or molecular groups caused by vibrations and rotations. The frequency of the incident light is thereby shifted relative to the exiting radiation and leads to the appearance of a characteristic Raman-shift. Specific molecular groups show a certain Raman shift, giving each compound a characteristic Raman spectrum.

The Raman spectroscopic measurements were performed by Dr. Ilias Efthimiopoulos at GFZ Potsdam. Therefore, a LabRAM HR800 VIS (HORIBA Jobin Yvon GmbH, Bensheim, Germany) spectrometer was used. The samples were excited using the 473 nm emission line of a diode-pumped solid-state laser, the incident power was thereby 0.1 mW. For focusing the laser beam on the samples a lens with x20 magnification was used. The scattered light was dispersed by an optical grating with 1800 lines  $\text{mm}^{-1}$  and collected by a 2048 x 512 CCD detector. The spectral resolution determined by measuring the Rayleigh scattering was 1  $\text{cm}^{-1}$ .

### 4.4. Diffuse reflectance UV-Vis spectroscopy

For the determination of the optical properties of a material UV/Vis spectroscopy is a common tool. As solids cannot be analyzed by transmission experiments diffuse reflected light measurements are hereby appropriate. Using the Kubelka-Munk function the diffuse reflectance spectra can be converted into absorbance spectra.

$$F(R_\infty) = \frac{(1 - R_\infty)}{2R_\infty} = \epsilon \cdot c \cdot \frac{1}{s} \quad (4.9)$$

$F(R_\infty)$	Kubelka Munk function
$R_\infty$	Reflectance of material
$\epsilon$	absorption coefficient
$c$	concentration of absorbing species
$s$	scattering coefficient

The direct and indirect optical band gaps can be determined using the Tauc plot method [169, 170] by plotting the product of the Kubelka-Munk function and the photon energy - modified with an exponent depending on the transition type - against the photon energy and applying a tangent to this curve. The intersection point with the  $x$ -axis equates to the value of the optical band gaps.

$$[F(R_\infty)]^{\frac{1}{n}} = A \cdot (h\nu - E_g) \quad (4.10)$$

$n$	$n = \frac{1}{2}$ for direct transition; $n = 2$ for indirect transition
$h\nu$	photon energy
$E_g$	band gap energy
$A$	constant

UV/Vis measurements were performed using a V670 UV/Vis-NIR (Jasco Deutschland GmbH, Pfungstadt, Germany), an Evolution 220 (Thermo Scientific<sup>TM</sup>, Waltham, USA) and a Cary 300 UV/Vis spectrometer (Varian Inc., Palo Alto, USA). For the measurements with the V670 UV/Vis-NIR spectrometer a non-absorbing standard (MgO) was used and mixed with the samples in a ratio of 1:1. The measurements with the V670 UV/Vis-NIR spectrometer were performed by Dr. Nina Genz (research group of Prof. Ressler) of the TU Berlin. The sample holder configuration of the Cary 300 UV/Vis spectrometer is especially suited for the measurement of air-sensitive samples, therefore this spectrometer was used to measure the Li-bearing thiospinel materials.

## 4.5. Electron microprobe analysis

Electron microprobe analysis is an accurate technique for qualitative and quantitative chemical analysis. Its physical principle is the X-ray fluorescence.

Samples are irradiated by a high-energy focused electron beam that interacts with electrons of the inner shell, resulting in the emission of secondary X-ray radiation at wavelengths characteristic for specific elements. For a quantitative analysis the emitted X-ray intensities are compared to those of standard samples. As X-ray photons

behave like a particle with a certain energy or an electromagnetic wave with a specific wavelength the detection can be carried out either using their energy by an energy-dispersive (EDX) or their wavelength by a wavelength-dispersive spectrometer (WDX).

### **EDX**

Energy-dispersive spectroscopy measures the energy of the incoming X-ray photons which creates an electron-hole pair in the detector. The number of the created electron-hole pairs is directly proportional to the energy of the X-rays. Statistical effects and electronic noise lead to a broadening of the natural line width and are reduced by cooling the detector. The typical energy resolution of an EDX detector is significantly lower than that of WDX detectors. Energy-dispersive X-ray fluorescence analysis is used for quick qualitative and quantitative analysis.

### **WDX**

In wavelength-dispersive X-ray fluorescence analysis the emitted polychromatic secondary radiation is diffracted by analyzing crystals and split into angle-dependent monochromatic beams. By known scattering angle and lattice plane distance of the analyzing crystal a wavelength is generated using Bragg's law. With this wavelength, the energy can be obtained by the following equation:

$$E = hv = h\frac{c}{\lambda} \quad (4.11)$$

The energy responds to the X-ray fluorescence of a particular element and is used for qualitative analysis. For quantitative analysis again the X-ray intensities are considered. WDX detectors are characterized by a higher resolution compared to EDX detectors and enable the splitting of two adjacent peaks.

In advance, the powder samples were prepared on a carbon plate and steamed with carbon to generate an electrically conductive surface. This is necessary to prevent loading of the samples during irradiation. Energy-dispersive spectroscopy was performed by Dr. Stefan Berendts and Rodrigo Beltrán-Suito at the ZELMI of the TU Berlin using a DSM 982 GEMINI (Carl Zeiss AG, Oberkochen, Germany) spectrometer. Wavelength-dispersive fluorescence analysis was carried out by Oona Appelt at the GFZ Potsdam using a JXA-8230 (JEOL, Tokyo, Japan) spectrometer.

#### **4.6. Inductively coupled plasma optical emission spectrometry**

Inductively coupled plasma optical emission spectrometry (ICP-OES) is a qualitative and quantitative analysis for element determination of liquid, gaseous and solid materials. Although, solid samples have to be brought into a soluble state first. ICP-OES is based on the emission of excited ions at characteristic wavelengths for each element. Excitation is caused by high frequency energy of an Ar plasma.

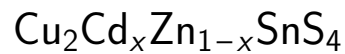
ICP-OES measurements were performed by Astrid Müller-Klauke of the TU Berlin using a 715 ES spectrometer (Varian Inc., Palo Alto, USA). About 1 mg of the analyzed sample was therefore dissolved in aqua regia and diluted with purified water.

**Part II.**

**Publications**

## 5. Publication 1

Experimental and theoretical investigations on the  
composition-dependent structural phase transition in



Eva M. Heppke, Tim Küllmey, Ilias Efthimiopoulos, Fatma D. Avcı, Oona Appelt,  
Beate Paulus, and Martin Lerch

*Postprint*

*Mater. Res. Express* **2019**, 6(12), 125525

doi:10.1088/2053-1591/ab59a0

<https://iopscience.iop.org/article/10.1088/2053-1591/ab59a0/meta>

© IOP Publishing.

Reproduced with permission. All rights are reserved.

Contribution to publication:

E. M. Heppke:	Sample preparation, structural characterization and evaluation, band gap determination, writing
T. Küllmey:	Quantum-chemical calculations, writing
I. Efthimiopoulos:	Raman measurements and evaluation, general advice, writing, proofreading
F. D. Avcı:	Sample preparation, structural characterization and evaluation
O. Appelt:	WDX measurements
B. Paulus:	General advice, proofreading
M. Lerch:	General advice, proofreading

**Authors:** E. M. Heppke<sup>[1]</sup>, T. Küllmey<sup>[2]</sup>, I. Efthimiopoulos<sup>\*[3]</sup>, F. D. Avci<sup>[1]</sup>,  
O. Appelt<sup>[3]</sup>, B. Paulus<sup>[2]</sup>, M. Lerch<sup>[1]</sup>

<sup>1</sup>Institut für Chemie: Technische Universität Berlin, Straße des 17. Juni 135, 10623 Berlin

<sup>2</sup>Institut für Chemie und Biochemie, Freie Universität Berlin, Arnimallee 22, 14195 Berlin

<sup>3</sup>Abteilung 3.6, Chemie und Physik der Geomaterialien, Deutsches Geo-ForschungsZentrum, Telegrafenberg, 14473 Potsdam

\* corresponding

**Supporting Information:** X-ray diffraction patterns with results of Rietveld refinements of each composition in 4 structural models including description of residual values, ionic positions and substituted atoms for DFT calculations in different phases, total energies at PBE level including corresponding lattice parameters, calculated band gaps for different phases. This material is available free of charge *via* the Internet at

[https://iopscience.iop.org/2053-1591/6/12/125525/media/Supplementary\\_Information.pdf](https://iopscience.iop.org/2053-1591/6/12/125525/media/Supplementary_Information.pdf)

## 5.1. Abstract

Samples of the  $\text{Cu}_2\text{Cd}_x\text{Zn}_{1-x}\text{SnS}_4$  solid solution series were synthesized by a mechano-chemical process, exhibiting high crystallinity due to an annealing step under flowing  $\text{H}_2\text{S}$  gas. The composition-dependent structural transition between the kesterite- and stannite-type phases was determined for Cd content close to  $x \approx 0.40$  by means of X-ray diffraction and Raman spectroscopic probes, in excellent agreement with earlier investigations. Our DFT calculations predicted a critical Cd concentration value of  $x = 0.5$  as the 'border' between the stannite- and kesterite-type structure in the  $\text{Cu}_2\text{Cd}_x\text{Zn}_{1-x}\text{SnS}_4$  solid solution series. The somewhat higher calculated Cd content value compared to the experimental case can be accounted by partial Cu/Zn disorder present in the synthesized samples. The measured optical band gaps  $E_g$  of the  $\text{Cu}_2\text{Cd}_x\text{Zn}_{1-x}\text{SnS}_4$  solid solution series decrease by  $\sim 0.3$  eV upon immediate introduction of Cd into the lattice, with  $E_g$  being almost constant with varying Cd concentration. All of our observations are interpreted within the framework of earlier reports on composition-dependent kesterite-to-stannite transition, where local structural variations due to the  $\text{Zn}^{2+}$  substitution by the larger  $\text{Cd}^{2+}$  cations appear to dictate the transition process.

## 5.2. Introduction

The series of quaternary  $\text{A}_2^+\text{B}^{2+}\text{C}^{4+}\text{X}_4$  compounds (where e. g.  $\text{A}^+ = \text{Cu, Ag}$ ;  $\text{B}^{2+} = \text{Mn, Fe, Zn, Cd}$ ;  $\text{C}^{4+} = \text{Ge, Sn}$ ;  $\text{X}^{2-} = \text{S, Se}$ ) constitute a class of materials that have gained significant attention over the last few years, mainly because of their highly promising photovoltaic properties [1–4]. For example, the  $\text{Cu}_2\text{ZnSnS}_4$  compound is considered as a potential candidate for use in solar cell applications, due to its almost optimal direct optical band gap ( $E_g \approx 1.5$  eV) and its high absorption coefficient in the visible energy range [5–7].

From a structural point of view, these  $\text{A}_2^+\text{B}^{2+}\text{C}^{4+}\text{X}_4$  compounds crystallize mainly in two tetragonal structures at ambient conditions, either a kesterite-type (KS, space group SG  $I\bar{4}$ ,  $Z = 2$ , Fig. 5.1) or a stannite-type (ST, SG  $I\bar{4}2m$ ,  $Z = 2$ , Fig. 5.1) phase [8]. Both structure types are composed of a cubic closed packed arrangement of the  $\text{X}^{2-}$  anions, with half of the tetrahedral voids filled with the  $\text{A}^+$ ,  $\text{B}^{2+}$ , and  $\text{C}^{4+}$  metal cations. In the ST structure, the  $\text{B}^{2+}$  cations are located at Wyckoff position  $2a$ , the  $\text{C}^{4+}$  cations at  $2b$ , and the  $\text{A}^+$  cations reside at the Wyckoff site  $4d$ , giving rise to an alternating arrangement of  $\text{B}^{2+}/\text{C}^{4+}$  - and  $\text{A}^+$  -layers along  $c$ -axis interrupted by  $\text{X}^{2-}$  anionic layers (Fig. 5.1). On the other hand, the KS phase is built up of consecutive  $\text{A}^+/\text{C}^{4+}$  - and  $\text{A}^+/\text{B}^{2+}$  -layers stacked also along  $c$ -axis, with the  $\text{A}^+$

cations occupying now two distinct sites ( $A^{+1}$  is located at  $2a$ , whereas  $A^{+2}$  occupies Wyckoff position  $2c$ ), and the remaining  $C^{4+}$  and  $B^{2+}$  cations reside at special sites  $2b$  and  $2d$ , respectively (Fig. 5.1). A statistical/random intermixing of the  $A^{+2}$  and  $C^{4+}$  cationic sites is quite common in the KS phase [9, 10]. Such cationic disorder results in a disordered kesterite phase (DKS), which is described with a higher (compared to KS) tetragonal symmetry SG  $I\bar{4}2m$  ( $Z = 2$ ).

Given the close structural relationship of the ST and KS phases (Fig. 5.1), the  $A_2^+B^{2+}C^{4+}X_4$  materials can undergo  $ST \leftrightarrow KS$  structural transitions by cationic substitution alone [11, 12]. For example, it is known that the gradual replacement of  $Zn^{2+}$  by  $Fe^{2+}$  in the  $Cu_2Fe_xZn_{1-x}SnS_4$  solid solution series can induce a  $KS \rightarrow ST$  structural transition for  $Fe^{2+}$  concentration close to  $x_{Fe} \approx 0.40$  [12]. Here we focus on the  $KS \rightarrow ST$  phase transition in the  $Cu_2Cd_xZn_{1-x}SnS_4$  solid solution series. The main reasons for selecting this particular composition series can be epitomized as follows: (a) the  $Cu_2Cd_xZn_{1-x}SnS_4$  compounds form a complete solid solution series [13–16], which allows in turn for systematic physico-chemical investigations of their properties, (b) earlier investigations on nano-structured and thin film  $Cu_2Cd_xZn_{1-x}SnS_4$  samples have indicated that a  $KS \rightarrow ST$  phase transition takes place for Cd content around  $x_{Cd} \approx 0.40$ , with concomitant effects in the electronic and vibrational properties [13–16]; similar conclusions were reached from the investigation of off-stoichiometric bulk samples [17], (c) the  $Zn^{2+} \rightarrow Cd^{2+}$  cationic exchange is isoelectronic, with both cations exhibiting the same number of valence electrons, hence the expected composition-dependent variation in properties should result mainly from the difference in cationic sizes, which is expected in turn to facilitate the interpretation of the results, (d) introduction of the larger  $Cd^{2+}$  cations in the lattice has been shown to suppress/limit the inherent Cu/Zn anti-site exchange disorder, as well as the appearance of any secondary phases, which constitute detrimental factors for the photovoltaic efficiency of these systems [14, 18, 19], hence (e) the substitution of  $Zn^{2+}$  by  $Cd^{2+}$  may improve the photovoltaic performance, with a thorough physico-chemical investigation of this solid solution series being particularly appealing for applications.

As we mentioned above, the structural phase transition between the KS and ST phases in  $Cu_2Cd_xZn_{1-x}SnS_4$  using nanostructured and thin film samples has been studied in detail [13–16]. For bulk materials, such investigations are surprisingly scarce, with only one recent investigation reporting the  $Cu_2Cd_xZn_{1-x}SnS_4$   $KS \rightarrow ST$  structural transition using crystalline off-stoichiometric samples [17]. In all of these studies, a critical Cd content of  $x_{Cd} \approx 0.40$  was determined to act as the ‘border’ between the ST and KS phase regions.

Enriching these investigations further as a means of understanding the effects of

stoichiometry and ‘dimensionality’ on the composition-dependent KS  $\rightarrow$  ST transition, we report here our investigations on bulk *stoichiometric*  $\text{Cu}_2\text{Cd}_x\text{Zn}_{1-x}\text{SnS}_4$  powder samples. All compounds were prepared by a mechanochemical synthesis route and characterized in detail by X-ray diffraction (XRD), Raman and UV/VIS spectroscopy. It should be mentioned that bulk material of such compounds has been usually produced by solid state reaction at high temperature of the elements in evacuated silica ampoules followed by a second annealing step. All these factors result in long reaction times and an enhanced possibility for the formation of secondary phases. Consequently, we used our recently developed easy and fast mechanochemical procedure [20] for the preparation of single phase materials in this contribution.

Our studies pinpoint the ST  $\rightarrow$  KS structural transition at a critical Cd content of  $x_{\text{Cd}} \approx 0.40$ , in very good agreement with the aforementioned studies [13-17]. Additionally, our density functional theory (DFT) calculations provided valuable insights on the effects of Cu/Zn disorder on the ST  $\rightarrow$  KS structural transition. Local structural variations upon the gradual  $\text{Zn}^{2+} \rightarrow \text{Cd}^{2+}$  cationic substitution suffice to explain the ST  $\rightarrow$  KS transition process, with the corresponding variations in the electronic and vibrational properties.

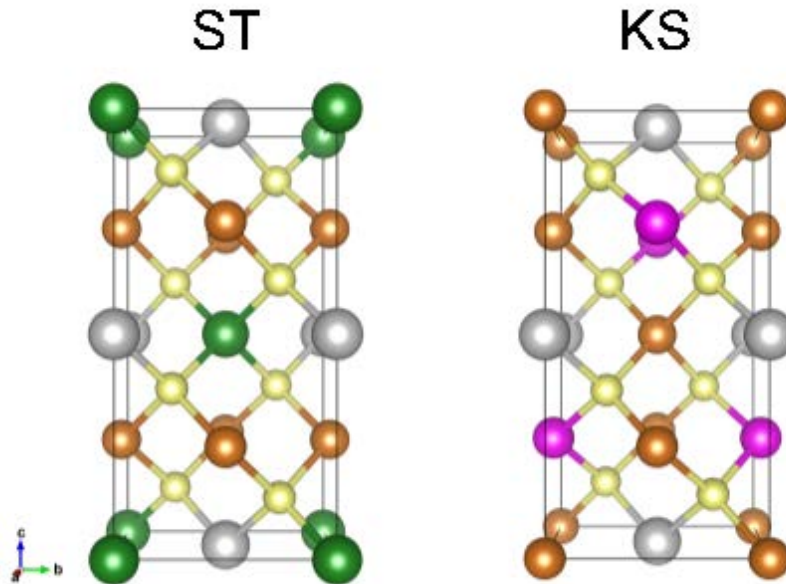


**Figure 5.1.:** Unit cell of the stannite-type (ST, left) and kesterite-type (KS, right) structure for the  $\text{Cu}_2\text{CdSnS}_4$  and  $\text{Cu}_2\text{ZnSnS}_4$  end-members, respectively (Cu: bronze, Zn: pink, Cd: green, Sn: grey, and S: yellow). The structural parameters are taken from our DFT calculations (**Tables S1-S8** in the **Supplement**).

## 5.3. Experimental and Theoretical Details

### 5.3.1. Synthesis details

All samples of the  $\text{Cu}_2\text{Cd}_x\text{Zn}_{1-x}\text{SnS}_4$  solid solution series with  $x = 0, 0.25, 0.33, 0.37, 0.40, 0.50, 0.60, 0.75, 1$  were prepared by a mechanochemical process. In the first step, the binary sulfides CdS, CuS, SnS, and ZnS were mixed in a stoichiometric ratio and milled in a high energy planetary Mono Mill PULVERISETTE 6 (Fritsch, Idar-Oberstein, Germany). The second step involved the annealing of the obtained samples in  $\text{H}_2\text{S}$ -atmosphere inside a tube furnace.

Cadmium sulfide and copper monosulfide were prepared by precipitation from 0.1 M  $\text{Cd}(\text{CH}_3\text{CO}_2)_2$ - and 0.1 M  $\text{Cu}(\text{NO}_3)_2$ -solutions with  $\text{H}_2\text{S}$  (Air Liquide, 99.5 %), respectively, followed by an annealing step at 230 °C for 2 hours in  $\text{H}_2\text{S}$  atmosphere inside a tube furnace. Tin monosulfide was prepared by the solid state reaction of tin (Merck, 99.9 %) and sulfur (Fuka, 99.99 %) in an evacuated and sealed silica glass ampoule inside a muffle furnace. Zinc sulfide was synthesized by sulfidation of zinc oxide (Merck, 99.5 %) at 650 °C in  $\text{H}_2\text{S}$  atmosphere for 3 hours inside a tube furnace.

For the multinary sulfides with the general formula  $\text{Cu}_2\text{Cd}_x\text{Zn}_{1-x}\text{SnS}_4$  ( $x_{\text{Cd}} = 0, 0.25, 0.33, 0.37, 0.40, 0.50, 0.60, 0.75, 1$ ), the corresponding binary sulfides were mixed and filled in a 45 mL zirconia grinding beaker with six zirconia grinding balls with a diameter of 15 mm. The grinding beaker was filled under argon atmosphere in order to prevent oxidation of the sulfidic powders during milling. For every composition, milling was performed by a rotational speed of 350 rpm and a milling time of 5 hours. After milling, the resulting products showed poor crystallinity. In order to obtain powders of higher crystallinity, the ground intermediates were annealed in  $\text{H}_2\text{S}$  atmosphere inside a silica glass tube furnace. For the  $\text{Cu}_2\text{CdSnS}_4$  sample a heating temperature of 600 °C was necessary, whereas for the other compositions a heating temperature of 550 °C was sufficient. For every sample, a heating time of 3 hours and a cooling rate of 100 K/h were set.

### 5.3.2. Characterization details

All XRD patterns were collected in Bragg-Brentano geometry using a Panalytical X'Pert PRO diffractometer with  $\text{Cu-K}\alpha$  radiation ( $\lambda_1 = 1.54056 \text{ \AA}$ ,  $\lambda_2 = 1.54439 \text{ \AA}$ ). Additional measurements were carried out with a RIGAKU SmartLab 3 kW system equipped with a  $K\alpha_1$  unit (Johansson-type Ge crystal,  $\text{Cu-K}\alpha_1$  radiation,  $\lambda = 1.54060 \text{ \AA}$ ).

Structural refinements were performed with the Rietveld method [21] using the program FULLPROF Suite [22] by applying a pseudo-Voigt function. Four different struc-

tural models were considered for our Rietveld refinements (Table 5.1): the ordered (1) KS and (2) ST phases, where the metal atoms occupy distinct Wyckoff sites without any cationic disorder, (3) the DKS structure with a statistical distribution of copper and zinc on positions  $2c$  and  $2d$  (Cu-Zn layers), and finally (4) a partially DKS phase (PDKS), where  $2/3$  of copper and  $1/3$  of zinc ions are located at  $2c$  and  $1/3$  copper and  $2/3$  zinc at Wyckoff position  $2d$ . We note that such Cu-Zn distribution was determined for  $\text{Cu}_2\text{ZnSnS}_4$  synthesized by a similar mechanochemical route [20] to the one described here. In order to facilitate comparison among the XRD refinements of the various samples using the four different structural models, the site occupancies, atomic coordinates, and the Debye-Waller factors for all compounds were taken from neutron diffraction refinements performed on the KS  $\text{Cu}_2\text{ZnSnS}_4$  end-member and kept fixed [23]. The background was fitted using a linear interpolation between a set of background points with refinable heights. To determine the actual phase of each composition, the residual values  $R_{\text{wp}}$  and  $R_{\text{Bragg}}$  of the four different refinements were taken into account, as they represent the overall refinement quality. The  $R_{\text{wp}}$  value equates to the mean deviation of the calculated data to the observed diffraction data:

$$R_{\text{wp}} = \sqrt{\frac{\sum_i w_i (y_i(\text{obs}) - y_i(\text{calc}))^2}{\sum_i w_i (y_i(\text{obs}))^2}} \quad (5.1)$$

with  $w_i$  standing for the weighting factor at point  $i$ ,  $y_i(\text{obs})$  indicating the measured intensity of point  $i$ , and  $y_i(\text{calc})$  representing the calculated intensity of point  $i$ . On the other hand, the  $R_{\text{Bragg}}$  factor is calculated from the intensities of the reflections that are present in the diffraction pattern:

$$R_{\text{Bragg}} = \sqrt{\frac{\sum_n |I_n(\text{obs}) - I_n(\text{calc})|}{\sum_n I_n(\text{obs})}} \quad (5.2)$$

where  $I_n(\text{obs})$  and  $I_n(\text{calc})$  denote the measured and calculated integral intensity of the  $n$  reflection.

**Table 5.1.:** The four different structural models considered for the Rietveld refinements of the measured  $\text{Cu}_2\text{Cd}_x\text{Zn}_{1-x}\text{SnS}_4$  XRD patterns. The respective Wyckoff positions and isotropic Debye-Waller factors  $B$  are also provided for each model.

Wyckoff position	Atom	$B$ [ $\text{\AA}^2$ ]
Stannite (ST, space group $I\bar{4}2m$ )		
$2a$	$1-x$ Zn1 $x$ Cd1	0.5
$2b$	Sn1	0.3
$4d$	Cu1	1.8
$8i$	S1	0.728
Kesterite (KS, space group $I\bar{4}$ )		
$2a$	Cu1	1.3
$2b$	Sn1	0.3
$2c$	Cu2	1.8
$2d$	$1-x$ Zn1 $x$ Cd1	0.5
$8g$	S1	0.728
Disordered kesterite (DKS, space group $I\bar{4}2m$ )		
$2a$	Cu1	0.5
$2b$	Sn1	0.3
$4d$	$1/2$ Cu2 $1/2$ $1-x$ Zn1 Zn1 $x$ Cd1	1.8
$8i$	S1	0.728
Partially disordered kesterite (KS, space group $I\bar{4}$ )		
$2a$	Cu1	1.3
$2b$	Sn1	0.3
$2c$	$2/3$ Cu2 $1/3$ $1-x$ Zn1 Zn1 $x$ Cd1	1.8
$2d$	$1/3$ Cu3 $2/3$ $1-x$ Zn2 Zn2 $x$ Cd2	0.5
$8g$	S1	0.728

The compositions of the annealed synthetic  $\text{Cu}_2\text{Cd}_x\text{Zn}_{1-x}\text{SnS}_4$  solid solution series were determined with wavelength-dispersive X-ray spectroscopy using a JEOL JXA-8230 electron microprobe. The analytical conditions included an acceleration voltage of 15 kV, a beam current of 20 nA, and a beam diameter of 1  $\mu\text{m}$ . The following natural and synthetic standards were used: chalcopyrite (for Cu and S), sphalerite (for Zn), CdS (for Cd), and cassiterite (for Sn). The CITZAF routine [24] in the JEOL software was used for data processing.

Raman spectroscopic measurements were performed with a LabRAM HR800 VIS (HORIBA Jobin Yvon GmbH, Bensheim, Germany) spectrometer, using a diode-pumped solid-state laser with excitation wavelength  $\lambda = 473$  nm and an incident power of  $\sim 0.1$  mW on the sample. Raman spectra were measured within the 200 – 480  $\text{cm}^{-1}$  frequency range. The scattered light was dispersed by a 1800  $\text{mm}^{-1}$  lines grating and collected by a 2048 x 512 CCD detector. A lens with x20 magnification was used for focusing the laser beam on the sample. The spectral resolution was 1  $\text{cm}^{-1}$ . A Si standard was used for calibration.

For the determination of the optical band gap  $E_g$ , UV/Vis measurements were performed using a V670 UV/Vis-NIR spectrometer (Jasco Deutschland GmbH, Pfungstadt, Germany). MgO was used as the white standard and was mixed with the sulfidic powders in a ratio of 1:1. The measured diffuse reflectance spectra were converted to absorption spectra by the Kubelka-Munk function:

$$F(R_\infty) = \frac{(1 - R_\infty)^2}{2R_\infty} = \epsilon \cdot c \cdot \frac{1}{s} \quad (5.3)$$

with  $R_\infty$  representing reflectance,  $\epsilon$  the absorption coefficient,  $c$  the concentration of the absorbing species, and  $s$  the scattering coefficient. From the absorption spectra, the direct  $E_g$  was determined using the following equation (Tauc plot method) [25, 26]:

$$[F(R)h\nu]^{1/2} = A(h\nu - E_g) \quad (5.4)$$

where  $h\nu$  the energy of light,  $E_g$  the optical band gap, and  $A$  a constant. The standard deviation for  $E_g$  was estimated close to  $\pm 0.05$  eV.

### 5.3.3. Computational details

The periodic DFT calculations were performed with VASP 5.3.5 [27–30]. A plane wave basis set with an energy cutoff of 550 eV with the projector augmented (PAW) potentials [31, 32] was used, whereby the 5s, 5p and 4d electrons of Sn, 3s, 3p electrons of S, and 4s, 3d electrons of Cu, Cd and Zn were explicitly considered. The electronic convergence criteria were set at least to  $10^{-5}$  eV, whereby the Blocked-Davidson algorithm was applied as implemented in VASP. The structural relaxation of internal and external lattice parameters was set to a force convergence of  $10^{-2}$  eV/Å<sup>2</sup>, while the conjugate-gradient algorithm implemented in VASP was used [33]. The freedom of spin polarization was enabled and a Gaussian smearing approach with a smearing factor  $\sigma$  of 0.01 eV was utilized. The supercells were fully optimized with a 4x4x4 k-grid

constructed via the Monkhorst-Pack scheme [34] and centered at the  $\Gamma$ -point with the Perdew-Burke-Ernzerhof (PBE) functional [35]. On top of the PBE-optimized structures, single point calculations for the band gap  $E_g$  and electronic density of states (DOS) with the HSE06-functional [36–39] were performed with a  $2 \times 2 \times 2$  k-grid, in order to account for an accurate electronic structure. The tetrahedron method with Blöchl corrections [40] was applied for the band structure evaluation.

We created  $2 \times 2 \times 1$  super cells (SC) from the KS and ST unit cells. In kesterites, Cu-Zn disorder is a common defect [41]. The exchange is thought to take place within the Cu-Zn planes. We have assumed kesterite-type phases with different degrees of Cu-Zn disorder. We classify them by their disorder fraction, i. e. the number of atoms in the two Cu-Zn planes within the cell that have mutually exchanged their position (compared to the fully ordered KS structure) divided by the total number of atoms in the planes. For example, there are four atoms within the Cu-Zn planes of the KS unit cell; exchanging two of them lead to a disorder fraction of 50 %. In the DKS structure, all positions in the Cu-Zn planes are occupied randomly. This corresponds again to a disorder fraction of 50 %. Therefore, we label the structural models of our DFT calculations with the same disorder fraction as that of DKS.

We need to point out that in this study we opted for uncovering the principle trends for disordered KS and ST systems, without aiming for a high degree of accuracy. Therefore, we restrict ourselves to a very limited number of disorder patterns, instead of considering all possible quasi-random structures. In an earlier investigation, we showed that for the  $\text{Cu}_2\text{SnZnS}_4$  kesterite-type material it is sufficient to consider only the most stable substitution patterns, in order to predict the properties of a disordered DKS system [42]. We start by restricting the size of the system to that of the KS unit cell. This gives rise to the first considered DKS pattern  $p_1$  (SG  $P\bar{4}$ , DKS- $p_1$ , Fig. 5.2). It is the only and, therefore, the most stable disordered configuration with 50 % cationic disorder within the KS unit cell [42]. Assuming a larger  $2 \times 2 \times 1$  KS super cell, we can find more DKS configurations described with 50 % disorder fractions. The chosen pattern  $p_2$  (SG  $P1$ , DKS- $p_2$ , Fig. 5.2) represents the second most probable disordered cationic configuration within the  $2 \times 2 \times 1$  super cell [42]. We note that the DKS- $p_1$  modification can also be realized in the  $2 \times 2 \times 1$  super cell, and still be the most stable configuration. Additionally, we included the most stable 12.5 % DKS structure (SG  $P2$ , Fig. 5.2) found within a  $2 \times 2 \times 1$  KS super cell. In order to compare the different structures directly and reduce the numerical errors, all calculations were performed with  $2 \times 2 \times 1$  super cells. Please note that the space groups of the simulated DKS phases differ from the space group of the ‘experimental’ DKS (SG  $I\bar{4}2m$ ), since only individual substitution patterns are simulated. To account for the full symmetry, we would have to

calculate all possible substitution patterns and average over them, a task which lies beyond the scope of the current work.

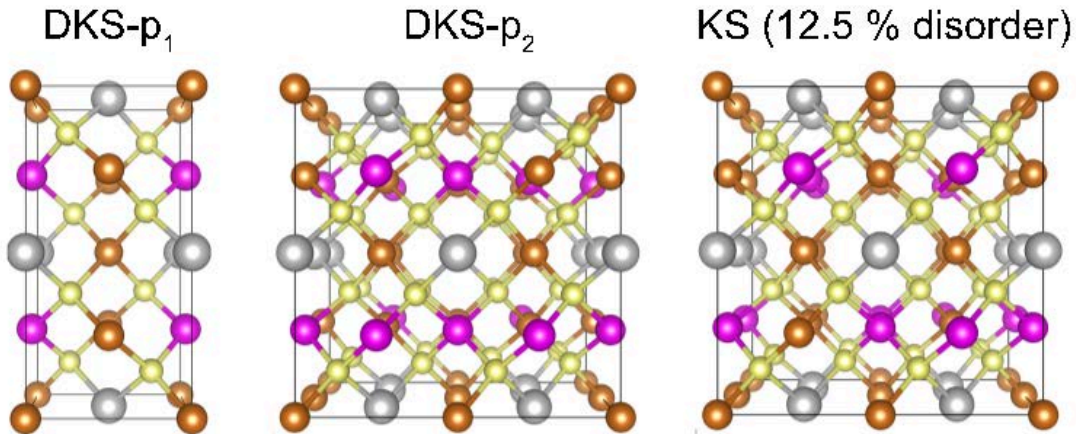


**Figure 5.2.:** Unit cells of the disordered kesterite-type substitution patterns  $p_1$  (DKS- $p_1$ , left) and  $p_2$  (DKS- $p_2$ , middle), and the most stable KS configuration with 12.5% Cu-Zn disorder (right). The DKS- $p_1$  is the most stable modification for the DKS phase, followed by DKS- $p_2$  which is 0.12 eV less stable per formula unit at the PBE level. The atom colors are Cu: bronze, Zn: pink, Sn: grey, and S: yellow.

For all presented structures, we substituted one zinc atom after another within the SCs with cadmium, in order to account for the different Cd content ( $x_{Cd}$ ) in the  $Cu_2Cd_xZn_{1-x}SnS_4$  solid solution series. For each  $x_{Cd}$ , we included all symmetry-inequivalent substitution patterns (for details see **Tables S1-S8** in the **Supplement**). We carried out full optimizations (lattice parameter and internal coordinates) for each pattern at the PBE level. The energies  $\bar{E}(x_{Cd})$  of the  $N$  different substitution patterns  $E_i$  are averaged with respect to their statistical weight  $n_i(x_{Cd})$  in the super cell:

$$\bar{E}(x_{Cd}) = \frac{1}{\sum_{i=1}^N n_i(x_{Cd})} \sum_{i=1}^N n_i(x_{Cd}) E_i(x_{Cd}) \quad (5.5)$$

with the statistical weight  $n_i(x_{Cd})$  indicating how often does a symmetry-equivalent substitution pattern occur for a given disorder fraction. The lattice parameters and internal coordinates are averaged in the same fashion for each  $x_{Cd}$ . To enable a comparison to the experimental band gaps, we have additionally calculated the DOS at the HSE06 level for the most stable structure at each Cd content. The data processing of the VASP calculations was done using the pymatgen package [43].

## 5.4. Results and Discussion

### 5.4.1. XRD refinements

All samples were synthesized as described in Section 5.3. The powders obtained after milling exhibit poor crystallinity, resulting in XRD patterns indexed to a sphalerite-type structure (Fig. 5.3). At this particular step of the synthesis process, a more accurate structural determination was not feasible.

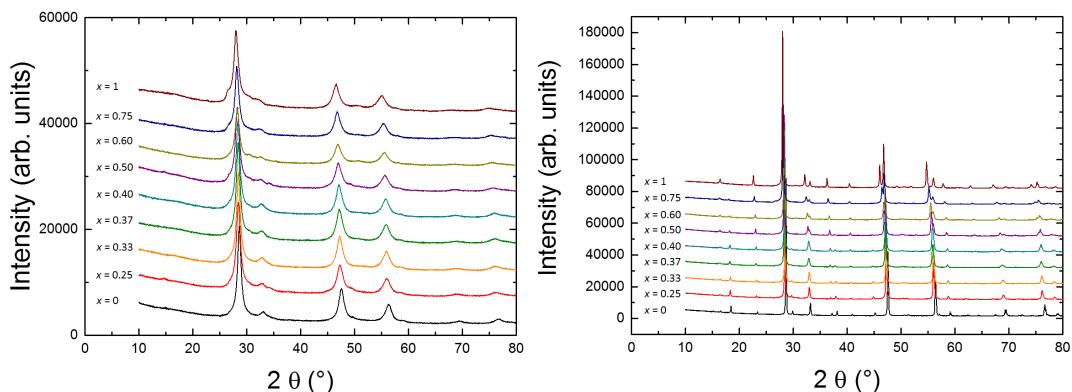


**Figure 5.3.:** XRD patterns of (left) poorly crystalline and (right) annealed  $\text{Cu}_2\text{Cd}_x\text{Zn}_{1-x}\text{SnS}_4$  samples with  $x_{\text{Cd}} = 0, 0.25, 0.33, 0.37, 0.40, 0.50, 0.60, 0.75, 1$  after milling.

Powders of higher crystallinity were prepared during the second synthesis step, with the annealing of the poorly crystalline intermediates (Fig. 5.3). Considering both the results of the X-ray measurements and electron microprobe analysis (Table 5.2), single-phase stoichiometric  $\text{Cu}_2\text{Cd}_x\text{Zn}_{1-x}\text{SnS}_4$  products with  $x_{\text{Cd}} = 0, 0.25, 0.33, 0.37, 0.40, 0.50, 0.60, 0.75, 1$  were successfully synthesized.

The XRD Rietveld refinements for all  $\text{Cu}_2\text{Cd}_x\text{Zn}_{1-x}\text{SnS}_4$  samples using the four different ST, KS, DKS, and PDKS structural models (Table 5.1) are presented in the **Supplement (Figs. S1-S9)**. Our refinements indicate that: (a) The KS and PDKS structural models lie very close to each other in terms of residual values for the  $x_{\text{Cd}} = 0, 0.25$  compounds (**Figs. S1-S2** in the **Supplement**). (b) For the  $x_{\text{Cd}} = 0.33$  material, the residual values  $R_{\text{wp}}$  for the DKS and PDKS model are very similar (**Fig. S3** in the **Supplement**); due to the somewhat lower  $R_{\text{Bragg}}$  value of the partial disordered kesterite model, however, we propose that  $\text{Cu}_2\text{Cd}_{0.33}\text{Zn}_{0.67}\text{SnS}_4$  crystallizes in the latter. We should note here that a complete cation distribution, especially the ordering of Cu and Zn on Wyckoff positions  $2c$  and  $2d$  cannot be determined using conventional X-ray diffraction data; the high absorption of neutron radiation in Cd-bearing materials [44], however, did not allow for complementary neutron diffraction measurements.

(c) For the  $x_{\text{Cd}} = 0.37$  member, the stannite-type and disordered kesterite models exhibit similar  $R_{\text{wp}}$  values; considering the respective  $R_{\text{Bragg}}$  values, nevertheless, the disordered kesterite phase appears to be favored (**Fig. S4** in the **Supplement**). (d) Similarly, the  $x_{\text{Cd}} = 0.40$  sample displays almost identical  $R_{\text{wp}}$  and  $R_{\text{Bragg}}$  values for the stannite-type and disordered kesterite structures (**Fig. S5** in the **Supplement**). (e) Finally, the remaining samples within the  $0.5 \leq x_{\text{Cd}} \leq 1$  composition range adopt the stannite-type structure (**Figs. S6-S9** in the **Supplement**).

**Table 5.2.:** Elemental composition of the synthetic  $\text{Cu}_2\text{Cd}_x\text{Zn}_{1-x}\text{SnS}_4$  solid solution series, as determined by electron microprobe measurements.

Cd-content	Cu	Cd	Zn	Sn	S
$x_{\text{Cd}} = 0$	1.97	0	0.99	1	4.04
$x_{\text{Cd}} = 0.25$	2.04	0.25	0.74	0.99	3.98
$x_{\text{Cd}} = 0.33$	2.02	0.32	0.69	1	3.98
$x_{\text{Cd}} = 0.37$	2.05	0.36	0.61	1.01	3.97
$x_{\text{Cd}} = 0.4$	2.05	0.4	0.61	1.02	3.92
$x_{\text{Cd}} = 0.5$	1.97	0.53	0.5	0.99	4
$x_{\text{Cd}} = 0.6$	2.03	0.6	0.4	1.04	3.93
$x_{\text{Cd}} = 0.75$	2.02	0.74	0.25	1	3.98
$x_{\text{Cd}} = 1$	2.04	1	0	0.99	3.96

Taken together, our XRD Rietveld refinements indicate that the  $\text{Cu}_2\text{Cd}_{0.37}\text{Zn}_{0.63}\text{SnS}_4$  and  $\text{Cu}_2\text{Cd}_{0.40}\text{Zn}_{0.60}\text{SnS}_4$  compositions set the structural transition ‘border’ between the KS and ST phases in  $\text{Cu}_2\text{Cd}_x\text{Zn}_{1-x}\text{SnS}_4$ , i. e. the  $\text{KS} \rightarrow \text{ST}$  transition occurs for Cd content close to  $x_{\text{Cd}} \approx 0.37/0.40$ , in excellent agreement with previous studies on bulk off-stoichiometric polycrystalline [17] and thin film samples [15]. In Table 5.3 we list the space groups and refined lattice parameters for each composition.

The composition-dependent  $\text{KS} \rightarrow \text{ST}$  structural transition in the  $\text{Cu}_2\text{Cd}_x\text{Zn}_{1-x}\text{SnS}_4$  solid solution series becomes more apparent from the evolution of the respective structural parameters (Table 5.3 and Fig. 5.4). The tetragonal  $a$ -axis and the volume  $V$  increase (almost) linearly upon increasing the Cd content  $x_{\text{Cd}}$ , whereas the  $c$ -axis increases up to  $x_{\text{Cd}} \approx 0.33$ , plateaus between  $0.33 \leq x \leq 0.5$ , and decreases for  $x_{\text{Cd}} \geq 0.6$ . Such diverse behavior of the  $c$ -axis is most likely connected with the two-stage  $\text{KS} \rightarrow \text{ST}$  cationic ordering process proposed earlier for the  $\text{Cu}_2\text{Fe}_x\text{Zn}_{1-x}\text{SnS}_4$  solid solution series [12]. We will return to this point later below. Finally, the lattice parameter ratio  $c/2a$  drops clearly below unity for Cd content higher than  $x_{\text{Cd}} \geq 0.6$ , in excellent agreement with the expected  $c/2a$  trend upon the  $\text{KS} \rightarrow \text{ST}$  structural transition [12, 17].

**Table 5.3.:** Refined lattice parameters and potential space groups for the synthetic  $\text{Cu}_2\text{Cd}_x\text{Zn}_{1-x}\text{SnS}_4$  samples with  $x_{\text{Cd}} = 0, 0.25, 0.33, 0.37, 0.40, 0.50, 0.60, 0.75, 1$ .

Cd-content	Phase	$a$ [Å]	$c$ [Å]	$c/2a$	$V$ [Å <sup>3</sup> ]
$x_{\text{Cd}} = 0$	$I\bar{4}$ , KS	5.42300(2)	10.8343(4)	0.999	318.63
$x_{\text{Cd}} = 0.25$	$I\bar{4}$ , KS/PDKS	5.4587(2)	10.8955(5)	0.998	324.66
$x_{\text{Cd}} = 0.33$	$I\bar{4}$ , PDKS	5.4689(3)	10.8992(6)	0.996	325.98
$x_{\text{Cd}} = 0.37$	$I\bar{4}2m$ , DKS	5.4746(4)	10.8995(8)	0.995	326.67
$x_{\text{Cd}} = 0.4$	$I\bar{4}2m$ , DKS/ST	5.4795(3)	10.8992(7)	0.995	327.25
$x_{\text{Cd}} = 0.5$	$I\bar{4}2m$ , ST	5.4980(3)	10.8998(7)	0.991	329.48
$x_{\text{Cd}} = 0.6$	$I\bar{4}2m$ , ST	5.5013(7)	10.8811(1)	0.989	329.3
$x_{\text{Cd}} = 0.75$	$I\bar{4}2m$ , ST	5.5288(8)	10.8760(2)	0.984	332.45
$x_{\text{Cd}} = 1$	$I42m$ , ST	5.5878(3)	10.8561(7)	0.971	338.97

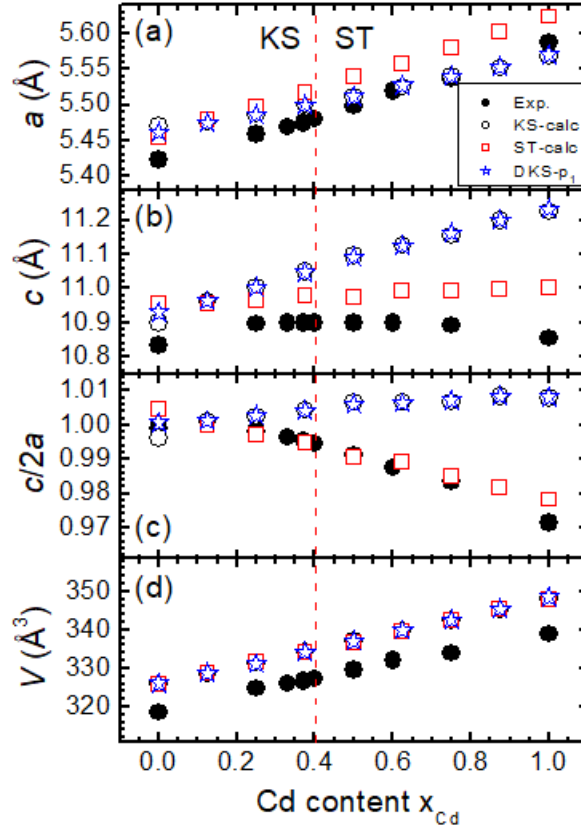


**Figure 5.4.:** Comparison of the experimental (solid black circles) and calculated structural parameters for the kesterite (KS, open circles), stannite (ST, open red squares) and disordered kesterite (DKS- $p_1$ , open blue star symbols) phases. The curves for the KS (12.5% disordered) and DKS- $p_2$  fall virtually on top of the DKS- $p_1$  curve and are omitted for clarity. The vertical dashed line indicates the KS  $\rightarrow$  ST transition, as determined experimentally from the XRD results.

### 5.4.2. DFT calculations

In order to validate our experimentally observed KS  $\rightarrow$  ST structural transition as a function of  $x_{\text{Cd}}$ , we compare the total PBE energies of the different  $\text{Cu}_2\text{Cd}_x\text{Zn}_{1-x}\text{SnS}_4$  compounds. Plotting the relative stability of the KS and ST phases with reference to the Cd content, we find the KS  $\rightarrow$  ST transition around  $x_{\text{Cd}} = 0.5$  (Fig. 5.5), deviating slightly from the experimental  $x_{\text{Cd}} = 0.37/0.40$  value. Possible reasons behind this discrepancy may stem from (a) the PBE functional used here to calculate the structural properties of the various polymorphs, may not provide highly accurate structural results, (b) the zero-point energy and thermal contributions of phonons were not considered, which can in turn influence the relative energetic stability of the various phases, and (c) the (partial) cationic disorder present in the synthetic samples (Table 5.3). Given that the first two points have been considered already in previous works, where it has been shown that (a) the energetically most stable phase for the  $\text{Cu}_2\text{ZnSnS}_4$  end-member is always the KS structure irrespective of the functional used (e.g. [4, 13, 19, 41]), and (b) taking into account the almost identical vibrational properties of the kesterite and stannite phases [48-50], i.e. inclusion of the phonon properties in our calculations is not expected to shift the relative energetics of the KS and ST phases, we tend to favor the cationic disorder scenario as the reason behind the experimental and theoretical ‘critical’  $x_{\text{Cd}}$  value discrepancy.

In order to test this hypothesis, we computed the total energies of the most stable 12.5% and the two most stable 50% disordered KS phases as a function of  $x_{\text{Cd}}$ . The trend for the highly symmetric DKS-p1 phase is very similar to the KS trend, with a DKS-p1  $\rightarrow$  ST transition taking place at  $x_{\text{Cd}} = 0.5$ . For low Cd content, i.e. for  $x_{\text{Cd}} \leq 0.5$ , there is no significant energy difference between the DKS-p1 and KS phases (Fig. 5.5). For higher Cd content, however, the DKS-p1 phase becomes less stable than the KS structure energy-wise. The similar behavior of the DKS-p1 and KS phases as a function of  $x_{\text{Cd}}$  can be explained from the close structural relationship of the two modifications, where a single cationic exchange within the Cu-Zn lattice planes is sufficient to ‘switch’ between the KS and DKS-p1 unit cells (Figs. 5.1 and 5.2).

Nevertheless, we think that the 12.5% disordered KS and the DKS-p2 (50% disorder) phases represent more realistic candidates for simulating disorder in this system, as their larger unit cells offer more Cu-Zn exchange combinations for achieving a 50% disorder fraction. Both of these disordered modifications are always less stable than the ST phase (Figure 5.5), whereas a higher cationic disorder leads to even less favorable structures for all the tested  $x_{\text{Cd}}$  values. Interestingly, the KS (12.5% disorder) and DKS-p2 (50% disorder) phases exhibit a similar trend to the ordered KS phase as a function of  $x_{\text{Cd}}$ . Thus, we conclude that there should be a disorder fraction  $<12.5\%$ , for which the

KS→ST transition agrees with the experimentally observed value of  $x_{Cd} = 0.37/0.40$  (exemplified by the grey line in Fig. 5.5). We deduce this proposition by weighting the KS and 12.5% disordered KS energies 2.7:1. The latter ratio is derived from the law of mass action for a two-state system, with an energy difference  $\Delta E$  of 70 meV at  $T = 550$  °C (annealing temperature):

$$K = \frac{p_{KS}}{p_{KS(12\%disorder)}} = e^{\Delta E/RT} = \frac{2.7}{1}, \quad (5.6)$$

where  $R$  denotes the universal gas constant. Our findings indicate that the deviation between the experimental and calculated  $x_{Cd}$  values leading to the KS→ST transition is mainly due to a cationic disorder fraction smaller than 12.5% in the synthetic samples.

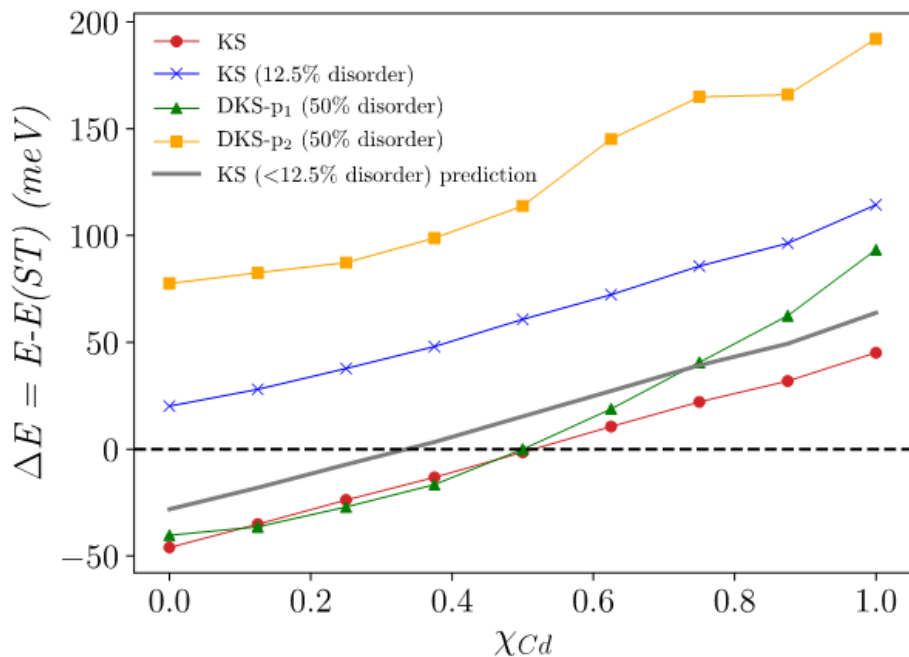


**Figure 5.5.:** Relative energies of the ordered and various disordered KS phases (solid lines) with respect to the stannite-type phase (black dotted baseline) for different Cd contents  $x_{Cd}$ . Energies below zero indicate that the respective (D)KS phases are more stable than the ST modification. The grey solid line is a prediction for a KS phase with cationic disorder fraction smaller than 12.5%, generated by mixing the ordered KS and 12.5% disordered KS energies with the ratio 2.7:1 (see text for more details).

In Fig. 5.4 we compare the calculated and experimental lattice parameters. The predicted lattice parameter  $a$  lies always within 0.1 Å from the experimental values. Similarly, the predicted lattice parameter  $c$  is within 0.2 Å of the experimentally ob-

served values. Thus, we have a satisfactory numerical agreement. Please note that we cannot distinguish between the KS phase and any of the disordered KS phases in terms of lattice parameters, due to the close numerical values (Fig. 5.4 and **Table S8** in the **Supplementary material**). For the lattice parameter  $a$ , the predicted KS and ST values lie relatively close to each other, thus the experimental trend is in agreement with both models (Fig. 5.4). Regarding the  $c$ -axis on the other hand, we can distinguish between the KS and ST phases more clearly. For the KS phase,  $c$  exhibits a constant growth with increasing  $x_{\text{Cd}}$ , whereas it plateaus for the ST modification. Experimentally, we observe a slight increase from  $x_{\text{Cd}} = 0$  to  $x_{\text{Cd}} = 0.37$ , consistent with the prediction for the KS phase, followed by a ‘‘plateaued’’ behavior above  $x_{\text{Cd}} = 0.37$ , compatible with the calculated ST trend (Table 5.3 and Fig. 5.4).

### 5.4.3. Raman spectroscopic investigations

In Fig. 5.6 we show the measured Raman spectra for the  $\text{Cu}_2\text{Cd}_x\text{Zn}_{1-x}\text{SnS}_4$  sample series. The Raman spectrum of the  $\text{Cu}_2\text{ZnSnS}_4$  kesterite end-member is consistent with the reported Raman spectra from the literature [45–47], with the most intense Raman band lying at  $339\text{ cm}^{-1}$ . This vibration is assigned to A symmetry and corresponds to sulfur motions (stretching vibrations) mainly along the  $c$ -axis [48].

The Raman spectra do not show appreciable changes upon varying the Cd content, except from the mode frequency variation of the intense KS A  $339\text{ cm}^{-1}$  Raman-active vibration. In particular, increase of  $x_{\text{Cd}}$  leads to a progressive downshift for this mode (Fig. 5.6), associated closely with the increase of the tetragonal  $c$ -axis (Table 5.2); increasing the Cd composition beyond  $x_{\text{Cd}} = 0.4$ , however, results in a noticeable change of the mode frequency variation, i.e. the A band frequency becomes almost insensitive to the Cd content. In addition, a sharp slope change is observed for the width (FWHM) of the A mode as a function of Cd content close to  $x_{\text{Cd}} = 0.4$ , with the FWHM increasing upon increasing the Cd concentration up to  $x_{\text{Cd}} \leq 0.4$ , whereas FWHM decreases between  $0.4 \leq x_{\text{Cd}} \leq 1$ .

Considering our aforementioned XRD results, which indicate a KS  $\rightarrow$  ST transition for  $x_{\text{Cd}} \approx 0.37/0.40$ , and given the similarity of the kesterite- and stannite-type Raman response [49], we interpret this change of the A mode frequency and FWHM trends as the Raman fingerprint of the KS  $\rightarrow$  ST structural transition in the  $\text{Cu}_2\text{Cd}_x\text{Zn}_{1-x}\text{SnS}_4$  sample series. The critical Cd-composition is found to be close to  $x_{\text{Cd}} \approx 0.40$ , in excellent agreement with our XRD results. We mention finally in passing that once in the ST phase region, the KS A mode is now assigned to  $A_1$  symmetry and is associated with sulfur motions mainly around the  $\text{Sn}^{4+}$  cations (also stretching vibrations along  $c$ -axis) [50].

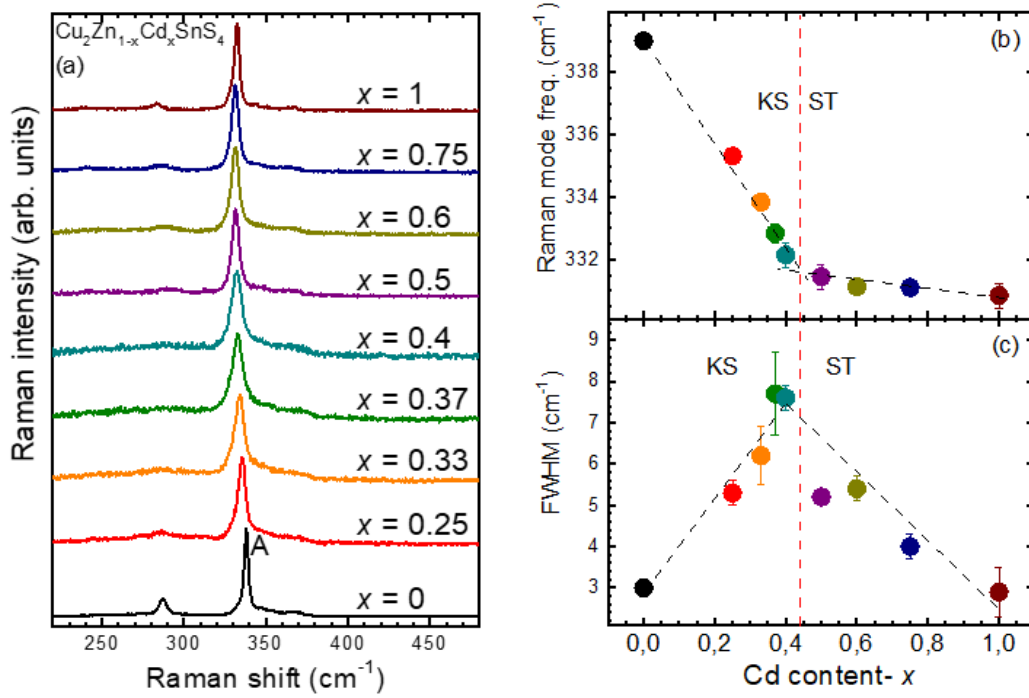
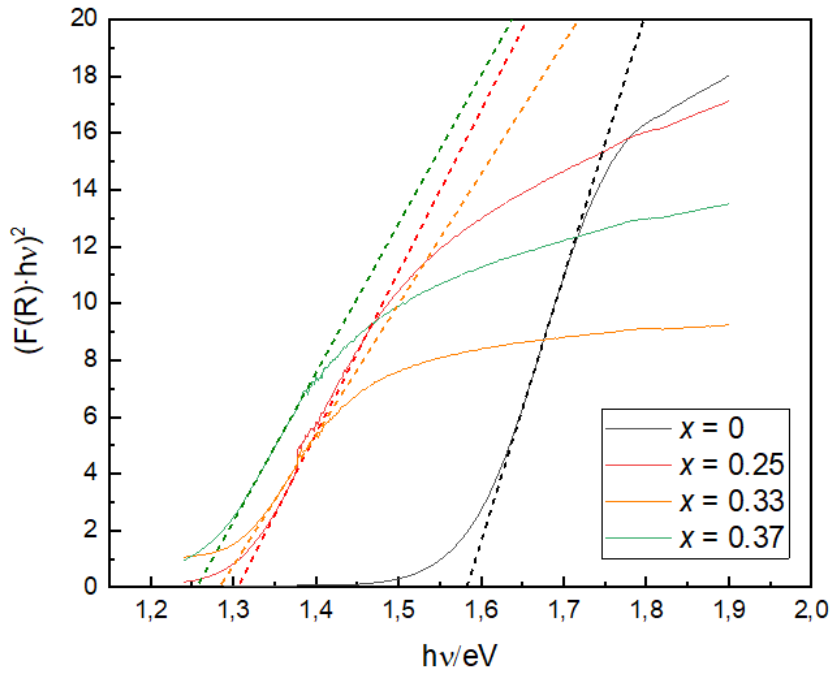


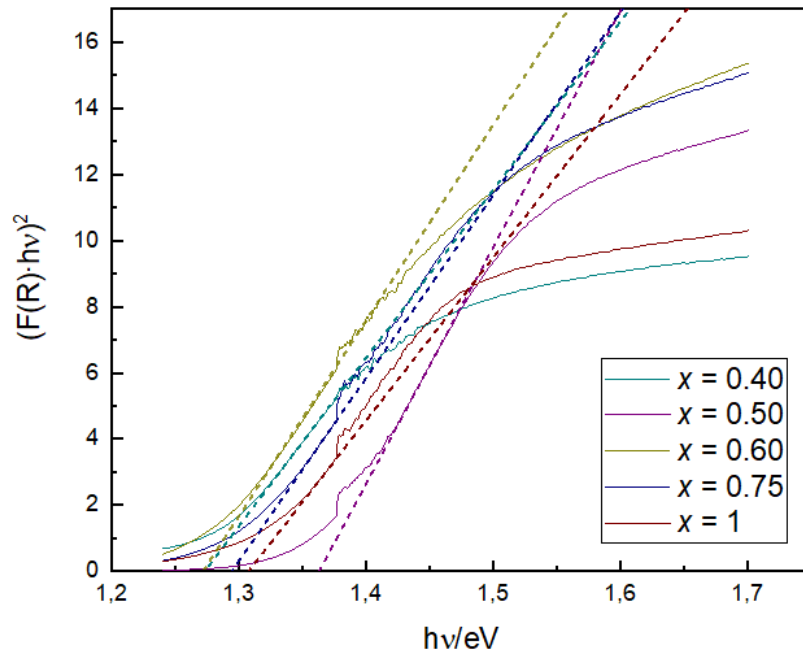
**Figure 5.6.:** (a) The as-measured Raman spectra of the synthetic  $\text{Cu}_2\text{Cd}_x\text{Zn}_{1-x}\text{SnS}_4$  sample series ( $x_{\text{Cd}} = 0, 0.25, 0.33, 0.37, 0.40, 0.50, 0.60, 0.75, 1$ ) with laser excitation wavelength  $\lambda = 473$  nm at ambient conditions. The determined (b) Raman mode frequency and (c) width (FWHM) of the strongest Raman-active vibration as a function of  $x_{\text{Cd}}$  are also plotted.

#### 5.4.4. Band gap

The optical band gaps  $E_g$  for the synthetic  $\text{Cu}_2\text{Cd}_x\text{Zn}_{1-x}\text{SnS}_4$  solid solution series were evaluated with UV/Vis spectroscopy (Fig. 5.7). The results are summarized in Table 5.4. For the  $\text{Cu}_2\text{ZnSnS}_4$  KS end-member ( $x = 0$ ), a direct  $E_g = 1.58(5)$  eV was determined, in excellent agreement with previous reports [5, 6]. Upon the  $\text{Zn}^{2+}$  substitution by  $\text{Cd}^{2+}$ , the direct  $E_g$  values drop by  $\sim 0.3$  eV; the  $E_g$  does not show any apparent dependence with the further variation of the Cd content, however, retaining a value close to 1.3 eV for the whole  $\text{Cu}_2\text{Cd}_x\text{Zn}_{1-x}\text{SnS}_4$  solid solution series, and the  $\text{Cu}_2\text{CdSnS}_4$  ST end-member (Fig. 5.7 and Table 5.4). Our data lie in very good agreement with the results of Pilvet et al. [17] on off-stoichiometric  $\text{Cu}_2\text{Cd}_x\text{Zn}_{1-x}\text{SnS}_4$  samples, where  $E_g$  was determined from quantum efficiency measurements. A slightly reduced optical band gap compared to  $\text{Cu}_2\text{ZnSnS}_4$  has the advantage of better optical absorption and, thus, higher photovoltaic efficiency in solar cell applications [14].



(a)  $x_{\text{Cd}} = 0, 0.25, 0.33, 0.37$



(b)  $x_{\text{Cd}} = 0.40, 0.50, 0.60, 0.75, 1$

**Figure 5.7.:** UV/Vis spectra of  $\text{Cu}_2\text{Cd}_x\text{Zn}_{1-x}\text{SnS}_4$  samples with Tauc plot determination of the direct optical band gap  $E_g$ .

**Table 5.4.:** Direct optical band gaps  $E_g$  of  $\text{Cu}_2\text{Cd}_x\text{Zn}_{1-x}\text{SnS}_4$ -samples with  $x_{\text{Cd}} = 0, 0.25, 0.33, 0.37, 0.40, 0.50, 0.60, 0.75, 1$ , as determined from UV/VIS measurements (Figure 5.7).

Cd-content $x_{\text{Cd}}$	Direct optical band gap $E_g$ [eV]
$x_{\text{Cd}} = 0$	1.58
$x_{\text{Cd}} = 0.25$	1.31
$x_{\text{Cd}} = 0.33$	1.28
$x_{\text{Cd}} = 0.37$	1.26
$x_{\text{Cd}} = 0.4$	1.27
$x_{\text{Cd}} = 0.5$	1.36
$x_{\text{Cd}} = 0.6$	1.27
$x_{\text{Cd}} = 0.75$	1.29
$x_{\text{Cd}} = 1$	1.31

Following our experimental observations, we calculated the band gaps at the HSE06 level for all phases as a function of the Cd content (Fig. 5.8, exemplary DOS shown in **Fig. S10** in the **Supplement**). We remind here that the disordered structures considered here are less stable than the ST phase for all compositions, with the exception of the DKS- $p_1$  modification (Fig. 5.5). We still consider them in the following discussion, however, because we think they give a good indication on how the band gap of a less stable disordered system is expected to behave as a function of composition. We note also that when the ordered KS phase is optimized at the HSE06 level, its band gap increases by 0.3 eV compared to the HSE06 band gap of a PBE-optimized structure [42, 51]. Since we optimized our structures at the PBE level, we shift the calculated HSE06 band gaps by 0.3 eV to account for this systematic error. In the following we will use the shifted theoretical predictions to directly compare to the experimentally measured band gaps. We need to point out that a direct comparison between the experimentally determined optical and the DFT-HSE06 calculated band gaps should be taken tentatively due to e.g. possible excitonic effects present in the experimental measurements; in the bulk KS and ST materials, however, a very good agreement between the optical and calculated band gaps has been established [4, 13], thus justifying such comparison.

All simulated KS band gaps decrease almost linearly with similar slopes upon increasing the Cd content (Fig. 5.8). The KS and DKS- $p_1$  phases exhibit very similar band gaps for all  $x_{\text{Cd}}$  values, decreasing from 1.5 eV to 0.9 eV upon increasing  $x_{\text{Cd}}$ . For the 12.5% disordered KS phase, the band gap is predicted to be 0.1 eV lower than the respective band gaps of the KS and DKS- $p_1$  phases for all Cd contents, whereas the band gap of the DKS- $p_2$  phase lies always 0.1 eV lower than the 12.5% disordered KS phase (Figure 5.8). On the contrary, the calculated ST band gaps are constant

at 1.32 eV for  $0 \leq x_{\text{Cd}} \leq 0.5$ , and decrease progressively for higher  $x_{\text{Cd}}$  values. The  $\text{Cu}_2\text{CdSnS}_4$  end-member is predicted to exhibit a band gap of 1.25 eV.

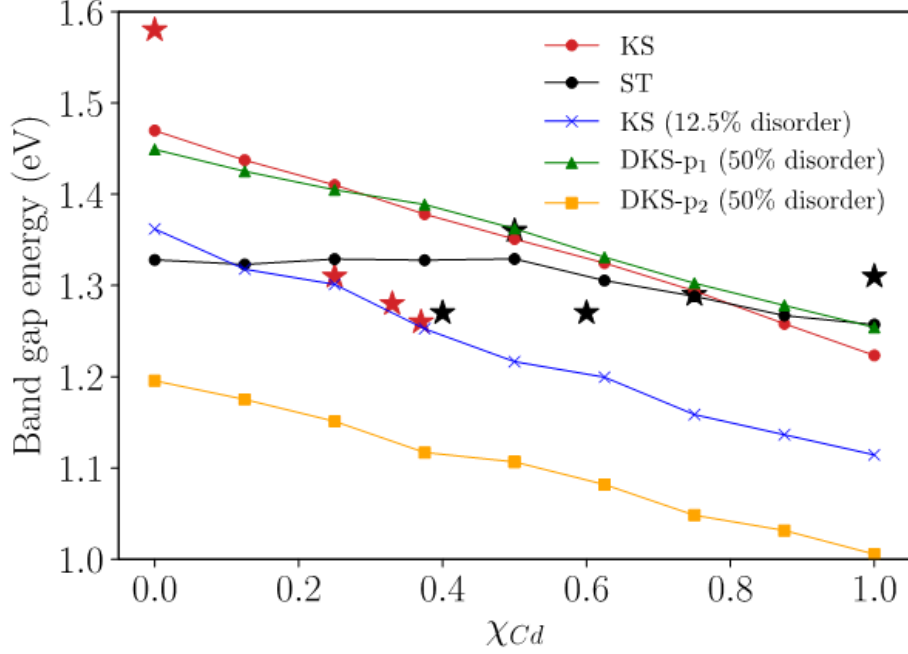


**Figure 5.8.:** Comparison of calculated band gaps to the experimentally measured band gaps for the ordered and disordered KS and ST phases. The experimental values are marked as stars (red for KS/DKS, black for ST phases). The calculated band gaps are upshifted by 0.3 eV.

For the  $\text{Cu}_2\text{ZnSnS}_4$  end-member, the experimental band gap indicates an ordered KS phase (Fig. 5.8). The next three experimental data points between  $0.25 \leq x_{\text{Cd}} \leq 0.37$  exhibit a substantial drop in the band gap ( $E_g \approx 1.3$  eV for  $x_{\text{Cd}} = 0.25$ ), with a decreasing trend upon increasing  $x_{\text{Cd}}$ . Such behavior indicates partial disorder within the synthetic samples, as the experimental band gaps approach the band gap predictions for the 12.5% disordered KS. The latter prediction lies in excellent agreement with our XRD results (Table 5.3).

Within the  $0.37 \leq x_{\text{Cd}} \leq 0.5$  Cd content range, the DKS $\rightarrow$ ST transition is expected to take place according to the XRD data. The transition is accompanied by a band gap increase of 0.1 eV (Table 5.4). This band gap upshift is consistent with a transition from the 12.5% disordered KS phase to the ST phase in our simulations (Fig. 5.8). In the experiment, the  $E_g$  value subsequently drops by 0.1 eV upon passing from  $x_{\text{Cd}} = 0.5$  to 0.6 Cd content, and then steadily increases to the final value of 1.31 eV. Our prediction exhibits a different trend for the ST phase, with a steadily decreasing band gap trend for  $x_{\text{Cd}} \geq 0.5$ . The absolute differences between the calculated and

experimental ST band gaps are always lower than 0.1 eV. This agreement is sufficiently good, considering that we calculated the band gaps for the most stable substitution pattern for each Cd content.

#### 5.4.5. The (D)KS $\rightarrow$ ST transition in $\text{Cu}_2\text{Cd}_x\text{Zn}_{1-x}\text{SnS}_4$ .

The structural transition between the kesterite- and stannite-type structures in  $\text{Cu}_2\text{Cd}_x\text{Zn}_{1-x}\text{SnS}_4$  is a continuous phase transition, as revealed by the linear change in volume upon varying  $x_{\text{Cd}}$  (Table 5.3 and Fig. 5.4). Close inspection of the lattice parameter evolution as a function of Cd content reveals that the  $a$ -axis exhibits also a linear variation, whereas the  $c$ -axis increases up to  $x_{\text{Cd}} = 0.33$ , plateaus between  $0.33 \leq x_{\text{Cd}} \leq 0.5$ , and then decreases continuously up to  $x_{\text{Cd}} = 1$ . Given this variation in the behavior of the  $c$ -axis, we identify three distinct  $x_{\text{Cd}}$  regions:

##### A. $x_{\text{Cd}} \leq 0.33$ :

For this Cd content, the  $\text{Cu}_2\text{Cd}_x\text{Zn}_{1-x}\text{SnS}_4$  compounds adopt the KS/PDKS phase (Table 5.3). Upon increasing  $x_{\text{Cd}}$ , both the  $a$ - and  $c$ -axis and the volume increase continuously, following the expected trend due to the isovalent substitution of the smaller  $\text{Zn}^{2+}$  (ionic radius 0.6 Å) by the larger  $\text{Cd}^{2+}$  (ionic radius 0.78 Å) cations in the Cu-Zn planes (Fig. 5.1). Such lattice expansion is also reflected in the mode frequency decrease of the strongest A Raman-active vibration of the S anions, which corresponds to stretching motions along the  $c$ -axis (Fig. 5.6). Additionally, the width of this band increases with increasing  $x_{\text{Cd}}$ , indicating a local structural ‘disorder’ introduced in the lattice due to the significant size difference between the  $\text{Zn}^{2+}$  and  $\text{Cd}^{2+}$  cations. Finally, the direct band gap  $E_g$  decreases upon increasing  $x_{\text{Cd}}$  (Table 5.4 and Fig. 5.8); considering that  $E_g$  reflects the energy difference between the hybridized Cu-S and Sn-S states making up the valence band maximum (VBM) and conduction band minimum (CBM), respectively (**Fig. S10** in the **Supplement**), the  $E_g$  drop with increasing  $x_{\text{Cd}}$  implies an enhanced overlap of these states upon  $\text{Zn}^{2+} \rightarrow \text{Cd}^{2+}$  substitution [52]. In a simplified view, insertion of the larger  $\text{Cd}^{2+}$  cations in the Cu-Zn KS planes is expected to expand the Cu2-S and Zn-S distances (Cu2 and Zn make up for the Cu-Zn planes in the KS phase, Fig. 5.1), and ‘push’ the S anions closer to the Cu1-Sn planes, thus shortening the respective Cu1-S and Sn-S bonds. Assuming that the shortening of the Cu1-S and the expansion of the Cu2-S bonds ‘cancel each other out’ in terms of electronic Cu-S overlap (i. e. the VBM will not shift with varying  $x_{\text{Cd}}$ ), the shortening of the Sn-S bond distance should increase the respective Sn-S electronic band overlap, thus ‘pushing’ the CBM to lower energies and resulting in turn to a band gap closure,

in excellent agreement with our observations (Table 5.4 and Fig. 5.8). Our DFT calculations have captured all of the aforementioned effects.

### B. $0.37 \leq x_{\text{Cd}} \leq 0.4$ :

Within this Cd content region, our investigations indicate that the (D)KS  $\rightarrow$  ST transition occurs for the  $\text{Cu}_2\text{Cd}_x\text{Zn}_{1-x}\text{SnS}_4$  series. The Cd/Zn cations shift from the  $2c / 2d$  Wyckoff positions of the PDKS phase (adopted for  $x_{\text{Cd}} = 0.33$ ) successively to the  $4d$  (DKS phase for  $x_{\text{Cd}} = 0.37$ ) and then finally to site  $2a$  (ST phase for  $x_{\text{Cd}} \geq 0.4$ ). The driving force for the (D)KS  $\rightarrow$  ST structural transformation is most likely the fact that the larger  $\text{Cd}^{2+}$  cations are better accommodated within the Sn/Zn planes comprising the ST phase, than in the Cu/Zn planes of the KS phase (Fig. 5.1). In the ST structure, the Sn/Zn layers provide more available space to the larger  $\text{Cd}^{2+}$  cations due to the smaller ionic radius of  $\text{Sn}^{4+}$  (0.55 Å) compared to that of  $\text{Cu}^+$  (0.6 Å) in the Cu/Zn layers comprising the KS/PDKS/DKS phases. Interestingly, the lattice parameters, the volume, the band gap, and the frequency of the most intense Raman-active mode do not show any distinct changes at the  $x_{\text{Cd}}$  transition point; on the other hand, the FWHM of the strongest Raman vibration exhibits its maximum between this  $0.37 \leq x_{\text{Cd}} \leq 0.4$  range (Fig. 5.6), reflecting probably the aforementioned reordering of the respective cationic layers upon the (D)KS  $\rightarrow$  ST transition.

### C. $0.5 \leq x_{\text{Cd}} \leq 1$ :

Finally, within this Cd content region, the  $\text{Cu}_2\text{Cd}_x\text{Zn}_{1-x}\text{SnS}_4$  members crystallize in the ST phase (Table 5.3). The  $a$ -axis and the volume increase upon increasing  $x_{\text{Cd}}$ , whereas the  $c$ -axis contracts (Table 5.3 and Fig. 5.4). The latter behavior is quite puzzling, as our DFT calculations predict a rather constant  $c$ -axis value for the ST phase within this  $x_{\text{Cd}}$  range (Fig. 5.4). In addition, the mode frequency of the strongest ST Raman-active vibration (now  $A_1$ ) is almost independent to the variation of  $x_{\text{Cd}}$ , whereas its FWHM decreases continuously (Fig. 5.6). Moreover, the  $E_g$  of the ST phase is not affected by  $x_{\text{Cd}}$  (Table 5.4 and Fig. 5.8), with the VBM and CBM bands again primarily consisting of hybridized Cu-S and Sn-S states, respectively (**Fig. S10** in the **Supplement**). In order to interpret all of these effects, we need to examine closely the layered structure of the ST phase. The ST modification is made up from alternating Zn/Sn and Cu layers (Fig. 5.1). This means that the  $\text{Zn}^{2+} \rightarrow \text{Cd}^{2+}$  substitution takes place now within the Zn/Sn layers, assuming no interplanar cationic disorder. In a similar simplified view as before, the incorporation of the larger  $\text{Cd}^{2+}$  cations in the Zn/Sn planes will expand the Sn-S bond distances, ‘push’ the S anions closer to the Cu layers and, consequently, shorten the Cu-S bonds. Such structural effects will result in an energy increase for

both the VBM and CBM [52], hence lead to a rather constant (within error)  $E_g$ , in excellent agreement with our experimental and theoretical investigations (Table 5.4 and Fig. 5.8). On the other hand, the contraction of the  $c$ -axis is not that straightforward to interpret. Taking into account that in the  $\text{Cu}_2\text{Fe}_x\text{Zn}_{1-x}\text{SnS}_4$  solid solution series, the angular distortion of the metal-sulfur tetrahedral units increases noticeably upon approaching the ST region (i. e. for  $\text{Fe}^{2+}$  content larger than  $x_{\text{Fe}} \geq 0.4$  [53]), one could expect that a similar tetrahedral distortion is taking place in the ST  $\text{Cu}_2\text{Cd}_x\text{Zn}_{1-x}\text{SnS}_4$  members investigated here. Such angular distortion may counteract the expected size effects (i. e. lattice expansion) of the  $\text{Zn}^{2+} \rightarrow \text{Cd}^{2+}$  substitution along the  $c$ -axis; indeed, such angular distortion was shown to be accompanied by the *contraction* of the ST  $c$ -axis (and expansion of the  $a$ -axis) in the  $\text{Cu}_2\text{Fe}_x\text{Zn}_{1-x}\text{SnS}_4$  solid solution series [53]. Moreover, such angular distortion would also influence the mode frequency of the ST  $A_1$  Raman-active vibration, which should upshift upon increasing the Cd content following the expansion of the Sn-S bonds [50]. The increase of the tetrahedral angular distortion upon increasing  $x_{\text{Cd}}$ , however, would oppose the expected trend and lead to an almost insensitive variation of the ST  $A_1$  Raman mode with  $x_{\text{Cd}}$ , as observed experimentally (Fig. 5.6). Finally, the continuous FWHM decrease of the ST  $A_1$  Raman-active mode with increasing  $x_{\text{Cd}}$  can be rationalized in a rather straightforward manner, as the more  $\text{Cd}^{2+}$  is introduced in the Zn-Cd/Sn lattice planes, the more ‘homogeneous’ (less disordered) the crystal lattice will become in terms of cationic size variations.

## 5.5. Conclusions

Single-phase and well-crystallized samples of the  $\text{Cu}_2\text{Cd}_x\text{Zn}_{1-x}\text{SnS}_4$  solid solution series with  $x_{\text{Cd}} = 0, 0.25, 0.33, 0.37, 0.40, 0.50, 0.60, 0.75, 1$  were synthesized by mechanochemical milling in a high energy planetary Mono Mill and following annealing in  $\text{H}_2\text{S}$ -atmosphere. The structural transition between the kesterite- and stannite-type structures was examined by Rietveld refinements of the XRD data using four different structural models, and Raman spectroscopy. The critical Cd content value was determined close to  $x_{\text{Cd}} \approx 0.40$ . It is a continuous structural transition, starting with the (partially disordered) kesterite-type structure for  $x_{\text{Cd}} \leq 0.33$ , followed by a transition towards a disordered kesterite structure for  $x_{\text{Cd}} \approx 0.37$ , and finally into a stannite-type structure for  $x_{\text{Cd}} \geq 0.4$ . All of the Cd-containing samples exhibit a  $\sim 0.3$  eV smaller direct optical band gap  $E_g$  compared to the KS  $\text{Cu}_2\text{ZnSnS}_4$  end-member, with  $E_g$  varying minimally with the Cd content.

Our DFT calculations show an overall good agreement with the experimental values in terms of structural and corrected HSE06 band gaps. The KS  $\rightarrow$  ST transition was

predicted at  $x_{\text{Cd}} = 0.50$ , based on total energy calculations for all symmetry inequivalent substitution patterns. We presume that the difference in the critical  $x_{\text{Cd}}$  value compared to the experimental counterpart is due to the presence of partial disorder in the synthetic samples, a plausible assumption according to the XRD refinements. The somewhat different variation of the predicted and experimental band gaps as a function of  $x_{\text{Cd}}$  can be also rationalized from the same argumentation.

## 5.6. Acknowledgements

The authors would like to thank Nina Genz (TU Berlin) for performing the UV/Vis measurements and Uwe Dittmann (GFZ Potsdam) for sample preparation for the electron microprobe experiments. This work is funded by the Deutsche Forschungsgemeinschaft (DFG): LE781/19-1, PA1360/14-1, EF112/3-1. The authors acknowledge the North-German Supercomputing Alliance (HLRN) for providing HPC resources that have contributed to the research results reported in this paper. Financial support from International Max Planck Research School (IMPRS) Functional Interfaces in Physics and Chemistry is gratefully acknowledged.

## 5.7. References

- [1] F.-J. Fan, L. Wu, S.-H. Yu. *Energy Environ. Sci.* **2014**, 7, 190–208.
- [2] M. Graetzel, R. A. J. Janssen, D. B. Mitzi, E. H. Sargent. *Nature* **2012**, 488, 305–312.
- [3] S. Siebentritt, S. Schorr. *Prog. Photovolt: Res. Appl.* **2012**, 20, 512–519.
- [4] A. Walsh, S. Chen, S.-H. Wei, X.-G. Gong. *Adv. Energy Mater.* **2012**, 2, 400–409.
- [5] K. Ito, T. Nakazawa. *Jpn. J. Appl. Phys.* **1988**, 11, 2094–2097.
- [6] H. Katagiri, K. Saitoh, T. Washio, H. Shinohara, T. Kurumadani, S. Miyajima. *Sol. Energy Mater. Sol. Cells* **2001**, 65, 141–148.
- [7] J. Seol, S. Lee, J. Lee, H. Nam, K. Kim. *Sol. Energy Mater. Sol. Cells* **2003**, 75, 155–162.

- [8] S. R. Hall, J. T. Szymanski, J. M. Stewart. *Can. Mineral.* **1978**, 16, 131–137.
- [9] S. Chen, J.-H. Yang, X.G. Gong, A. Walsh, S.-H. Wei. *Phys. Rev. B: Condens. Matter and Mater. Phys.* **2010**, 81, 245204/1-245204/10.
- [10] A. Nagoya, R. Asahi, R. Wahl, G. Kresse. *Phys. Rev. B: Condens. Matter and Mater. Phys.* **2010**, 81, 113202/1-113202/4.
- [11] L. Chen, H. Deng, J. Cui, J. Tao, W. Zhou, H. Cao, L. Sun, P. Yang, J. Chu. *J. Alloys Compd.* **2015**, 627, 388–392.
- [12] S. Schorr, H.-J. Hoebler, M. Tovar. *Eur. J. Mineral.* **2007**, 19, 65–73.
- [13] Z.-Y. Xiao, Y.-F. Li, B. Yao, R. Deng, Z.-H. Ding, T. Wu, G. Yang, C.-R. Li, Z.-Y. Dong, L. Liu, L.-G. Zhang, H.-F. Zhao. *J. Appl. Phys.* **2013**, 114, 183506/1-183506/7.
- [14] Z. Su, J. M. R. Tan, X. Li, X. Zeng, S. K. Batabyal, L. H. Wong. *Adv. Energy Mater.* **2015**, 5, 1500682/1-1500682/7.
- [15] Q. Zhang, H. Deng, L. Chen, L. Yu, J. Tao, L. Sun, P. Yang, J. Chu. *J. Alloys Compd.* **2017**, 695, 482–488.
- [16] A. S. Ibraheam, Y. Al-Douri, U. Hashim, D. Prakash, K. D. Verma, M. Ameri. *J. Mater. Sci.* **2016**, 51, 6876–6885.
- [17] M. Pilvet, M. Kauk-Kuusik, M. Altosaar, M. Grossberg, M. Danilson, K. Timmo, A. Mere, V. Mikli. *Thin Solid Films* **2015**, 582, 180–183.
- [18] J. Fu, Q. Tian, Z. Zhou, D. Kou, Y. Meng, W. Zhou, S. Wu. *Chem. Mater.* **2016**, 28, 5821–5828.
- [19] G. S. Gautam, T. P. Senftle, E. A. Carter. *Chem. Mater.* **2018**, 30, 4543–4555.
- [20] A. Ritscher, J. Just, O. Dolotko, S. Schorr, M. Lerch. *J. Alloys Compd.* **2016**, 670, 289–296.

- [21] H. M. Rietveld. *J. Appl. Crystallogr.* **1969**, 2, 65–71.
- [22] J. Rodriguez-Carvajal. *Abstracts of the Satellite Meeting on Powder Diffraction of the XV. Congress of the IUCr* **1990**, p. 127.
- [23] A. Ritscher, M. Hoelzel, M. Lerch. *J. Solid State Chem.* **2016**, 238, 68–73.
- [24] J. T. Armstrong. CITZAF: A package of correction programs for the quantitative electron microbeam X-ray analysis of thick polished materials, thin films, and particles. *Microbeam Analysis* **1995**, 4, 177–200.
- [25] J. Tauc. *Mater. Res. Bull* **1968**, 3, 37–46.
- [26] J. Tauc, R. Grigorovici, A. Vancu. *Physica Status Solidi b* **1966**, 15, 627–637.
- [27] G. Kresse, J. Hafner. *Phys. Rev. B* **1993**, 47, 558–561.
- [28] G. Kresse, J. Hafner. *Phys. Rev. B* **1994**, 49, 14251–14259.
- [29] G. Kresse, J. Furthmüller. *Phys. Rev. B* **1996**, 54, 11169–11186.
- [30] G. Kresse, J. Furthmüller. *Comput. Mater. Sci.* **1996**, 6, 15–50.
- [31] P. E. Blöchl. *Phys. Rev. B* **1994**, 50, 17953–17979.
- [32] G. Kresse, D. Joubert. *Phys. Rev. B* **1999**, 59, 1758–1775.
- [33] J. E. Jackson. Review of Numerical Recipes: The Art of Scientific Computing, by W. Press, B. Flannery, S. Teukolsky and W. Vetterling. *Technometrics* **1986**, 2, 501–502.
- [34] H. J. Monkhorst, J. D. Pack. *Phys. Rev. B* **1976**, 13, 5188–5192.
- [35] J. P. Perdew, K. Burke, M. Ernzerhof. *Phys. Rev. Lett.* **1996**, 77, 3865–3868.
- [36] J. Heyd, G. E. Scuseria, M. Ernzerhof. *J. Chem. Phys.* **2003**, 118, 8207–8215.

- [37] J. Heyd, G. E. Scuseria. *J. Chem. Phys.* **2004**, 121, 1187–1192.
- [38] J. Heyd, G. E. Scuseria, M. Ernzerhof. Erratum: “Hybrid functionals based on a screened Coulomb potential” [J. Chem. Phys. 118, 8207 (2003)]. *J. Chem. Phys.* **2006**, 124, 219906.
- [39] A. V. Krukau, O. A. Vydrov, A. F. Izmaylov, G. E. Scuseria. *J. Chem. Phys.* **2006**, 125, 224106/1-224106/5.
- [40] P. E. Blöchl, O. Jepsen, O. K. Andersen. *Phys. Rev. B* **1994**, 49, 16223–16233.
- [41] S. Chen, A. Walsh, X.-G. Gong, S.-H. Wei. *Adv. Mater.* **2013**, 25, 1522–1539.
- [42] M. Quennet, A. Ritscher, M. Lerch, B. Paulus. *J. Solid State Chem.* **2017**, 250, 140–144.
- [43] S. P. Ong, W. D. Richards, A. Jain, G. Hautier, M. Kocher, S. Cholia, D. Gunter, V. L. Chevrier, K. A. Persson, G. Ceder. *Comput. Mater. Sci.* **2013**, 68, 314–319.
- [44] V. F. Sears. *Neutron News* **1992**, 3, 26–37.
- [45] R. Caballero, E. Garcia-Llamas, J. M. Merino, M. León, I. Babichuk, V. Dzhagan, V. Strelchuk, M. Valakh. *Acta Materialia* **2014**, 65, 412–417.
- [46] P. A. Fernandes, P. M. P. Salomé, A. F. da Cunha. *J. Alloys Compd.* **2011**, 509, 7600–7606.
- [47] I. Efthimiopoulos, A. Ritscher, M. Lerch, S. Speziale, A. S. Pakhomova, H. P. Liermann, M. Koch-Müller. *Appl. Phys. Lett.* **2017**, 110, 041905/1-041905/5.
- [48] J. M. Skelton, A. J. Jackson, M. Dimitrievska, S. K. Wallace, A. Walsh. *APL Materials* **2015**, 3, 041102/1-041102/6.
- [49] X. Fontané, V. Izquierdo-Roca, E. Saucedo, S. Schorr, V. O. Yukhymchuk, M. Ya. Valakh, A. Pérez-Rodríguez, J. R. Morante. *J. Alloys Compd.* **2012**, 539, 190–194.
- [50] C. Rincón, M. Quintero, Ch. Power, E. Moreno, E. Quintero, J. A. Henao, M.

A. Macías, M. Morocoima. *J. Appl. Phys.* **2015**, 117, 205701/1-205701/6.

[51] M. Quennet. *Dissertation* **2016**, Freie Universität Berlin.

[52] A. Miglio, C.P. Heinrich, W. Tremel, G. Hautier, W. G. Zeier. *Adv. Sci.* **2017**, 4, 1700080/1-1700080/7.

[53] P. Bonazzi, L. Bindi, G. P. Bernardini, S. Menchetti. *Can. Mineral.* **2003**, 41, 639–647.

## 6. Publication 2

### Crystal structure of mechanochemically synthesized $\text{Ag}_2\text{CdSnS}_4$

Eva M. Heppke, Stefan Berendts and Martin Lerch

*Postprint*

*Z. Naturforsch. B* **2020**, 75(4), 393-402

doi:10.1515/znb-2020-0022

<https://www.degruyter.com/view/journals/znb/75/4/article-p393.xml>

Contribution to publication:

- E. M. Heppke: Sample preparation, structural characterization and evaluation, group theory, band gap determination, writing
- S. Berendts: X-ray diffraction measurements
- M. Lerch: General advice, proofreading

**Authors:** E. M. Heppke<sup>[1]</sup>, S. Berendts<sup>[1]</sup>, M. Lerch<sup>\*[1]</sup>

<sup>1</sup>Institut für Chemie: Technische Universität Berlin, Straße des 17. Juni 135, 10623 Berlin

\* corresponding

**Keywords:** Ag<sub>2</sub>CdSnS<sub>4</sub>; HT-XRD; mechanochemical synthesis; phase transition; Rietveld refinement

**Dedicaton:** Dedicated to Professor Rüdiger Kniep on the Occasion of his 75<sup>th</sup> birthday

Eva M. Heppke, Stefan Berendts and Martin Lerch\*

# Crystal structure of mechanochemically synthesized $\text{Ag}_2\text{CdSnS}_4$

<https://doi.org/10.1515/znb-2020-0022>

Received January 27, 2020; accepted February 20, 2020

**Abstract:**  $\text{Ag}_2\text{CdSnS}_4$  was synthesized by a two step mechanochemical synthesis route. From a detailed analysis of the observed reflections in the X-ray powder diffraction pattern, the crystal structure proposed in the literature (space group  $Cmc2_1$  [E. Parthé, K. Yvon, R. H. Deitch, *Acta Crystallogr.* **1969**, B25, 1164–1174; O. V. Parasyuk, I. D. Olekseyuk, L. V. Piskach, S. V. Volkov, V. I. Pekhnyo, *J. Alloys Compd.* **2005**, 399, 173–177]) is questionable. Our structural investigations presented in this contribution point to the fact that  $\text{Ag}_2\text{CdSnS}_4$  crystallizes in the monoclinic wurtzkesterite-type structure (space group  $Pn$ ). At around  $T=200^\circ\text{C}$ , a phase transition to the orthorhombic wurtzstannite-type structure (space group  $Pmn2_1$ ) is observed.

**Keywords:**  $\text{Ag}_2\text{CdSnS}_4$ ; HT-XRD; mechanochemical synthesis; phase transition; Rietveld refinement.

**Dedicated to:** Professor Rüdiger Kniep on the Occasion of his 75<sup>th</sup> birthday.

## 1 Introduction

$A_2B^{\text{II}}C^{\text{IV}}X_4$  ( $X^{2-} = \text{S}, \text{Se}, \text{Te}$ ) compounds are semiconductors exhibiting either a cubic or a hexagonal diamond-related structure [1–3]. The most prominent group of  $A_2B^{\text{II}}C^{\text{IV}}X_4$  semiconductors are Cu-bearing compounds [4–9]. Among them,  $\text{Cu}_2\text{ZnSnS}_4$  has gained much attention as a potential candidate for absorber layers in thin film solar cells [10–12]. Ag-containing compounds are more difficult to synthesize and less stable. Nevertheless, a few  $A_2B^{\text{II}}C^{\text{IV}}X_4$  phases with  $A = \text{Ag}$  are known so

far [4, 13–19]. For most Ag compounds, a stannite- or wurtzstannite-/wurtzkesterite-type structure has been presented in the literature. However, there are some compounds that deviate from these two structures. For  $\text{Ag}_2\text{CdSnS}_4$ , the space group  $Cmc2_1$  is proposed which can be considered as a hexagonal diamond-/wurtzite-derived structure with a statistical distribution of Ag, Cd, and Sn on Wyckoff position  $4a$  with (0, 0.167, 0.370); sulfur is located at another  $4a$  position with (0, 0.176, 0.997) [4, 20]. The results of our investigations on the aforementioned compound indicate a different crystal structure. Due to additional reflections in the X-ray powder diffraction pattern of our synthesized sample, space group  $Cmc2_1$  can be excluded.  $\text{Ag}_2\text{CdSnS}_4$  was synthesized via a mechanochemical process which has proven its suitability for the successful preparation of phase-pure and well crystallized quaternary  $A_2B^{\text{II}}C^{\text{IV}}S_4$  compounds such as  $\text{Cu}_2\text{ZnSnS}_4$  [21]. The crystal structure of our mechanochemically prepared  $\text{Ag}_2\text{CdSnS}_4$  has been determined using powder X-ray diffraction. Additionally, UV/Vis and DTA measurements were performed. Surprisingly, a phase transition at around  $T=200^\circ\text{C}$  could be observed and the crystal structures of both the high- and low-temperature phases were investigated by *in-situ* XRD.

## 2 Results and discussion

The mechanochemical synthesis approach with a subsequent annealing step as described in the experimental section results in the formation of phase-pure and well crystallized  $\text{Ag}_2\text{CdSnS}_4$ . Phase composition was determined by EDX and combustion analysis and is in accordance with the theoretical one (Table 1). EDX mapping also confirmed a homogenous distribution of Ag, Cd, Sn, and S in the individual particles (Fig. 1).

Interestingly, in the DTA curve of our  $\text{Ag}_2\text{CdSnS}_4$  sample thermal effects were observed. An endothermic peak occurs in the heating process ( $T_p = -205^\circ\text{C}$ ) and an exothermic one is observed during cooling ( $T_p = -199^\circ\text{C}$ ). This points to a reversible phase transition at around  $200^\circ\text{C}$  (Fig. 2). The reversibility of the phase transition was also proven by *in-situ* X-ray diffraction.

\*Corresponding author: Martin Lerch, Institut für Chemie, Technische Universität Berlin, Straße des 17. Juni 135, 10623 Berlin, Germany, Fax: +493031479656, E-mail: martin.lerch@tu-berlin.de  
Eva M. Heppke and Stefan Berendts: Institut für Chemie, Technische Universität Berlin, Straße des 17. Juni 135, 10623 Berlin, Germany

**Table 1:** Phase composition of  $\text{Ag}_2\text{CdSnS}_4$  calculated from EDX data and sulfur content determined by elemental analysis.

$\text{Ag}_2\text{CdSnS}_4$		
	Ideal (wt.-%)	Measured (wt.-%)
Ag	37.5	36.4
Cd	19.5	20.7
Sn	20.6	21.2
S (EDX)	22.3	21.7
S (EA)	22.3	22.0

## 2.1 Structural relationship between hexagonal diamond and the wurtzstannite-/wurtzkesterite-type structure

As it can be seen in the Bärnighausen tree [22, 23], elucidating the relationship between the hexagonal diamond (lonsdaleite) and the wurtzstannite-/wurtzkesterite-type structures (Fig. 3), space group  $Cmc2_1$ , as a subgroup to that of the wurtzite-type structure, is proposed either for binary compounds as well as for compounds with a statistical distribution of their cations/anions on one position. For  $\text{Ag}_2\text{CdSnS}_4$ , space group  $Cmc2_1$  is mentioned in the literature with Ag, Cd, and Sn distributed statistically on the position  $4a$  with (0, 0.167, 0.370) and S on another  $4a$  position with (0, 0.176, 0.997) [20].

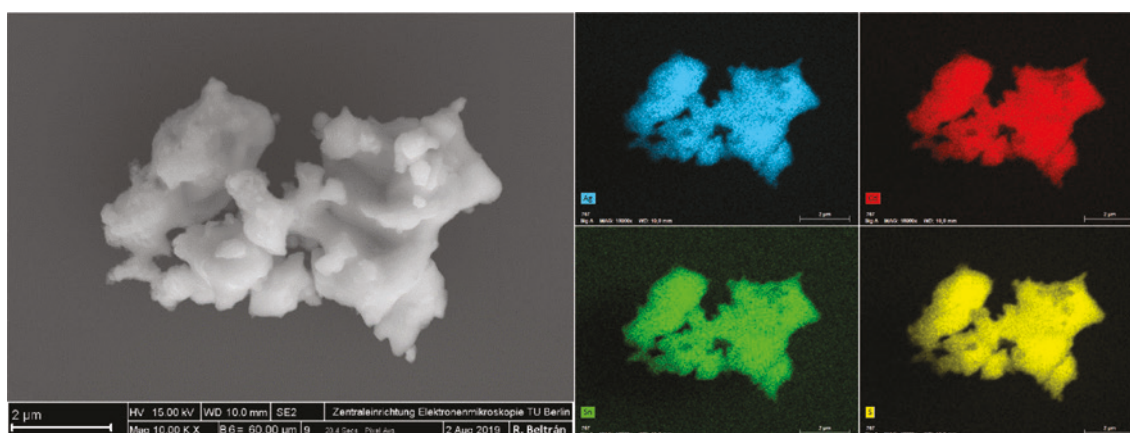
Similar compounds containing silver either crystallize in cubic diamond/sphalerite-related structures such as the stannite- or kesterite-type structure (such as  $\text{Ag}_2\text{ZnSnS}_4$  [14],  $\text{Ag}_2\text{FeSnS}_4$  [13],  $\text{Ag}_2\text{ZnGeS}_4$  [24]) or in crystal structures derived from the hexagonal diamond/wurtzite type providing non-equivalent positions for the cations/anions

(the wurtzstannite-type structure (space group  $Pmn2_1$ ) and its derivatives with space group  $Pn$  (wurtzkesterite-type structure) or  $Pna2_1$ ). Compounds crystallizing in the wurtzstannite-type structure are  $\text{Ag}_2\text{CdGeS}_4$  [4] and  $\text{Ag}_2\text{HgSnS}_4$  [15], whereas  $\text{Ag}_2\text{MnSnS}_4$  [18] and Si-bearing compounds such as  $\text{Ag}_2\text{FeSiS}_4$  [16] and  $\text{Ag}_2\text{ZnSiS}_4$  [17] crystallize in the wurtzkesterite-type structure. Due to the close structural relationships between these three structures, it can be quite difficult to distinguish between them when using conventional methods. For  $\text{Ag}_2\text{CdGeS}_4$ , two polymorphs have been reported exhibiting the space groups  $Pmn2_1$  [4] and  $Pna2_1$  [25], respectively.

## 2.2 The high-temperature phase of $\text{Ag}_2\text{CdSnS}_4$

Starting with the high-temperature phase, it should be noted that an orthorhombic unit cell could be found by the Werner algorithm using the program WINXPOW 1.2 (STOE & Cie GmbH, Darmstadt, Germany) [29] for the sample at  $T=300^\circ\text{C}$ . The lattice parameters were refined to  $a=8.2263 \text{ \AA}$ ,  $b=7.0655 \text{ \AA}$ , and  $c=6.7051 \text{ \AA}$  leaving no reflection behind. The volume of the unit cell was calculated to  $389.7 \text{ \AA}^3$ . It should be mentioned that the lattice parameter  $a$  given by the Werner algorithm is two times larger than that of the proposed crystal structure with space group  $Cmc2_1$  for  $\text{Ag}_2\text{CdSnS}_4$  [4, 20]. Examples of  $A_2^I B^II C^IV X_4$  compounds with a lattice parameter  $a$  of around  $8.23 \text{ \AA}$  (and similar values for the lattice parameters  $b$  and  $c$ ) within the orthorhombic crystal system have also been described by other authors [15].

For the Rietveld refinement of the high-temperature phase space group  $Pmn2_1$  (wurtzstannite-type structure)

**Fig. 1:** SEM images of  $\text{Ag}_2\text{CdSnS}_4$  particles and EDX mapping of homogeneously distributed Ag (blue), Cd (red), Sn (green), and S (yellow) in the  $\text{Ag}_2\text{CdSnS}_4$  particles.

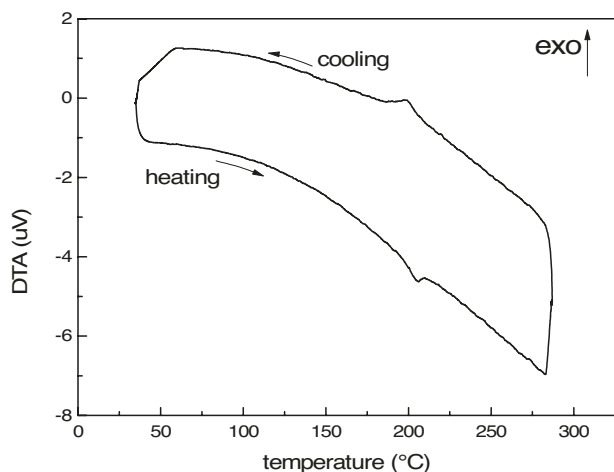


Fig. 2: DTA curve of  $\text{Ag}_2\text{CdSnS}_4$  under nitrogen atmosphere.

is used. As depicted in Fig. 4, the experimental pattern is in good agreement with the theoretical one. Crystallographic details as well as atomic and structural parameters are listed in Tables 2 and 3. The Debye Waller factors of sulfur were set to a value of 1 and not refined, also the site occupation factors of all atoms. As  $Pmn2_1$  is a polar space group and therefore possesses one origin-free direction (the  $z$  direction), the  $z$  parameter of the Ag atom position was fixed. As Ag, Cd, and Sn are not distinguishable using conventional X-ray diffraction methods, the distribution of these cations in the wurtzstannite- (and also wurtzkesterite-) type structure was set to that of the related compounds described in the literature.

The wurtzstannite-type structure (space group  $Pmn2_1$ ) of the high-temperature phase of  $\text{Ag}_2\text{CdSnS}_4$  can be described as a hexagonal diamond/wurtzite-derived structure with a hexagonal closest packing of sulfur anions. Ag is located at a fourfold position whereas Cd and Sn occupy two non-equivalent twofold positions. Three crystallographically independent sulfur positions are present, where S1 is located on a fourfold position and S2 as well as S3 atoms occupy two twofold positions. Considering the honeycomb set-up, the wurtzstannite-type structure is built up of consecutive Ag and Cd/Sn layers (in general:  $A^I$  and  $B^{II}/C^{IV}$  layers). This is manifested in alternating layers of Ag-centered and Cd/Sn-centered polyhedra along the  $b$  axis (Fig. 5). These alternating stacking sequence appears to be in line with that of the stannite type [5, 30], the analogous structure type derived from the cubic diamond/sphalerite-type structure. All atoms in the wurtzstannite-type structure are surrounded tetrahedrally. Each cation is coordinated by two S1 atoms, one S2 atom, and one S3 atom. The sulfur atoms are coordinated by two Ag and one Cd atom as well as one Sn atom.

### 2.3 The low-temperature phase of $\text{Ag}_2\text{CdSnS}_4$

For the crystal structure determination of the low-temperature phase, all four direct subgroups of  $Pmn2_1$  ( $P2_1$ ,  $Pm$ ,  $Pn$ , and  $Pna2_1$ ) (Fig. 6) were considered and tested as refinement models. For example, the symmetry reduction from space group  $Pmn2_1$  to  $Pn$  is expressed by the splitting of the fourfold Ag atom position  $4b$  into two non-equivalent twofold positions  $2a$ . The atomic and lattice parameters for the refinements in the four subgroups were generated by the program TRANSTRU found on the Bilbao Crystallographic Server [31–33]. For the space groups  $Pna2_1$  and  $Pn$ , we also used reported structural parameter of related compounds [25, 28] as starting values in the Rietveld refinements.

In the subgroups  $P2_1$ ,  $Pm$ , and  $Pna2_1$  convergence problems occurred during the refinements (profile, atomic positions, Debye-Waller factors). However, a successful refinement was achieved in space group  $Pn$ , the wurtzkesterite-type structure. The experimental diffraction pattern is in good agreement with the theoretical one (Fig. 7). Crystallographic details are summarized in Table 2; atomic and structural parameters are presented in Table 4. The Debye-Waller factors of the sulfur atoms were kept fixed at a value of 1, and the site occupation factors were not refined. Space group  $Pn$  also belongs to the group of polar/origin-free space groups. This particular space group exhibits two origin-free directions ( $x$  and  $z$ ). For the refinement in  $Pn$ , the  $x$  and  $z$  parameters of the Ag1 atom position were kept fixed to define the origin.

The low-temperature phase of  $\text{Ag}_2\text{CdSnS}_4$  crystallizes in the space group  $Pn$  (wurtzkesterite-type structure) with  $a=6.704$ ,  $b=7.038$ ,  $c=8.217$  Å, and  $\beta=90.16^\circ$ . The wurtzkesterite-type structure can be derived from the hexagonal diamond structure and is composed of a hexagonal closest packed arrangement of the sulfur anions (Fig. 8). The crystal structure contains two independent Ag positions Ag1 and Ag2, one Cd, and one Sn position where all cations are located on twofold positions. This setup occurs also for the anions with in total four independent sulfur positions on twofold positions. Keeping in mind the honeycomb set-up, alternating Ag/Cd and Ag/Sn layers (in general  $A^I/B^{II}$  and  $A^I/C^{IV}$  layers) are distinguishable which is analogous to the kesterite-type structure [5] derived from the cubic diamond structure. Interatomic Ag–S distances range from 2.46(3) to 2.52(4) Å with an average of 2.50 Å for Ag1–S and from 2.52(3) to 2.58(2) Å with an average of 2.55 Å for Ag2–S. The Ag–S bond lengths correlate quite well with those known from  $\text{Ag}_2\text{CdGeS}_4$  (Ag–S: 2.52–2.57 Å) [34] and are slightly smaller than those reported for  $\text{Ag}_2\text{FeSiS}_4$

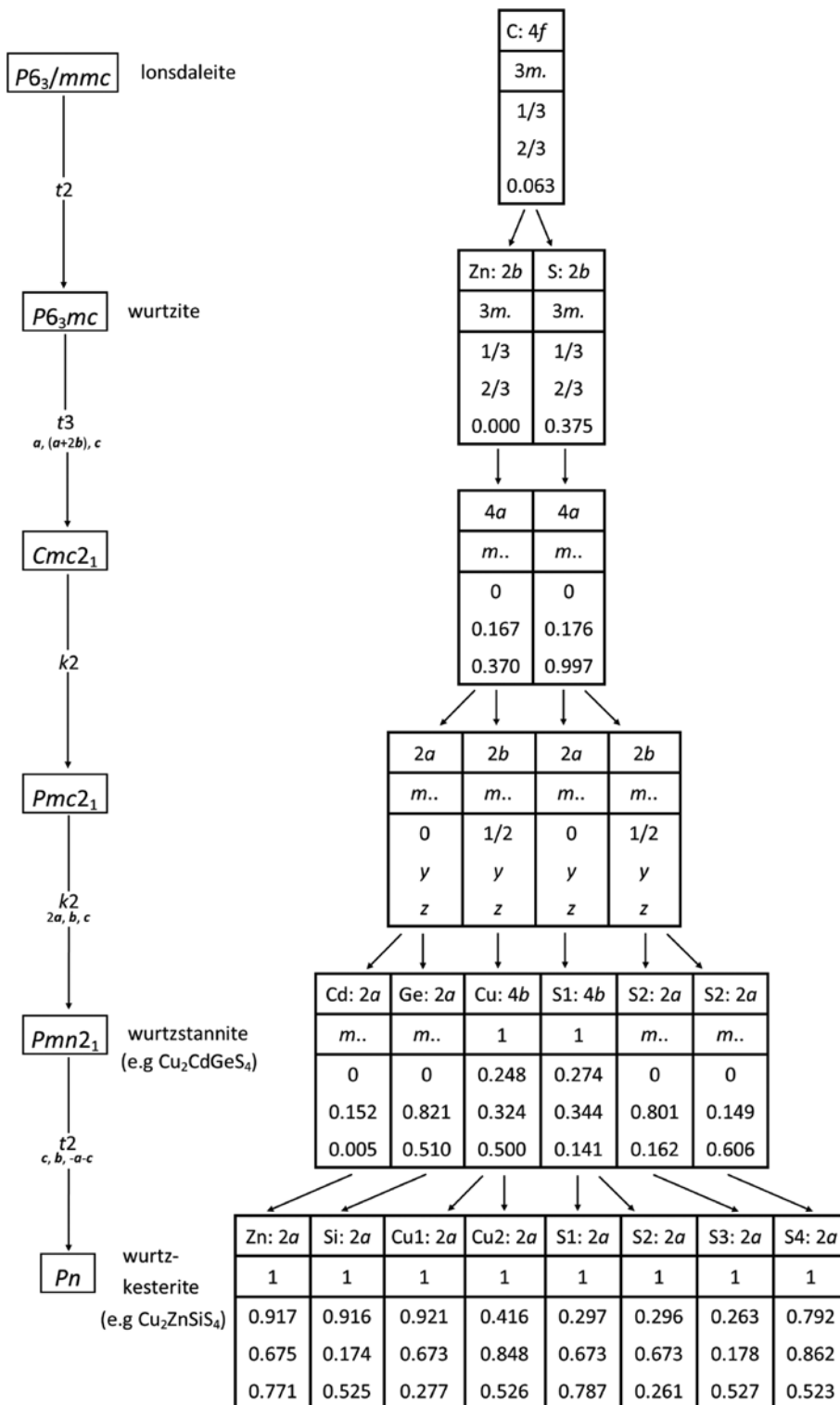
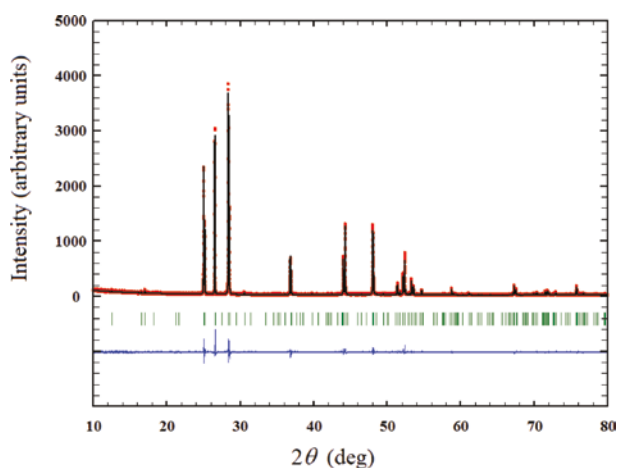


Fig. 3: Group-subgroup scheme (Bärnighausen formalism) for the group-theoretical relation between hexagonal diamond (lonsdaleite) and the wurtzstannite-/wurtzkesterite-type structure with data taken from [26] for lonsdaleite, [27] for wurtzite, [20] for space group  $Cmc2_1$ , [4] for wurtzstannite-type  $\text{Cu}_2\text{CdGeS}_4$ , and [28] for wurtzkesterite-type  $\text{Cu}_2\text{ZnSiS}_4$ .

( $\text{Ag}_1\text{-S}$ : 2.52–2.58 Å;  $\text{Ag}_2\text{-S}$ : 2.54–2.61 Å) [16].  $\text{Cd-S}$  bond lengths range from 2.51(3) to 2.58(3) Å with an average of 2.55 Å and are in good agreement with those found in

$\text{Cu}_2\text{CdGeS}_4$  ( $\text{Cd-S}$ : 2.51–2.60 Å) [4] and  $\text{Ag}_2\text{CdGeS}_4$  ( $\text{Cd-S}$ : 2.49–2.57 Å) [34]. Interatomic  $\text{Sn-S}$  distances vary from 2.39(3) to 2.51(3) Å and are in average 2.43 Å which is



**Fig. 4:** X-ray diffraction pattern of the high-temperature phase (measured at  $T=300^\circ\text{C}$ ) of  $\text{Ag}_2\text{CdSnS}_4$  with the results of the Rietveld refinement in space group  $Pmn2_1$  (red: measured; black: calculated; blue: measured–calculated).

somewhat longer than those in  $\text{Li}_2\text{CdSnS}_4$  (Sn–S: 2.38–2.39 Å) [35] and  $\text{Li}_2\text{ZnSnS}_4$  (Sn–S: 2.35–2.42 Å) [36].

## 2.4 Stabilization of the high-temperature phase at room temperature

The observed phase transition seems to be of first order. Consequently, it is no surprise that the stabilization of the high-temperature phase of  $\text{Ag}_2\text{CdSnS}_4$  at room temperature

was feasible by annealing the sample at  $T=300^\circ\text{C}$  for 3 h in an evacuated and closed silica tube in a vertically positioned tube furnace (Nabertherm RT 50-250/13; C450 controller) and subsequently quenching it in dry ice. Rietveld refinements were done in space group  $Pmn2_1$  as well as in  $Pn$  and confirmed that the quenched sample crystallizes in the orthorhombic space group  $Pmn2_1$ . As expected, the difference of the residual values  $R_{\text{wp}}$  between the space groups  $Pmn2_1$  and  $Pn$  is not significant ( $R_{\text{wp}}=10.9$  for  $Pmn2_1$  and  $R_{\text{wp}}=10.7$  for  $Pn$ , respectively). Additionally, convergence problems occurred for the refinement in space group  $Pn$ . The powder diffraction pattern of the stabilized high-temperature phase of  $\text{Ag}_2\text{CdSnS}_4$  quenched to room temperature is shown in Fig. 9. Crystallographic details as well as atomic and structural parameters are presented in Tables 2 and 5. The refinement strategy was similar to that of the sample measured *in-situ*.

The interatomic Ag–S distances in the quenched high-temperature phase vary from 2.505(12) to 2.521(15) Å with an average of 2.52 Å and correlate well with the Ag1–S distances (2.46(3)–2.52(4) Å) found in the low-temperature phase of  $\text{Ag}_2\text{CdSnS}_4$ . However, they are somewhat smaller than the Ag2–S distances (2.52(3)–2.58(2) Å) reported for  $\text{Ag}_2\text{CdGeS}_4$  (Ag–S: 2.52–2.57 Å) [34] and  $\text{Ag}_2\text{FeSiS}_4$  (Ag1–S: 2.52–2.58 Å; Ag2–S: 2.54–2.61 Å) [16]. Cd–S bond lengths range from 2.531(17) to 2.59(3) Å with an average value of 2.56 Å. This correlates pretty well with reported Cd–S distances for  $\text{Cu}_2\text{CdGeS}_4$  (Cd–S: 2.51–2.60 Å) [4] and  $\text{Ag}_2\text{CdGeS}_4$  (Cd–S: 2.49–2.57 Å) [34] as well with the ones in our

**Table 2:** Results of the refinements for the high- and low-temperature phases of  $\text{Ag}_2\text{CdSnS}_4$  (standard deviations in parenthesis).

	$\text{Ag}_2\text{CdSnS}_4$		
	High-temperature phase $T=300^\circ\text{C}$	Quenched high-temperature phase at r. t.	Low-temperature phase
Crystal system	Orthorhombic	Orthorhombic	Monoclinic
Space group	$Pmn2_1$	$Pmn2_1$	$Pn$
Z	2	2	2
Unit cell dimensions	$a=8.2171(6)$ Å $b=7.0641(5)$ Å $c=6.7029(5)$ Å	$a=8.2137(4)$ Å $b=7.0403(4)$ Å $c=6.7033(2)$ Å	$a=6.7036(2)$ Å $b=7.0375(3)$ Å $c=8.2166(3)$ Å $\beta=90.1577(9)^\circ$
Cell volume, Å <sup>3</sup>	389.08(5)	387.63(3)	387.63(2)
Calculated density, g cm <sup>-3</sup>	4.91	4.93	4.93
Diffractometer	RIGAKU SmartLab 3 kW system		
Radiation	$\text{CuK}\alpha_1$ radiation		
Wavelength, Å	$\lambda=1.54060$ Å		
Number of refined parameters	34	34	48
$R_p$	0.096	0.081	0.100
$R_{\text{wp}}$	0.128	0.109	0.138
$R_{\text{exp}}$	0.138	0.098	0.152
$R_{\text{Bragg}}$	0.049	0.049	0.050
S	0.93	1.13	0.91

**Table 3:** Refined atomic parameters for the high-temperature phase ( $T=300^\circ\text{C}$ ) of  $\text{Ag}_2\text{CdSnS}_4$  in space group  $Pmn2_1$  (standard deviations in parenthesis).

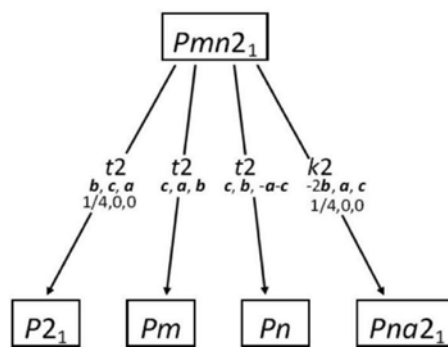
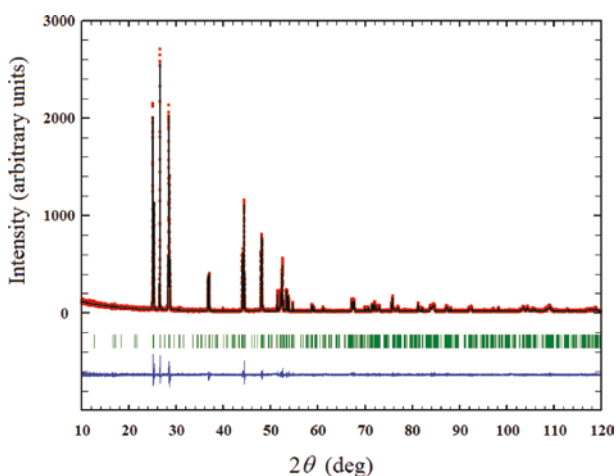
Atom	Wyckoff	x	y	z	s.o.f	$B_{\text{iso}}$ ( $\text{\AA}^2$ )
Ag	4b	0.2543(7)	0.3242(7)	-0.01018 <sup>a</sup>	1	3.8(2)
Cd	2a	0	0.8440(10)	0.988(3)	0.5	5.3(3)
Sn	2a	0	0.1770(8)	0.487(3)	0.5	1.0(2)
S1	4b	0.239(2)	0.336(2)	0.378(3)	1	1
S2	2a	0	0.180(4)	0.834(3)	0.5	1
S3	2a	0	0.855(4)	0.363(4)	0.5	1

<sup>a</sup>Fixed z value.

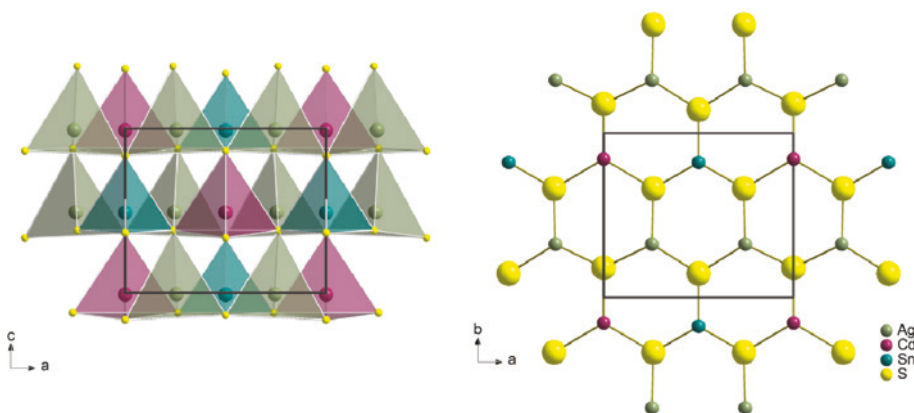
low-temperature phase of  $\text{Ag}_2\text{CdSnS}_4$  (2.51(3)–2.58(3)  $\text{\AA}$ ). For the Sn–S distances, the values vary from 2.39(3) to 2.491(17)  $\text{\AA}$  with an average of 2.45  $\text{\AA}$ . They are in agreement with those found in the low-temperature phase (2.39(3)–2.51(3)  $\text{\AA}$ ) and also with those reported for  $\text{Li}_2\text{CdSnS}_4$  (Sn–S: 2.38–2.39  $\text{\AA}$ ) [35] and  $\text{Li}_2\text{ZnSnS}_4$  (Sn–S: 2.35–2.42  $\text{\AA}$ ) [36].

For the high- and the low-temperature phase of our  $\text{Ag}_2\text{CdSnS}_4$  sample, additional refinements were undertaken in different space groups. These include the centrosymmetric space group  $Pnma$  as well as the non-centrosymmetric space group  $Pmc2_1$ . In addition, refinements in the triclinic crystal system have been performed. All refinements in these aforementioned space groups resulted in severe convergence problems. Consequently, we exclude all these space groups as possible candidates for  $\text{Ag}_2\text{CdSnS}_4$ .

Rietveld refinements in  $Pmn2_1$  and  $Pn$  were done for all temperatures (25–300 $^\circ\text{C}$ , 25 K steps). The monoclinic angle  $\beta$  was plotted against the temperature for the whole temperature range (black dots in Fig. 10). The plotted results point to the fact that  $\beta$  abruptly becomes

**Fig. 6:** Group-theoretical relation (Barnighausen formalism) between space group  $Pmn2_1$  (wurtzstannite-type structure) and its direct subgroups  $P2_1$ ,  $Pm$ ,  $Pn$ , and  $Pna2_1$ .**Fig. 7:** X-ray diffraction pattern of the low-temperature phase (measured at  $T=25^\circ\text{C}$ ) of  $\text{Ag}_2\text{CdSnS}_4$  with the results of the Rietveld refinement in space group  $Pn$  (red: measured; black: calculated; blue: measured–calculated).

90 $^\circ$ , the value of the orthorhombic high-temperature phase, at about 200 $^\circ\text{C}$ . This again indicates a first order

**Fig. 5:** Crystal structure of the high-temperature phase of  $\text{Ag}_2\text{CdSnS}_4$  ( $Pmn2_1$ ) with cation-centered polyhedra viewed along the [010] direction (left) and the honeycomb set-up with stacking sequence of alternating Ag and Cd/Sn layers viewed along the [001] direction (right).

**Table 4:** Refined atomic parameters for the low-temperature phase of  $\text{Ag}_2\text{CdSnS}_4$  ( $T=25^\circ\text{C}$ ) in space group  $Pn$  (standard deviations in parenthesis).

Atom	Wyckoff	$x$	$y$	$z$	s.o.f	$B_{\text{iso}} (\text{\AA}^2)$
Ag1	$2a$	0.91670 <sup>a</sup>	0.675(4)	0.27782 <sup>a</sup>	1	1.5(6)
Ag2	$2a$	0.407(3)	0.8454(8)	0.533(3)	1	2.5(3)
Cd1	$2a$	0.913(2)	0.674(4)	0.773(3)	1	1.99(6)
Sn1	$2a$	0.908(2)	0.1759(7)	0.523(2)	1	0.22(13)
S1	$2a$	0.298(7)	0.665(7)	0.783(4)	1	1
S2	$2a$	0.284(6)	0.669(8)	0.278(5)	1	1
S3	$2a$	0.267(4)	0.182(3)	0.526(5)	1	1
S4	$2a$	0.791(4)	0.851(3)	0.521(4)	1	1

<sup>a</sup>Fixed  $x$  and  $z$  values.

transition from the wurtzkesterite-type structure to the wurtzstannite-type structure. The area around 200–225°C may be considered as two-phase region. The error bars at temperatures  $\leq 200^\circ\text{C}$  are smaller than those  $> 200^\circ\text{C}$ . For the refined cell volume, no significant jump in the region around 200°C can be observed (red squares in Fig. 10).

## 2.5 UV/Vis spectroscopy

The optical properties of  $\text{Ag}_2\text{CdSnS}_4$  were measured in reflectance mode, and the optical band gaps were determined using the Tauc plot method [37, 38]. For the direct optical band gap a value of  $E_g = 1.93$  eV was calculated whereas a narrower indirect optical band gap of  $E_g = 1.82$  eV was obtained (Fig. 11). The color of our sample (black with violet accents) points to a direct optical band gap of  $E_g = 1.93$  eV which is in good agreement with the experimentally determined band gap mentioned in literature [39].

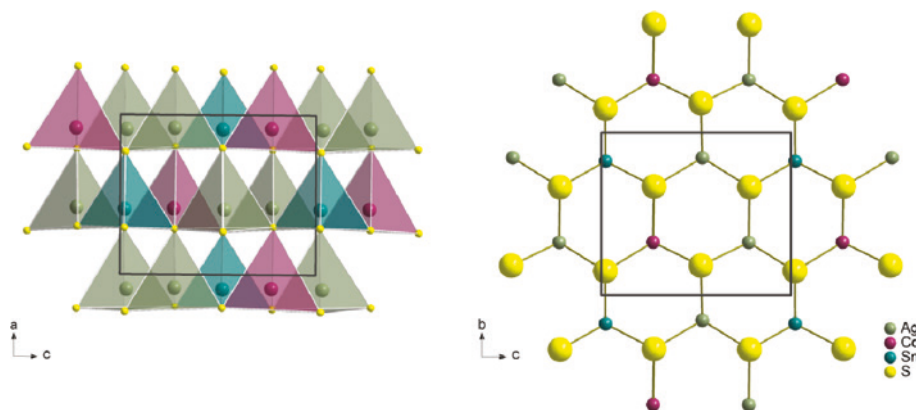


**Fig. 8:** Crystal structure of the low-temperature phase of  $\text{Ag}_2\text{CdSnS}_4$  crystallizing in space group  $Pn$  with cation-centered polyhedra (view along the  $[0\bar{1}0]$  direction, left) and the honeycomb set-up with a stacking sequence of alternating Ag/Cd and Ag/Sn layers viewed along the  $[100]$  direction.

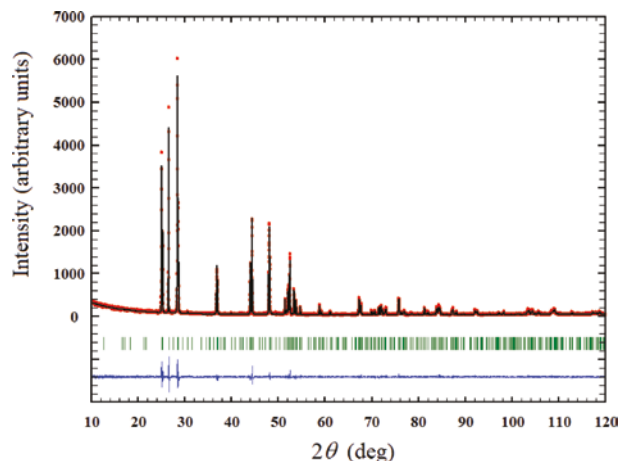


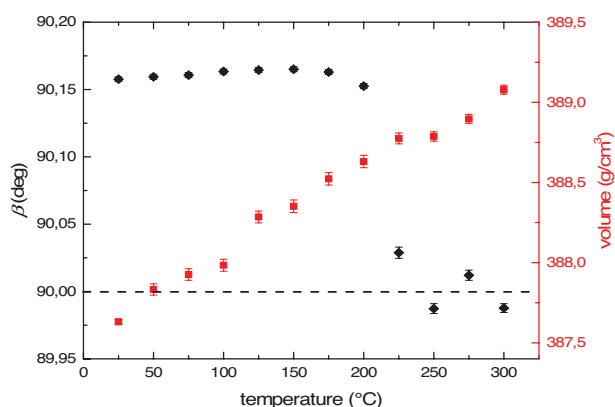
**Fig. 9:** X-ray diffraction pattern of the high-temperature phase of  $\text{Ag}_2\text{CdSnS}_4$  stabilized at room temperature with the results of the Rietveld refinement in space group  $Pmn2_1$  (red: measured; black: calculated; blue: measured–calculated).

## 3 Conclusions

Phase-pure and well crystallized  $\text{Ag}_2\text{CdSnS}_4$  was synthesized by ball milling (350 rpm, 5 h) and subsequent annealing at  $T = 550^\circ\text{C}$  under  $\text{H}_2\text{S}$  atmosphere for 2 h in a tube furnace. The observed reflections in the X-ray powder diffraction pattern are not in agreement with the crystal structure proposed in literature (space group  $Cmc2_1$ ) where all cations are statistically distributed on one position. Structural investigations including Rietveld refinements using our mechanochemically prepared  $\text{Ag}_2\text{CdSnS}_4$  sample point, in accordance to the calculations of Chen et al. [42], to the presence of the wurtzkesterite-type structure (space group  $Pn$ ) with an ordered arrangement of the cations. A reversible

**Table 5:** Refined atomic parameters for the high-temperature phase of  $\text{Ag}_2\text{CdSnS}_4$  in space group  $Pmn2_1$  quenched to room temperature (standard deviations in parenthesis).

Atom	Wyckoff	$x$	$y$	$z$	s.o.f	$B_{\text{iso}} (\text{\AA}^2)$
Ag1	4b	0.2532(9)	0.3255(8)	-0.00662 <sup>a</sup>	1	1.5(2)
Cd1	2a	0	0.8445(11)	0.983(3)	0.5	2.4(3)
Sn1	2a	0	0.1767(9)	0.491(3)	0.5	0.28(15)
S1	4b	0.251(3)	0.337(3)	0.368(5)	1	1
S2	2a	0	0.184(4)	0.847(4)	0.5	1
S3	2a	0	0.851(4)	0.369(6)	0.5	1

<sup>a</sup>Fixed  $z$  value.**Fig. 10:** Monoclinic angle  $\beta$  and cell volume plotted against temperature (from Rietveld refinements in space group  $Pn$  for  $\beta$  and from refinements in  $Pn$  ( $T \leq 200^\circ\text{C}$ ) and  $Pmn2_1$  ( $T > 200^\circ\text{C}$ ) for the cell volume).

first-order phase transition at around  $200^\circ\text{C}$  from a low-temperature wurtzkesterite- to a high-temperature wurtzstannite-type structure has been observed. Additionally, a direct optical band gap of  $E_g = 1.93 \text{ eV}$ , which is in agreement to that reported in the literature, was found. In the present work, the mechanochemical synthetic route was again successful for the preparation of

phase-pure multinary sulfides. This particular way of synthesis appears to have a strong effect on the crystal structure of the resulting compounds. This may be an explanation for our different observations compared to the literature results presented in [4, 20].

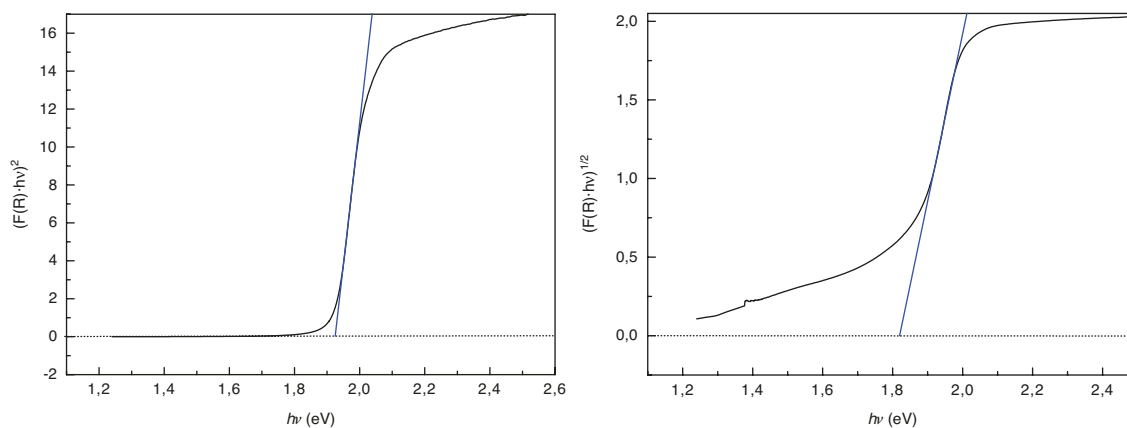
## 4 Experimental Section

### 4.1 Synthesis

$\text{Ag}_2\text{CdSnS}_4$  was synthesized by ball milling in a high-energy planetary Mono Mill (Pulverisette 6, Fritsch, Idar-Oberstein, Germany), followed by an annealing step under an atmosphere of  $\text{H}_2\text{S}$ . As starting materials  $\text{Ag}_2\text{S}$  (Schuchardt),  $\text{CdS}$ ,  $\text{SnS}$ , and sulfur (Fluka, 99.99%) were used which were filled in a 45 mL zirconia-made grinding beaker with 6 zirconia balls with a diameter of 15 mm. A rotational speed of 350 rpm and a milling time of 5 h were set. In order to obtain a highly crystalline product, the grounded powder was annealed at  $T = 550^\circ\text{C}$  for 2 h under  $\text{H}_2\text{S}$  atmosphere. A 0.1 M  $\text{Cd}(\text{CH}_3\text{CO}_2)_2$  solution and  $\text{H}_2\text{S}$  (Air Liquide, 99.5%) were used for precipitation of  $\text{CdS}$ .  $\text{SnS}$  was synthesized using the high-temperature solid-state reaction of the elements tin (Merck, 99.9%) and sulfur (Fluka, 99.99%) in an evacuated and sealed  $\text{SiO}_2$  ampoule.

### 4.2 Structural and chemical characterization

X-ray powder diffraction investigations as well as *in-situ* high-temperature X-ray diffraction experiments ( $25\text{--}300^\circ\text{C}$ ,  $\text{N}_2$  atmosphere) were carried out with a RIGAKU SmartLab 3 kW system equipped with a  $\text{K}\alpha 1$  unit (Johansson-type Ge crystal,  $\text{CuK}\alpha_1$  radiation,  $\lambda = 1.54060 \text{ \AA}$ ). The diffraction data were obtained in Bragg-Brentano geometry over an angular range

**Fig. 11:** UV/Vis spectra of  $\text{Ag}_2\text{CdSnS}_4$  with Tauc plot determinations of the direct (left) and indirect (right) optical band gap.

of  $2\theta=10\text{--}120^\circ$  for room temperature and  $2\theta=10\text{--}80^\circ$  for high-temperature measurements. Rietveld refinements [40] were performed using the program FULLPROF [41] by applying a pseudo-Voigt function. Backgrounds were fitted using a set of various background points with refinable heights. It should be mentioned that anisotropic strain broadening terms were used due to anisotropic reflection broadening.

Further details of the crystal structure investigation may be obtained from Fachinformationszentrum Karlsruhe, 76344 Eggenstein-Leopoldshafen, Germany (fax: +49-7247-808-666; e-mail: crysdata@fiz-karlsruhe.de, [http://www.fiz-informationsdienste.de/en/DB/icsd/depot\\_anforderung.html](http://www.fiz-informationsdienste.de/en/DB/icsd/depot_anforderung.html)) on quoting the deposition numbers CSD-1979198 and CSD-1979199.

For the chemical characterization of  $\text{Ag}_2\text{CdSnS}_4$ , energy dispersive X-ray spectroscopy (EDX) using a DSM 982 GEMINI spectrometer (Carl Zeiss AG, Oberkochen, Germany) equipped with a XFlash 6 | 60 detector (Bruker, Billerica, USA) were performed. For the determination of the sulfur content, an instrumental error of 5% is given. The EDX measurements were carried out at the Zentrum für Elektronenmikroskopie (ZELMI) of the TU Berlin. For the confirmation of the sulfur content, additional analyses were carried out using a FlashEA 1112 elemental analyzer (Thermo Scientific™, Waltham, USA). Hereby, a device error of 2% is assumed.

Thermoanalytical analysis (DTA) were carried out using a STA 7300 thermogravimeter (Hitachi, Chiyoda, Japan). These measurements were performed under nitrogen atmosphere up to  $300^\circ\text{C}$  with a heating and cooling rate of  $3\text{ K min}^{-1}$ ; alumina crucibles were used as reference and sample container.

### 4.3 UV/Vis spectroscopy

The optical band gaps were determined by UV/Vis measurements using a V670 UV/Vis-NIR spectrometer (Jasco Deutschland GmbH, Pfungstadt, Germany). The spectra obtained in diffuse reflectance mode were converted into absorption spectra by the Kubelka-Munk function; the optical band gaps were received from the absorption spectra using the Tauc plot method [37, 38]. The standard deviation for  $E_g$  was estimated close to 0.05 eV. For sample preparation,  $\text{Ag}_2\text{CdSnS}_4$  was mixed with a white standard (MgO) in a mass ratio of 1:1.

**Acknowledgements:** Special thanks to the Zentrum für Elektronenmikroskopie (ZELMI) of the TU Berlin giving access to the EDX measurements. EDX measurements were carried out by Rodrigo Beltran-Suito; combustion

analysis was performed by Juana Krone (both TU Berlin). DTA and UV/Vis measurements were carried out by Dr. Nina Genz (TU Berlin). This project was supported by the German Science Foundation (DFG, LE 781/19-1).

## References

- [1] C. H. L. Goodman, *J. Phys. Chem. Solids* **1958**, *6*, 305–314.
- [2] B. R. Pamplin, *Nature* **1960**, *188*, 136–137.
- [3] B. R. Pamplin, *J. Phys. Chem. Solids* **1964**, *25*, 675–684.
- [4] E. Parthé, K. Yvon, R. H. Deitch, *Acta Crystallogr.* **1969**, *B25*, 1164–1174.
- [5] S. R. Hall, J. T. Szymanski, J. M. Stewart, *Can. Mineral.* **1978**, *16*, 131–137.
- [6] W. Schäfer, R. Nitsche, *Mater. Res. Bull.* **1974**, *9*, 645–654.
- [7] A. F. Moodie, H. J. Whitfield, *Acta Crystallogr.* **1986**, *B42*, 236–247.
- [8] B. Lui, M. Zhang, Z. Zhao, H. Zeng, F. Zheng, G. Guo, J. Huang, *J. Solid State Chem.* **2013**, *204*, 251–256.
- [9] I. D. Olekseyuk, O. V. Marchuk, L. D. Gulay, O. Y. Zhibankov, *J. Alloys Compd.* **2005**, *398*, 80–84.
- [10] K. Ito, T. Nakazawa, *Jpn. J. Appl. Phys.* **1988**, *27*, 2094–2097.
- [11] H. Katagiri, K. Saitoh, T. Washio, H. Shinohara, T. Kurumadani, S. Miyajima, *Sol. Energy Mater. Sol. Cells* **2001**, *65*, 141–148.
- [12] J. Seol, S. Lee, J. Lee, H. Nam, K. Kim, *Sol. Energy Mater. Sol. Cells* **2003**, *75*, 155–162.
- [13] R. Caye, Y. Laurent, P. Picot, R. Pierrot, C. Lévy, *Bull. Minéral.* **1968**, *91*, 383–387.
- [14] Z. Johan, P. Picot, *Bull. Minéral.* **1982**, *105*, 229–235.
- [15] H. Haeuseler, M. Himmrich, *Z. Naturforsch.* **1989**, *44b*, 1035–1036.
- [16] C. D. Brunetta, J. A. Brant, K. A. Rosmus, K. M. Henline, E. Karey, J. H. MacNeil, J. A. Aitken, *J. Alloys Compd.* **2013**, *574*, 495–503.
- [17] C. D. Brunetta, B. Karuppanan, K. A. Rosmus, J. A. Aitken, *J. Alloys Compd.* **2012**, *516*, 65–72.
- [18] S. Greil, Untersuchungen an ternären und quaternären Kupfer-, Lithium- und Silbersulfiden mit Diamantstruktur. *Dissertation*, Universität Regensburg, Regensburg **2015**.
- [19] C. L. Teske, *Z. Naturforsch.* **1979**, *34b*, 544–547.
- [20] O. V. Parasyuk, I. D. Olekseyuk, L. V. Piskach, S. V. Volkov, V. I. Pekhnyo, *J. Alloys Compd.* **2005**, *399*, 173–177.
- [21] A. Ritscher, J. Just, O. Dolotko, S. Schorr, M. Lerch, *J. Alloys Compd.* **2016**, *670*, 289–296.
- [22] H. Bärnighausen, *MATCH Commun. Math. Chem.* **1980**, *9*, 139–175.
- [23] U. Müller, *Z. Anorg. Allg. Chem.* **2004**, *630*, 1519–1537.
- [24] O. V. Parasyuk, A. O. Fedorchuk, Y. M. Kogut, L. V. Piskach, I. D. Olekseyuk, *J. Alloys Compd.* **2010**, *500*, 26–29.
- [25] C. D. Brunetta, W. C. Minsterman, C. H. Lake, J. A. Aitken, *J. Solid State Chem.* **2012**, *187*, 177–185.
- [26] F. P. Bundy, J. S. Kasper, *J. Chem. Phys.* **1967**, *46*, 3437–3446.
- [27] G. Aminoff, XI. *Z. Kristallogr.* **1923**, *58*, 203–219.
- [28] K. A. Rosmus, C. D. Brunetta, M. N. Srnc, B. Karuppanan, J. A. Aitken, *Z. Anorg. Allg. Chem.* **2012**, *638*, 2578–2584.
- [29] WINXPOW (version 1.2), STOE & Cie GmbH, Darmstadt (Germany) **2001**.
- [30] L. O. Brockway, *Z. Kristallogr.* **1934**, *89*, 434–441.

- [31] M. I. Aroyo, J. M. Perez-Mato, D. Orobengoa, E. Tasci, G. de La Flor, A. Kirov, *Bulg. Chem. Commun.* **2011**, *43*, 183–197.
- [32] M. I. Aroyo, A. Kirov, C. Capillas, J. M. Perez-Mato, H. Wondratschek, *Acta Crystallogr.* **2006**, *A62*, 115–128.
- [33] M. I. Aroyo, J. M. Perez-Mato, C. Capillas, E. Kroumova, S. Ivantchev, G. Madariaga, A. Kirov, H. Wondratschek, *Z. Kristallogr.* **2006**, *221*, 15–27.
- [34] O. V. Parasyuk, L. V. Piskach, I. D. Olekseyuk, V. I. Pekhnyo, *J. Alloys Compd.* **2005**, *397*, 95–98.
- [35] J. W. Lekse, M. A. Moreau, K. L. McNerny, J. Yeon, P. S. Halasyamani, J. A. Aitken, *Inorg. Chem.* **2009**, *48*, 7516–7518.
- [36] J. W. Lekse, B. M. Leverett, C. H. Lake, J. A. Aitken, *J. Solid State Chem.* **2008**, *181*, 3217–3222.
- [37] J. Tauc, R. Grigorovici, A. Vancu, *Phys. Stat. Sol. (b)* **1966**, *15*, 627–637.
- [38] J. Tauc, *Mater. Res. Bull.* **1968**, *3*, 37–46.
- [39] G. E. Davydyuk, G. L. Myronchuk, I. V. Kityk, S. P. Danyl'chuk, V. V. Bozhko, O. V. Parasyuk, *Opt. Mater.* **2011**, *33*, 1302–1306.
- [40] H. M. Rietveld, *J. Appl. Crystallogr.* **1969**, *2*, 65–71.
- [41] J. Rodríguez-Carvajal, FULLPROF, A Program for Rietveld Refinement and Pattern Matching Analysis, Satellite Meeting on Powder Diffraction of the 15<sup>th</sup> International Congress of the IUCr, Toulouse (France) **1990**, p. 127.
- [42] S. Chen, A. Walsh, Y. Luo, J. Yang, X. G. Gong, S. Wei, *Phys. Rev. B.* **2010**, *82*, 195203-1–195203-8.

## 7. Publication 3

### $\text{Na}_2\text{MgSnS}_4$ – a new member of the $\text{A}^{\text{I}}_2\text{B}^{\text{II}}\text{C}^{\text{IV}}\text{X}^{\text{VI}}_4$ family of compounds

Eva M. Heppke and Martin Lerch

*Postprint*

*Z. Naturforsch.* **2020**, 75(8), 721-726

doi:10.1515/znb-2020-0102

<https://www.degruyter.com/document/doi/10.1515/znb-2020-0102/html>

Contribution to publication:

E. M. Heppke: Sample preparation, structural characterization and evaluation, writing

M. Lerch: General advice, proofreading

**Authors:** E. M. Heppke<sup>[1]</sup>, M. Lerch<sup>\*[1]</sup>

<sup>1</sup>Institut für Chemie: Technische Universität Berlin, Straße des 17. Juni 135, 10623 Berlin

\* corresponding

**Keywords:** mechanochemical synthesis; multinary sulfides; tin sulfide; X-ray powder diffraction; Rietveld refinement; NaCrS<sub>2</sub> type

Eva M. Heppke and Martin Lerch\*

# Na<sub>2</sub>MgSnS<sub>4</sub> – a new member of the A<sub>2</sub><sup>I</sup>B<sup>II</sup>C<sup>IV</sup>X<sub>4</sub> family of compounds

<https://doi.org/10.1515/znb-2020-0102>

Received June 8, 2020; accepted July 5, 2020; published online August 3, 2020

**Abstract:** A new member of the A<sub>2</sub><sup>I</sup>B<sup>II</sup>C<sup>IV</sup>X<sub>4</sub> compound family, Na<sub>2</sub>MgSnS<sub>4</sub>, has been synthesized by ball milling of the binary sulfides SnS, Na<sub>2</sub>S, and MgS with elemental sulfur in a high-energy planetary mill, followed by annealing in an atmosphere of H<sub>2</sub>S (*T* = 600 °C/3 h). Na<sub>2</sub>MgSnS<sub>4</sub> adopts the NaCrS<sub>2</sub>-type structure (rhombohedral, space group *R* $\bar{3}m$ ) with *a* = 3.7496(11) and *c* = 19.9130(6) Å. The Na atoms occupy Wyckoff position 3*b*, whereas the Mg and Sn atoms are statistically distributed on the cation sites 3*a*; all cations are surrounded by six sulfur atoms.

**Keywords:** mechanochemical synthesis; multinary sulfides; NaCrS<sub>2</sub> type; Rietveld refinement; tin sulfide; X-ray powder diffraction.

## 1 Introduction

A<sub>2</sub><sup>I</sup>B<sup>II</sup>C<sup>IV</sup>X<sub>4</sub> compounds are a well-known class of materials with interesting properties. Cu<sub>2</sub>ZnSnS<sub>4</sub>, for example, is a candidate as an absorber material for thin-film solar cell applications due to its high absorption coefficient and direct optical band gap [1, 2]. A<sub>2</sub><sup>I</sup>B<sup>II</sup>C<sup>IV</sup>X<sub>4</sub> compounds belong to the adamantine family, being structurally derived from the cubic or hexagonal diamond structure and forming so-called tetrahedral structures implying tetrahedral surroundings of the contained atoms.

In the tetragonal crystal system, two space groups, *I* $\bar{4}2m$  and *I* $\bar{4}$  (both derived from the cubic diamond-/sphalerite-type structure) [3, 4], are listed for quaternary sulfides of the type A<sub>2</sub><sup>I</sup>B<sup>II</sup>C<sup>IV</sup>X<sub>4</sub>. Cu<sub>2</sub>ZnSnS<sub>4</sub> crystallizes in the kesterite-type structure with space group *I* $\bar{4}$  [3, 5, 6], whereas Cu<sub>2</sub>MSnS<sub>4</sub> (*M* = Mn, Fe, Co, Cd, Hg) [7] as well as Cu<sub>2</sub>MGeS<sub>4</sub> (*M* = Zn, Fe, Co, Hg) [7, 8] and Ag<sub>2</sub>MSnS<sub>4</sub> (*M* = Fe, Zn) [9, 10] belong to the stannite-type structure

(space group *I* $\bar{4}2m$ ). Both crystal structure types exhibit a cubic closest packing of the sulfur anions. The kesterite-type structure consists of alternating A<sup>I</sup>-C<sup>IV</sup> and A<sup>I</sup>-B<sup>II</sup> layers along the crystallographic *c* axis, whereas in the stannite-type structure, the monovalent cation occupies another Wyckoff position, which leads to a different cation stacking along the *c* axis (A<sup>I</sup>-/B<sup>II</sup>-C<sup>IV</sup> layers). It should be mentioned that compressed chalcopyrite-like structures with a larger divalent cation such as Ba<sup>2+</sup>, Pb<sup>2+</sup>, and Eu<sup>2+</sup> also adopt space group *I* $\bar{4}2m$ . The compression along the *c* axis leads to an eightfold instead of a tetrahedral coordination of the divalent cations. This type of structure is realized for Li<sub>2</sub>Ba(Ge/Sn)S<sub>4</sub> [11], Li<sub>2</sub>(Eu/Pb)GeS<sub>4</sub> [12], and Ag<sub>2</sub>BaGeS<sub>4</sub> [13].

Hexagonal diamond-related structures have been reported for quaternary sulfides in the orthorhombic crystal system with space group *Pmn*2<sub>1</sub> as well as in the monoclinic crystal system with space group *Pn* [4]. Especially Si-containing compounds such as Cu<sub>2</sub>MSiS<sub>4</sub> with *M* = Mn, Fe, Zn, Cd, Mg, Hg [7, 14], several Ag compounds [15–19], Ge-bearing compounds with partly larger divalent cations such as Cu<sub>2</sub>MGeS<sub>4</sub> with *M* = Mn, Zn, Cd, Mg, Hg [7, 14, 20], and Li compounds such as Li<sub>2</sub>*M*(Sn/Ge)S<sub>4</sub> with *M* = Cd, Mn, Zn, Co, Fe [16, 18, 21–24] crystallize either in the orthorhombic wurtzstannite- or the monoclinic wurtzkesterite-type structure. Both structure types exhibit a hexagonal closest packed arrangement of the sulfur anions but differ in their cation stacking sequences (*Pmn*2<sub>1</sub>: A<sup>I</sup>-/B<sup>II</sup>-C<sup>IV</sup> layers; *Pn*: A<sup>I</sup>-C<sup>IV</sup>-/A<sup>I</sup>-B<sup>II</sup> layers) considering the honeycomb set-up. A further subgroup of *Pmn*2<sub>1</sub> is listed in the literature for A<sub>2</sub><sup>I</sup>B<sup>II</sup>C<sup>IV</sup>X<sub>4</sub> compounds: Ag<sub>2</sub>CdGeS<sub>4</sub> crystallizes in the wurtzstannite-type structure (space group *Pmn*2<sub>1</sub>) [19] but has also been reported to exist in space group *Pna*2<sub>1</sub> [25] which shows a different arrangement of the cations.

Apart from these structures, there are a few A<sub>2</sub><sup>I</sup>B<sup>II</sup>C<sup>IV</sup>X<sub>4</sub> sulfides which crystallize in different space groups. In Cu<sub>2</sub>NiSnS<sub>4</sub>, a disordered alternative in the form of the sphalerite-type structure (a direct subgroup of the cubic diamond structure) with a statistical distribution of the cations on position 4*a* (0,0,0) is realized [7]. The Si analogue Cu<sub>2</sub>NiSiS<sub>4</sub> adopts a deformed sphalerite-type structure with statistically distributed cations comparable to the arrangement in Cu<sub>2</sub>NiSnS<sub>4</sub> (monoclinic space group *P*2<sub>1</sub>/*m*) [7]. Ag<sub>2</sub>CdSnS<sub>4</sub> crystallizes in space group *Cmc*2<sub>1</sub> [4,

\*Corresponding author: Martin Lerch, Institut für Chemie, Technische Universität Berlin, Straße des 17. Juni 135, 10623 Berlin, Germany, E-mail: martin.lerch@tu-berlin.de

Eva M. Heppke: Institut für Chemie, Technische Universität Berlin, Straße des 17. Juni 135, 10623 Berlin, Germany

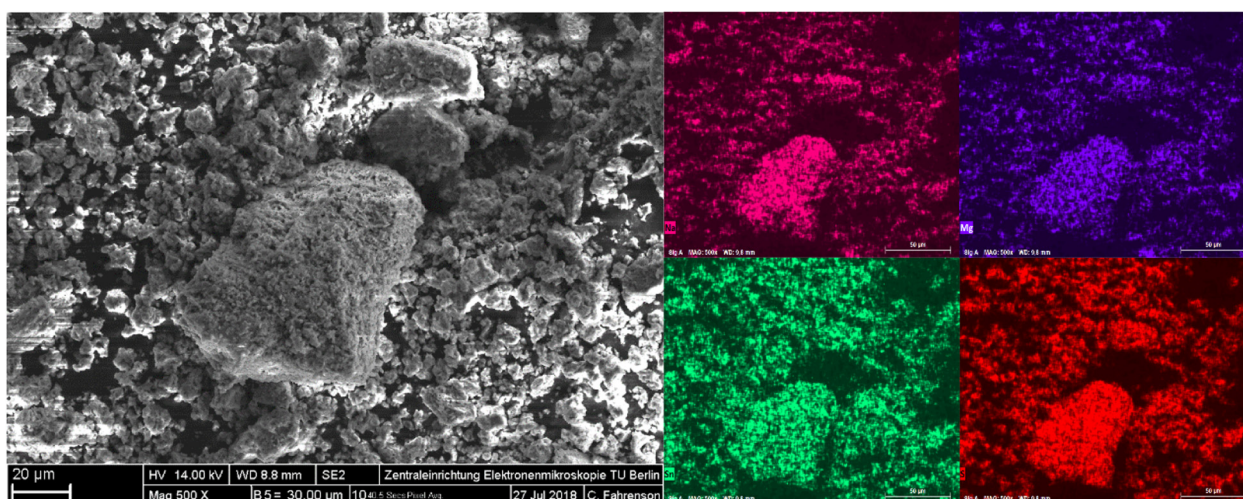


**Figure 1:** Scanning electron microscope (SEM) images of  $\text{Na}_2\text{MgSnS}_4$  particles showing the distribution of Na (pink), Mg (blue), Sn (green), and S (red).

26] where all cations are located on one Wyckoff position, as well as in space group  $Pn$  with an ordering of the cations [27]; both structures are derived from the hexagonal diamond/wurtzite-type structure.

According to literature reports, several compounds with the general formula  $A_2B^{II}C^{IV}X_4$  do not form tetrahedral structures but exhibit a higher coordination of the contained atoms (especially the divalent cations ( $B$ ) and the sulfur atoms ( $X$ )) [28–34].

The  $A_2B^{II}C^{IV}X_4$  compounds mentioned above contain Cu and Ag as monovalent cations ( $A$ ). Up to now, several Li-bearing sulfides of the type  $A_2B^{II}C^{IV}X_4$  are also known [11, 12, 18, 21–24, 35, 36]. The substitution with Na was less successful and has led to only a few representatives:  $\text{Na}_2\text{CdSnS}_4$  crystallizes in the monoclinic space group  $C2$  and shows a slightly distorted tetrahedral surrounding of the cations [36].  $\text{Na}_2\text{ZnSnS}_4$  crystallizes in the kesterite-type structure ( $I\bar{4}$ ) and exhibits a slight compression along the  $c$  axis [37]. Two more Na-containing  $A_2B^{II}C^{IV}X_4$  sulfides with earth-alkaline atoms ( $B$ ) are known [38]:  $\text{Na}_2\text{BaSnS}_4$  belongs to the tetragonal crystal system (space group  $I\bar{4}2d$ ) but forms a tunnel structure with partly higher coordinated

cations instead of a tetrahedral structure. The same applies to the Ge analogue  $\text{Na}_2\text{BaGeS}_4$  crystallizing in space group  $R\bar{3}c$ .

In this contribution, we present a new Na-bearing  $A_2B^{II}C^{IV}X_4$  compound with Mg as the divalent cation.  $\text{Na}_2\text{MgSnS}_4$  crystallizes in a space group hitherto unknown for the  $A_2B^{II}C^{IV}X_4$  family, the rhombohedral space group  $R\bar{3}m$ . This space group is more common among ternary chalcogenides like  $\text{NaCrS}_2$  [39] or  $3R\text{-LiTiS}_2$  [40].

## 2 Results and discussion

A phase-pure and well-crystallized product of the formula  $\text{Na}_2\text{MgSnS}_4$  was synthesized mechanochemically with a subsequent annealing step in  $\text{H}_2\text{S}$  atmosphere as described in Section 4. Energy dispersive X-ray spectroscopy (EDX) measurements showed a homogenous distribution of the contained elements Na, Mg, Sn, and S in the  $\text{Na}_2\text{MgSnS}_4$  samples (Figure 1). The analytical data are consistent with the theoretical ones, except for those of Sn which differ slightly from the ideal value due to the difficult fitting of the background around those peaks (Table 1).

The crystal structure of  $\text{Na}_2\text{MgSnS}_4$  has been determined using X-ray powder diffraction. The diffraction pattern was analyzed using the software X'PERT HIGHSCORE PLUS (PANalytical, Almelo, The Netherlands) which refers to the Inorganic Crystal Structure Database ICSD (FIZ Karlsruhe). Thereby, the  $\text{NaCrS}_2$ -type structure was suggested indicating a rhombohedral symmetry with space group  $R\bar{3}m$ . Thus, Rietveld refinement [41] was performed in space group  $R\bar{3}m$  which turned out to be quite successful exhibiting a statistical mixture of Mg and Sn. Results of the

**Table 1:** Phase composition of  $\text{Na}_2\text{MgSnS}_4$  calculated from EDX analysis compared to the ideal values.

	$\text{Na}_2\text{MgSnS}_4$	
	Ideal (at%)	Measured (at%)
Na	25	24.7
Mg	12.5	12.1
Sn	12.5	14.4
S	50	48.9

Rietveld refinement are depicted in Figure 2. The experimental diffraction pattern is in good agreement with the theoretical one with a residual value  $R_{wp} = 0.0308$ . The atomic and structural parameters are summarized in Tables 2 and 3. Site occupation factors of positions  $3a$ ,  $3b$ , and  $6c$  as well as the Debye Waller factor of sulfur on position  $6c$  were kept fixed during refinement. The structure contains two independent cation sites, Mg and Sn, which are statistically distributed on position  $3a$  in a molar ratio of 1:1.

$Na_2MgSnS_4$  crystallizes rhombohedral in the  $NaCrS_2$ -type structure in space group  $R\bar{3}m$  with  $a = 3.750(3)$  and  $c = 19.9130(14)$  Å. The crystal structure is derived from the NaCl structure type and is based on a cubic closest packing of the sulfur anions. Sulfur and Mg/Sn form a  $CdCl_2$ -type arrangement where the octahedral voids of every other layer are statistically filled with Mg and Sn. The remaining octahedral voids are occupied by Na (Figure 3). All cations show an octahedral coordination.  $NaS_6$  octahedra are edge-sharing with  $(Mg/Sn)S_6$  octahedra, and all octahedra are edge-sharing with each other. The calculated average bond lengths for the  $NaS_6$  polyhedra with 2.873(2) Å and for the  $(Mg/Sn)S_6$  polyhedra with 2.595(2) Å (Figure 4) are in accordance with standard ionic radii:  $Na^+$ : 1.16 Å;  $Mg^{2+}$ : 0.86 Å;  $Sn^{4+}$ : 0.83 Å; and  $S^{2-}$ : 1.70 Å [42]. The ionic radii of  $Mg^{2+}$  and  $Sn^{4+}$  are very close to each other, which allows for a statistical distribution on one position. It should be mentioned that magnesium and sodium cannot be distinguished by conventional X-ray diffractions techniques, but due to their different ionic radii, a significant degree of mixed occupation is not probable. The interatomic Na–S distances correlate quite well with those reported for compounds such as  $NaCrS_2$  (Na–S: 2.773(14) Å) [39]. (Mg/Sn)–S bond lengths are in agreement with those of spinel-type chalcogenides where Mg and Sn atoms are also statistically distributed on one position and octahedrally surrounded by sulfur atoms:  $Cu_2MgSn_3S_8$ : (Mg/Sn)–S: 2.5658(10) Å; and  $Ag_2MgSn_3S_8$ : (Mg/Sn)–S: 2.5721(16) Å [43]. Sulfur atoms are coordinated by 3 Na and 3 (Mg/Sn) atoms forming slightly distorted octahedra. Due to the larger difference in the electronegativities of the contained cations and anions,  $Na_2MgSnS_4$  tends to a more ionic character and crystallizes in a structure type derived from rocksalt and not from sphalerite or wurtzite [44, 45].

As mentioned above, the  $NaCrS_2$ -type structure is derived from the rocksalt type. The corresponding group-subgroup scheme using the Bärnighausen formalism [46, 47] is presented in Figure 5. We start with space group  $Fm\bar{3}m$  for the rock salt type exhibiting a cubic closest packing of Cl atoms and an occupation of every octahedral void with Na atoms [48]. The first symmetry reduction leads

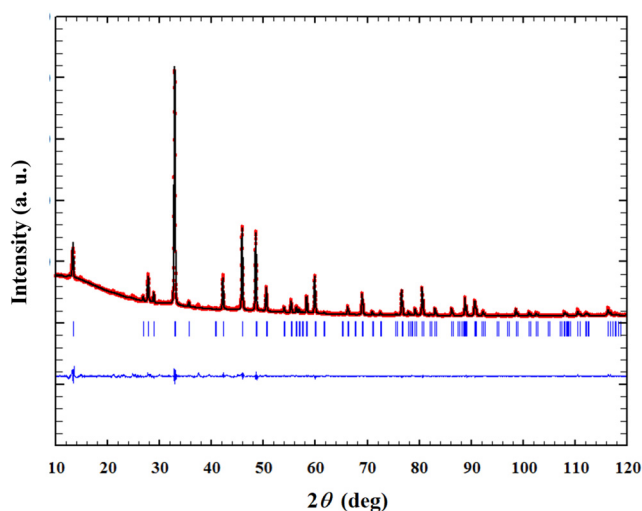


**Figure 2:** X-ray diffraction pattern of  $Na_2MgSnS_4$  with results of the Rietveld refinement.

**Table 2:** Results of the Rietveld refinement for  $Na_2MgSnS_4$  (standard deviations in parenthesis).

Empirical formula	$Na_2MgSnS_4$
Color	Olive
Structure type	$NaCrS_2$
Space group	$R\bar{3}m$
Crystal system	Rhombohedral
Z	1.5
$a = b$ , Å	3.750(3)
$c$ , Å	19.9130(14)
$V$ , Å <sup>3</sup>	242.46(3)
Calculated density, g cm <sup>-3</sup>	3.26
Diffractometer	PANalytical X'Pert MDP Pro
Radiation	$CuK\alpha$ radiation
Wavelengths $\lambda_1/\lambda_2$ , Å	1.54056/1.54439
$R_p$	0.0222
$R_{wp}$	0.0308
$R_{exp}$	0.0194
$R_{Bragg}$	0.0289
S	1.59

**Table 3:** Refined atomic parameters for  $Na_2MgSnS_4$  (standard deviations in parenthesis).

Atom	Wyckoff	x	y	z	s.o.f	$B_{iso}$ (Å <sup>2</sup> )
Na1	3b	0	0	1/2	1	2.27(19)
Mg1	3a	0	0	0	0.5	0.45(7)
Sn1	3a	0	0	0	0.5	0.45(7)
S1	6c	0	0	0.26148(19)	1	1

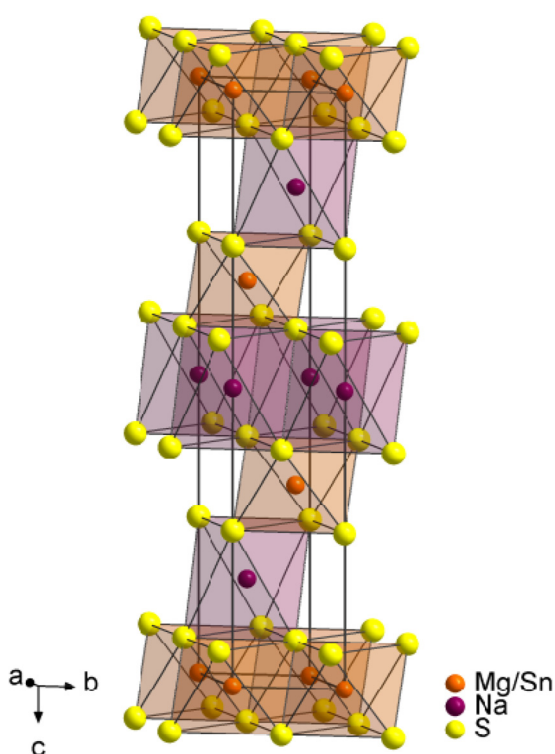


**Figure 3:** Crystal structure of  $\text{Na}_2\text{MgSnS}_4$  ( $\text{NaCrS}_2$  type) with  $\text{NaS}_6$  and  $(\text{Mg/Sn})\text{S}_6$  octahedra.

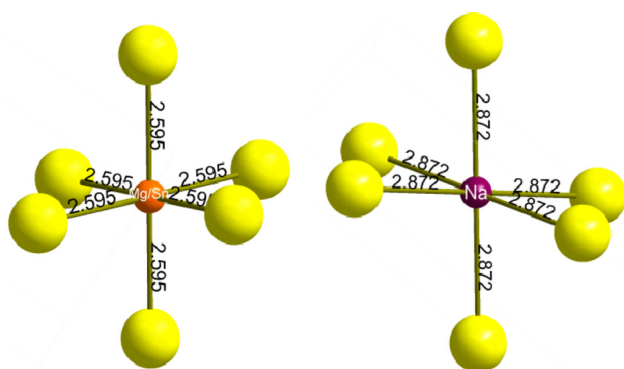


**Figure 4:**  $\text{NaS}_6$  and  $(\text{Mg/Sn})\text{S}_6$  octahedra in  $\text{Na}_2\text{MgSnS}_4$  (bond lengths in Å).

already to space group  $R\bar{3}m$  via a *translationengleiche* transition of index 4. The face-centered lattice changes here to an *R*-centered lattice. Two crystallographically independent atom positions are maintained in this case; as an example for this arrangement, antiferromagnetic NiO (af-NiO) can be given [49]. In the next step, we have an *isomorphic* transition with index two resulting in a doubling of the *c* axis. At this step, Wyckoff position  $3a$  splits up into two crystallographic independent positions

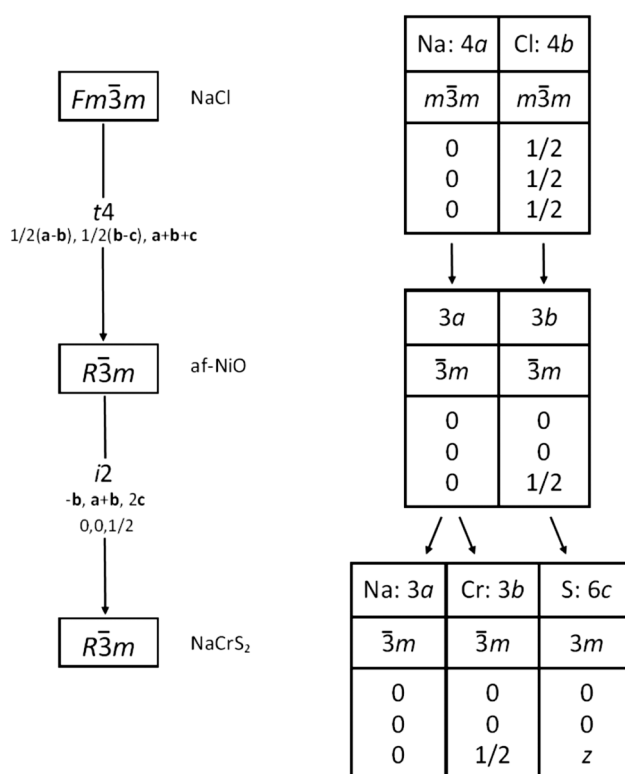


**Figure 5:** Group-subgroup scheme (Bärnighausen formalism) for the group theoretical relation between rocksalt and  $\text{NaCrS}_2$  type.

$3a$  (Na) and  $3b$  (Cr). The anion position  $3b$  changes to Wyckoff position  $6c$  in the  $\text{NaCrS}_2$  type.

### 3 Conclusions

Using the mechanochemical synthesis route, a new member of the  $A_2B^II C^IV X_6$  compound family has been synthesized.  $\text{Na}_2\text{MgSnS}_4$  exhibits the  $\text{NaCrS}_2$ -type structure (space group  $R\bar{3}m$ ) with  $a = 3.750(3)$  and  $c = 19.9130(14)$  Å. The  $\text{NaCrS}_2$  type is derived from the rocksalt type and exhibits an atomic arrangement similar to the  $\text{CdCl}_2$  type with additional atoms occupying the remaining voids. The successful synthesis of this compound again shows the large potential of the mechanochemical route for the preparation of multinary sulfides.

## 4 Experimental section

### 4.1 Synthesis

$\text{Na}_2\text{MgSnS}_4$  was synthesized by ball milling of  $\text{Na}_2\text{S}$  (Sigma Aldrich),  $\text{MgS}$ ,  $\text{SnS}$ , and sulfur (Fluka, 99.99%) in a high

energy planetary mill (Pulverisette 7, Fritsch, Idar-Oberstein, Germany) followed by annealing under flowing  $H_2S$  gas stream. The reactants were filled in a 45-mL zirconia grinding beaker with six zirconia balls (diameter: 15 mm) and ground at a rotational speed of 450 rpm for 4 h. The milled material was annealed at  $T = 600$  °C for 3 h in an atmosphere of  $H_2S$  to increase its crystallinity. MgS was prepared using high-temperature sulfidation of amorphous MgO (750 °C, 3 h); MgO was prepared by a modified Pechini method [50] with a calcination temperature of 450 °C. Solid state reaction of Sn (Merck, 99.9%) and S (Fluka, 99.99%) in an evacuated and sealed  $SiO_2$  ampoule was used for the preparation of SnS.

## 4.2 Structural and chemical characterization

$Na_2MgSnS_4$  was structurally characterized by X-ray powder diffraction in Bragg–Brentano geometry using a PANalytical X'Pert MDP Pro diffractometer. The diffractometer operates with  $CuK\alpha$  radiation at 40 kV and 40 mA. Structural refinements were carried out using the program suite FULLPROF [51] by applying a pseudo-Voigt function. To determine the phase composition of  $Na_2MgSnS_4$ , EDX was performed using a DSM 982 GEMINI spectrometer (Carl Zeiss AG, Oberkochen, Germany) equipped with a XFlash 6|60 detector (Bruker, Billerica, USA). Three independent measurements were performed, and their average value was used to calculate the chemical composition. Including the determination of the sulfur content, a device error of 5% is presumed for the EDX analysis. The EDX measurements were performed at the Zentrum für Elektronenmikroskopie (ZELMI) of the Technische Universität Berlin.

Further details of the crystal structure investigations may be obtained from the joint CCDC/FIZ Karlsruhe online deposition service: <https://www.ccdc.cam.ac.uk/structures/> by quoting the deposition number CSD-2007152.

**Acknowledgments:** The authors thank the ZELMI of the TU Berlin giving access to the EDX measurements which were performed by Dr. Stefan Berendts.

**Author contribution:** All the authors have accepted responsibility for the entire content of this submitted manuscript and approved submission.

**Research funding:** This work was supported by the German Science Foundation (DFG) under LE781/19-1.

**Conflict of interest statement:** The authors declare no conflicts of interest regarding this article.

## References

1. Katagiri H., Saitoh K., Washio T., Shinohara H., Kurumadani T., Miyajima S. Development of thin film solar cell based on  $Cu_2ZnSnS_4$  thin films. *Sol. Energy Mater. Sol. Cells* 2001, *65*, 141–148.
2. Seol J.-S., Lee S.-Y., Lee J.-C., Nam H.-D., Kim K.-H. Electrical and optical properties of  $Cu_2ZnSnS_4$  thin films prepared by rf magnetron sputtering process. *Sol. Energy Mater. Sol. Cells* 2003, *75*, 155–162.
3. Hall S. R., Szymanski J. T., Stewart J. M. Kesterite,  $Cu_2(Zn,Fe)SnS_4$ , and stannite,  $Cu_2(Fe,Zn)SnS_4$ , structurally similar but distinct minerals. *Can. Mineral.* 1978, *16*, 131–137.
4. Parthé E., Yvon K., Deitch R. H. The crystal structure of  $Cu_2CdGeS_4$  and other quaternary normal tetrahedral structure compounds. *Acta Crystallogr. B Struct. Sci.* 1969, *25*, 1164–1174.
5. Schorr S., Hoebler H.-J., Tovar M. A neutron diffraction study of the stannite-kesterite solid solution series. *Eur. J. Mineral.* 2007, *19*, 65–73.
6. Choubac L., Paris M., Lafond A., Guillot-Deudon C., Rocquefelte X., Jobic S. Multinuclear ( $^{67}Zn$ ,  $^{119}Sn$  and  $^{65}Cu$ ) NMR spectroscopy—an ideal technique to probe the cationic ordering in  $Cu_2ZnSnS_4$  photovoltaic materials. *Phys. Chem. Chem. Phys.* 2013, *15*, 10722–10725.
7. Schäfer W., Nitsche R. Tetrahedral quaternary chalcogenides of the type  $Cu_2 II IV S_4(Se_4)$ . *Mater. Res. Bull.* 1974, *9*, 645–654.
8. Moodie A. F., Whitfield H. J. Determination of the structure of  $Cu_2ZnGeS_4$  polymorphs by lattice imaging and convergent-beam electron diffraction. *Acta Crystallogr. B Struct. Sci.* 1986, *42*, 236–247.
9. Caye R., Laurent Y., Picot R., Pierrot R., Levy C. La hocartite,  $Ag_2SnFeS_4$ , une nouvelle espèce minérale. *Bull. Soc. Fr. Mineral. Cristallogr.* 1968, *91*, 383–387.
10. Zdenek J., Picot P. La pirquitasite,  $Ag_2ZnSnS_4$ , un nouveau membre du groupe de la stannite. *Bull. Mineral.* 1982, *105*, 229–235.
11. Wu K., Zhang B., Yang Z., Pan S. New compressed chalcopyrite-like  $Li_2BaM^IVQ_4$  ( $M^IV = Ge, Sn; Q = S, Se$ ): promising infrared nonlinear optical materials. *J. Am. Chem. Soc.* 2017, *139*, 14885–14888.
12. Aitken J. A., Larson P., Mahanti S. D., Kanatzidis M. G.  $Li_2PbGeS_4$  and  $Li_2EuGeS_4$ : polar chalcopyrites with a severe tetragonal compression. *Chem. Mater.* 2001, *13*, 4714–4721.
13. Teske C. L. Darstellung und Kristallstruktur von silber-bariumthio germanat(IV).  $Ag_2BaGeS_4$ /preparation and crystal structure of silver-barium-thio germanate(IV).  $Ag_2BaGeS_4$ . *Z. Naturforsch.* 1979, *34b*, 544–547.
14. Liu B.-W., Zhang M.-J., Zhao Z.-Y., Zeng H.-Y., Zheng F.-K., Guo G.-C., Huang J.-S. Synthesis, structure, and optical properties of the quaternary diamond-like compounds  $I_2-II-IV-VI_4$  ( $I=Cu; II=Mg; IV=Si, Ge; VI=S, Se$ ). *J. Solid State Chem.* 2013, *204*, 251–256.
15. Haeuseler H., Himmrich M. Neue Verbindungen  $Ag_2HgMX_4$  mit Wurtzstannitstruktur/new compounds  $Ag_2HgMX_4$  with the Wurtzstannite type structure. *Z. Naturforsch.* 1989, *44b*, 1035–1036.
16. Brunetta C. D., Brant J. A., Rosmus K. A., Henline K. M., Karey E., MacNeil J. H., Aitken J. A. The impact of three new quaternary sulfides on the current predictive tools for structure and composition of diamond-like materials. *J. Alloys Compd.* 2013, *574*, 495–503.

17. Brunetta C. D., Karuppanan B., Rosmus K. A., Aitken J. A. The crystal and electronic band structure of the diamond-like semiconductor  $\text{Ag}_2\text{ZnSiS}_4$ . *J. Alloys Compd.* 2012, 516, 65–72.
18. Greil S. *Untersuchungen an ternären und quaternären Kupfer-, Lithium-, und Silbersulfiden mit Diamantstruktur*; Dissertation, Universität Regensburg: Regensburg, 2015.
19. Parasyuk O. V., Piskach L. V., Olekseyuk I. D., Pekhnyo V. I. The quasi-ternary system  $\text{Ag}_2\text{ScdSgeS}_2$  and the crystal structure of  $\text{Ag}_2\text{CdGeS}_4$ . *J. Alloys Compd.* 2005, 397, 95–98.
20. Olekseyuk I. D., Marchuk O. V., Gulay L. D., Zhibankov O.Y. Isothermal section of the  $\text{Cu}_2\text{Se-HgSe-GeSe}_2$  system at 670K and crystal structures of the compounds  $\text{Cu}_2\text{HgGeSe}_4$  and HT-modification of  $\text{Cu}_2\text{HgGeS}_4$ . *J. Alloys Compd.* 2005, 398, 80–84.
21. Lekse J. W., Moreau M. A., McNerny K. L., Yeon J., Halasyamani P. S., Aitken J. A. Second-harmonic generation and crystal structure of the diamond-like semiconductors  $\text{Li}_2\text{CdGeS}_4$  and  $\text{Li}_2\text{CdSnS}_4$ . *Inorg. Chem.* 2009, 48, 7516–7518.
22. Lekse J. W., Leverett B. M., Lake C. H., Aitken J. A. Synthesis, physicochemical characterization and crystallographic twinning of  $\text{Li}_2\text{ZnSnS}_4$ . *J. Solid State Chem.* 2008, 181, 3217–3222.
23. Brant J. A., Clark D. J., Kim Y. S., Jang J. I., Weiland A., Aitken J. A. Outstanding laser damage threshold in  $\text{Li}_2\text{MnGeS}_4$  and tunable optical nonlinearity in diamond-like semiconductors. *Inorg. Chem.* 2015, 54, 2809–2819.
24. Brant J. A., Devlin K. P., Bischoff C., Watson D., Martin S. W., Gross M. D., Aitken J. A. A new class of lithium ion conductors with tunable structures and compositions: quaternary diamond-like thiogermanates. *Solid State Ion.* 2015, 278, 268–274.
25. Brunetta C. D., Minsterman W. C., Lake C. H., Aitken J. A. Cation ordering and physicochemical characterization of the quaternary diamond-like semiconductor  $\text{Ag}_2\text{CdGeS}_4$ . *J. Solid State Chem.* 2012, 187, 177–185.
26. Parasyuk O. V., Olekseyuk I. D., Piskach L. V., Volkov S. V., Pekhnyo V. I. Phase relations in the  $\text{Ag}_2\text{S-CdS-SnS}_2$  system and the crystal structure of the compounds. *J. Alloys Compd.* 2005, 399, 173–177.
27. Heppke E. M., Berendts S., Lerch M. Crystal structure of mechanochemically synthesized  $\text{Ag}_2\text{CdSnS}_4$ . *Z. Naturforsch.* 2020, 75b, 393–402.
28. Kogut Y. M., Fedorchuk A., Zhibankov O., Romanyuk Y., Kityk I., Piskach L. V., Parasyuk O. V. Isothermal section of the  $\text{Ag}_2\text{S-PbS-GeS}_2$  system at 300K and the crystal structure of  $\text{Ag}_2\text{PbGeS}_4$ . *J. Alloys Compd.* 2011, 509, 4264–4267.
29. Teske C. L., Vetter O. Präparative und röntgenographische Untersuchung am System  $\text{Cu}_{2-x}\text{Ag}_x\text{BaSnS}_4$ . *Z. Anorg. Allg. Chem.* 1976, 426, 281–287.
30. Teske C. L. Über die Darstellung und röntgenographische Untersuchung von  $\text{Cu}_2\text{SrGeS}_4$  und  $\text{Cu}_2\text{BaGeS}_4$ /on the preparation and X-ray investigation of  $\text{Cu}_2\text{SrGeS}_4$  and  $\text{Cu}_2\text{BaGeS}_4$ . *Z. Naturforsch.* 1979, 34b, 386–389.
31. Llanos J., Mujica C., Sánchez V., Peña O. Physical and optical properties of the quaternary sulfides  $\text{SrCu}_2\text{MS}_4$  and  $\text{EuCu}_2\text{MS}_4$  (M=Ge and Sn). *J. Solid State Chem.* 2003, 173, 78–82.
32. Olekseyuk I. D., Piskach L. V., Zhibankov O. Y., Parasyuk O. V., Kogut Y. M. Phase diagrams of the quasi-binary systems  $\text{Cu}_2\text{S-SiS}_2$  and  $\text{Cu}_2\text{SiS}_3\text{-PbS}$  and the crystal structure of the new quaternary compound  $\text{Cu}_2\text{PbSiS}_4$ . *J. Alloys Compd.* 2005, 399, 149–154.
33. Teske C. L. Darstellung und Kristallstruktur von gold-barium-thiostannat(IV),  $\text{Au}_2\text{BaSnS}_4$ . *Z. Anorg. Allg. Chem.* 1978, 445, 193–201.
34. Teske C. L., Vetter O. Ergebnisse einer Röntgenstrukturanalyse von silber-barium-thiostannat(IV),  $\text{Ag}_2\text{BaSnS}_4$ . *Z. Anorg. Allg. Chem.* 1976, 427, 200–204.
35. Kanno R. Synthesis of a new lithium ionic conductor, thio-LISICON—lithium germanium sulfide system. *Solid State Ion.* 2000, 130, 97–104.
36. Devi M. S., Vidyasagar K. First examples of sulfides in the quaternary A/Cd/Sn/S (A = Li, Na) systems: molten flux synthesis and single crystal X-ray structures of  $\text{Li}_2\text{CdSnS}_4$ ,  $\text{Na}_2\text{CdSnS}_4$  and  $\text{Na}_6\text{CdSn}_4\text{S}_{12}$ . *J. Chem. Soc. Dalton Trans.* 2002, 9, 2092–2096.
37. He J., Guo Y., Huang W., Zhang X., Yao J., Zhai T., Huang F. Synthesis, crystal structure, and optical properties of noncentrosymmetric  $\text{Na}_2\text{ZnSnS}_4$ . *Inorg. Chem.* 2018, 57, 9918–9924.
38. Wu K., Yang Z., Pan S.  $\text{Na}_2\text{BaMQ}_4$  (M=Ge, Sn; Q=S, Se): infrared nonlinear optical materials with excellent performances and that undergo structural transformations. *Angew. Chem. Int. Ed.* 2016, 55, 6713–6715.
39. Rüdorff W., Stegemann K. Kristallstruktur und magnetisches Verhalten der Alkalithiochromite. *Z. Anorg. Allg. Chem.* 1943, 251, 376–395.
40. Nakhla S., Lerch M., Koopman J., Islam M. M., Bredow T. Crystal structure of  $3\text{R-LiTiS}_2$  and its stability compared to other polymorphs. *Z. Anorg. Allg. Chem.* 2013, 639, 2822–2825.
41. Rietveld H. M. A profile refinement method for nuclear and magnetic structures. *J. Appl. Crystallogr.* 1969, 2, 65–71.
42. Shannon R. D. Revised effective ionic radii and systematic studies of interatomic distances in halides and chalcogenides. *Acta Cryst. A* 1976, 32, 751–767.
43. Heppke E. M., Klenner S., Janka O., Pöttgen R., Lerch M. Mechanochemical synthesis of  $\text{Cu}_2\text{MgSn}_3\text{S}_8$  and  $\text{Ag}_2\text{MgSn}_3\text{S}_8$ . *Z. Anorg. Allg. Chem.* 2020, 646, 5–9.
44. Mooser E., Pearson W. B. On the crystal chemistry of normal valence compounds. *Acta Cryst.* 1959, 12, 1015–1022.
45. Goodman C. H. L. The prediction of semiconducting properties in inorganic compounds. *J. Phys. Chem. Solids* 1958, 6, 305–314.
46. Bärnighausen H. Group-subgroup relations between space groups a useful tool in crystal chemistry. *MATCH Commun. Math. Chem.* 1980, 9, 139–175.
47. Müller U. Kristallographische Gruppe-Untergruppe-Beziehungen und ihre Anwendung in der Kristallchemie. *Z. Anorg. Allg. Chem.* 2004, 630, 1519–1537.
48. Bragg W. L. The structure of some crystals as indicated by their diffraction of X-rays. *Proc. R. Soc. Lond. A* 1913, 89, 248–277.
49. Rodic D., Spasojevic V., Kusigerski V., Tellgren R., Rundlof H. Magnetic ordering in polycrystalline  $\text{Ni}_x\text{Zn}_{1-x}\text{O}$  solid solutions. *Phys. Status Solidi B* 2000, 218, 527–536.
50. Pechini M. P. US Patent No 3330697, 1967.
51. Rodríguez-Carvajal R. FULLPROF, A program for Rietveld refinement and pattern matching analysis. In *Satellite Meeting on Powder Diffraction of the 15th International Congress of the IUCr, Toulouse (France)*, 1990, p. 127.

## 8. Publication 4

### Stannites - a new promising class of durable electrocatalysts for efficient water oxidation

J. Niklas Hausmann, Eva M. Heppke, Rodrigo Beltrán-Suito, Johannes Schmidt, Martin Mühlbauer, Martin Lerch, Prashanth W. Menezes and Matthias Driess

*Postprint*

*ChemCatChem* **2020**, 12(4), 1161-1168

doi:10.1002/cctc.201901705

<https://chemistry-europe.onlinelibrary.wiley.com/doi/full/10.1002/cctc.201901705>

CC BY 4.0



#### Contribution to publication:

- |                   |  |
|-------------------|--|
| J. N. Hausmann:   | Electrochemical and TEM measurements, general data evaluation, writing |
| E. M. Heppke:     | Sample preparation, structural characterization and evaluation         |
| R. Beltrán-Suito: | SEM and electrochemical measurements                                   |
| J. Schmidt:       | XPS measurements   |
| M. Mühlbauer:     | Neutron diffraction measurements                                       |
| M. Lerch:         | General advice, proofreading   |
| P. W. Menezes:    | Project design, general advice and proofreading                        |
| M. Driess:        | General advice, proofreading   |

**Authors:** J. N. Hausmann<sup>[1]</sup>, E. M. Heppke<sup>[2]</sup>, R. Beltrán-Suito<sup>[1]</sup>, J. Schmidt<sup>[3]</sup>,  
M. Mühlbauer<sup>[4]</sup>, M. Lerch<sup>[2]</sup>, P. W. Menezes<sup>\*[1]</sup>, M. Driess<sup>\*[1]</sup>

<sup>1</sup>Institut für Chemie: Metallorganische Chemie und Anorganische Materialien, Technische Universität Berlin, Straße des 17. Juni 135, 10623 Berlin

<sup>2</sup>Institut für Chemie: Festkörperchemie, Technische Universität Berlin, Straße des 17. Juni 135, 10623 Berlin

<sup>3</sup>Institut für Chemie: Funktionale Materialien, Technische Universität Berlin, Hardenbergstraße 40, 10623 Berlin

<sup>4</sup>Heinz Maier-Leibnitz Zentrum (MLZ) Technische Universität München, Lichtenbergstraße 1, 85748 Garching

\* corresponding

**Keywords:** oxygen evolution reaction (OER); stannite; water splitting; iron (Fe) oxyhydroxide; *in-situ* transformation

**Supporting Information:** Characterization of the as prepared material and electrodes, additional electrochemistry data, characterization of electrodes after OER, powder diffraction patterns of reference materials. This material is available free of charge *via* the Internet at

<https://chemistry-europe.onlinelibrary.wiley.com/doi/full/10.1002/cctc.201901705>

## 8.1. Abstract

The oxygen evolution reaction (OER) through water oxidation is a key process for multiple energy storage technologies required for a sustainable energy economy such as the formation of the fuel hydrogen from water and electricity or metal-air batteries. Herein, we investigate the suitability of  $\text{Cu}_2\text{FeSnS}_4$  for the OER and demonstrate its superiority over iron sulfide, iron (oxy)hydroxides and benchmark noble-metal catalysts in alkaline media. Electrodeposited  $\text{Cu}_2\text{FeSnS}_4$  yields the current densities of 10 and 1000  $\text{mA}/\text{cm}^2$  at overpotentials of merely 228 and 330 mV, respectively. State-of-the-art analytical methods are applied before and after electrocatalysis to uncover the fate of the  $\text{Cu}_2\text{FeSnS}_4$  precatalyst during OER conditions and to deduce structure-activity relationships.  $\text{Cu}_2\text{FeSnS}_4$  is the first compound reported for OER among the broad class of stannite structure type materials containing multiple members with highly active earth-abundant transition-metals for OER.

## 8.2. Introduction

Among the driving forces of global warming, the release of  $\text{CO}_2$  into the atmosphere by burning of fossils is one of the predominant factors [1]. An energy economy based on regenerative sources such as wind and sun is potentially carbon neutral [2]. A key requirement for the implementation of a sustainable energy economy is an efficient large scale energy storage technology such as the formation of fuels out of abundant and recyclable resources powered by electrical energy [3, 4]. In this regard, electrocatalytic water splitting can be utilized to yield the carbon-neutral fuel hydrogen from electricity and water. Electrocatalytic water splitting is composed of two half-reactions: the hydrogen and oxygen evolution reaction (OER). The highest loss of efficiency of this process results from the overpotential ( $\eta$ ) of the OER, which involves four sequential proton-coupled electron transfer steps [5].

To overcome this disadvantage, a vast amount of suitable OER catalyst have been investigated [6, 7]. Among these highly promising materials are transition-metal (TM) oxides, phosphates, chalcogenides, pnictides and carbides [8, 9]. The strongly oxidizing conditions required to achieve the oxidation of water is in most cases accompanied by a more or less severe transformation of the materials to (oxy)hydroxides species [10]. Therefore, many of the oxides and most of the non-oxidic materials are merely precatalysts for the OER [11]. Even though the anion is often exchanged or depleted from the electrocatalytic active structure, it plays a significant role in tuning the properties of the active catalyst either by creating high surface areas and defects through leaching or by providing a conductive core [10–15].

Bi- and multi-nuclear-TM (pre)catalysts have proven superior to mononuclear ones, as the variation of the metal composition enables the tuning of the intrinsic properties affecting the OER [16, 17]. In this regard, it has been shown that a multinuclear assembling of metals helps to vary adsorption energies [2, 18] and can afford higher stabilities [19–21], conductivities [22–24] and surfaces areas [25, 26] of OER catalysts.

An intensively investigated example is the inclusion of Fe into other TM systems such as Ni and Co [27–36]. In these materials, the included Fe cations drastically increase the OER activity, where Fe is proposed to act as the catalytically most active site [27, 30, 31, 33, 37–38]. However, poor catalytic activities are observed for heterometal-free  $\text{FeO}_x\text{H}_y$  [37, 39, 40], due to its low electric conductivity [29, 37, 41]. Similarly, homometallic iron sulfides usually show low catalytic activities for the OER [8, 42]. An exception represent pyrrhotite  $\text{Fe}_7\text{S}_8$  nanosheets bearing mixed Fe valence states and metallic conductivity [42]. On the contrary to homometallic iron sulfides, hetero- and heteromulti-metallic iron sulfides and especially selenides belong to the most active OER catalysts reported yet [5, 43, 44].

Quaternary sulfides or selenides of the formula  $\text{A}_2^{+\text{I}}\text{B}^{+\text{II}}\text{C}^{+\text{IV}}\text{S}_4^{-\text{II}}$  usually contain three different metals. A great variety of (semi)metals can be implemented for example  $\text{A} = \text{Li, Na, Ag, Cu}$ ;  $\text{B} = \text{Mn, Fe, Co, Ni, Zn, Cd}$ ; and  $\text{C} = \text{Si, Ge, Sn}$  [45–52]. Many members of this class of materials crystallize in the stannite structure type named after the mineral stannite with the formula  $\text{Cu}_2\text{FeSnS}_4$ . The stannite-type structure (space group  $I\bar{4}2m$ , see unit cell in Fig. 8.1) can be described as a cubic closed packed array of anions with half of the tetrahedral voids filled with cations. Its basis is the cubic diamond structure and all atoms are coordinated tetrahedrally by their closest neighbors. Stannites have been intensively investigated, due to their application as thin film solar cells [53–56]. In this regard, comprehensive efforts have been undertaken to fabricate thin films thereof [57–59]. This expertise could be used to realize stannite-based electrodes and to probe the material for its OER suitability. To the best of our knowledge, stannite-type materials have not been tested yet as OER precatalysts.

Herein, we report the superior electrocatalytic properties of  $\text{Cu}_2\text{FeSnS}_4$  on fluorine doped tin oxide (FTO) and nickel foam (NF) compared to iron sulfide, iron (oxy)hydroxide and the benchmark noble-metal precatalysts  $\text{IrO}_2$  and  $\text{RuO}_2$ . We found that  $\text{Cu}_2\text{FeSnS}_4$  acts as a precursor for the catalytically active phase, where tin is depleted completely from the active structure and sulfur leaches as well in the form of elemental  $\text{S}_8$ . The severe structural changes lead to an X-ray amorphous high surface area structure containing nanocrystalline  $\text{FeOOH}$  embedded into an amorphous copper-containing matrix. This nanocomposite shows a significantly improved charge transfer resistance ( $R_{\text{ct}}$ ) compared to the pure iron component, most likely due to an improved

electron transport to the FeOOH nanocrystallites. The presented results demonstrate the great potential of stannites for efficient OER. Bearing in mind that stannites containing the most active earth-abundant TM are synthetically accessible [50]; this report may trigger further interest to explore the OER properties of this class of quaternary materials.

### 8.3. Results and Discussion

#### Structural characterization of $\text{Cu}_2\text{FeSnS}_4$

$\text{Cu}_2\text{FeSnS}_4$  was synthesized by mechanochemical milling starting from the respective binary sulfides and followed by annealing in a tube furnace [60]. All reflections of the neutron diffraction pattern depicted in Figure 8.1 (top) could be unambiguously assigned to the stannite structure with space group  $I\bar{4}2m$  and the unit cell parameters  $a = 5.451 \text{ \AA}$  and  $c = 10.746 \text{ \AA}$  (see Tabs. S1 and S2 in the supporting information for refinement data). Further, a powder X-ray diagram (pXRD) is shown in Figure S1 confirming the neutron diffraction data. The cations are arranged in  $\text{Cu}^{\text{I}}\text{-Cu}^{\text{I}}$  layers alternating with  $\text{Fe}^{2+\text{(II)}}\text{-Sn}^{4+\text{(IV)}}$  layers in the tetrahedral voids of the cubic closed packed  $\text{S}^{2-\text{(II)}}$  anionic partial structure (see Fig. 8.1, top left). The scanning electron microscopy (SEM) images displayed in Figure S3 exhibit the formation of particles without a clearly defined morphology and a size ranging from 0.1 to 4  $\mu\text{m}$ . Further, energy dispersive X-ray (EDX) mapping using SEM was conducted to determine the elemental distribution in  $\text{Cu}_2\text{FeSnS}_4$ . The images shown in Figure 8.1 (bottom) confirm a homogeneous distribution of the elements Cu, Fe, Sn and S, and the EDX spectrum excludes the presence of other elements (see Fig. S3). Additionally, inductively coupled plasma atomic emission spectroscopy (ICP-AES) yielded an elemental ratio of 2.1 : 1.0 : 1.0 : 4.2 of Cu : Fe : Sn : S, which is in accordance to the formula composition (see Tab. S3). The selected area diffraction pattern (SAED) obtained by transmission electron microscopy (TEM) shows bright diffraction spots confirming the highly crystalline nature of the material (see Fig. S4 (a)). The crystallographic planes (112), (004), (204), (301) and (224) could be assigned in agreement with the neutron diffraction data. High-resolution TEM images display a lattice spacing of 0.521 nm and 0.314 nm revealing the crystallographic planes (002) and (112) (see Fig. S4 (e) and (f)).

The surface bonding and oxidation states of  $\text{Cu}_2\text{FeSnS}_4$  were unveiled by X-ray photoelectron spectroscopy (XPS). The Cu 2p, Fe 2p, Sn 3d and S 2p spectra (see Fig. S5) exhibit the expected oxidation states of  $\text{Cu}^{\text{I}}$ ,  $\text{Fe}^{\text{II}}$ ,  $\text{Sn}^{\text{IV}}$  and  $\text{S}^{\text{-II}}$  with minor amounts of  $\text{Cu}^{\text{II}}$  and a significant amount of  $\text{S}^{\text{IV}}$  caused by surface oxidation. These data are consistent with those reported for  $\text{Cu}_2\text{FeSnS}_4$  in the literature [54].

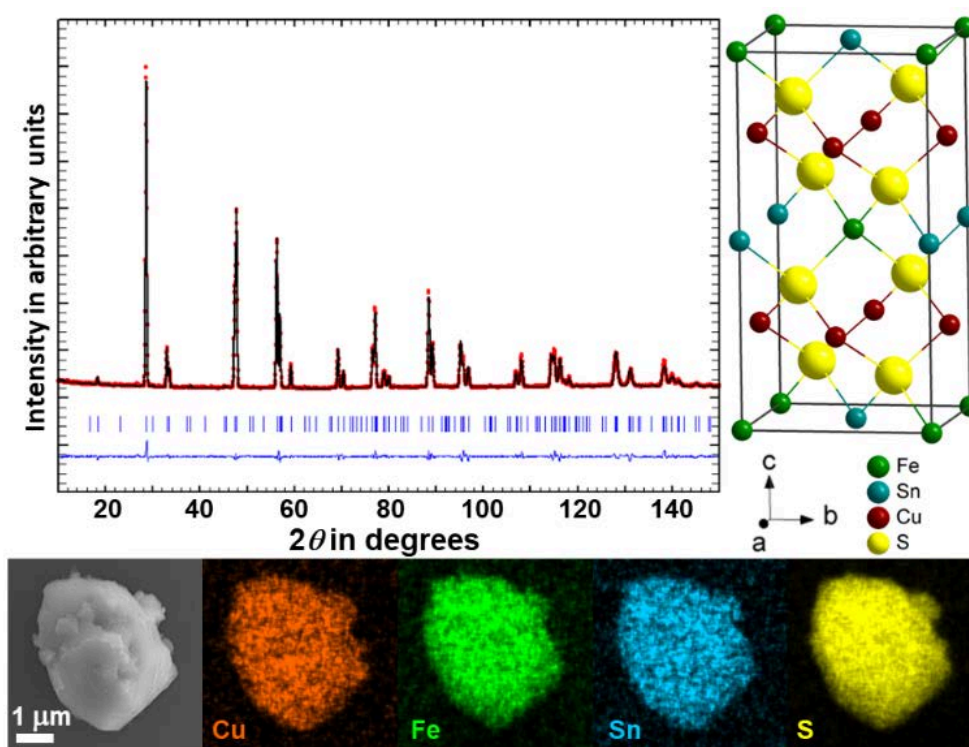


**Figure 8.1.:** Top: Neutron diffraction pattern (red points) of stannite,  $\text{Cu}_2\text{FeSnS}_4$ , with Rietveld refinement (black line), difference (blue line), Bragg reflections (blue stripes) and unit cell on the right. Bottom: SEM/EDX mapping of a  $\text{Cu}_2\text{FeSnS}_4$  particle.

### Electrocatalytic characterization and OER performance

The electrocatalytic activity of the  $\text{Cu}_2\text{FeSnS}_4$  towards the OER was investigated in 1 M aqueous KOH using linear sweep voltammetry (LSV). The  $\text{Cu}_2\text{FeSnS}_4$  was first electrophoretically deposited on a  $2 \times 1 \text{ cm}^2$  FTO glass plate substrate with a mass loading of 1 mg on an area of  $1 \text{ cm}^2$  (see Fig. S6 for pXRD from  $\text{Cu}_2\text{FeSnS}_4/\text{FTO}$ ). The LSVs of  $\text{Cu}_2\text{FeSnS}_4$  and the reference iron materials attained at a scan rate of  $5 \text{ mV/s}$  are shown in Figure 8.2 (a). The overpotentials of 365 and 550 mV are needed for  $\text{Cu}_2\text{FeSnS}_4$  to reach current densities of 10 and  $100 \text{ mA/cm}^2$ , respectively. This is significantly less than in case of  $\text{FeS}/\text{FTO}$ ,  $\text{Fe}(\text{OH})_3/\text{FTO}$  and  $\text{FeOOH}/\text{FTO}$  with the same mass loading as well as bare FTO, even though the weight percent of iron in  $\text{Cu}_2\text{FeSnS}_4$  (13%) is much lower compared to the sulfides and oxides.

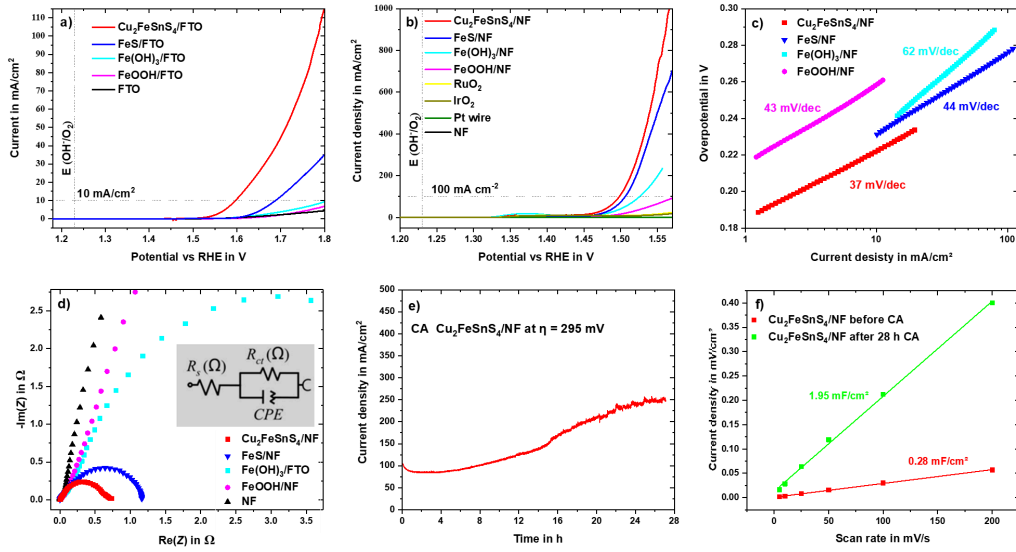


**Figure 8.2.:** (a) LSV (5 mV/s) of  $\text{Cu}_2\text{FeSnS}_4$  and various Fe containing materials loaded on FTO ( $1 \text{ mg/cm}^2$ ), (b) LSV (5 mV/s) of various materials loaded on NF ( $2 \text{ mg/cm}^2$ ), (c) Tafel slopes obtained from LSV (1 mV/s), (d) EIS responses ( $R_{\text{ct}}(\text{Cu}_2\text{FeSnS}_4) = 0.64 \Omega$  and  $R_{\text{ct}}(\text{FeS}) = 1.18 \Omega$ ), (e) long term CA measurement, (f) linear fits (derived by Figure S10) to obtain Cdl of the as prepared electrode and after CA measurement (e).

Motivated by this promising result, we loaded 2 mg of the same materials on a NF. NF has recently become an attractive choice as an electrode material, due to its low cost along with a high conductivity, large electro-active surface area, impeccable mechanical stability and good corrosion resistance [62, 63]. Further, its 3D porosity enhances the catalyst-substrate contact for efficient electron transport and lowers electrolyte mass transport limitations. SEM images and an EDX mapping of  $\text{Cu}_2\text{FeSnS}_4/\text{NF}$  are displayed in Figures S7 and S8. LSV scans with NF based electrodes loaded with Fe containing materials are shown in Fig. 8.2 (b). They were obtained by cycling in a potential range of 1.15 to 1.58 V with a scan rate of 5 mV/s until three similar consecutive scans were obtained. Bare NF treated under the same applied electrophoretic deposition (EPD) potentials in similar conditions exhibited a deplorable OER activity. The overpotentials of  $\text{Cu}_2\text{FeSnS}_4/\text{NF}$  to reach the current densities of 10, 100 and  $1000 \text{ mA/cm}^2$  were 228, 267 and 330 mV, respectively. The activity trend for the iron-based materials were the same as on FTO. Additionally, the benchmark noble metal-based catalysts  $\text{MO}_x$  ( $M = \text{Ru}, \text{Ir}$ ) were deposited on NF and investigated similarly (see Fig. S9 (a)). Most notable,  $\text{Cu}_2\text{FeSnS}_4/\text{NF}$  shows a significantly higher activity than these reference materials. Furthermore, we synthesized the referring homo- and bimetallic phases SnS, CuS,  $\text{Cu}_2\text{SnS}_3$  and  $\text{CuFeS}_2$  following exactly the same synthetic procedure as done for  $\text{Cu}_2\text{FeSnS}_4$ . The referring pXRDs are shown in figure S23. These

four materials were investigated similarly concerning their OER performance (see Fig. S9 (b)). This investigation reveals that the activity increases in the order  $\text{SnS} < \text{CuS} < \text{Cu}_2\text{SnS}_3 < \text{CuFeS}_2 < \text{FeS} < \text{Cu}_2\text{FeSnS}_4$ . Two conclusions can be deduced from this activity trend: (i) Fe is crucial to obtain a high electrocatalytic activity and most likely the active site and (ii) the trimetallic stannite phase is indeed required to achieve an exceptional electrocatalytic performance.

To gain insight into the electrocatalytic kinetics, Tafel plots (see Fig. 8.2 (c)) were obtained from LSVs with a scan rate of 1 mV/s.  $\text{Cu}_2\text{FeSnS}_4/\text{NF}$  showed the lowest Tafel slope of the investigated electrodes with 37 mV/dec indicating a higher transfer coefficient and superior OER kinetics [6]. This value is in the range ( $\sim 30\text{--}45$  mV/dec) of FeOOH and other bi- and multinuclear-TM, iron-containing oxyhydroxides and identical with the Tafel slope obtained for  $\text{Cu}_2\text{FeSnS}_4/\text{FTO}$  (see Fig. S10) [23]. This result suggests that in both cases iron is the catalytically active site. The linear Tafel behavior could be observed until a current density of 11 mA/cm<sup>2</sup> for  $\text{Cu}_2\text{FeSnS}_4/\text{NF}$  in contrast to  $< 1$  mA/cm<sup>2</sup> for  $\text{Cu}_2\text{FeSnS}_4/\text{FTO}$ , indicating that other effects such as surface coverage or electron/proton transport are influencing the catalytic behavior on FTO negatively at much lower current densities already [63–65]. Hence, the utilization of NF as an electrode substrate proved to be suitable to overcome these disadvantages to a certain extent.

Additionally, electrochemical impedance spectroscopy (EIS) was performed to evaluate the electrode transfer kinetics under OER conditions [66]. As shown in Figure 8.2 (d),  $\text{Cu}_2\text{FeSnS}_4$  possesses a significantly smaller charge transfer resistance ( $R_{\text{ct}}$ ) than the other aforementioned iron-based catalysts on NF. On FTO the  $R_{\text{ct}}$  of  $\text{Cu}_2\text{FeSnS}_4$  is seven times smaller than the one of FeS and more than 28 times smaller than the lowest one of the investigated  $\text{FeO}_x\text{H}_y$  catalysts (see Fig. S10). This reveals superior electron transfer and catalytic kinetics, in agreement with the Tafel data.

Chronoamperometry (CA) at an overpotential of 295 mV was performed over a period of 27 h to investigate the stability under comparably high current densities (see Fig. 8.2e). Initially, a current density of 100 mA/cm<sup>2</sup> was obtained, but a constant increase could be observed in the first 24 h until the current response stabilized at 250 mA/cm<sup>2</sup>. This proves the excellent stability and activity of the investigated system.

We determined the electrochemical double-layer capacitance ( $C_{\text{dl}}$ ), which is proportional to the electrochemically active surface area (ECSA), by performing cyclic voltammetry with different scan rates in a potential range, where no apparent Faradaic process occurred (see Fig. 8.2f). Before electrocatalytic testing, a value of 0.28 mF/cm<sup>2</sup> for  $\text{Cu}_2\text{FeSnS}_4/\text{NF}$  was obtained. After the CA measurement, the  $C_{\text{dl}}$  increased to 1.95 mF/cm<sup>2</sup> (see Fig. 8.2f) revealing a transformation of the material during OER

conditions to a phase with multiple times higher ECSA.

To rule out that other oxidation reactions such as the oxidation of  $S^{2-(-II)}$  are responsible for the high currents observed, we performed two Faradaic efficiency tests at different current densities. In a closed electrochemical cell  $Cu_2FeSnS_4/NF$ , after performing a CA measurement at  $\eta = 295$  mV for 1 h, was used as an anode and CP measurements at  $10$  mA/cm<sup>2</sup> and  $100$  mA/cm<sup>2</sup> for 8 min and 2 min were performed. The resulting quantity of  $O_2$  was compared to the current and the Faradaic efficiencies of 94 % and 96 % were obtained for the experiment at 10 and 100 mV/cm<sup>2</sup>, respectively.

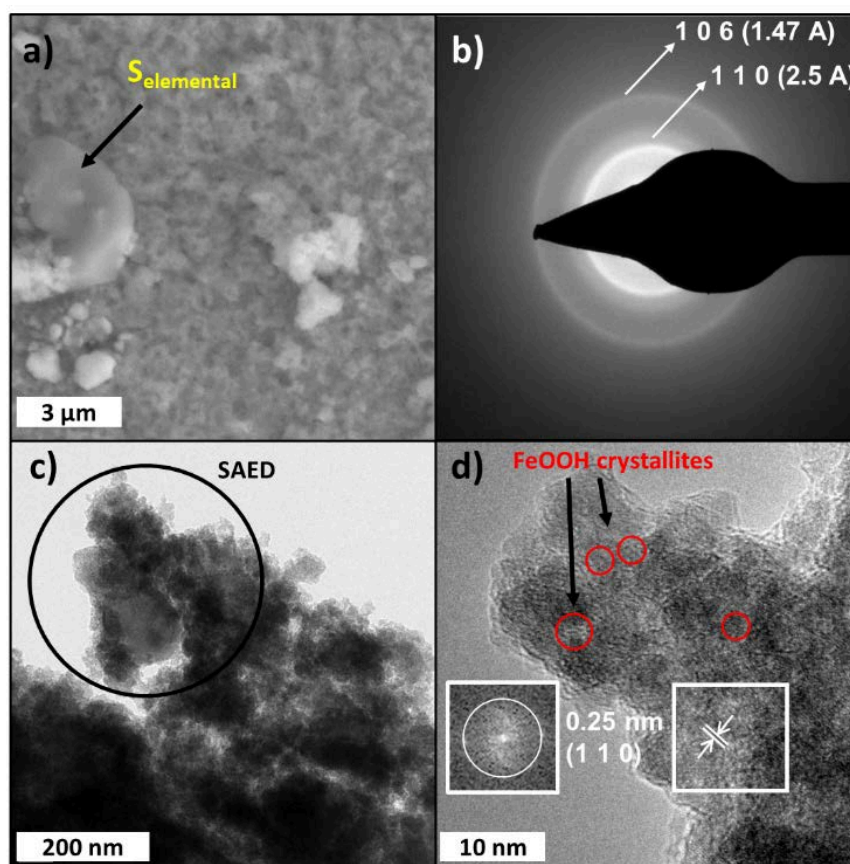


**Figure 8.3.:** Electron microscopy of  $Cu_2FeSnS_4$  after OER: (a) SEM image, the arrow indicates a particle of elemental sulfur, (b) SAED with crystallographic planes of FeOOH, (c) TEM image, the black circle indicates the area of the SAED, (d) HR-TEM image with the Fourier transformation of the selected area revealing fringes of the crystallographic plane (110) of FeOOH, the red circles indicate regions of uninterrupted ordered lattice fringes.

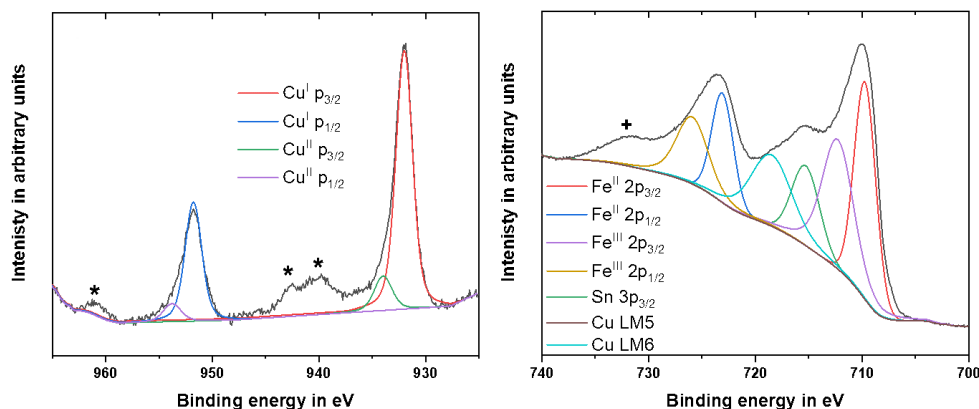


**Figure 8.4.:** XPS analysis of  $\text{Cu}_2\text{FeSnS}_4/\text{FTO}/\text{OER}$ ; a) Cu 2p spectrum with  $\text{Cu}^{\text{II}}$  satellites marked with \*; b) Fe 2p spectrum with  $\text{Fe}^{\text{III}}$  satellites marked with +.

### Post catalytic characterization

Even though  $\text{Cu}_2\text{FeSnS}_4$  does not show any changes by pXRD or ICP after several hours of 1 M KOH exposure (see Tab. S3), the electrocatalytic tests indicate a transformation of the material during OER conditions induced by the strongly oxidizing potential. Thus, to gain in-depth insight into the structural transformation, and, therefore, the origin of the prominent electrocatalytic activity, we characterized  $\text{Cu}_2\text{FeSnS}_4$  after CA measurements with pXRD, SEM, EDX, TEM and XPS.

A pXRD measurement taken directly from the FTO substrate after electrocatalytic testing ( $\text{Cu}_2\text{FeSnS}_4/\text{FTO}/\text{OER}$ ) reveals the absence of every reflex of the original  $\text{Cu}_2\text{FeSnS}_4$  structure (see Fig. S12). Instead, reflexes with a significant weaker intensity are present, which were unambiguously assigned to elemental sulfur. SEM measurements (see Figs. 8.3 a and S13) of the same electrode show the absence of the irregular shaped particles with a size close to 1  $\mu\text{m}$  as present in the as-prepared material (see Fig. S2) and the deposited one (see Fig. S7). Instead, a nanoscale rough morphology with a high surface area is present. EDX mapping (see Fig. S13) displays particles containing only sulfur; one of these is indicated in Figure 8.3a. The EDX spectrum (see Fig. S14) unveils that only Cu, Fe, K and O are present after the electrocatalytic testing in an area without a sulfur particle. For  $\text{Cu}_2\text{FeSnS}_4/\text{NF}/\text{OER}$  the SEM and EDX (see Figs. S16-S18) results are similar even though the morphology of the nanoscale rough surface differs.

TEM investigations were performed by scratching off used catalyst from a  $\text{Cu}_2\text{FeSnS}_4/\text{FTO}/\text{OER}$  electrode. The images taken at various magnifications (see Figs. 8.3c and S15) show nanoparticles with a rough morphology and high surface area. The selected

area electron diffraction (SAED) presented in Figure 8.3b exhibits two broad rings indicating nanocrystallinity. The SAED intensities fit perfectly well to the one of the iron oxyhydroxide, 2-line ferrihydrite, and lattice distances determined from diffraction rings are in good agreement with the crystallographic (110) and (106) planes of 2-line ferrihydrite [67, 68]. In the HR-TEM image shown in Figure 8.3d, ordered and uninterrupted lattice fringes can be seen in an area of up to at most 2 nm diameter. The Fourier transform of such an area reveals a lattice spacing of 0.25 nm, consistent with the (110) crystallographic plane of 2-line ferrihydrite. The fact that the uninterrupted, ordered crystalline domains are so small leads to a big amount of disordered iron surface sites that can act as catalytic centers. No crystalline phase containing copper could be found, and therefore, we assume that copper is present in form of an amorphous matrix in between the FeOOH nanocrystallites.

Figure 8.4 shows the Cu 2p, Fe 2p and O 1s XPS spectra of a sample of the  $\text{Cu}_2\text{FeSnS}_4/\text{FTO}/\text{OER}$  electrode material. The Cu  $2p_{3/2}$  and Cu  $2p_{1/2}$  spectrum exhibits sharp peaks at the binding energy of 931.9 and 951.7 eV, indicating the presence of a  $\text{Cu}^{\text{I}}$  species [69]. Additionally, satellite peaks typical for  $\text{Cu}^{\text{II}}$  are located at the binding energies of 939.9, 942.6 and 961.2 eV [14, 69]. The low intensity of these satellites is in agreement with the deconvolution of the Cu  $2p_{3/2}$  and Cu  $2p_{1/2}$  peaks, revealing that most of the Cu is in the  $\text{Cu}^{\text{I}}$  state with a minor contribution of  $\text{Cu}^{\text{II}}$ . The presence of mainly  $\text{Cu}^{\text{I}}$  species strongly supports the hypothesis that iron is the actual active site and that the role of copper is likely another one such as facilitating electron transport. This is further indicated by the low  $R_{\text{ct}}$  of  $\text{Cu}_2\text{FeSnS}_4/\text{FTO}$  compared to the other copper-free iron compounds investigated by EIS (see Fig. S10). The Fe core-level spectrum (see Fig. 8.4b) exhibits two major, rather broad peaks located at 710.1 eV for Fe  $2p_{3/2}$  and 723.6 eV for Fe  $2p_{1/2}$ . These binding energies are in-between those expected for  $\text{Fe}^{\text{II}}$  and  $\text{Fe}^{\text{III}}$  [70, 71]. The Fe  $2p_{3/2}$  peak overlaps with the ones of Sn 3p and Cu LM5/6 located at slightly higher binding energies. However, no additional peaks interfere with the Fe  $2p_{1/2}$  region allowing a deconvolution of Fe 2p signals originating from  $\text{Fe}^{\text{II}}$  and  $\text{Fe}^{\text{III}}$ . Such an analysis reveals the coexistence of these two oxidation states in approximately equal amounts. The presence of  $\text{Fe}^{\text{III}}$  is further supported by the satellite peak at 732.0 eV [70, 71]. The increased oxidation state strengthens the hypothesis that iron is the catalytically active site, as indicated already by the Tafel slope of 37 mV/dec [23]. The O 1s core-level spectrum reveals a peak with two maxima and one shoulder, suggesting the presence of at least three chemically distinct oxygen environments. The deconvoluted XPS spectrum of pure FeOOH [71] exhibits three peaks at similar binding energies like those shown in Figure 8.4c. These peaks could be assigned to Fe-O-Fe, Fe-O-H and surface absorbed water [71–73]. This confirms

the conclusion of the TEM results that FeOOH, 2-line ferrihydrite, nanocrystallites are formed during OER conditions. However, other metal oxide such as the SnO<sub>2</sub> from the FTO overlap with these peaks. This can be clearly seen if one compares the O 1s core-level spectrum of Cu<sub>2</sub>FeSnS<sub>4</sub>/FTO/OER to the one of Cu<sub>2</sub>FeSnS<sub>4</sub>/NF/OER shown in Figure S19. The metal oxide peak is strongly reduced in the Cu<sub>2</sub>FeSnS<sub>4</sub>/NF/OER spectrum, as no SnO<sub>2</sub> is present. The Cu and Fe 2p spectra of Cu<sub>2</sub>FeSnS<sub>4</sub>/NF/OER are also displayed in Figure S19 and indicate the same oxidation states in slightly different ratios than those found for Cu<sub>2</sub>FeSnS<sub>4</sub>/FTO/OER.

## 8.4. Conclusions

Herein, the superior electrocatalytic properties of Cu<sub>2</sub>FeSnS<sub>4</sub> on FTO and NF compared to single component iron sulfide, iron (oxy)hydroxide and the benchmark noble-metal-based catalyst MO<sub>x</sub> (M = Ru, Ir) with the same mass loading are presented. We reveal that Cu<sub>2</sub>FeSnS<sub>4</sub> consisting only out of earth-abundant elements acts as a precursor for the catalytically active phase, which is nanocrystalline FeOOH embedded into an amorphous copper-containing matrix. This phase is formed by the complete depletion of tin and sulfur and severe reorganization of the precursor structure. We could identify three major reasons for the superior electrocatalytic activity: First, a significantly increased surface area caused by the *in-situ* formed nanoscale rough morphology, second, an improved  $R_{ct}$  most likely caused by a facilitated electron transport through the presence of mixedvalence Cu<sup>I/II</sup>, and third, a large amount of disordered Fe surface sites of the X-ray amorphous nanocrystalline (<2 nm) FeOOH. Cu<sub>2</sub>FeSnS<sub>4</sub> is the first stannite material reported for OER. As stannites are known containing the most OER active earth-abundant elements, this report opens a new avenue to novel, highly efficient and robust OER catalysts.

## 8.5. Experimental Section

### Materials and Synthesis

1 M aqueous KOH and other reagents used in the synthetic procedures were obtained from Sigma Aldrich. The commercial RuO<sub>2</sub> (99 %) and IrO<sub>2</sub> (99 %) were purchased from Alfa Aesar. Nickel foam (NF) and fluorine doped tin oxide (FTO, resistivity 8-12 Ω/sq) were purchased from Recemat BV and Sigma Aldrich, respectively.

**Cu<sub>2</sub>FeSnS<sub>4</sub>.** Cu<sub>2</sub>FeSnS<sub>4</sub> was synthesized by mechanochemical milling in a high energy planetary Mono Mill PULVERISETTE 6 (Fritsch, Idar-Oberstein, Germany) starting

from the binary sulfides and followed by an annealing procedure in a tube furnace [60]. Stoichiometric amounts of CuS, FeS<sub>2</sub> (Sigma Aldrich, 99.8 %) and SnS were filled in a 45 ml zirconia grinding beaker with six zirconia grinding balls (diameter 15 mm) and milled at a rotational speed of 350 rpm for five hours. In order to obtain a highly crystalline product, the ground material was annealed in a subsequent step at 1023 K for two hours under flowing reaction gas (H<sub>2</sub>S). The Cu<sub>2</sub>FeSnS<sub>4</sub>-sample was quenched from 1023 K to room temperature to avoid phase transformation from the high-temperature stannite-type polymorph (space group  $I\bar{4}2m$ ) to low-temperature phase in space group  $P\bar{4}$ . CuS was prepared by precipitation from a 0.1 M Cu(NO<sub>3</sub>)<sub>2</sub> solution with H<sub>2</sub>S (Air Liquide, 99.5 %) followed by annealing at 503 K for two hours in H<sub>2</sub>S-atmosphere. For SnS a solid-state reaction of tin (Merck, 99.9 %) and sulfur (Fluka, 99.99 %) in an evacuated and sealed silica glass ampoule was applied.

**FeS, Fe(OH)<sub>3</sub> & FeOOH.** Amorphous Fe(OH)<sub>3</sub> was synthesized by precipitation of an iron(III) nitrate following a reported protocol and FeOOH by precipitation of iron(II) sulfate followed by oxidation with H<sub>2</sub>O<sub>2</sub> [74, 75]. Hexagonal crystalline FeS was synthesized by a solid-state reaction following a reported protocol [76]. The corresponding pXRD data to the three materials can be found in the supporting information (see Figs. S19 and S20).

## Characterization

**Powder X-ray and neutron diffraction.** A Panalytical X'Pert PRO diffractometer (Bragg-Brentano geometry, Cu-K $\alpha$  radiation) was used for powder XRD measurements. Neutron powder diffraction data were collected at the Forschungs-Neutronenquelle Heinz-Maier-Leibnitz Zentrum (MLZ, Garching) using the high-resolution powder diffractometer SPODI (Ge (551)  $\lambda=1.54816$  Å). For neutron experiments the sample was encapsulated in a vanadium container with 0.15 mm wall thickness and 9 mm inner diameter (Ar atmosphere). Structural refinements were performed by the Rietveld method [77] using the program FULLPROF [78] Suite Version 2015 by applying a Thompson-Cox-Hastings pseudo-Voigt function for the neutron data, respectively.

**Inductively coupled plasma atomic emission spectroscopy.** The inductively coupled plasma atomic emission spectroscopy (ICP-AES) was conducted on a Thermo Jarrell Ash Trace Scan analyser. The materials were digested in aqua regia HCl: HNO<sub>3</sub> 4:1 v/v (nitric acid, SUPRA-Qualität ROTIPURAN<sup>®</sup> Supra 69 % and hydrochloric acid, SUPRA-Qualität ROTIPURAN<sup>®</sup> Supra 30 %). The digestion volume (2.5 ml) was diluted with milli-Q water up to 10 ml. Calibration curves were prepared for

copper, iron, tin and sulfur with concentrations between 1 mg/l and 100 mg/l from standard solutions (1000 mg/l Single-Element ICP-Standard Solution ROTI STAR).

**Scanning electron microscopy.** Scanning electron microscopy (SEM) was performed on a GeminiSEM500 NanoVP microscope (ZEISS) integrated with an EDX detector (Bruker Quantax XFlash<sup>®</sup> 6|60). The most abundant elements were selected from the EDX spectrum. Data handling and analysis were achieved with the software package EDAX. The SEM experiments were conducted at the Zentrum für Elektronenmikroskopie (ZELMI) of the TU Berlin.

**Transmission electron microscopy.** Transmission electron microscopy (TEM) was performed on an FEI Tecnai G2 20 S-TWIN transmission electron microscope (FEI Company, Eindhoven, Netherlands) equipped with a LaB6 source at 200 kV acceleration voltage. For the investigation of the films after electrocatalysis, the films were scraped from the electrode substrate and transferred onto a carbon-coated copper grid. EDX analyses were achieved with an EDAX r-TEM SUTW detector (Si (Li) detector), and the images were recorded with a GATAN MS794 P CCD camera. The TEM experiments were conducted at the Zentrum für Elektronenmikroskopie (ZELMI) of the TU Berlin.

**X-ray photoelectron spectroscopy.** X-ray photoelectron spectroscopy (XPS) measurements were carried out using a ThermoScientific K-Alpha+ X-ray photoelectron spectrometer. All samples were analysed using a microfocused, monochromated Al-K $\alpha$  X-ray source (1486.68 eV; 400  $\mu$ m spot size). The analyser had a pass energy of 200 eV (survey), and 50 eV (high-resolution spectra), respectively. Binding energies were calibrated to the C 1s peak at 284.8 eV. To prevent any localized charge build up during analysis the K-Alpha+ charge compensation system was employed at all measurements. The samples were mounted on conductive carbon tape or measured directly from the electrode substrates (FTO and NF). The resulting spectra were analysed using the Advantage software from ThermoScientific.

## **Electrochemical measurements**

All measurements were performed at 25 °C regulated by a thermostat. A typical electrocatalytic run was carried out in a standard three-electrode (working, counter and reference) electrochemical cell in 50 ml 1M aqueous KOH with a potentiostat (SP-200, BioLogic Science Instruments) controlled by the EC-Lab v10.20 software package. The electrodes (NF/FTO) with samples deposited served as the working electrodes, Pt wire

(0.5 mm diameter x 230 mm length; A-002234, BioLogic) as a counter and Hg/HgO as the reference electrode (CH Instruments, Inc.).

**Cyclic and linear sweep voltammetry.** CV and LSV was performed without stirring and with an applied iR compensation of 90 %. The uncompensated resistance ( $R_u$ ) was acquired by impedance spectroscopy at 100 MHz. The potentials of the reference electrodes in this work were referenced to the reversible hydrogen electrode (RHE) through calibration, and in 1 M aqueous KOH the potential was calculated using the following equation:

$$E(RHE) = E(Hg/HgO) + 0.098V + (0.059 \times pH)V. \quad (8.1)$$

**Chronoamperometry.** The chronoamperometric measurements were performed with intensive stirring and an applied iR compensation of 90 % in 1 M aqueous KOH at selected constant potentials with respect to RHE.

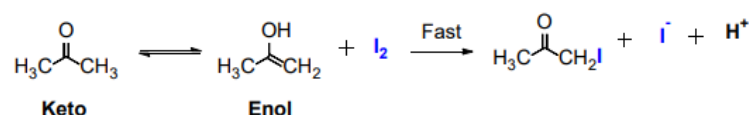
**Tafel analysis.** The Tafel slope was calculated according to the Tafel equation  $\eta = b \log j + a$ , where  $\eta$  is the overpotential (V),  $j$  is the current density (mA/cm<sup>2</sup>), and  $b$  is the Tafel slope (mV/dec).

**Double-layer capacitance.** The double-layer capacitance ( $C_{dl}$ ) was determined from the CV (cycled between 0.875 and 0.925 V vs. RHE) at a potential range, where no apparent faradaic process occurred. The anodic charging currents measured at 0.9 V vs. RHE were plotted as a function of the scan rate and from the slope the  $C_{dl}$  was attained [79–81]. The ECSA of the catalysts can be calculated using the equation  $ECSA = C_{dl}/C_s$ , where  $C_s$  can be defined as the specific capacitance of the material per unit area under identical electrolyte conditions [82]. Therefore, the ECSA is directly proportional to  $C_{dl}$ .

**Electrochemical impedance spectroscopy.** Electrochemical impedance spectroscopy (EIS) was recorded at 1.57 V vs. RHE for FTO samples and at 1.49 V vs RHE for NF samples to obtain the Nyquist plots. The amplitude of the sinusoidal wave was examined in a frequency range of 100 kHz to 1 mHz. All impedance spectra were fitted using an equivalent RC circuit model. The charge-transfer resistance ( $R_{ct}$ ) was then obtained from the diameter of the semicircle in the Nyquist plots [79, 82].

**Electrophoretic deposition.** The investigated materials were deposited electrophoretically by a well-established method on both, NF and FTO [62, 75, 82–84]. A potential

difference of 10 V, using FTO as both counter and reference electrode or NF for both, in a mixture of iodine and acetone on a  $1 \times 1 \text{ cm}^2$  area was applied. The electric charge on the catalyst in acetone is insufficient for EPD, as very small amounts of free ions exist in acetone. When iodine is used as the dispersant, it can react with acetone through the keto-enol tautomerisation to produce protons as per the following equation



Thus, formed protons are adsorbed on the surface of the suspended particles by making them positively charged. The applied electric field induces the positively charged particles to migrate towards and deposit on the cathode. Typically, 30 mg of the catalyst powder was suspended in 10 ml acetone and sonicated for 2 h then 2 mg of iodine was added and the suspension sonicated for another 3 min. The EPD was conducted at 10 V for 4 min and thin uniform films were obtained. The sample loading on each NF and FTO was 2 and 1  $\text{mg}/\text{cm}^2$ , respectively. A similar procedure was also followed to deposit all other electrocatalytically tested compounds.

**Faradaic efficiency.** The Faradaic efficiency (FE) of the materials in 1 M KOH towards oxygen evolution reaction was measured in a two-electrode configuration where nickel foam loaded with the catalysts were used as anode and Pt wire as a cathode in a closed electrochemical cell. The electrolyte and cell were first degassed with Argon for 30 min under stirring. Afterwards, constant current density of 10  $\text{mAcm}^{-2}$  or 100  $\text{mAcm}^{-2}$  was applied for 8 min or 2 min, respectively. At the end of electrolysis, the gaseous samples were drawn from the headspace by a gas tight syringe and analyzed by a GC calibrated  $\text{O}_2$ .

The Faradaic efficiency (FE) was calculated based on:

$$FE(\text{O}_2, \%) = \frac{V_{\text{O}_2} \times 4 \times F}{V_m \times j \times t} \times 100 \% \quad (8.2)$$

$V_{\text{O}_2}$  is the evolved volume of oxygen,  $F$  is the Faraday constant (96485.33289 C/mol),  $V_m$  is the molar volume of the gas,  $j$  is the current density (10  $\text{mAcm}^{-2}$ ) and  $t$  is the time of electrolysis.

## 8.6. Acknowledgements

We are grateful to the Einstein Center of Catalysis (EC<sup>2</sup>) for financial support. This project was also supported by the Deutsche Forschungsgemeinschaft (Deutschland's Exzellenzstrategie – EXC 2008/1– 390540038 and Normalverfahren LE 781/19-1).

## 8.7. References

- [1] S. Solomon, G.-K. Plattner, R. Knutti, P. Friedlingstein, *Proc. Natl. Acad. Sci.* **2009**, 106, 1704–1709.
- [2] Z. W. Seh, J. Kibsgaard, C. F. Dickens, I. Chorkendorff, J. K. Nørskov, T. F. Jaramillo, *Science* **2017**, 355, 1-12.
- [3] S. Chu, Y. Cui, N. Liu, *Nat. Mater.* **2016**, 16, 16–22.
- [4] H. B. Gray, *Nat. Chem.* **2009**, 1, 7.
- [5] F. Lyu, Q. Wang, S. M. Choi, Y. Yin, *Small* **2019**, 15, 1804201.
- [6] N.-T. Suen, S.-F. Hung, Q. Quan, N. Zhang, Y.-J. Xu, H. M. Chen, *Chem. Soc. Rev.* **2017**, 46, 337–365.
- [7] C. Panda, P. W. Menezes, M. Driess, *Angew. Chemie Int. Ed.* **2018**, 57, 11130–11139.
- [8] S. Anantharaj, S. R. Ede, K. Sakthikumar, K. Karthick, S. Mishra, S. Kundu, *ACS Catal.* **2016**, 6, 8069–8097.
- [9] P. W. Menezes, C. Panda, C. Walter, M. Schwarze, M. Driess, *Adv. Funct. Mater.* **2019**, 29, 1808632.
- [10] B. R. Wygant, K. Kawashima, C. B. Mullins, *ACS Energy Lett.* **2018**, 3, 2956–2966.
- [11] S. Jin, *ACS Energy Lett.* **2017**, 2, 1937–1938.
- [12] C. Walter, P. W. Menezes, S. Orthmann, J. Schuch, P. Connor, B. Kaiser, M. Lerch, M. Driess, *Angew. Chemie Int. Ed.* **2018**, 57, 698– 702.

- [13] O. Mabayoje, A. Shoola, B. R. Wygant, C. B. Mullins, *ACS Energy Lett.* **2016**, 1, 195–201.
- [14] C. Panda, P. W. Menezes, M. Zheng, S. Orthmann, M. Driess, *ACS Energy Lett.* **2019**, 4, 747–754.
- [15] A. Dutta, N. Pradhan, *J. Phys. Chem. Lett.* **2017**, 8, 144–152.
- [16] J. S. Kim, B. Kim, H. Kim, K. Kang, *Adv. Energy Mater.* **2018**, 8, 1–26.
- [17] C. Yuan, H. Bin Wu, Y. Xie, X. W. D. Lou, *Angew. Chemie Int. Ed.* **2014**, 53, 1488–1504.
- [18] O. Diaz-Morales, I. Ledezma-Yanez, M. T. M. Koper, F. Calle-Vallejo, *ACS Catal.* **2015**, 5, 5380–5387.
- [19] R. Kötz, S. Stucki, *Electrochim. Acta* **1986**, 31, 1311–1316.
- [20] M. Chatti, J. L. Gardiner, M. Fournier, B. Johannessen, T. Williams, T. R. Gengenbach, N. Pai, C. Nguyen, D. R. MacFarlane, R. K. Hocking, A. N. Simonov, *Nat. Catal.* **2019**, 2, 457–465.
- [21] I. Katsounaros, S. Cherevko, A. R. Zeradjanin, K. J. J. Mayrhofer, *Angew. Chemie Int. Ed.* **2014**, 53, 102–121.
- [22] M. Hamdani, R. N. Singh, P. Chartier, *Int. J. Electrochem. Sci.* **2010**, 5, 556–577.
- [23] M. S. Burke, L. J. Enman, A. S. Batchellor, S. Zou, S. W. Boettcher, *Chem. Mater.* **2015**, 27, 7549–7558.
- [24] L. Hu, Z. Wu, W. Tian, Y. Jiang, L. Jiang, P. Yang, Z. Pan, *Nanoscale* **2018**, 10, 12003–12010.
- [25] P. Zhang, L. Li, D. Nordlund, H. Chen, L. Fan, B. Zhang, X. Sheng, Q. Daniel, L. Sun, *Nat. Commun.* **2018**, 9, 1–10.
- [26] P. W. Menezes, C. Panda, S. Garai, C. Walter, A. Guillet, M. Driess, *Angew.*

- Chemie Int. Ed.* **2018**, 57, 15237–15242.
- [27] D. A. Corrigan, *J. Electrochem. Soc.* **1987**, 134, 377.
- [28] M. Gong, H. Dai, *Nano Res.* **2015**, 8, 23–39.
- [29] M. S. Burke, S. Zou, L. J. Enman, J. E. Kellon, C. A. Gabor, E. Pledger, S. W. Boettcher, *J. Phys. Chem. Lett.* **2015**, 6, 3737–3742.
- [30] M. Görlin, P. Chernev, J. F. De Araújo, T. Reier, S. Dresch, B. Paul, R. Krähnert, H. Dau, P. Strasser, *J. Am. Chem. Soc.* **2016**, 138, 5603–5614.
- [31] N. Li, D. K. Bediako, R. G. Hadt, D. Hayes, T. J. Kempa, F. von Cube, D. C. Bell, L. X. Chen, D. G. Nocera, *Proc. Natl. Acad. Sci.* **2017**, 114, 1486–1491.
- [32] C. Roy, B. Sebok, S. B. Scott, E. M. Fiordaliso, J. E. Sørensen, A. Bodin, D. B. Trimarco, C. D. Damsgaard, P. C. K. Vesborg, O. Hansen, I. E. L. Stephens, J. Kibsgaard, I. Chorkendorff, *Nat. Catal.* **2018**, 1, 820–829.
- [33] B. M. Hunter, N. B. Thompson, A. M. Müller, G. R. Rossman, M. G. Hill, J. R. Winkler, H. B. Gray, *Joule* **2018**, 2, 747–763.
- [34] X.-F. Lu, L.-F. Gu, J.-W. Wang, J.-X. Wu, P.-Q. Liao, G.-R. Li, *Adv. Mater.* **2017**, 29, 1604437.
- [35] R. D. L. Smith, C. Pasquini, S. Loos, P. Chernev, K. Klingan, P. Kubella, M. R. Mohammadi, D. Gonzalez-Flores, H. Dau, *Nat. Commun.* **2017**, 8, 2022.
- [36] B. Zhang, X. Zheng, O. Voznyy, R. Comin, M. Bajdich, M. García-Melchor, L. Han, J. Xu, M. Liu, L. Zheng, *Science* **2016**, 352, 333–337.
- [37] S. Zou, M. S. Burke, M. G. Kast, J. Fan, N. Danilovic, S. W. Boettcher, *Chem. Mater.* **2015**, 27, 8011–8020.
- [38] M. B. Stevens, C. D. M. Trang, L. J. Enman, J. Deng, S. W. Boettcher, *J. Am. Chem. Soc.* **2017**, 139, 11361–11364.

- [39] M. E. G. Lyons, M. P. Brandon, *Int. J. Electrochem. Sci.* **2008**, 3, 1425–1462.
- [40] R. Subbaraman, D. Tripkovic, K. C. Chang, D. Strmcnik, A. P. Paulikas, P. Hirunsit, M. Chan, J. Greeley, V. Stamenkovic, N. M. Markovic, *Nat. Mater.* **2012**, 11, 550–557.
- [41] L. Han, S. Dong, E. Wang, *Adv. Mater.* **2016**, 28, 9266–9291.
- [42] S. Chen, Z. Kang, X. Zhang, J. Xie, H. Wang, W. Shao, X. Zheng, W. Yan, B. Pan, Y. Xie, *ACS Cent. Sci.* **2017**, 3, 1221–1227.
- [43] N. Yang, C. Tang, K. Wang, G. Du, A. M. Asiri, X. Sun, *Nano Res.* **2016**, 9, 3346–3354.
- [44] L. Peng, S. S. A. Shah, Z. Wei, *Chinese J. Catal.* **2018**, 39, 1575–1593.
- [45] M. S. Devi, K. Vidyasagar, *J. Chem. Soc. Dalt. Trans.* **2002**, 0, 2092–2096.
- [46] J. W. Lekse, M. A. Moreau, K. L. McNerny, J. Yeon, P. S. Halasyamani, J. A. Aitken, *Inorg. Chem.* **2009**, 48, 7516–7518.
- [47] C. D. Brunetta, J. A. Brant, K. A. Rosmus, K. M. Henline, E. Karey, J. H. MacNeil, J. A. Aitken, *J. Alloys Compd.* **2013**, 574, 495–503.
- [48] H. Hahn, H. Schulze, *Naturwissenschaften* **1965**, 52, 426.
- [49] R. Nitsche, D. F. Sargent, P. Wild, *J. Cryst. Growth* **1967**, 1, 52–53.
- [50] W. Schäfer, R. Nitsche, *Mater. Res. Bull.* **1974**, 9, 645–654.
- [51] R. Caye, Y. Laurent, P. Picot, R. Pierrot, C. Lévy, *Bull. la Société française Minéralogie Cristallogr.* **1968**, 91, 383–387.
- [52] A. M. Lamarche, A. Willsher, L. Chen, G. Lamarche, J. C. Woolley, *J. Solid State Chem.* **1991**, 94, 313–318.
- [53] K. Ito, T. Nakazawa, *Jpn. J. Appl. Phys.* **1988**, 27, 2094–2097.

- [54] A. M. Alanazi, F. Alam, A. Salhi, M. Missous, A. G. Thomas, P. O'Brien, D. J. Lewis, *RSC Adv.* **2019**, 9, 24146–24153.
- [55] Y. Xie, C. Zhang, G. Yang, J. Yang, X. Zhou, J. Ma, *J. Alloys Compd.* **2017**, 696, 938–946.
- [56] T. Shibuya, Y. Goto, Y. Kamihara, M. Matoba, K. Yasuoka, L. A. Burton, A. Walsh, *Appl. Phys. Lett.* **2014**, 104, 021912.
- [57] N. Nakayama, K. Ito, *Appl. Surf. Sci.* **1996**, 92, 171–175.
- [58] M. Ganchev, J. Iljina, L. Kaupmees, T. Raadik, O. Volobujeva, A. Mere, M. Altosaar, J. Raudoja, E. Mellikov, *Thin Solid Films* **2011**, 519, 7394–7398.
- [59] Y. B. Kishore Kumar, G. Suresh Babu, P. Uday Bhaskar, V. Sundara Raja, *Sol. Energy Mater. Sol. Cells* **2009**, 93, 1230–1237.
- [60] A. Ritscher, J. Just, O. Dolotko, S. Schorr, M. Lerch, *J. Alloys Compd.* **2016**, 670, 289–296.
- [61] N. K. Chaudhari, H. Jin, B. Kim, K. Lee, *Nanoscale* **2017**, 9, 12231–12247.
- [62] P. W. Menezes, C. Panda, S. Loos, F. Bunschei-Bruns, C. Walter, M. Schwarze, X. Deng, H. Dau, M. Driess, *Energy Environ. Sci.* **2018**, 11, 1287–1298.
- [63] T. Shinagawa, A. T. Garcia-Esparza, K. Takanabe, *Sci. Rep.* **2015**, 5, 1–21.
- [64] C. Costentin, D. K. Bediako, D. G. Nocera, J.-M. Savéant, E. C. Jones, *J. Am. Chem. Soc.* **2013**, 135, 10492–10502.
- [65] C. P. Andrieux, J. M. Dumas-Bouchiat, J. M. Savéant, *J. Electroanal. Chem. Interfacial Electrochem.* **1982**, 131, 1–35.
- [66] R. L. Doyle, M. E. G. Lyons, *Phys. Chem. Chem. Phys.* **2013**, 15, 5224.
- [67] D. E. Janney, J. M. Cowley, P. R. Buseck, *Clays Clay Miner.* **2000**, 48, 111–119.

- [68] R. K. Kukkadapu, J. M. Zachara, J. K. Fredrickson, S. C. Smith, A. C. Dohnalkova, C. K. Russell, *Am. Mineral.* **2003**, 88, 1903–1914.
- [69] S. K. Chawla, N. Sankarraman, J. H. Payer, *J. Electron Spectros. Relat. Phenomena* **1992**, 61, 1–18.
- [70] N. S. McIntyre, D. G. Zetaruk, *Anal. Chem.* **1977**, 49, 1521–1529.
- [71] H. Abdel-Samad, P. R. Watson, *Appl. Surf. Sci.* **1997**, 108, 371–377.
- [72] J. Liu, M. Zheng, X. Shi, H. Zeng, H. Xia, *Adv. Funct. Mater.* **2016**, 26, 919–930.
- [73] L. Shen, Y. Cao, Z. Du, W. Zhao, K. Lin, L. Jiang, *Appl. Surf. Sci.* **2017**, 425, 212–219.
- [74] F. Gilbert, P. Refait, F. Lévêque, C. Remazeilles, E. Conforto, *J. Phys. Chem. Solids* **2008**, 69, 2124–2130.
- [75] P. W. Menezes, A. Indra, I. Zaharieva, C. Walter, S. Loos, S. Hoffmann, R. Schlögl, H. Dau, M. Driess, *Energy Environ. Sci.* **2019**, 12, 988–999.
- [76] L. Debeer-Schmitt, K. C. Littrell, M. A. McGuire, W. M. Chance, L. Li, J. Ermentrout, A. S. Sefat, *Phys. C Supercond. its Appl.* **2017**, 534, 29–36.
- [77] H. M. Rietveld, *J. Appl. Crystallogr.* **1969**, 2, 65–71.
- [78] J. Rodriguez-Carvajal, *Abstracts of the Satellite Meeting on Powder Diffraction of the XV. Congress of the IUCr* **1990**, p. 127.
- [79] C. C. L. McCrory, S. Jung, J. C. Peters, T. F. Jaramillo, *J. Am. Chem. Soc.* **2013**, 135, 16977–16987.
- [80] C. C. L. McCrory, S. Jung, I. M. Ferrer, S. M. Chatman, J. C. Peters, T. F. Jaramillo, *J. Am. Chem. Soc.* **2015**, 137, 4347–4357.
- [81] S. Anantharaj, S. R. Ede, K. Karthick, S. Sam Sankar, K. Sangeetha, P. E. Karthik,

S. Kundu, *Energy Environ. Sci.* **2018**, 11, 744–771.

[82] R. Beltrán-Suito, P. W. Menezes, M. Driess, *J. Mater. Chem. A* **2019**, 7, 15749–15756.

[83] N. Koura, T. Tsukamoto, HiromasaShoji, T. Hotta, *Jpn. J. Appl. Phys.* **1995**, 34, 1643–1647.

[84] C. Panda, P. W. Menezes, S. Yao, J. Schmidt, C. Walter, J. N. Hausmann, M. Driess, *J. Am. Chem. Soc.* **2019**, 141, 13306–13310.

## 9. Publication 5

### Mechanochemical synthesis of $\text{Cu}_2\text{MgSn}_3\text{S}_8$ and $\text{Ag}_2\text{MgSn}_3\text{S}_8$

Eva M. Heppke, Steffen Klenner, Oliver Janka, Rainer Pöttgen and Martin Lerch

*Postprint*

*Z. Allg. Anorg. Chem.* **2019**, 646, 5-9

doi:10.1002/zaac.201900190

<https://onlinelibrary.wiley.com/doi/full/10.1002/zaac.201900190>

CC BY-NC-ND 4.0



Contribution to publication:

E. M. Heppke:	Sample preparation, structural characterization and evaluation, UV/Vis measurements and band gap determination, writing
S. Klenner:	} Magnetic and Mößbauer measurements, writing, proofreading
O. Janka:	
R. Pöttgen:	
M. Lerch:	General advice, proofreading

**Authors:** E. M. Heppke<sup>[1]</sup>, S. Klenner<sup>[2]</sup>, O. Janka<sup>[2]</sup>, R. Pöttgen<sup>[2]</sup>, M. Lerch<sup>\*[1]</sup>

<sup>1</sup>Institut für Chemie, Technische Universität Berlin, Straße des 17. Juni 135, 10623 Berlin

<sup>2</sup>Institut für Anorganische und Analytische Chemie, Universität Münster, Corrensstraße 30, 48149 Münster

\* corresponding

**Keywords:** Mechanochemical synthesis; Planetary ball mill; Thiospinels; Rietveld refinement; Magnetic properties

**Dedication:** Dedicated to Prof. Martin Jansen on the Occasion of his 75<sup>th</sup> Birthday

## 9.1. Abstract

Two new thiospinels of the type  $A_2^I B^{II} C_3^{IV} S_8^{VI}$  were successfully synthesized via a mechanochemical route from binary sulfides and sulfur.  $Cu_2MgSn_3S_8$  and  $Ag_2MgSn_3S_8$  are the first  $A_2^I B^{II} C_3^{IV} S_8^{VI}$  compounds with magnesium as divalent cation. The crystal structures of  $Cu_2MgSn_3S_8$  and  $Ag_2MgSn_3S_8$  were refined in the cubic space group  $Fd\bar{3}m$  using X-ray powder diffraction. According to UV/Vis measurements, a direct optical band gap of 1.65 eV was determined for both  $Cu_2MgSn_3S_8$  and  $Ag_2MgSn_3S_8$ . Temperature-dependent magnetic susceptibility measurements of the  $Cu_2MgSn_3S_8$  sample indicate diamagnetism. A  $^{119}Sn$  Mössbauer spectrum confirms the tetravalent state of tin, underlining the electron-precise description.

## 9.2. Introduction

Some complex Cu- and Ag-based thiospinels with the general formula  $A_2^I B^{II} C_3^{IV} S_8^{VI}$  have been described in literature. Most of these compounds are associated with tin such as  $Cu_2MSn_3S_8$  with  $M = Mn, Fe, Co, Ni$  or  $Ag_2MnSn_3S_8$  [1–8]. In addition, titanium-containing compounds [9, 10] and even one zirconium analogue [11] are hitherto known. The cation-deficient structure of the compounds  $A_2^I B^{II} C_3^{IV} S_8^{VI}$  offers the possibility of  $Li^+$  intercalation and therefore these phases are interesting materials for Li-battery cathodes [2, 4, 7, 12]. The compounds  $A_2^I B^{II} C_3^{IV} S_8^{VI}$  have been described in the cubic space group  $Fd\bar{3}m$  [2–4, 7, 9–12] or the tetragonal space group  $I4_1/a$  [1, 5]. Copper deficiency is also mentioned for this class of materials [13, 14]. By mechanochemical milling, two new compounds of the type  $A_2^I B^{II} C_3^{IV} S_8^{VI}$  have been successfully synthesized. The main focus of the present study concerns the synthesis, crystal structure, and magnetic behavior of  $Cu_2MgSn_3S_8$  and  $Ag_2MgSn_3S_8$ .

## 9.3. Results and Discussion

### Chemical analysis and crystal structure

Two new phase-pure thiospinels,  $Cu_2MgSn_3S_8$  and  $Ag_2MgSn_3S_8$ , were successfully synthesized via a mechanochemical procedure with a subsequent annealing step in  $H_2S$ -atmosphere. Both compounds crystallize in the cubic space group type  $Fd\bar{3}m$  with  $a = 10.4173(2)$  and  $a = 10.6938(2)$  Å, respectively. The composition of  $Cu_2MgSn_3S_8$  /  $Ag_2MgSn_3S_8$  was confirmed by energy dispersive X-ray spectroscopy and combustion analysis and is summarized in Table 9.1. X-ray powder diffraction patterns with the results of the Rietveld refinements are depicted in Figure 9.1 and Figure 9.2. Details and

refined structural parameters are listed in Table 9.2, Table 9.3, and Table 9.4. The experimental diffraction patterns are in good agreement with the calculated ones, reflected by residual values of  $R_{\text{wp}} = 0.022$  for  $\text{Cu}_2\text{MgSn}_3\text{S}_8$  and  $R_{\text{wp}} = 0.032$  for  $\text{Ag}_2\text{MgSn}_3\text{S}_8$ . The total occupancies of the cation positions  $8a$  and  $16d$  were fixed. Wyckoff position  $16d$  is occupied statistically by Mg and Sn. Relatively high Debye-Waller factors were obtained for Cu and Ag at position  $8a$  (Table 9.3, Table 9.4). This has also been observed for monovalent cations in other quaternary thiospinels like  $\text{Cu}_2\text{CdSn}_3\text{S}_8$  [5] or other crystal structures of quaternary chalcogenides, for example  $\text{Ag}_2\text{In}_2\text{GeSe}_6$  [15]. As mentioned in the introduction, some  $\text{A}_2^{\text{I}}\text{B}^{\text{II}}\text{C}_3^{\text{IV}}\text{S}_8^{\text{VI}}$ -type phases such as  $\text{Cu}_2\text{CdSn}_3\text{S}_8$  [5] are reported to crystallize in the tetragonal space group  $I4_1/a$ . However, structural refinements for  $\text{Cu}_2\text{MgSn}_3\text{S}_8$  and  $\text{Ag}_2\text{MgSn}_3\text{S}_8$  in lower tetragonal symmetry were also performed but no improvement of the refinement quality has been achieved.

**Table 9.1.:** Phase composition of  $\text{Cu}_2\text{MgSn}_3\text{S}_8$  and  $\text{Ag}_2\text{MgSn}_3\text{S}_8$  calculated from EDX and elemental analysis.

	$\text{Cu}_2\text{MgSn}_3\text{S}_8$		$\text{Ag}_2\text{MgSn}_3\text{S}_8$	
	ideal [at-%]	measured [at-%]	ideal [at-%]	measured [at-%]
Cu	14.3	15.1	Ag	14.3
Mg	7.1	6.8	Mg	7.1
Sn	21.4	24.6	Sn	21.4
$S_{\text{EDX}}$	57.1	53.9	$S_{\text{EDX}}$	57.1
$S_{\text{EA}}$	57.1	55.4	$S_{\text{EA}}$	57.1

**Table 9.2.:** Results of the Rietveld refinements for  $\text{Cu}_2\text{MgSn}_3\text{S}_8$  and  $\text{Ag}_2\text{MgSn}_3\text{S}_8$  (standard deviations in parenthesis).

Empirical formula	$\text{Cu}_2\text{MgSn}_3\text{S}_8$	$\text{Ag}_2\text{MgSn}_3\text{S}_8$
Structure type	Spinel	
Space group	$Fd\bar{3}m$	
Crystal system	cubic	
$Z$	4	
$a$ , Å	10.4173(2)	10.6938(2)
$V$ , Å <sup>3</sup>	1130.49(4)	1222.92(4)
Calculated density, g/cm <sup>3</sup>	4.49	4.63
Diffractometer	PANalytical X'Pert MDP Pro	
Radiation	Cu- $K_\alpha$ radiation	
Wavelength, Å	$\lambda_1 = 1.54056$ , $\lambda_2 = 1.54439$	
$R_p$	0.0161	0.0237
$R_{\text{wp}}$	0.0215	0.0324
$R_{\text{Bragg}}$	0.0272	0.0212
$S$	1.23	1.36

**Table 9.3.:** Refined atomic parameters for  $\text{Cu}_2\text{MgSn}_3\text{S}_8$  (standard deviations in parenthesis).

Atom	Wyckoff	$x$	$y$	$z$	s.o.f.	$B_{\text{iso}}, \text{\AA}^2$
Cu1	$8a$	1/8	1/8	1/8	1	2.01(3)
Mg1	$16d$	1/2	1/2	1/2	0.25	0.46(2)
Sn1	$16d$	1/2	1/2	1/2	0.75	0.46(2)
S1	$32e$	0.74624(9)	$x$	$x$	1	1

**Table 9.4.:** Refined atomic parameters for  $\text{Ag}_2\text{MgSn}_3\text{S}_8$  (standard deviations in parenthesis).

Atom	Wyckoff	$x$	$y$	$z$	s.o.f.	$B_{\text{iso}}, \text{\AA}^2$
Ag1	$8a$	1/8	1/8	1/8	1	1.83(3)
Mg1	$16d$	1/2	1/2	1/2	0.25	0.78(4)
Sn1	$16d$	1/2	1/2	1/2	0.75	0.78(4)
S1	$32e$	0.74097(11)	$x$	$x$	1	1

The spinel-type crystal structures of  $\text{Cu}_2\text{MgSn}_3\text{S}_8$  and  $\text{Ag}_2\text{MgSn}_3\text{S}_8$  are composed of a cubic closest-packed arrangement of sulfide anions. One eighth of the tetrahedral voids is occupied by Cu/Ag which are coordinated by four sulfur anions and form  $[\text{CuS}_4]^{7-}$  and  $[\text{AgS}_4]^{7-}$  tetrahedra, respectively. Half of the octahedral voids are filled statistically with Mg and Sn. The Cu-/Ag-centered sulfide tetrahedra share corners with the octahedra which are edge-shared between themselves. The sulfur anion is coordinated by 3 kinds of atoms including 1 Cu/Ag and 3 Mg/Sn with distances varying from 2.3233(10) to 2.5658(10) Å for  $\text{Cu}_2\text{MgSn}_3\text{S}_8$  and 2.4825(13) to 2.5805(13) Å for  $\text{Ag}_2\text{MgSn}_3\text{S}_8$  (Table 9.5). Due to the larger ionic radius of  $\text{Ag}^+$  with 1.14 Å for a coordination number of four compared to that of  $\text{Cu}^+$  with 0.74 Å [16], the unit cell of  $\text{Ag}_2\text{MgSn}_3\text{S}_8$  is larger than that of  $\text{Cu}_2\text{MgSn}_3\text{S}_8$ . The unit cells of  $\text{Cu}_2\text{MgSn}_3\text{S}_8$  and  $\text{Ag}_2\text{MgSn}_3\text{S}_8$  are smaller as compared to those of the corresponding Cd-bearing Cu- and Ag-compounds which can be simply explained by the smaller ionic radii of  $\text{Mg}^{2+}$  (six-fold coordination) of 0.86 Å compared to that of octahedrally surrounded  $\text{Cd}^{2+}$  with 1.09 Å [16]. The interatomic distances Cu/Ag–S and (Mg/Sn)–S in  $\text{Cu}_2\text{MgSn}_3\text{S}_8$  and  $\text{Ag}_2\text{MgSn}_3\text{S}_8$  (Table 9.5) correlate well with those observed for  $\text{Cu}_2\text{CdSn}_3\text{S}_8$  (Cu–S: 2.30(1) Å; (Cd/Sn)–S: 2.61(2) Å) [5] and  $\text{Ag}_2\text{CdSn}_3\text{S}_8$  (Ag–S: 2.489(3) Å; (Cd/Sn)–S: 2.602(3) Å) [6] with slightly larger Cu- and Ag-centered sulfide tetrahedra and smaller Mg/Sn-centered sulfide octahedra.

**Table 9.5.:** Interatomic distances in  $\text{Cu}_2\text{MgSn}_3\text{S}_8$  and  $\text{Ag}_2\text{MgSn}_3\text{S}_8$  (standard deviations in parenthesis).

$\text{Cu}_2\text{MgSn}_3\text{S}_8$		$\text{Ag}_2\text{MgSn}_3\text{S}_8$	
Cu-S	2.3233(10) Å	Ag-S	2.4825(13) Å
(Mg/Sn)-S	2.5658(10) Å	(Mg/Sn)-S	2.5805(13) Å

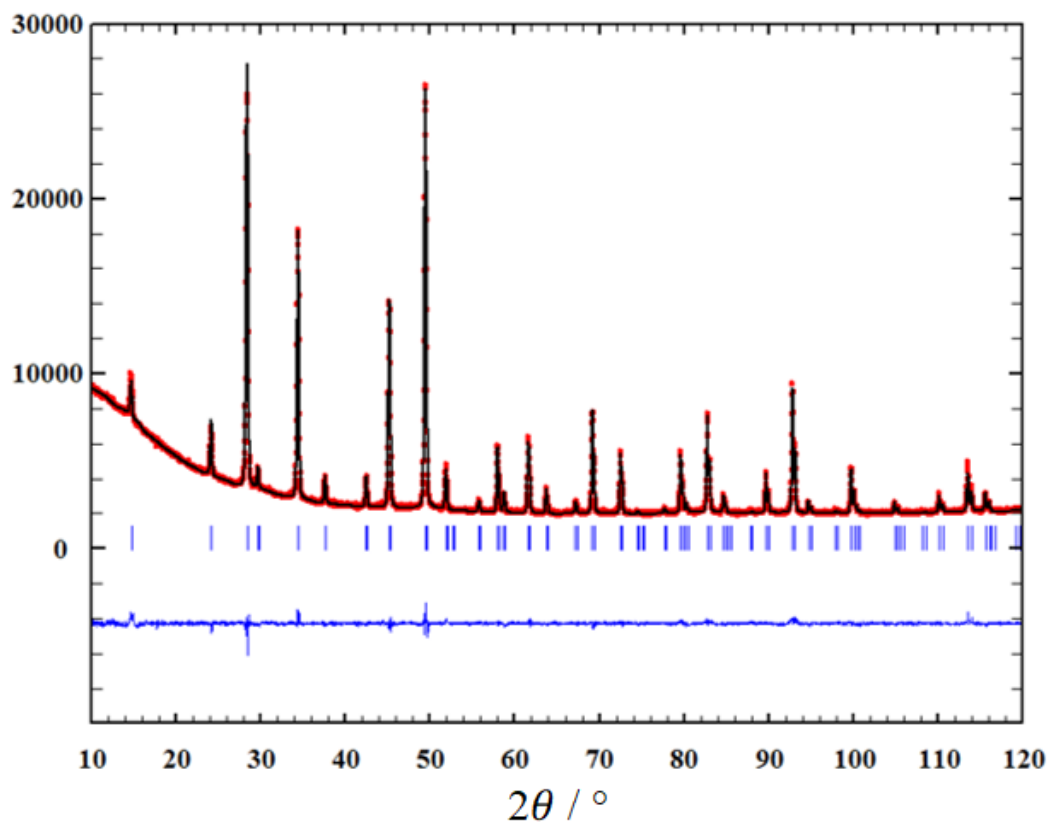


**Figure 9.1.:** X-ray diffraction pattern of  $\text{Cu}_2\text{MgSn}_3\text{S}_8$  with the results of the Rietveld refinement.

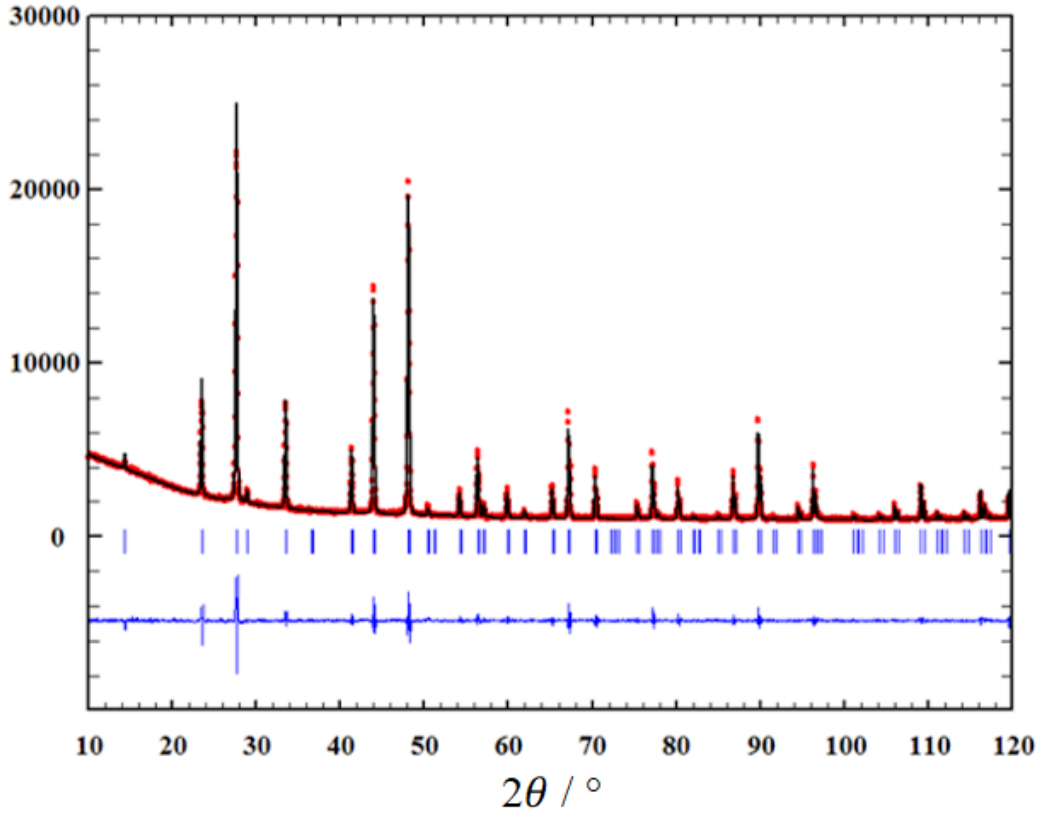


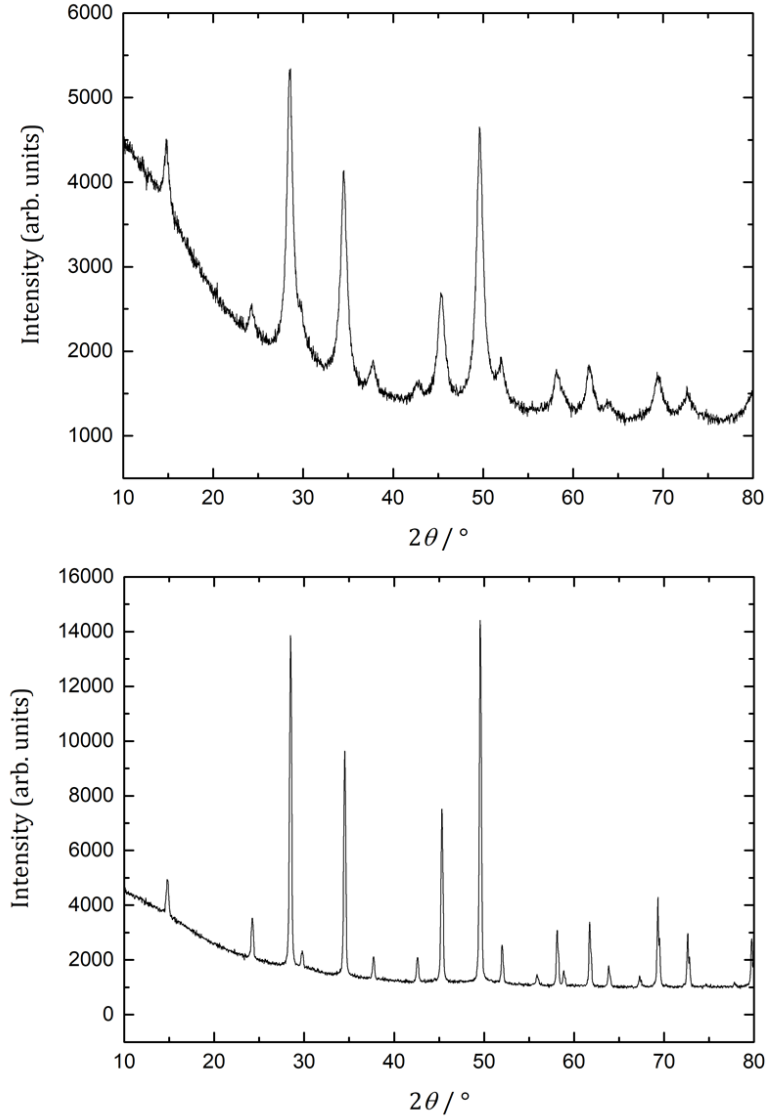
**Figure 9.2.:** X-ray diffraction pattern of  $\text{Ag}_2\text{MgSn}_3\text{S}_8$  with the results of the Rietveld refinement.

In order to give more detailed information on the formation of well-crystalline powders, some details for  $\text{Cu}_2\text{MgSn}_3\text{S}_8$  are presented in the following: first of all, it can be seen that the thiospinel was formed during milling (Figure 9.3). Broadened reflections clearly point to small particle sizes. Consequently, the crystallite sizes of the milled and annealed samples were calculated using the Scherrer equation [17]:

$$\delta(2\theta) = K\lambda/(L\cos\theta_0), \quad (9.1)$$

where  $\delta(2\theta)$  is the full width at half maximum (FWHM),  $K$  the Scherrer form factor (for this determination a factor of 0.9 was used),  $\lambda$  the wavelength,  $L$  the mean size of the crystallites, and  $\theta_0$  the diffraction angle. The crystallites after the milling procedure are rather small (in the range of  $9.3\pm 0.4$  nm to  $11.0\pm 0.3$  nm). After the subsequent annealing step, described in the experimental part, the mean crystallite sizes for  $\text{Cu}_2\text{MgSn}_3\text{S}_8$  are in the range from  $31.8\pm 0.3$  nm to  $35.1\pm 0.3$  nm. In comparison to  $\text{Cu}_2\text{MgSn}_3\text{S}_8$ , smaller particles were calculated for  $\text{Ag}_2\text{MgSn}_3\text{S}_8$  after the milling

treatment (in the range of  $4.7\pm 0.7$  nm to  $5.9\pm 0.2$  nm) while similar crystallite sizes were observed after the annealing step (in the range of  $32.7\pm 0.4$  nm to  $35.6\pm 0.5$  nm).



hkl	$2\theta$ [°]	Crystallite size after milling [nm]	Crystallite size after annealing [nm]
311	28.5	$11.0\pm 0.3$	$31.8\pm 0.3$
400	34.5	$9.3\pm 0.4$	$33.6\pm 0.3$
333	45.3	$9.3\pm 0.3$	$35.1\pm 0.3$

**Figure 9.3.:** X-ray diffraction patterns of milled (top) and annealed (middle)  $\text{Cu}_2\text{MgSn}_3\text{S}_8$  samples, supplemented by a Table presenting the calculated crystallite sizes for selected reflections.

## UV/Vis spectroscopy

The optical properties of black-colored  $\text{Cu}_2\text{MgSn}_3\text{S}_8$  and  $\text{Ag}_2\text{MgSn}_3\text{S}_8$  powders were measured in diffuse reflectance geometry. The optical band gaps were calculated using the Tauc plot method [18, 19]. A direct optical band gap of 1.65 eV was determined for both Mg-containing compounds whereas narrower indirect optical band gaps of 1.42 eV for  $\text{Cu}_2\text{MgSn}_3\text{S}_8$  and 1.40 eV for  $\text{Ag}_2\text{MgSn}_3\text{S}_8$  were observed (Figure 9.4).

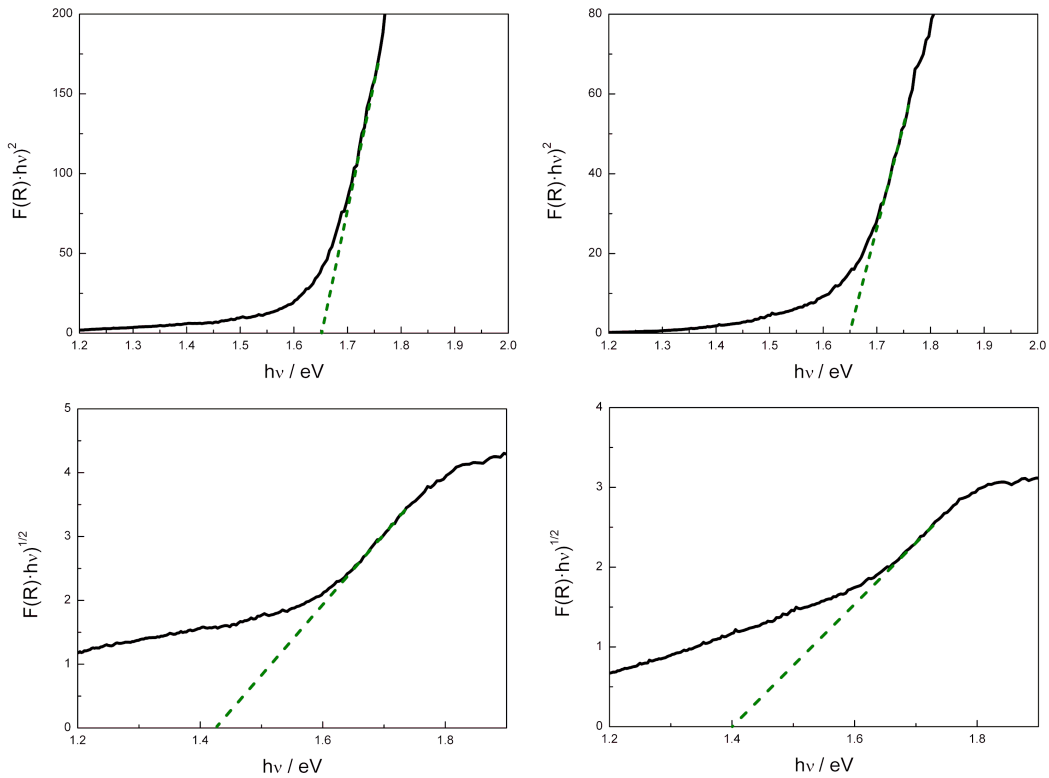


**Figure 9.4.:** UV/Vis spectra of  $\text{Cu}_2\text{MgSn}_3\text{S}_8$  (left) and  $\text{Ag}_2\text{MgSn}_3\text{S}_8$  (right) with Tauc plot determination of the direct (top) and indirect (bottom) optical band gaps.

## Magnetic properties

The temperature dependence of the magnetic susceptibility of the polycrystalline  $\text{Cu}_2\text{MgSn}_3\text{S}_8$  sample is presented in Figure 9.5. Down to about 50 K we observe almost temperature independent behavior. The room temperature value of  $-150 \times 10^{-6} \text{ emu} \cdot \text{mol}^{-1}$  indicates diamagnetism, i. e. closed-shell behavior in agreement with the electron-precise description. The increase of the susceptibility towards lower temperature results from small amounts of paramagnetic impurity phases (Curie tail).

Since we deal with an electron-precise compound, one can compare the experimentally determined susceptibilities with those calculated from diamagnetic increments [20]. Using the increments (in units of  $-106 \text{ emu}\cdot\text{mol}^{-1}$ ) for  $\text{Cu}^+$  (12),  $\text{Mg}^{2+}$  (5),  $\text{Sn}^{4+}$  (16) and  $\text{S}^{2-}$  (30) we obtain a value of  $-307 \times 10^{-6} \text{ emu}\cdot\text{mol}^{-1}$  for the intrinsic diamagnetic contribution of  $\text{Cu}_2\text{MgSn}_3\text{S}_8$ . The experimental value is of the same order of magnitude. Due to the small paramagnetic impurity phase we observe a smaller experimental value.

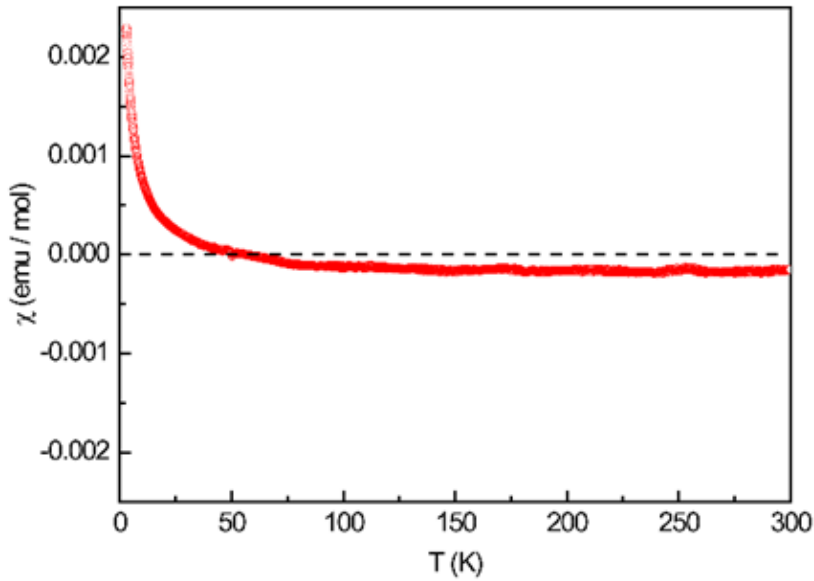


**Figure 9.5.:** Temperature dependence of the magnetic susceptibility  $\chi$  of  $\text{Cu}_2\text{MgSn}_3\text{S}_8$  measured in ZFC mode with an applied magnetic field strength of 10 kOe.

### Mössbauer spectroscopy

The experimental and simulated  $^{119}\text{Sn}$  Mössbauer spectrum of  $\text{Cu}_2\text{MgSn}_3\text{S}_8$  (6 K data) is presented in Figure 9.6. The corresponding fitting parameters are listed in Table 9.6. The spectrum could reliably be reproduced with a single signal with a small quadrupole splitting contribution, most likely a consequence of the mixed site occupancy on the 16*d* position, generating small distortions. The isomer shift value is in excellent agreement with thioannates (IV) [21]. The slightly enhanced line widths parameter also accounts for domain formation, resulting from the 16*d* mixed occupied site.

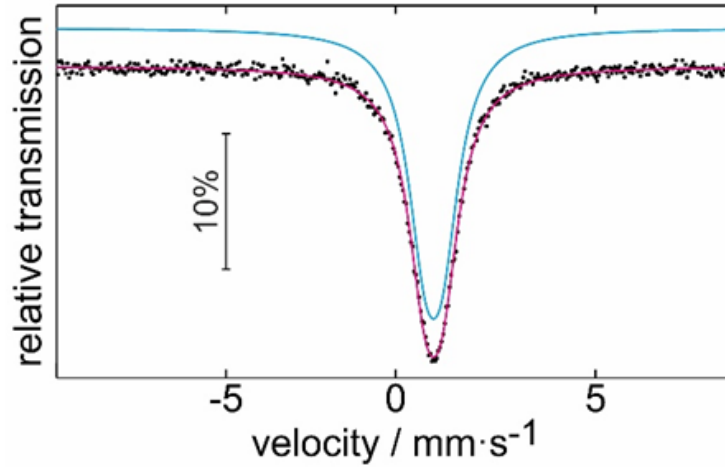


**Figure 9.6.:** Experimental (black dots) and simulated (red line)  $^{119}\text{Sn}$  Mössbauer spectrum of  $\text{Cu}_2\text{MgSn}_3\text{S}_8$  at 6 K.

**Table 9.6.:** Fitting parameters of the  $^{119}\text{Sn}$  Mössbauer spectroscopic measurement on  $\text{Cu}_2\text{MgSn}_3\text{S}_8$  at 6 K.  $\delta$  = isomer shift,  $\Delta E_Q$  = electric quadrupole splitting,  $\Gamma$  = experimental line width.

compound	$\delta / \text{mm} \cdot \text{s}^{-1}$	$\Delta E_Q / \text{mm} \cdot \text{s}^{-1}$	$\Gamma / \text{mm} \cdot \text{s}^{-1}$
$\text{Cu}_2\text{MgSn}_3\text{S}_8$	1.113(3)	0.512(14)	1.254(14)

## 9.4. Conclusions

Two new thiospinels of general formula  $\text{A}_2^{\text{I}}\text{B}^{\text{II}}\text{C}_3^{\text{IV}}\text{S}_8^{\text{VI}}$  were synthesized via a two step mechanochemical synthesis route.  $\text{Cu}_2\text{MgSn}_3\text{S}_8$  and  $\text{Ag}_2\text{MgSn}_3\text{S}_8$  were formed after milling in a high energy planetary ball Mill. Powders of good crystallinity were obtained after annealing in  $\text{H}_2\text{S}$ -atmosphere at 823 K. X-ray diffraction studies supported by EDX analyses show that phase-pure  $\text{Cu}_2\text{MgSn}_3\text{S}_8$  and  $\text{Ag}_2\text{MgSn}_3\text{S}_8$  samples have been synthesized. All compounds crystallize in the cubic space group  $Fd\bar{3}m$  with a statistical distribution of Mg and Sn at Wyckoff position 16*d*. The direct optical band gap is determined to 1.65 eV for both compounds. These experiments again show the large potential of mechanochemical routes for synthesizing complex sulfides. Magnetic susceptibility studies and  $^{119}\text{Sn}$  Mössbauer spectra manifest the electron-precise description and thio-stannate (IV) character.

## 9.5. Experimental Section

### Synthesis

The quaternary thiospinels  $\text{Cu}_2\text{MgSn}_3\text{S}_8$  and  $\text{Ag}_2\text{MgSn}_3\text{S}_8$  were synthesized in a high energy planetary Mono Mill PULVERISETTE 7 (Fritsch, Idar-Oberstein, Germany) with a subsequent annealing step in a tube furnace. Stoichiometric amounts of the corresponding binary sulfides ( $\text{Ag}_2\text{S}$  (Schuchardt),  $\text{CuS}$ ,  $\text{MgS}$ ,  $\text{SnS}$ ) and sulfur (Fluka, 99.99%) were filled in a 45 mL zirconia grinding beaker with six zirconia balls and ground at a rotational speed of 450 rpm for four hours. In order to obtain highly crystalline powders, the thiospinels were annealed at 823 K for three hours under flowing  $\text{H}_2\text{S}$  gas after milling. An 0.1 M  $\text{Cu}(\text{NO}_3)_2$ -solution and  $\text{H}_2\text{S}$  gas (Air Liquide, 99.5%) were used for the precipitation of  $\text{CuS}$ . For  $\text{MgS}$ , amorphous  $\text{MgO}$  was prepared by a modified Pechini method [22] followed by sulfidation of the obtained magnesia in  $\text{H}_2\text{S}$ -atmosphere at 1023 K for three hours.  $\text{SnS}$  was synthesized using a high-temperature solid-state synthesis route based on the elements  $\text{Sn}$  (Merck, 99.9%) and  $\text{S}$  (Fluka, 99.99%) as starting materials (evacuated and sealed  $\text{SiO}_2$ -ampoules).

### Chemical and structural characterization

A Panalytical X'Pert PRO diffractometer with  $\text{Cu-}K_\alpha$  radiation (Bragg-Brentano geometry) was used for the X-ray diffraction measurements. The diffraction data was obtained over an angular range of 10–120° with a step size of 0.026° and an exposure time of 60 s at each point. Rietveld refinements [23] were carried out using the program FULLPROF Suite [24] by applying a pseudo-Voigt function. For elementary analysis, energy dispersive X-ray spectroscopy (EDX) was carried out using a DSM 982 GEMINI spectrometer (Carl Zeiss AG, Oberkochen, Germany) equipped with a XFlash 6|60 detector (Bruker, Billerica, USA). EDX measurements were performed at the Zentrum für Elektronenmikroskopie (ZELMI) of TU Berlin. For the determination of the phase composition using EDX analysis a device error of 5% is presumed. Furthermore, the sulfur content of both samples was determined using a FLashEA 1112 elemental analyzer (Thermo Scientific™, Waltham, USA) with a given device error of about 2%. Additional measurements were carried out with a RIGAKU SmartLab 3 kW system equipped with a  $K_{\alpha 1}$  unit (Johansson-type Ge crystal,  $\text{Cu-}K_{\alpha 1}$  radiation,  $\lambda = 1.54060 \text{ \AA}$ ). Further details of the crystal structures investigations may be obtained from the Fachinformationszentrum Karlsruhe, 76344 Eggenstein-Leopoldshafen, Germany (Fax: +49-7247-808-666; E-Mail: [crysdata@fiz-karlsruhe.de](mailto:crysdata@fiz-karlsruhe.de), [http://www.fiz-karlsruhe.de/request for deposited data.html](http://www.fiz-karlsruhe.de/request%20for%20deposited%20data.html)) on quoting the depository numbers CSD-1946219 and CSD-1946220.

### UV/Vis measurements

UV/Vis measurements in diffuse reflectance mode were performed using an Evolution 220 UV/Vis spectrometer (Thermo Scientific™, Waltham, USA) equipped with a Xenon Flash lamp and a dual silicon photodiode detector. The obtained spectra were converted by the Kubelka-Munk function to absorption spectra, the optical band gaps were determined using the Tauc plot method [18, 19]. The standard deviation for  $E_g$  was estimated close to  $\pm 0.5$  eV.

### Magnetic properties

$\text{Cu}_2\text{MgSn}_3\text{S}_8$  was used as a polycrystalline powder, packed in a PE capsule and attached to the sample holder rod of a Vibrating Sample Magnetometer unit (VSM) for measuring the magnetization  $M(T,H)$  in a Quantum Design Physical-Property-Measurement-System (PPMS). The sample was investigated in the temperature range of 2.5–300 K with an applied external magnetic field of 10 kOe.

### Mössbauer spectroscopy

A  $\text{Ca}^{119\text{m}}\text{SnO}_3$  source was used for the  $^{119}\text{Sn}$  Mössbauer spectroscopic investigation. The sample was placed within a thin-walled PMMA container. A palladium foil of 0.05 mm thickness was used to reduce the tin K X-rays concurrently emitted by this source. The measurement was conducted in a continuous flow cryostat system (Janis Research Co LLC) at 6 K. The spectrum was fitted with the Normos-90 software package [25].

## 9.6. Acknowledgements

Special thanks to the Zentrum für Elektronenmikroskopie (ZELMI) of the TU Berlin giving access to EDX measurements. All EDX measurements were carried out by Dr. Stefan Berendts (TU Berlin). Combustion analysis were performed by Juana Krone (TU Berlin).

## 9.7. Bibliography

- [1] J. C. Jumas, E. Philippot, M. Maurin. *Acta Crystallogr. B* **1979**, 35, 2195–2197.
- [2] P. Lavela, J. L. Tirado, J. Morales, J. Olivier-Fourcade, J. C. Jumas. *J. Mater. Chem.* **1996**, 6, 41–47.

- [3] G. Garg, S. Bobev, A. K. Ganguli. *J. Alloys Compd.* **2001**, 327, 113–115.
- [4] G. Garg, K. V. Ramanujachary, S. E. Loffland, M. V. Lobanov, M. Greenblatt, T. Maddanimath, K. Vijayamohanan, A. K. Ganguli. *J. Solid State Chem.* **2003**, 174, 229–232.
- [5] S. I. Chykhrij, L. V. Sysa, O. V. Parasyuk, L. V. Piskach. *J. Alloys Compd.* **2000**, 307, 124–126.
- [6] O. V. Parasyuk, I. D. Olekseyuk, L. V. Piskach, S. V. Volkov, V. I. Pekhnyo. *J. Alloys Compd.* **2005**, 399, 173–177.
- [7] M. A. Cochez, J. C. Jumas, P. Lavela, J. Morales, J. Olivier-Fourcade, J. L. Tirado. *J. Power Sources* **1996**, 62, 101–105.
- [8] J. Yajima, E. Ohta, Y. Kanazawa. *Mineral J.* **1991**, 15, 222–232.
- [9] C. Branci, M. Womes, P. E. Lippens, J. Olivier-Fourcade, J. C. Jumas. *J. Solid State Chem.* **2000**, 150, 363–370.
- [10] V. P. Sachanyuk, A. O. Fedorchuk, I. D. Olekseyuk, O. V. Parasyuk. *Mater. Res. Bull.* **2007**, 42, 143–148.
- [11] Z. Kormosh, A. Fedorchuk, K. Wojciechowski, N. Tataryn, O. Parasyuk. *Mater. Sci. Eng. C* **2011**, 31, 540–544.
- [12] C. Branci, J. Sarradin, J. Olivier-Fourcade, J. C. Jumas. *J. Power Sources* **1999**, 81-82, 282–285.
- [13] G. Garg, S. Bobev, A. Roy, J. Ghose, D. Das, A. K. Ganguli. *Mater. Res. Bull.* **2001**, 36, 2429–2435.
- [14] G. Garg, S. Bobev, A. K. Ganguli. *Solid State Ion.* **2002**, 146, 195–198.
- [15] O. V. Krykhovets, L. V. Sysa, I. D. Olekseyuk, T. Glowiyak. *J. Alloys Compd.* **1999**, 287, 181–184.

- [16] R. D. Shannon. *Acta Crystallogr. A* **1976**, 32, 751–767.
- [17] P. Debye, P. Scherrer. *Nachrichten von der Gesellschaft der Wissenschaften zu Göttingen, Mathematisch-Physikalische Klasse* **1918**, 101–120.
- [18] J. Tauc, R. Grigorovici, A. Vanacu. *Phys. Status Solidi B* **1966**, 15, 627–637.
- [19] J. Tauc. *Mater. Res. Bull.* **1968**, 3, 37–46.
- [20] G. A. Bain, J. F. Berry. *J. Chem. Educ.* **2008**, 85, 532–536.
- [21] P. E. Lippens. *Phys. Rev. B* **1999**, 60, 4576–4586.
- [22] M. P. Pechini. US Patent No. 3330697 1967.
- [23] H. M. Rietveld. *J. Appl. Crystallogr.* **1969**, 2, 65–71.
- [24] J. Rodriguez-Carvajal. *Abstracts of the Satellite Meeting on Powder Diffraction of the XV. Congress of the IUCr* **1990**, p. 127.
- [25] R. A. Brand. WINNORMOS for IGOR6, version for IGOR 6.2 or above: 22.02.2017, Universität Duisburg, Duisburg, Germany **2017**.

## 10. Publication 6

### New compounds of the $\text{Li}_2\text{MSn}_3\text{S}_8$ type

Eva M. Heppke, Shamini Mahadevan and Martin Lerch

*Postprint*

*Z. Naturforsch. B* **2020**, 75(6-7), 625-631

doi:10.1515/znb-2020-0050

<https://www.degruyter.com/view/journals/znb/75/6-7/article-p625.xml>

Contribution to publication:

- E. M. Heppke: Sample preparation, structural characterization and evaluation, UV/Vis measurements and band gap determination, writing
- S. Mahadevan: Sample preparation, structural characterization and evaluation
- M. Lerch: General advice, proofreading

**Authors:** E. M. Heppke<sup>[1]</sup>, S. Mahadevan<sup>[1]</sup>, M. Lerch<sup>\*[1]</sup>

<sup>1</sup>Institut für Chemie, Technische Universität Berlin, Straße des 17. Juni 135, 10623 Berlin

\* corresponding

**Keywords:** lithium; thiospinels; mechanochemical synthesis; Rietveld refinement; band gap determination

Eva M. Heppke, Shamini Mahadevan and Martin Lerch\*

# New compounds of the $\text{Li}_2\text{MSn}_3\text{S}_8$ type

<https://doi.org/10.1515/znb-2020-0050>

Received April 16, 2020; accepted April 27, 2020; published online July 6, 2020

**Abstract:** The substitution of Cu/Ag by lithium in complex thiospinels with the general formula  $A^I_2B^{II}C^{IV}_3X^{VI}_8$  was achieved by ball milling and a subsequent annealing step in an atmosphere of  $\text{H}_2\text{S}$ . Four hitherto unknown compounds  $\text{Li}_2\text{MSn}_3\text{S}_8$  with  $M = \text{Mg, Mn, Fe, Ni}$  were obtained without side phases and have been structurally investigated. From X-ray powder diffraction experiments, space group  $Fd\bar{3}m$  and a spinel-type structure are suggested. In these so-called normal spinels, lithium occupies one eighth of the tetrahedral voids (Wyckoff position  $8a$ ) of the cubic closest packing of the sulfide ions whereas  $M$  and Sn can be found on one half of the octahedral voids (Wyckoff position  $16d$ ).

**Keywords:** band gap determination; lithium; mechanochemical synthesis; Rietveld refinement; thiospinels.

## 1 Introduction

Quaternary thiospinels of the type  $A^I_2B^{II}C^{IV}_3X^{VI}_8$  with copper or silver as monovalent cations have been described in the literature [1–11]. The largest group among this class of materials are Sn-containing compounds. However, also a few thiospinels containing titanium [6, 10] or zirconium [11] have been synthesized. Most of the reported compounds crystallize in space group  $Fd\bar{3}m$  while a few examples such as  $\text{Cu}_2\text{CdSn}_3\text{S}_8$  exhibit space groups with lower symmetry, for example  $I4_1/a$  [1, 5]. Due to the similar atomic arrangements in the crystal structures with the space groups  $Fd\bar{3}m$  and  $I4_1/a$  it can be difficult to distinguish between these groups unambiguously using conventional X-ray powder techniques. For some  $A^I_2B^{II}C^{IV}_3X^{VI}_8$  compounds, Li<sup>+</sup> intercalation experiments were carried out [3, 4, 8, 12]. These materials may be promising cathode materials for lithium batteries. In this contribution we present the results

of our work concerning Cu/Ag substitution by lithium in  $A^I_2B^{II}C^{IV}_3X^{VI}_8$  thiospinels, which has afforded five compounds  $\text{Li}_2\text{MSn}_3\text{S}_8$  with  $M = \text{Mg, Mn, Fe, Co, Ni}$ . We used a mechanochemical route followed by an annealing step under flowing  $\text{H}_2\text{S}$  gas.

## 2 Results and discussion

Four new thiospinels  $\text{Li}_2\text{MSn}_3\text{S}_8$  with  $M = \text{Mg, Mn, Fe, Ni}$  have been prepared without side phase by mechanochemical synthesis. Samples of the corresponding Co compound always contained  $\text{CoS}_2$  and are not presented here in detail. The crystallinity of the obtained powders was increased by a subsequent annealing procedure. The cation contents of the  $\text{Li}_2\text{MSn}_3\text{S}_8$  phases were determined by inductively coupled plasma optical emission spectroscopy (ICP-OES) analysis and are in accordance with the molar ratio derived from the chemical formulas (Table 1). No loss of  $\text{Li}_2\text{S}$  was observed after annealing up to  $T = 550^\circ\text{C}$ .

Rietveld refinements were performed for space groups  $Fd\bar{3}m$  and  $I4_1/a$ . Convergence problems occurred during the refinements in the tetragonal space group concerning the positions of the sulfur atoms, while successful refinements were achieved in cubic space group  $Fd\bar{3}m$ . Figures 1–4 show the powder diffraction patterns with the results of the Rietveld refinements. Details are summarized in Table 2. Tables 3–6 list the atomic and structural parameters for each compound. The diffraction patterns point to phase purity for  $\text{Li}_2\text{MSn}_3\text{S}_8$  with  $M = \text{Mg, Mn, Fe, Ni}$ . The total occupancies of cations on the Wyckoff positions  $8a/16d$  were fixed to the ideal cation value which was proofed by ICP-OES analysis. The Debye Waller factors of Li and S were also set and kept fixed during the refinements. As described in the literature, monovalent cations in this structure type [5] or related chalcogenide phases [13] show high Debye–Waller factors. Therefore, the Debye–Waller factor for Li on position  $8a$  was set to a value of 2, keeping in mind that lithium is a poor X-ray scatterer. Mg/Mn/Fe/Ni, and Sn are located on Wyckoff position  $16d$  in a molar ratio of 1:3.  $\text{Li}_2\text{MgSn}_3\text{S}_8$  and  $\text{Li}_2\text{FeSn}_3\text{S}_8$  are not stable in air; therefore, capton foils were used for the X-ray powder diffraction experiments with these two compounds resulting in a “hill” in the range of  $2\theta = 15\text{--}30^\circ$  of the diffraction patterns.

One computational study on the investigation of the probable crystal structure of  $\text{Li}_2\text{ZnSn}_3\text{S}_8$  is mentioned in literature [14]. Unfortunately, attempts to synthesize this

\*Corresponding author: Martin Lerch, Institut für Chemie, Technische Universität Berlin, Straße des 17. Juni 135, 10623 Berlin, Germany, E-mail: martin.lerch@tu-berlin.de

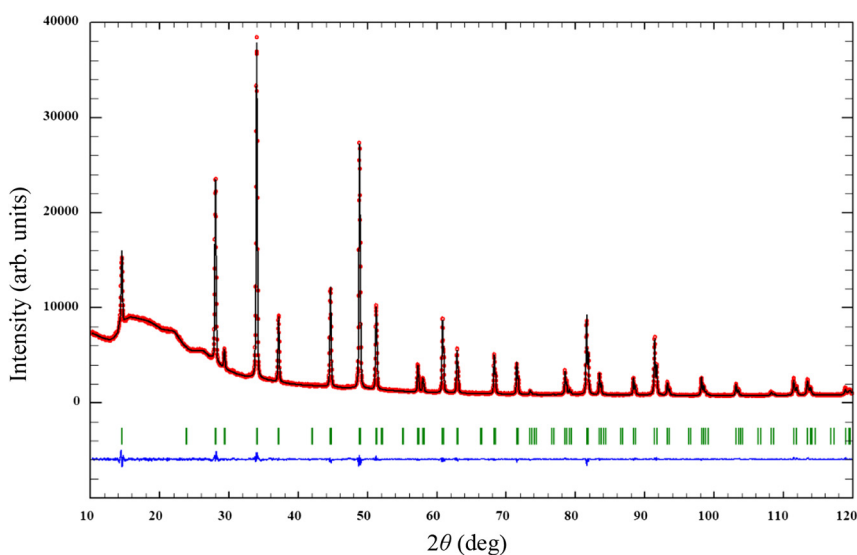
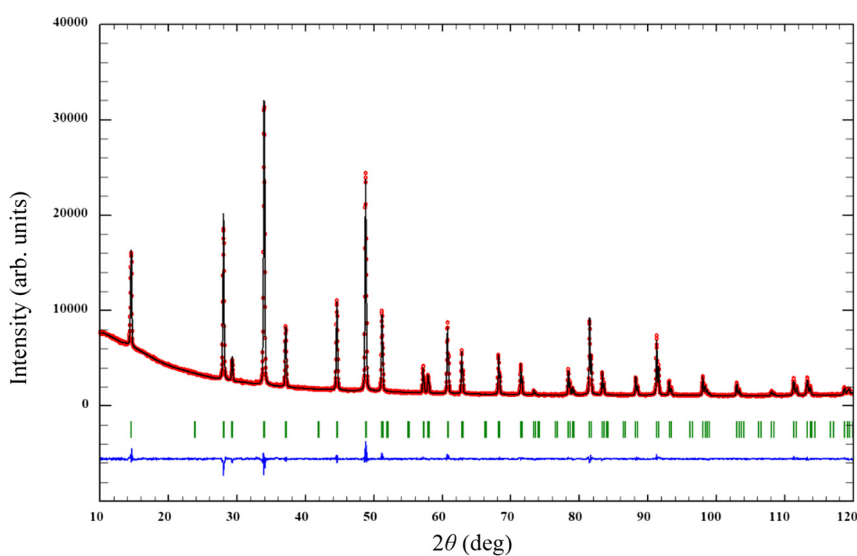
Eva M. Heppke and Shamini Mahadevan: Institut für Chemie, Technische Universität Berlin, Straße des 17. Juni 135, 10623 Berlin, Germany

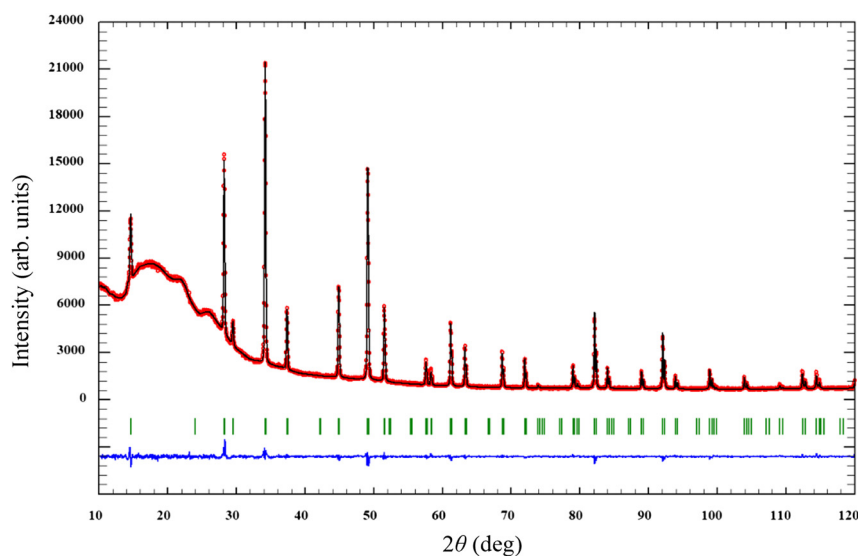
**Table 1:** Cation contents of  $\text{Li}_2\text{MSn}_3\text{S}_8$  phases with  $M = \text{Mg}, \text{Mn}, \text{Fe}, \text{Ni}$  calculated from ICP-OES analyses together with the calculated ideal compositions.

	$\text{Li}_2\text{MgSn}_3\text{S}_8$		$\text{Li}_2\text{MnSn}_3\text{S}_8$	
	Ideal (wt%)	Measured (wt%)	Ideal (wt%)	Measured (wt%)
Li	2.1	2.2	2.0	2.1
Mg	3.7	3.8	Mn	7.7
Sn	54.7	55.2	Sn	52.3

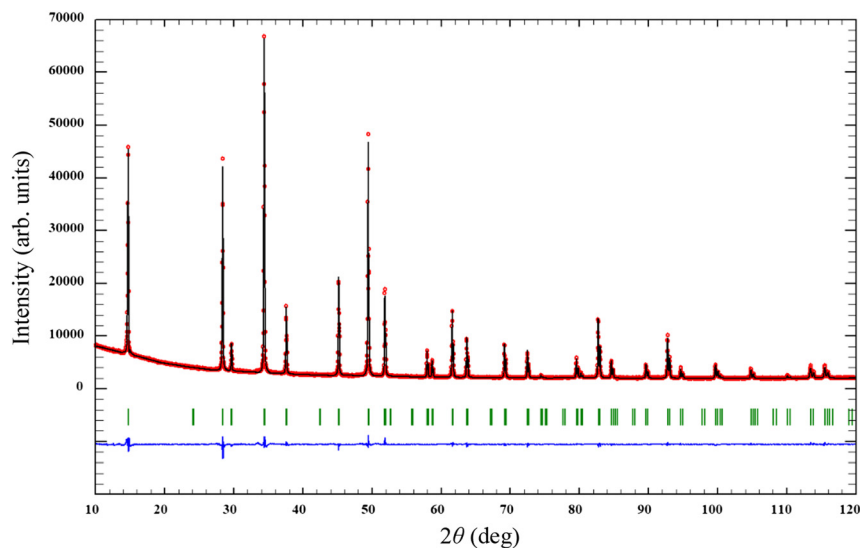
  

	$\text{Li}_2\text{FeSn}_3\text{S}_8$		$\text{Li}_2\text{NiSn}_3\text{S}_8$	
	Ideal (wt%)	Measured (wt%)	Ideal (wt%)	Measured (wt%)
Li	2.0	2.0	Li	2.1
Fe	8.2	8.0	Ni	8.9
Sn	52.2	51.2	Sn	54.6

**Figure 1:** X-ray diffraction pattern of  $\text{Li}_2\text{MgSn}_3\text{S}_8$  with the results of the Rietveld refinement.**Figure 2:** X-ray diffraction pattern of  $\text{Li}_2\text{MnSn}_3\text{S}_8$  with the results of the Rietveld refinement.



**Figure 3:** X-ray diffraction pattern of  $\text{Li}_2\text{FeSn}_3\text{S}_8$  with the results of the Rietveld refinement.



**Figure 4:** X-ray diffraction pattern of  $\text{Li}_2\text{NiSn}_3\text{S}_8$  with the results of the Rietveld refinement.

compound by mechanochemical synthesis have not been successful yet.

$\text{Li}_2\text{MSn}_3\text{S}_8$  phases with  $M = \text{Mg}, \text{Mn}, \text{Fe}, \text{Ni}$  crystallize in the normal spinel-type structure (space group  $Fd\bar{3}m$ ). This structure type can be described as a cubic closest packing of the sulfide ions where one eighth of the tetrahedral voids is occupied by lithium and one half of the octahedral voids by  $M$  and Sn. Interatomic lithium–sulfur distances range from 2.4048(11) Å for  $\text{Li}_2\text{MgSn}_3\text{S}_8$ , 2.4114(16) Å for  $\text{Li}_2\text{MnSn}_3\text{S}_8$ , 2.4051(19) Å for  $\text{Li}_2\text{FeSn}_3\text{S}_8$  to 2.3917(16) Å for  $\text{Li}_2\text{NiSn}_3\text{S}_8$  and are in agreement with those found for other tetrahedrally coordinated Li-bearing chalcogenides such as  $\text{NaLiS}$  (Li–S: 2.456(5) Å) [15] or  $\text{Li}_2(\text{Pb}/\text{Eu})\text{GeS}_4$  (Li–S: 2.4534(9) Å/2.4581(4) Å) [16]. Bond lengths for  $M/\text{Sn}$ –S vary

from 2.5669(11) Å for  $\text{Li}_2\text{MgSn}_3\text{S}_8$ , 2.5677(16) Å for  $\text{Li}_2\text{MnSn}_3\text{S}_8$ , 2.5461(19) Å for  $\text{Li}_2\text{FeSn}_3\text{S}_8$  to 2.5305(16) Å for  $\text{Li}_2\text{NiSn}_3\text{S}_8$  and correlate well with those reported for other complex thiospinels which exhibit a statistical distribution of octahedrally surrounded  $M$  and Sn with  $M = \text{Mg}, \text{Mn}, \text{Fe}, \text{Ni}$  (Figure 5) [17–19]. Bond angles are depicted in Table 7. Sulfur is coordinated by 1 Li and 3 ( $M/\text{Sn}$ ), the tetrahedra being slightly distorted. As the ionic radii of  $\text{Mg}^{2+}/\text{Mn}^{2+}/\text{Fe}^{2+}/\text{Ni}^{2+}$  and  $\text{Sn}^{4+}$  are close to each other, a statistical distribution of these ions on position 16d is quite plausible (C.N. = 6:  $\text{Mg}^{2+}$ : 0.90 Å;  $\text{Mn}^{2+}$ : 0.915 Å high spin;  $\text{Fe}^{2+}$ : 0.825 Å high spin;  $\text{Ni}^{2+}$ : no value given,  $\text{Sn}^{4+}$ : 0.86 Å) [20]. It should be mentioned that the refined bond lengths fit well with the values from ionic radii calculations.

**Table 2:** Results of the Rietveld refinements for  $\text{Li}_2\text{MSn}_3\text{S}_8$  with  $M = \text{Mg, Mn, Fe, Ni}$  (standard deviations in parenthesis).

Empirical formula	$\text{Li}_2\text{MgSn}_3\text{S}_8$	$\text{Li}_2\text{MnSn}_3\text{S}_8$	$\text{Li}_2\text{FeSn}_3\text{S}_8$	$\text{Li}_2\text{NiSn}_3\text{S}_8$
Color	Orange	Black-brown	Black	Black-brown
Structure type	Spinel			
Space group	$Fd\bar{3}m$			
Crystal system	Cubic			
Z	4			
$a$ , Å	10.5422(3)	10.5543(3)	10.4862(4)	10.4241(3)
$V$ , Å <sup>3</sup>	1171.63(5)	1175.67(6)	1153.08(7)	1132.69(5)
Calc. density, g cm <sup>-3</sup>	3.69	3.85	3.93	4.02
Diffractometer	PANalytical X'Pert MDP Pro			
Radiation	CuK $\alpha$ radiation			
Wavelength, Å	$\lambda_1 = 1.54056, \lambda_2 = 1.54439$			
$R_p$	0.0162	0.0197	0.0167	0.0181
$R_{wp}$	0.0227	0.0268	0.0244	0.0246
$R_{exp}$	0.0193	0.0206	0.0209	0.0173
$R_{Bragg}$	0.0176	0.0284	0.0309	0.0201
S	1.18	1.30	1.17	1.42

## 2.1 UV-Vis spectroscopy

For the determination of the optical band gaps, UV-Vis measurements were performed and the Tauc plot method [21, 22] was applied. As an example, the Tauc plot of the absorbance spectra for the direct optical band gap of  $\text{Li}_2\text{MgSn}_3\text{S}_8$  is depicted in Figure 6. The results for all four

investigated  $\text{Li}_2\text{MSn}_3\text{S}_8$  phases with  $M = \text{Mg, Mn, Fe, Ni}$  are presented in Table 8. For  $\text{Li}_2\text{FeSn}_3\text{S}_8$ , the optical band gap could not be determined because the measuring range of the instrument is limited to  $\lambda = 900$  nm. As the determined value of  $E_g = 2.36$  eV for  $\text{Li}_2\text{MgSn}_3\text{S}_8$  correlates well with its orange color, the direct optical band gap seems to be the most reliable value; this applies also to the other  $\text{Li}_2\text{MSn}_3\text{S}_8$  phases.

**Table 3:** Refined atomic parameters for  $\text{Li}_2\text{MgSn}_3\text{S}_8$  (standard deviations in parenthesis).

Atom	Wyckoff position	$x$	$y$	$z$	s.o.f	$B_{iso}$ (Å <sup>2</sup> )
Li	8a	1/8	1/8	1/8	1	2
Mg	16d	1/2	1/2	1/2	0.25	0.87(2)
Sn	16d	1/2	1/2	1/2	0.75	0.87(2)
S	32e	0.25670(9)	$x$	$x$	1	1

**Table 4:** Refined atomic parameters for  $\text{Li}_2\text{MnSn}_3\text{S}_8$  (standard deviations in parenthesis).

Atom	Wyckoff position	$x$	$y$	$z$	s.o.f	$B_{iso}$ (Å <sup>2</sup> )
Li	8a	1/8	1/8	1/8	1	2
Mn	16d	1/2	1/2	1/2	0.25	0.56(3)
Sn	16d	1/2	1/2	1/2	0.75	0.56(3)
S	32e	0.25691(14)	$x$	$x$	1	1

**Table 5:** Refined atomic parameters for  $\text{Li}_2\text{FeSn}_3\text{S}_8$  (standard deviations in parenthesis).

Atom	Wyckoff position	$x$	$y$	$z$	s.o.f	$B_{iso}$ (Å <sup>2</sup> )
Li	8a	1/8	1/8	1/8	1	2
Fe	16d	1/2	1/2	1/2	0.25	1.44(4)
Sn	16d	1/2	1/2	1/2	0.75	1.44(4)
S	32e	0.25742(19)	$x$	$x$	1	1

**Table 6:** Refined atomic parameters for  $\text{Li}_2\text{NiSn}_3\text{S}_8$  (standard deviations in parenthesis).

Atom	Wyckoff position	$x$	$y$	$z$	s.o.f	$B_{iso}$ (Å <sup>2</sup> )
Li	8a	1/8	1/8	1/8	1	2
Ni	16d	1/2	1/2	1/2	0.25	0.95(4)
Sn	16d	1/2	1/2	1/2	0.75	0.95(4)
S	32e	0.25747(15)	$x$	$x$	1	1

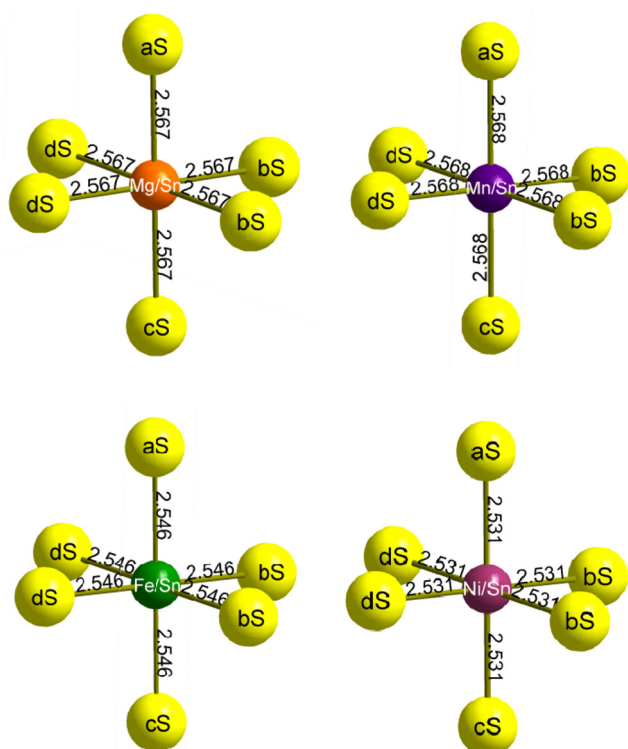


**Figure 5:** M/Sn octahedra in  $\text{Li}_2\text{MSn}_3\text{S}_8$  phases ( $M = \text{Mg}, \text{Mn}, \text{Fe}, \text{Ni}$ ) with determined bond lengths (Å) and description of the different sulfur atoms for selected angles in Table 7.

**Table 7:** Selected bond angles (deg) for  $\text{Li}_2\text{MSn}_3\text{S}_8$  phases with  $M = \text{Mg}, \text{Mn}, \text{Fe}, \text{Ni}$  (standard deviations in parentheses).

	$\text{Li}_2\text{MgSn}_3\text{S}_8$	$\text{Li}_2\text{MnSn}_3\text{S}_8$	$\text{Li}_2\text{FeSn}_3\text{S}_8$	$\text{Li}_2\text{NiSn}_3\text{S}_8$
S–Li–S	109.47(7)	109.47(10)	109.47(12)	109.47(10)
aS–M–bS	93.20(7)	93.30(10)	93.55(6)	93.58(10)
aS–M–cS	179.98(7)	180.00(12)	180.00(14)	180.00(12)
aS–M–dS	86.80(5)	86.70(10)	86.45(10)	86.42(10)
Li–S–M	123.03(4)	122.96(6)	122.79(6)	122.77(6)
M–S–M	93.11(4)	93.21(6)	93.45(6)	93.47(6)

**Table 8:** Optical band gaps (eV) of  $\text{Li}_2\text{MSn}_3\text{S}_8$  phases with  $M = \text{Mg}, \text{Mn}, \text{Fe}, \text{Ni}$ .

	$\text{Li}_2\text{MgSn}_3\text{S}_8$	$\text{Li}_2\text{MnSn}_3\text{S}_8$	$\text{Li}_2\text{FeSn}_3\text{S}_8$	$\text{Li}_2\text{NiSn}_3\text{S}_8$
Direct band gap	2.36	1.74	/	1.60
Indirect band gap	2.03	1.30	/	1.12

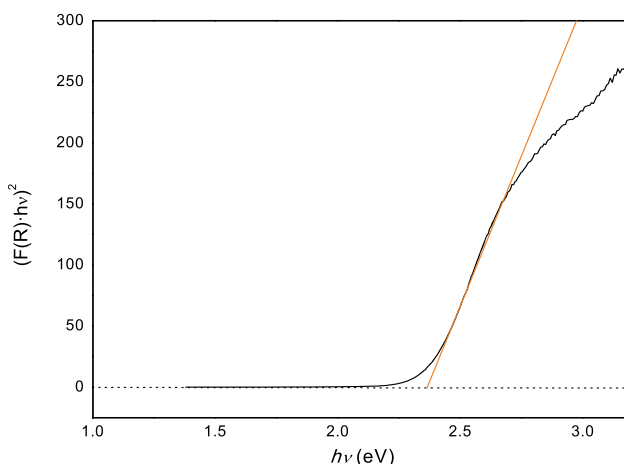


**Figure 6:** UV-Vis spectra of  $\text{Li}_2\text{MgSn}_3\text{S}_8$  with Tauc plot determination of the direct optical band gap (orange).

### 3 Conclusion

The substitution of Cu/Ag by lithium in complex thio-spinels with the general formula  $A_2^I B^II C^{IV}_3 X^{VI}_8$  led to the formation of four hitherto unknown compounds:  $\text{Li}_2\text{MSn}_3\text{S}_8$  with  $M = \text{Mg}, \text{Mn}, \text{Fe}, \text{Ni}$ . A mechanochemical method was used for the preparation. Its success again shows the great potential of this kind of synthetic approach for the preparation of multinary sulfides.

## 4 Experimental section

### 4.1 Synthesis

$\text{Li}_2\text{MSn}_3\text{S}_8$  phases with  $M = \text{Mg}, \text{Mn}, \text{Fe}, \text{Co}, \text{Ni}$  have been synthesized by ball milling of the corresponding binary sulfides  $\text{Li}_2\text{S}$  (Sigma–Aldrich, 99.9%),  $\text{MgS}$ ,  $\text{MnS}$  (Alfa Aesar, 99.9%),  $\text{FeS}_2$  (Sigma–Aldrich, 99.8%),  $\text{CoS}_2$  (Sigma–Aldrich, 99.98%),  $\text{NiS}$ ,  $\text{SnS}$ , and sulfur (Fluka, 99.99%) in a high energy planetary mill (Pulverisette 7, Fritsch, Idar-Oberstein, Germany) at a rotational speed of 450 rpm for 4 h in a 45 mL zirconia grinding breaker with six zirconia balls with a diameter of 15 mm. To increase the crystallinity, the milled products were annealed in a tube furnace at 550 °C for 2–3 h in  $\text{H}_2\text{S}$  atmosphere.  $\text{MgS}$  was synthesized by annealing of amorphous  $\text{MgO}$  at 750 °C for 3 h under flowing  $\text{H}_2\text{S}$  gas. Amorphous  $\text{MgO}$  was prepared using the modified Pechini method [23] with a calcination temperature of 450 °C. A hot and weakly acidic 0.1 M  $\text{NiSO}_4 \cdot 6\text{H}_2\text{O}$  solution and  $\text{H}_2\text{S}$  (Air Liquide, 99.5%) were used for the precipitation of  $\text{NiS}$ . For the preparation of  $\text{SnS}$  a solid state reaction of the elements

Sn (Merck, 99.9%) and S (Fluka, 99.99%) in an evacuated and sealed silica ampoule was applied.

## 4.2 Structural and chemical characterization

Powder diffraction data was collected using a Panalytical X'Pert Pro diffractometer with  $\text{CuK}\alpha$  radiation (Bragg–Brentano geometry). Rietveld refinements [24] were performed with the program FULLPROF [25] by applying a pseudo-Voigt function. For chemical characterization, ICP-OES was used (715 ES spectrometer, Varian Inc., Palo Alto, USA). For these analyses about 1 mg of the annealed powder was dissolved in small volumes of aqua regia and the solution obtained diluted with purified water up to 15 mL.

Further details of the crystal structure investigation may be obtained from Fachinformationszentrum Karlsruhe, 76344 Eggenstein-Leopoldshafen, Germany (Fax: +49 7247 808 666; E-mail: crysdata@fiz-karlsruhe.de, [https://www.fiz-informationsdienste.de/en/DB/icsd/depot\\_anforderung.html](https://www.fiz-informationsdienste.de/en/DB/icsd/depot_anforderung.html)) on quoting the deposition numbers CSD-1999952–CSD-1999955.

## 4.3 UV–Vis spectroscopy

The optical properties of the prepared thiospinel phases were measured in diffuse reflectance mode using a Cary 300 UV–Vis spectrometer (Varian Inc., Palo Alto, USA). The obtained spectra were converted into absorption spectra with the Kubelka–Munk function. The standard deviation for  $E_g$  was estimated close to 0.05 eV.

**Acknowledgment:** The authors would like to thank Astrid Müller-Klauke for performing the ICP-OES analysis and Leo Sagurna for his support and provision of the UV–Vis spectrometer (both TU Berlin).

**Author contribution:** All the authors have accepted responsibility for the entire content of this submitted manuscript and approved submission.

**Research funding:** This project was partially supported by the German Science Foundation (DFG, LE 781/19-1).

**Conflict of interest statement:** The authors declare no conflicts of interest regarding this article.

## References

- Jumas J. C., Philippot E., Maurin M. Structure du rhodostannite synthétique. *Acta Crystallogr.* 1979, B35, 2195–2197.
- Yajima J., Ohta E., Kanazawa Y. Toyohaite  $\text{Ag}_2\text{FeSn}_3\text{S}_8$  a new mineral. *Mineral. J.* 1991, 15, 222–232.
- Lavela P., Tirado J. L., Morales J., Olivier-Fourcade J., Jumas J. C. Lithium intercalation and copper extraction in spinel sulfides of general formula  $\text{Cu}_2\text{MSn}_3\text{S}_8$  M-Mn-Fe-Co-Ni. *J. Mater. Chem.* 1996, 6, 41–47.
- Cochez M. A., Jumas J. C., Lavela P., Morales J., Olivier-Fourcade J., Tirado J. L. New tin-containing spinel sulfide electrodes for ambient temperature rocking chair cells. *J. Power Sources* 1996, 62, 101–105.
- Chykhrij S. I., Sysa L. V., Parasyuk O. V., Piskach L. V. Crystal structure of the  $\text{Cu}_2\text{CdSn}_3\text{S}_8$  compound. *J. Alloys Compd.* 2000, 307, 124–126.
- Branci C., Womes M., Lippens P. E., Olivier-Fourcade J., Jumas J. C. Use of X-ray absorption spectra as a “fingerprint” of the local environment in complex chalcogenides. *J. Solid State Chem.* 2000, 150, 363–370.
- Garg G., Bobev S., Ganguli A. K. Single Crystal structure and electrical properties of  $\text{Cu}_8\text{Ni}_4\text{Sn}_{12}\text{S}_{32}$ . *J. Alloys Compd.* 2001, 327, 113–115.
- Garg G., Ramanujachary K. V., Lofland S. E., Lobanov M. V., Greenblatt M., Maddanimath T., Vijayamohan K., Ganguli A. K. Crystal structure, magnetic and electrochemical properties of a quaternary thiospinel:  $\text{Ag}_2\text{MnSn}_3\text{S}_8$ . *J. Solid State Chem.* 2003, 174, 229–232.
- Parasyuk O. V., Olekseyuk I. D., Piskach L. V., Volkov S. V., Pekhnyo V. I. Phase relations in the  $\text{Ag}_2\text{S}$ – $\text{CdS}$ – $\text{SnS}_2$  system and the crystal structure of the compounds. *J. Alloys Compd.* 2005, 399, 173–177.
- Sachanyuk V. P., Fedorchuk A. O., Olekseyuk I. D., Parasyuk O. V. New compounds  $\text{Cu}_2\text{MnTi}_3\text{S}_8$  and  $\text{Cu}_2\text{NiTi}_3\text{S}_8$  with thiospinel structure. *Mater. Res. Bull.* 2007, 42, 143–148.
- Kormosh Z., Fedorchuk A., Wojciechowski K., Tataryn N., Parasyuk O. The  $\text{Cu}_2\text{FeTi}_3\text{S}_8$  and  $\text{Cu}_2\text{FeZr}_3\text{S}_8$  compounds: Crystal structure and electroanalytical application. *Mater. Sci. Eng. C* 2011, 31, 540–544.
- Branci C., Sarradin J., Olivier-Fourcade J., Jumas J. C. Structural modifications related to lithium intercalation into iron thiospinels. *J. Power Sources* 1999, 81–82, 282–285.
- Krykhovets O. V., Sysa L. V., Olekseyuk I. D., Glowiyak T. Crystal structure of  $\text{Ag}_2\text{In}_2\text{GeSe}_6$ . *J. Alloys Compd.* 1999, 287, 181–184.
- Besse R., Da Silva J. L. F. The role of the alkali and chalcogen atoms on the stability of the layered chalcogenide  $\text{A}_2\text{M}^{\text{M}}\text{M}_3^{\text{IV}}\text{Q}_8$  (A = alkali-metal; M = metal-cations; Q = chalcogen) compounds: a density functional theory investigation within van der Waals corrections. *J. Phys.: Condens. Matter* 2017, 29, 035402.
- Sabrowsky H., Thimm A., Vogt-Mertens P. NaLiS: Ein weiteres interalkalimetallsulfid / NaLiS: A nother inter alkaline metal sulphide. *Z. Naturforsch.* 1985, 40b, 1759–1760.
- Aitken J. A., Larson P., Mahanti S. D., Kanatzidis M. G.  $\text{Li}_2\text{PbGeS}_4$  and  $\text{Li}_2\text{EuGeS}_4$  polar chalcopyrites with a severe tetragonal compression. *Chem. Mater.* 2001, 13, 4714–4721.
- Garg G., Bobev S., Roy A., Ghose J., Das D., Ganguli A. K. Single crystal structure and Mössbauer studies of a new cation-deficient thiospinel:  $\text{Cu}_{5.47}\text{Fe}_{2.9}\text{Sn}_{13.1}\text{S}_{32}$ . *Mater. Res. Bull.* 2001, 36, 2429–2435.
- Garg G., Bobev S., Ganguli A. K. Single crystal structures of two new cation-deficient thiospinels:  $\text{Cu}_{7.38(11)}\text{Mn}_4\text{Sn}_{12}\text{S}_{32}$  and  $\text{Cu}_{7.07(6)}\text{Ni}_4\text{Sn}_{12}\text{S}_{32}$ . *Solid State Ionics* 2002, 146, 195–198.
- Heppke E. M., Klenner S., Janka O., Pöttgen R., Lerch M. Mechanochemical Synthesis of  $\text{Cu}_2\text{MgSn}_3\text{S}_8$  and  $\text{Ag}_2\text{MgSn}_3\text{S}_8$ . *Z. Anorg. Allg. Chem.* 2020, 646, 5–9.
- Shannon R. D. Bond distances in sulfides and a preliminary table of sulfide crystal radii. In *Structure and Bonding in Crystals*;

- O'Keeffe M., Navrotsky A., Eds., Vol. 2. Academic Press, Inc.: New York, 1981; pp. 53–70.
21. Tauc J. Optical properties and electronic structure of amorphous Ge and Si. *Mater. Res. Bull.* 1968, 3, 37–46.
  22. Tauc J., Grigorovici R., Vanco A. Optical properties and electronic structure of amorphous germanium. *Phys. Status Solidi B* 1966, 15, 627–637.
  23. Pechini M. P. US Patent No. 3330697, 1967.
  24. Rietveld H. M. A profile refinement method for nuclear and magnetic structures. *J. Appl. Crystallogr.* 1969, 2, 65–71.
  25. Rodríguez-Carvajal J. FullProf, A Program for Rietveld Refinement and Pattern Matching Analysis. *Abstracts of the Satellite Meeting on Powder Diffraction of the 15th International Congress of the IUCr, Toulouse, France, 1990*; p. 127.

## **Part III.**

# **Conclusion and Prospects**

## 11. Conclusion

The aim of this thesis was the production of new and already known members of  $A_2^I B^{II} C^{IV} S_4^{VI}$  and  $A_2^I B^{II} C_3^{IV} S_8^{VI}$  material classes with focus on the structural characterization to gain a deeper insight of the correlation between structural and physicochemical properties of these materials.

The synthesis of the compounds mentioned in the present work was done mechanochemically. The underlying idea of the so-called mechanochemical synthesis is that the compounds are already formed in the first step of the synthesis by grinding in a high energy ball mill. Highly crystalline products are then obtained in the subsequent step, annealing under flowing  $H_2S$  gas.

For the accurate determination of the crystal structure, X-ray diffraction measurements were performed on all prepared compounds and the data subsequently processed by Rietveld refinement. Rietveld refinements were partly carried out in several space groups in order to distinguish between potential structure candidates and to find out which one is the most appropriate. In order to distinguish between Cu and Zn, neutron diffraction measurements actually would be necessary for samples of the  $Cu_2Cd_xZn_{1-x}SnS_4$  solid solution series. Such measurements would also be necessary for  $Ag_2CdSnS_4$  samples as all three contained cations exhibit similar scattering factors. As Cd is a great neutron radiation absorber [171] such measurements cannot be performed for Cd-containing compounds. The cation distribution in  $Cu_2Cd_xZn_{1-x}SnS_4$  and  $Ag_2CdSnS_4$  samples is analogous to that of already described compounds adopting these structure types. The same applies for the thiospinel  $Ag_2MgSn_3S_8$  presented in this thesis where the monovalent cation occupy the tetrahedra and the di- and tetravalent cations statistically the octahedra positions. In return, neutron diffraction measurements were carried out for  $Cu_2FeSnS_4$  to be able to distinguish between Cu and Fe.

### 11.1. $A_2^I B^{II} C^{IV} S_4^{VI}$ compounds

With this work new structural insights of some members of the  $A_2^I B^{II} C^{IV} S_4^{VI}$  compound family could be achieved and existing knowledge could be extended. Additionally, a new compound to this material class could be added and an already known was

tested in a new field of application for these materials.

The investigation on the structural transition between the stannite- and kesterite-type structure in the  $\text{Cu}_2\text{Cd}_x\text{Zn}_{1-x}\text{SnS}_4$  solid solution series was complemented in this work with a further study using highly crystalline bulk materials (**publication 1**). Prior to this, the structural transition was investigated exclusively on thin film/nanostructured and off-stoichiometric samples. Selected compositions of the  $\text{Cu}_2\text{Cd}_x\text{Zn}_{1-x}\text{SnS}_4$  solid solution series were synthesized mechanochemically and analyzed by X-ray diffraction including Rietveld refinements in four different structure models (ST, KS, DKS, partial DKS). Herewith the structural transition was determined to a value of  $x = 0.40$ . This value is supported by Raman spectroscopy with a change of the mode frequency and of the FWHM of the most intense Raman band which is associated with the sulfur motions along  $c$ -axis. The study also includes quantum-chemical calculations that complement the results of the experimental work.

In **publication 2** a detailed investigation on the structure of already known  $\text{Ag}_2\text{CdSnS}_4$  is presented. Mechanochemically prepared  $\text{Ag}_2\text{CdSnS}_4$  does not adopt the proposed structure in space group  $Cmc2_1$  with a statistical distribution of the cations, but crystallizes in wurtzkesterite-type structure with space group  $Pn$  and an ordering of the contained cations. At around 200 °C a reversible first-order phase transition to the higher symmetric wurtzstannite-type structure with space group  $Pmn2_1$  was observed. The results concerning the crystal structure of  $\text{Ag}_2\text{CdSnS}_4$ , which deviate from the literature, can be attributed to the differently used synthesis method.

Furthermore, a new compound to the  $\text{A}_2\text{B}^{\text{II}}\text{C}^{\text{IV}}\text{S}_4^{\text{VI}}$  compound family could be produced which is summarized in **publication 3**.  $\text{Na}_2\text{MgSnS}_4$  crystallizes in the  $\text{NaCrS}_2$  structure type with space group  $R\bar{3}m$ . Mg and Sn are statistically distributed and form a  $\text{CdCl}_2$ -type structure in which the remaining voids are filled with Na. Due to the larger difference of the electronegativities of the contained ions,  $\text{Na}_2\text{MgSnS}_4$  has a more ionic character and therefore adopts a structure deriving from NaCl-type structure. The contained cations and anions are octahedrally coordinated which is in contrast to usual tetrahedral compounds.

**Publication 4** contains the collaboration with the research group of Prof. Driess of the TU Berlin where mechanochemically prepared  $\text{Cu}_2\text{FeSnS}_4$  was tested as potential electrocatalyst for OER. OER (oxygen evolution reaction) is one of the two half-reactions of electrocatalytically water splitting which plays an important role for the sustainable

generation of  $H_2$ . Hereby,  $Cu_2FeSnS_4$  has proven to be superior over  $FeS$ ,  $Fe(OH)_3$ ,  $FeOOH$  and other noble-catalysts such as  $MO_x$  with  $M = Ir, Ru$  in alkaline conditions. The paper consists of structural analysis of  $Cu_2FeSnS_4$ , electrocatalytic characterization and OER performance and also post catalytic characterization and opens up a new applicational field for  $A_2^I B^I C^IV S_4^{VI}$  semiconductors as this class of materials consists of various compounds containing OER active earth-abundant elements. Some members of that compound family have been already studied for HER [172–175] as well as  $Cu_2ZnSnS_4$  for OER [176], however, in this paper the first promising  $A_2^I B^I C^IV S_4^{VI}$  candidate for OER is presented.

## 11.2. $A_2^I B^I C_3^IV S_8^{VI}$ compounds

In the course of this work, the group of  $A_2^I B^I C_3^IV S_8^{VI}$  compounds could be extended by a total of six new compounds. For the first time, compounds of this type containing Mg were produced and the substitution with Li was investigated.

**Publication 5** presents the Mg-containing Cu- and Ag-thiospinels of the type  $A_2^I B^I C_3^IV S_8^{VI}$ . A detailed description about the formation of the thiospinels is also included in this paper. Crystallite sizes after milling range from 9.3–11.0 nm for  $Cu_2MgSn_3S_8$  and from 4.7–5.9 nm for  $Ag_2MgSn_3S_8$  samples whereas similar crystallite sizes of about 31.8–35.6 nm have been attained for both compounds after annealing. The direct optical band gaps for both black-colored thiospinels were determined to  $E_g = \sim 1.65$  eV. The diamagnetic behavior of the Cu-bearing compound  $Cu_2MgSn_3S_8$  was confirmed using susceptibility measurements. The results obtained by means of Mößbauer spectroscopy point to a thiostannate character with an oxidation state of +4 for tin and a mixed site occupancy for the octahedral position 16*d*.

In **publication 6** the results of the substitution of Cu and Ag in  $A_2^I B^I C_3^IV S_8^{VI}$  thiospinels by lithium are described. The four new compounds with following formula  $Li_2MSn_3S_8$  and  $M = Mg, Mn, Fe, Ni$  could be synthesized without any side phases. Additionally, the formation of  $Li_2CoSn_3S_8$  was also possible, however, a phase-pure sample could not be achieved and therefore this compound is not presented in detail. Li-thiospinels containing transition metals have an almost black color while the Mg compound shows a bright orange color. For the direct optical bandgaps this means that  $Li_2MSn_3S_8$  with  $M = Mn, Fe, Ni$  exhibit values close to 1.7 eV (or are not measurable) and  $Li_2MgSn_3S_8$  assumes a wider band gap with a value of  $E_g = 2.37$  eV.

### 11.3. Outlook

The determination of the structural transition was successfully done for the  $\text{Cu}_2\text{Cd}_x\text{Zn}_{1-x}\text{SnS}_4$  solid solution series whereas Raman measurements have proved to be a great support to the diffraction data. Raman spectroscopy using synchrotron radiation is already scheduled for the  $\text{Cu}_2\text{Cd}_x\text{Zn}_{1-x}\text{SnS}_4$  samples to get more precise information about the vibrational characteristics. This knowledge may be helpful to differ between kesterite and stannite phases in other solid solution series where X-ray diffraction is not sufficient enough. As an example,  $\text{Cu}_2\text{Mn}_x\text{Zn}_{1-x}\text{SnS}_4$  and  $\text{Cu}_2\text{Fe}_x\text{Zn}_{1-x}\text{SnS}_4$  solid solution series can be mentioned here, where two to three cations cannot be distinguished using X-ray diffraction.

In addition, it is planned to use some  $\text{A}_2\text{I}^{\text{B}}\text{C}^{\text{IV}}\text{S}_4^{\text{VI}}$  compounds for HT/HP-experiments to investigate their structural properties under pressure. For  $\text{Cu}_2\text{ZnSnS}_4$ , for example, a pressure induced transition to a GeSb-type phase (considered as a distorted NaCl-type structure with tetragonal symmetry) with a higher coordination number and metallic properties was observed by Efthimiopoulos et al. [177]. For  $\text{Ag}_2\text{CdSnS}_4$  it would be also interesting to know if the thermally observed phase transition can also be observed under pressure or if other structure types may occur.

Besides, further attempts could be undertaken to produce more Na-containing compounds as these have been relatively little researched so far.

As some new  $\text{A}_2\text{I}^{\text{B}}\text{C}_3^{\text{IV}}\text{S}_8^{\text{VI}}$  compounds were produced and the substitution with lithium was successful a detailed electrochemical investigation of the prepared samples would be preferable.

Sn-containing compounds are the biggest group among these materials, however, some Ti- and even one Zr-bearing compounds are described in the literature. Further experiments using the mechanochemical synthesis method to expand this group could be undertaken.

The replacement of divalent cations with monovalent cations in  $\text{A}_2\text{I}^{\text{B}}\text{C}_3^{\text{IV}}\text{S}_8^{\text{VI}}$  compounds has already been carried out and was partially successful. There are still some difficulties in the examination of the proper crystal structure which will have to be solved in the future.

Attempts for the substitution of Cu/Ag/Li by Na have also been started so far; even one similar compound is mentioned in the literature [125]. The correct structure of these materials has not been solved so far and is also considered to be a task for future investigations.

By using highly crystalline samples it is easier to figure out the proper structure.

## CONCLUSION

---

The second step of the mechanochemical synthesis route, the annealing of the milled materials, is essential for this purpose. With this thesis it could be shown that the mechanochemical synthesis route is suitable to produce sulfides of the types  $A_2^I B^{II} C^{IV} X_4^{VI}$  and  $A_2^I B^{II} C_3^{IV} X_8^{VI}$  and is advantageous for their accurate structural characterization.

## A. Appendices

### A.1. Additional information, Supplementary material

#### A.1.1. Chemicals

Table A.1.: List of utilized chemicals.

Name	Purity	Producer
H <sub>2</sub> S	99.5 %	Air Liquide
Cu(NO <sub>3</sub> ) <sub>2</sub>	99.5 %	Merck
Cd(CH <sub>3</sub> CO <sub>2</sub> ) <sub>2</sub>	zur Analyse	Merck
ZnO	99.5 %	Merck
Sn	99.9 %	Merck
S	99.99 %	Fluka
Ag <sub>2</sub> S		Schuchardt
MgCl <sub>2</sub> wasserfrei	99 %	Alfa Aesar
Ethanol	99.5 %	Acros Organics
Citric acid	99 %	Sigma-Aldrich
Ethylene glycol	99 %	Alfa Aesar
FeS <sub>2</sub>	99.8 %	Sigma-Aldrich
Li <sub>2</sub> S	99.9 %	Sigma-Aldrich
MnS	99.9 %	Alfa Aesar
NiSO <sub>4</sub> · 6 H <sub>2</sub> O	99 %	Merck
CoS <sub>2</sub>	99.98 %	Sigma-Aldrich

### A.1.2. Diffraction pattern of binary starting materials

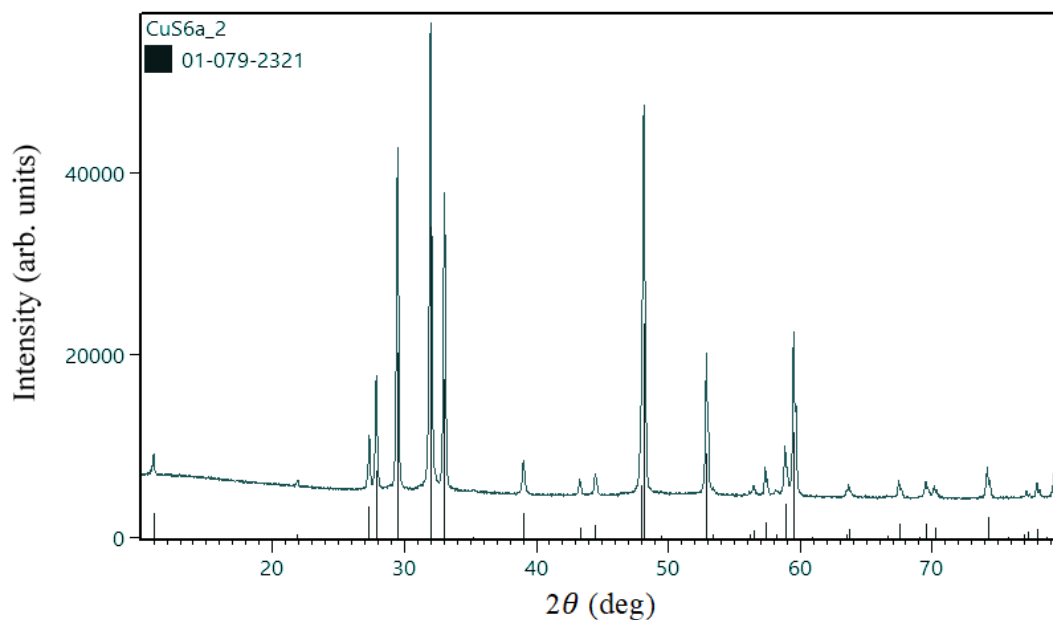


Figure A.1.: X-ray diffraction pattern of synthesized CuS, covellite (space group  $P6_3/mmc$ ).

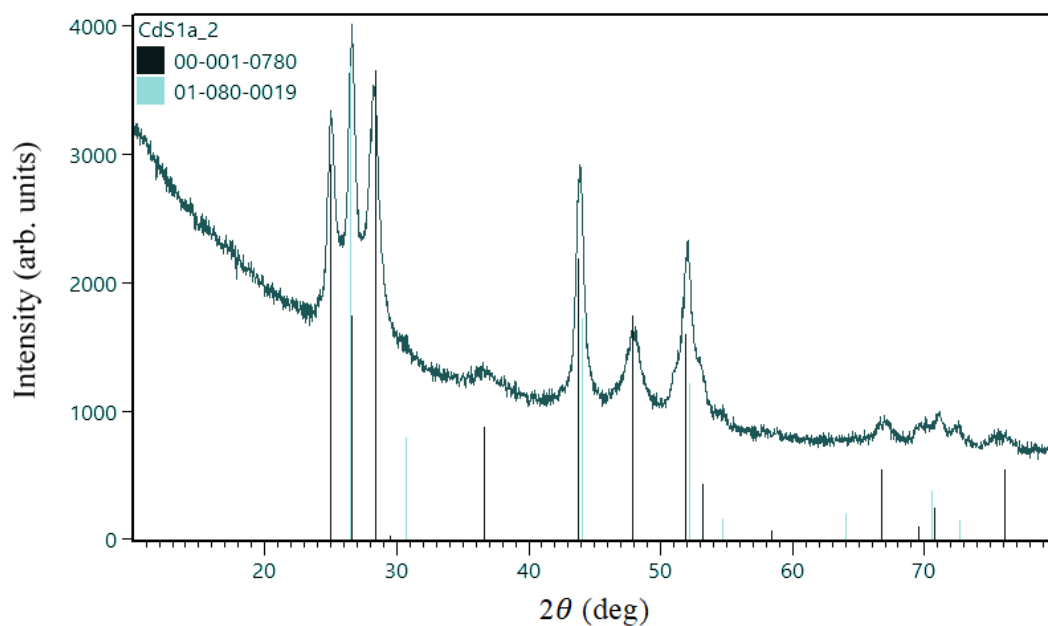
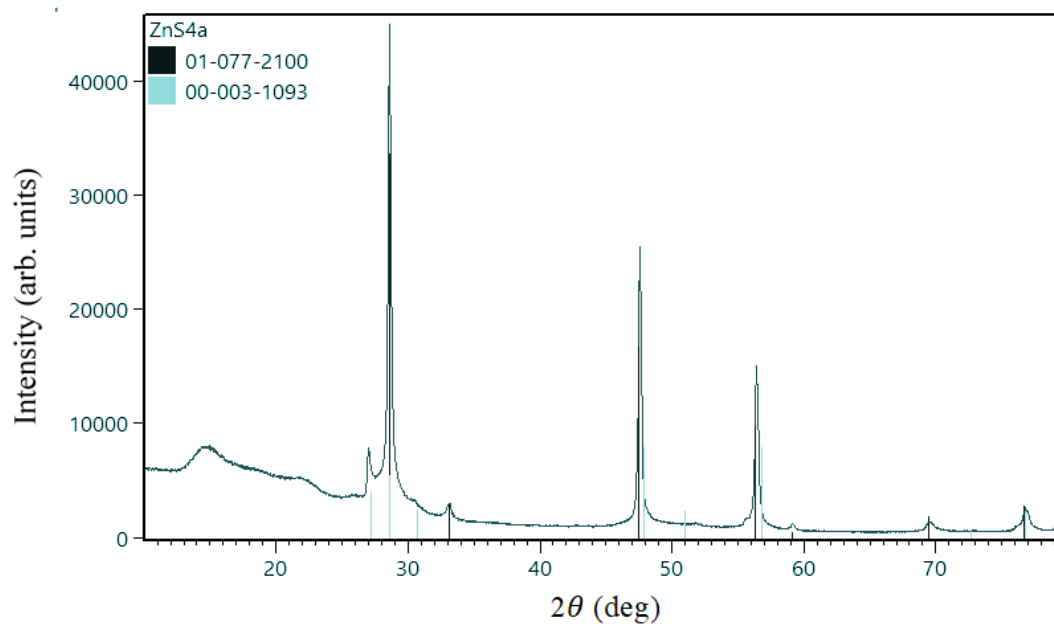
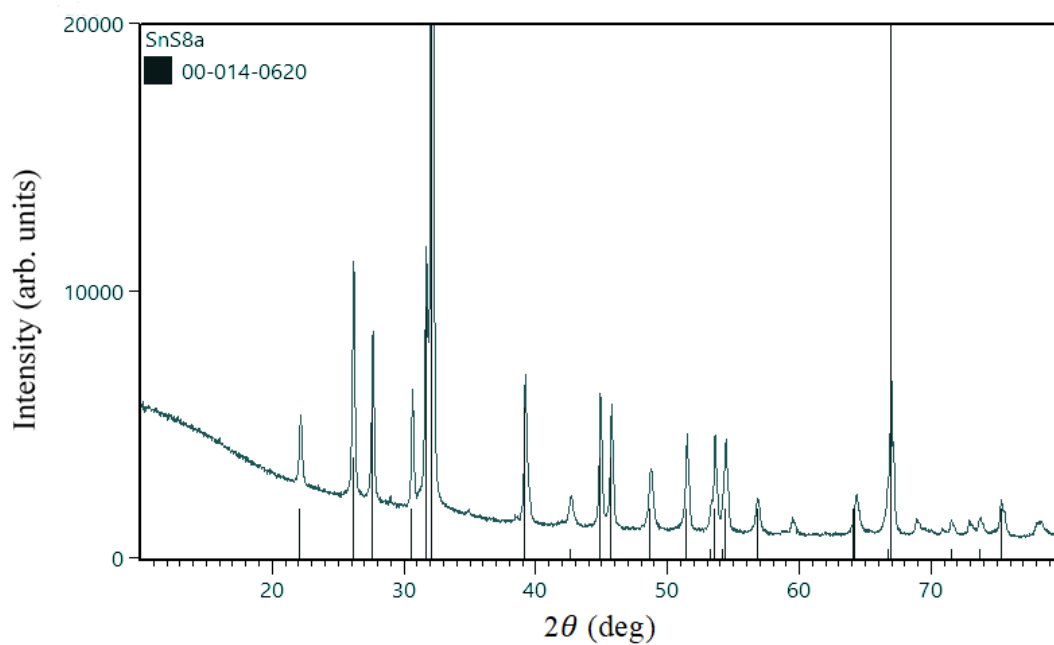


Figure A.2.: X-ray diffraction pattern of synthesized CdS, greenockite (black, space group  $P6_3mc$ ) with additional hawleyite (blue, space group  $F43m$ ).



**Figure A.3.:** X-ray diffraction pattern of synthesized ZnS, sphalerite (black, space group  $F\bar{4}3m$ ) with additional wurtzite (blue, space group  $P6_3mc$ ).



**Figure A.4.:** X-ray diffraction pattern of synthesized SnS, herzenbergite (space group  $Pnma$ ).

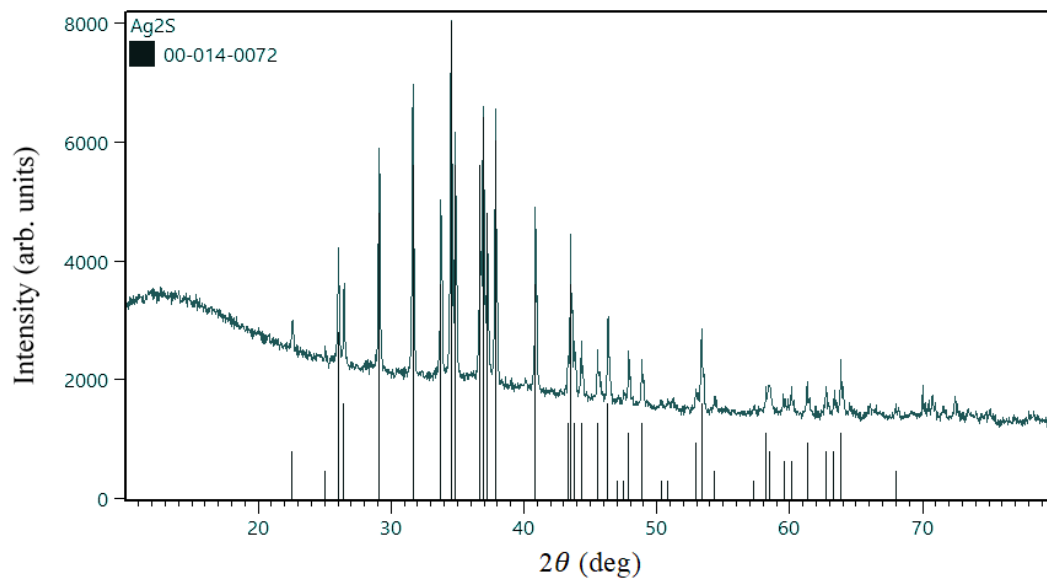


Figure A.5.: X-ray diffraction pattern of Ag<sub>2</sub>S, acanthite (space group  $P2_1/m$ ).

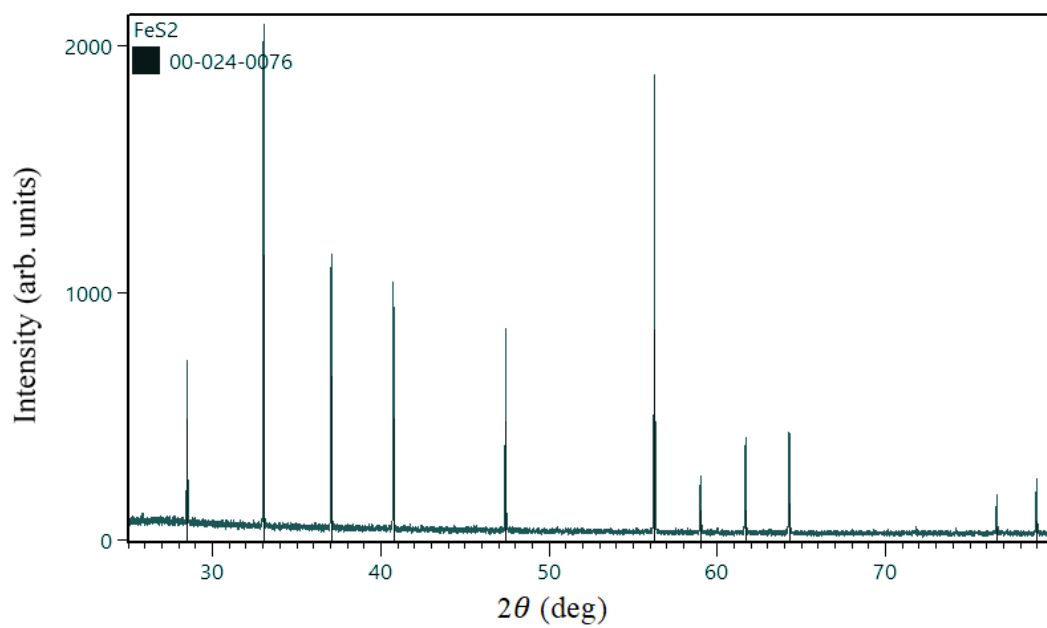


Figure A.6.: X-ray diffraction pattern of FeS<sub>2</sub>, pyrite (space group  $Pa\bar{3}$ ).

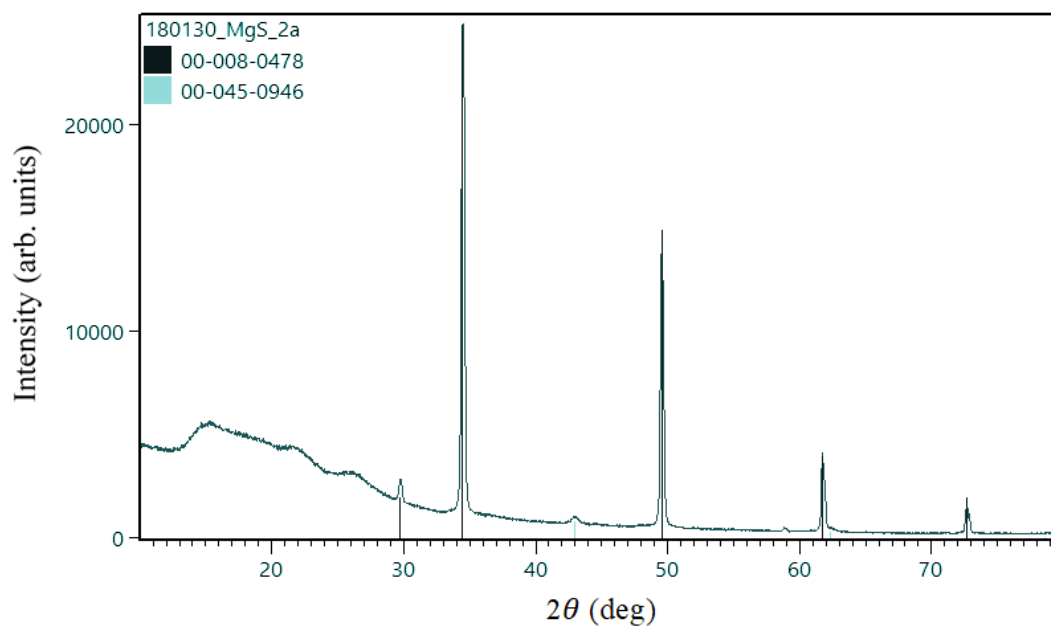


Figure A.7.: X-ray diffraction pattern of synthesized MgS (black, space group  $Fm\bar{3}m$ ) with additional impurities of MgO (blue, space group  $Fm\bar{3}m$ ).

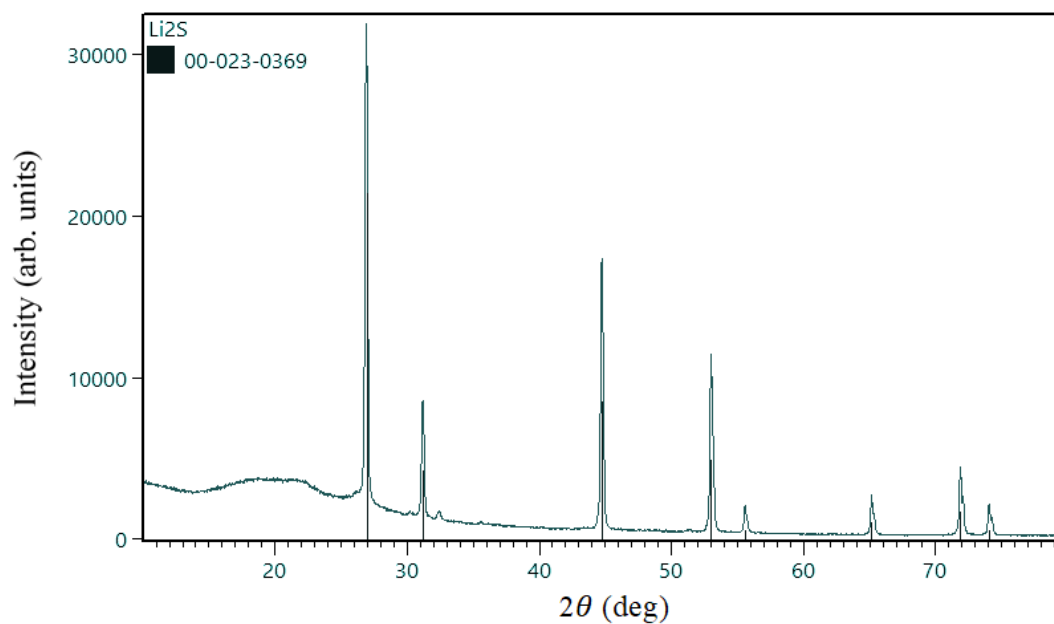


Figure A.8.: X-ray diffraction pattern of Li<sub>2</sub>S (space group  $Fm\bar{3}m$ ).

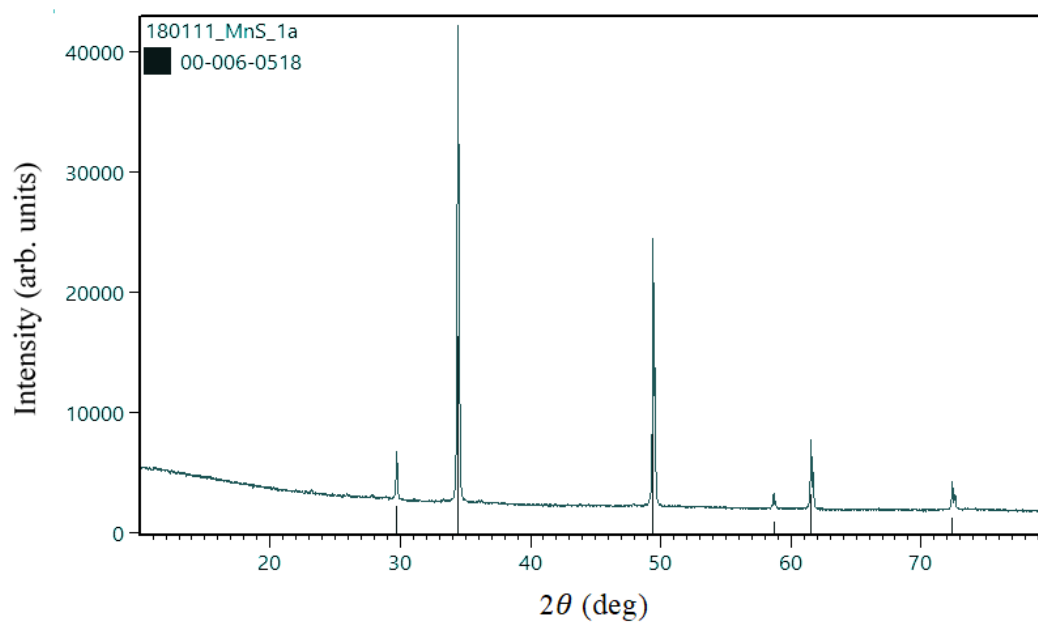


Figure A.9.: X-ray diffraction pattern of MnS, alabandite (space group  $Fm\bar{3}m$ ).

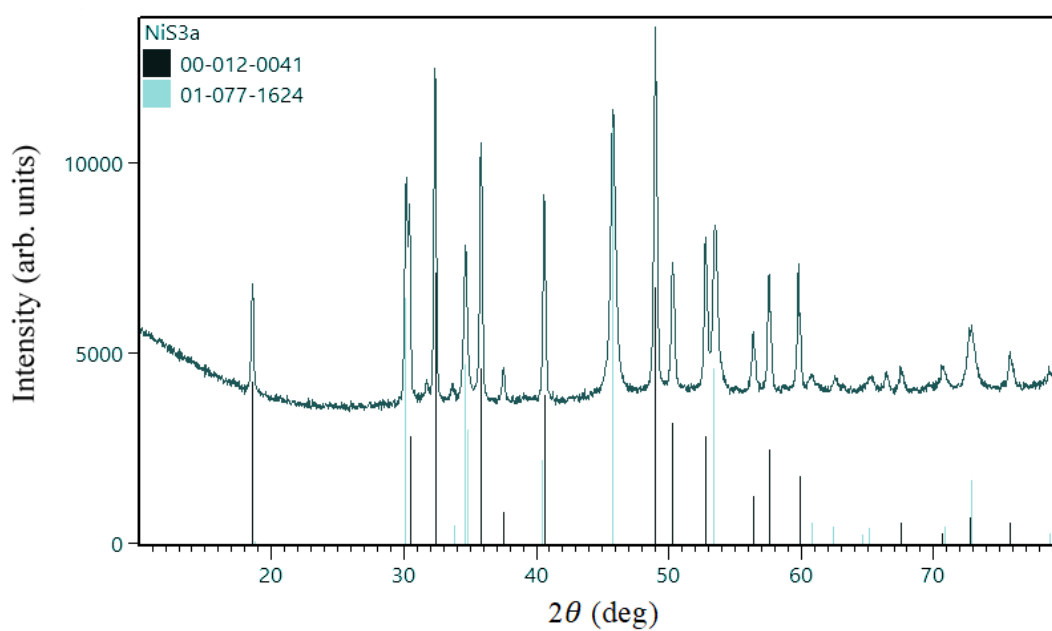


Figure A.10.: X-ray diffraction pattern of synthesized NiS, millerite (black, space group  $R3m$ ) with additional NiS (blue, space group  $P6_3/mmc$ ).

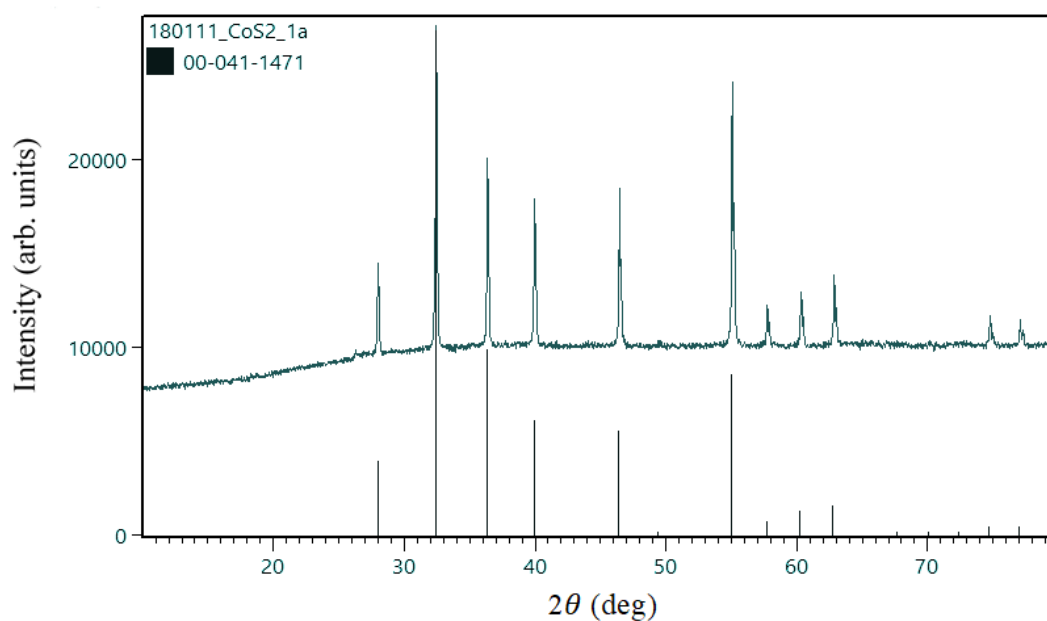


Figure A.11.: X-ray diffraction pattern of  $\text{CoS}_2$ , cattierite (space group  $Pa\bar{3}$ ).

### A.1.3. Software

Table A.2.: List of utilized software.

Name	Latest version	Producer
X'PERT HIGHSCORE PLUS	4.6a	PANalytical
WINXPOW	2.1	STOE & Cie GmbH
FULLPROF	June-2015	JGP-JRC
Diamond	4.3.1	Crystal Impact GbR
FindIt	1.9.6	FIZ Karlsruhe
Origin	2016G;b9.3.226	OriginLab Corporation
Citavi	6.4	Swiss Academic Software GmbH
Gimp	2.10.18	GIMP-Team

## A.2. List of Publications

1. K. Neuhaus, M. Bernemann, K. V. Hansen, T. Jacobsen, G. Ulbrich, E. M. Heppke, M. Paun, M. Lerch, H. D. Wiemhöfer. Study of the polarization behavior of  $\text{Ce}_{0.9}\text{Gd}_{0.1}\text{O}_{2-\delta}$  single crystals below 350 °C to room temperature. *J. Electrochem. Soc.* **2016**, 163(14), H1179-H1185.
2. E. M. Heppke, T. Küllmey, I. Efthimiopoulos, F. D. Avci, O. Appelt, B. Paulus, M. Lerch. Experimental and theoretical investigations on the composition-dependent structural phase transition in  $\text{Cu}_2\text{Cd}_x\text{Zn}_{1-x}\text{SnS}_4$ . *Mat. Res. Express* **2019**, 6(12), 125525.
3. D. Wiedemann, E. M. Heppke, A. Franz. And Yet It Moves: A high-temperature neutron diffraction study of ion diffusion in the inverse perovskites  $\text{BaLiX}_3$  ( $X = \text{F}, \text{H}, \text{D}$ ). *Eur. J. Inorg. Chem.* **2019**, 5085-5088.
4. J. N. Hausmann, E. M. Heppke, R. Beltrán-Suito, J. Schmidt, M. Mühlbauer, M. Lerch, P. W. Menezes, M. Driess. Stannites—a new promising class of durable electrocatalysts for efficient water oxidation. *ChemCatChem* **2020**, 12(4), 1161-1168.
5. E. M. Heppke, S. Klenner, O. Janka, R. Pöttgen, M. Lerch. Mechanochemical Synthesis of  $\text{Cu}_2\text{MgSn}_3\text{S}_8$  and  $\text{Ag}_2\text{MgSn}_3\text{S}_8$ . *Z. Anorg. Allg. Chem.* **2020**, 646, 5-9.
6. E. M. Heppke, S. Berendts, M. Lerch. Crystal structure of mechanochemically synthesized  $\text{Ag}_2\text{CdSnS}_4$ . *Z. Naturforsch. B* **2020**, 75(4), 393-402.
7. E. M. Heppke, S. Mahadevan, M. Lerch. New compounds of the  $\text{Li}_2\text{MSn}_3\text{S}_8$  type. *Z. Naturforsch. B* **2020**, 75(6-7), 625-631.
8. E. M. Heppke, M. Lerch.  $\text{Na}_2\text{MgSnS}_4$  – a new member of the  $\text{A}^{\text{I}}_2\text{B}^{\text{II}}\text{C}^{\text{IV}}\text{X}^{\text{VI}}_4$  family of compounds. *Z. Naturforsch. B* **2020**, 75(8), 721-726.

### A.3. List of Conference Contributions

- 03/2015 23<sup>th</sup> Annual Meeting of the German Crystallographic Society (DGF), 2015, Göttingen, Germany - *Poster*  
Matthias Paun, Eva Heppke, Martin Lerch. Growth of luminescent single crystal Zirconia by means of induction Skull-Melting.
- 08/2015 15<sup>th</sup> European Conference on Solid State Chemistry (ECSSC15), 2015, Vienna, Austria - *Poster*  
Eva Heppke, Stefan Berendts, Suliman Nakhal, Martin Lerch. Sodium Ion Substitution in Barium Zirconate.
- 09/2016 19. Vortragstagung Fachgruppe Festkörperchemie und Materialforschung, 2016, Innsbruck, Austria - *Poster*  
Eva Heppke, Sebastian Eickholt, Aditya Maheshwari, Hans-Dieter Wiemhöfer, Martin Lerch. Züchtung und elektrochemische Charakterisierung von Cerdioxid-basierten Einkristallen.
- 09/2018 19. Vortragstagung für Anorganische Chemie der Fachgruppen Wöhler-Vereinigung und Festkörperchemie und Materialforschung, 2018, Regensburg, Germany - *Poster*  
Eva Heppke, Tim Küllmey, Ilias Efthimiopoulos, Fatma D. Avcı, Ina Speckmann, Beate Paulus, Martin Lerch. Strukturübergang zwischen der Stannit- und Kesterit-Struktur in  $\text{Cu}_2\text{Cd}_x\text{Zn}_{1-x}\text{SnS}_4$ .  
Eva Heppke, Martin Lerch. Mechanochemische Synthese von  $\text{Cu}_2\text{MgSn}_3\text{S}_8$  und  $\text{Ag}_2\text{MgSn}_3\text{S}_8$ .  
Steven Orthmann, Eva Heppke, Prashanth W. Menezes, Carsten Walter, Martin Lerch, Matthias Driess. Quaternary Sulfides as Efficient Water Splitting Electrocatalysts.  
Tim Küllmey, Ilias Efthimiopoulos, Eva Heppke, Sergio Speziale, Anna S. Pakhomova, Marcel Quennet, Beate Paulus, Anna Ritscher, Martin Lerch, Monika Koch-Müller. Pressure-induced structural and electronic transitions in kesterite-type  $\text{Cu}_2\text{ZnSnS}_4$ .
- 03/2019 27<sup>th</sup> Annual Meeting of the German Crystallographic Society (DGK), 2019, Leipzig, Germany - *Poster*  
Dennis Wiedemann, Eva Heppke, Alexandra Franz. And yet it moves - anion diffusion in the inverse perovskites  $\text{BaLiX}_3$  ( $X = \text{H}, \text{D}, \text{F}$ ).

## List of Figures

2.1. Two- and three-dimensional representation of the crystal structures of cubic diamond [96], sphalerite [97], chalcopyrite [98], stannite [37] and kesterite [85]. . . . .	12
2.2. Two- and three-dimensional representation of the crystal structures of lonsdaleite [88], wurtzite [91] and BeSiN <sub>2</sub> [92]. . . . .	13
2.3. Two- and three-dimensional representation of the crystal structures of wurtzstannite- using Cu <sub>2</sub> CdGeS <sub>4</sub> [36] and wurtzkesterite-type structure using Cu <sub>2</sub> ZnSiS <sub>4</sub> [95] as example. . . . .	14
2.4. Group-subgroup scheme for the grouptheoretical relation between cubic diamond and stannite-/kesterite-type structure. . . . .	16
2.5. Group-subgroup scheme for the grouptheoretical relation between hexagonal diamond and wurtzstannite-/wurtzkesterite-type structure. . . . .	18
2.6. Structural comparison of chalcopyrite-type CuFeS <sub>2</sub> (left) [98] and compressed chalcopyrite-like Ag <sub>2</sub> BaGeS <sub>4</sub> (right) [34] with indication of the occurring bonds between cations and anions. . . . .	20
2.7. Coordination polyhedra of two sulfur atoms in form of edge-sharing quadratic pyramids (top) and of the divalent Ba <sup>2+</sup> cation in form of a distorted dodecahedra (bottom) in compressed chalcopyrite-type Ag <sub>2</sub> BaGeS <sub>4</sub> [34]. . . . .	21
3.1. Unit cell of MgAl <sub>2</sub> O <sub>4</sub> [132]; octahedral coordination of Al is presented by bonds between aluminium and oxygen; tetrahedral surrounding of Mg is indicated as MgO <sub>4</sub> -tetrahedra. . . . .	24
3.2. Group-subgroup relations - without description of corresponding Wyck-off positions - between ideal spinel-type structure (space group <i>Fd<math>\bar{3}m</math></i> ) and selected derived structures of known eyamples exhibiting specific distortions. . . . .	27
4.1. Schematic illustration of milling set-up in planetary ball mills with two grinding beakers (left) and ball motion inside the grinding beakers according to [154] (right). . . . .	29

LIST OF FIGURES

---

4.2.	High energy Mill Pulverisette 6 (left) and 7 classic line (right). . . . .	30
4.3.	Gero furnace with H <sub>2</sub> S equipment used for the crystallization of the milled products. . . . .	31
4.4.	HTM Reetz furnace with H <sub>2</sub> S equipment used for the crystallization of the milled products. . . . .	31
5.1.	Unit cell of the stannite-type (ST, left) and kesterite-type (KS, right) structure for the Cu <sub>2</sub> CdSnS <sub>4</sub> and Cu <sub>2</sub> ZnSnS <sub>4</sub> end-members, respectively (Cu: bronze, Zn: pink, Cd: green, Sn: grey, and S: yellow). The structural parameters are taken from our DFT calculations ( <b>Tables S1-S8</b> in the <b>Supplement</b> ). . . . .	45
5.2.	Unit cells of the disordered kesterite-type substitution patterns p <sub>1</sub> (DKS-p <sub>1</sub> , left) and p <sub>2</sub> (DKS-p <sub>2</sub> , middle), and the most stable KS configuration with 12.5% Cu-Zn disorder (right). The DKS-p <sub>1</sub> is the most stable modification for the DKS phase, followed by DKS-p <sub>2</sub> which is 0.12 eV less stable per formula unit at the PBE level. The atom colors are Cu: bronze, Zn: pink, Sn: grey, and S: yellow. . . . .	51
5.3.	XRD patterns of (left) poorly crystalline and (right) annealed Cu <sub>2</sub> Cd <sub>x</sub> Zn <sub>1-x</sub> SnS <sub>4</sub> samples with x <sub>Cd</sub> = 0, 0.25, 0.33, 0.37, 0.40, 0.50, 0.60, 0.75, 1 after milling. . . . .	52
5.4.	Comparison of the experimental (solid black circles) and calculated structural parameters for the kesterite (KS, open circles), stannite (ST, open red squares) and disordered kesterite (DKS-p <sub>1</sub> , open blue star symbols) phases. The curves for the KS (12.5% disordered) and DKS-p <sub>2</sub> fall virtually on top of the DKS-p <sub>1</sub> curve and are omitted for clarity. The vertical dashed line indicates the KS → ST transition, as determined experimentally from the XRD results. . . . .	54
5.5.	Relative energies of the ordered and various disordered KS phases (solid lines) with respect to the stannite-type phase (black dotted baseline) for different Cd contents x <sub>Cd</sub> . Energies below zero indicate that the respective (D)KS phases are more stable than the ST modification. The grey solid line is a prediction for a KS phase with cationic disorder fraction smaller than 12.5%, generated by mixing the ordered KS and 12.5% disordered KS energies with the ratio 2.7:1 (see text for more details). .	56

LIST OF FIGURES

---

5.6. (a) The as-measured Raman spectra of the synthetic $\text{Cu}_2\text{Cd}_x\text{Zn}_{1-x}\text{SnS}_4$ sample series ( $x_{\text{Cd}} = 0, 0.25, 0.33, 0.37, 0.40, 0.50, 0.60, 0.75, 1$ ) with laser excitation wavelength $\lambda = 473$ nm at ambient conditions. The determined (b) Raman mode frequency and (c) width (FWHM) of the strongest Raman-active vibration as a function of $x_{\text{Cd}}$ are also plotted. .	58
5.7. UV/Vis spectra of $\text{Cu}_2\text{Cd}_x\text{Zn}_{1-x}\text{SnS}_4$ samples with Tauc plot determination of the direct optical band gap $E_g$ . . . . .	59
5.8. Comparison of calculated band gaps to the experimentally measured band gaps for the ordered and disordered KS and ST phases. The experimental values are marked as stars (red for KS/DKS, black for ST phases). The calculated band gaps are upshifted by 0.3 eV. . . . .	61
8.1. Top: Neutron diffraction pattern (red points) of stannite, $\text{Cu}_2\text{FeSnS}_4$ , with Rietveld refinement (black line), difference (blue line), Bragg reflections (blue stripes) and unit cell on the right. Bottom: SEM/EDX mapping of a $\text{Cu}_2\text{FeSnS}_4$ particle. . . . .	95
8.2. (a) LSV (5 mV/s) of $\text{Cu}_2\text{FeSnS}_4$ and various Fe containing materials loaded on FTO (1 mg/cm <sup>2</sup> ), (b) LSV (5 mV/s) of various materials loaded on NF (2 mg/cm <sup>2</sup> ), (c) Tafel slopes obtained from LSV (1 mV/s), (d) EIS responses ( $R_{\text{ct}}(\text{Cu}_2\text{FeSnS}_4) = 0.64 \Omega$ and $R_{\text{ct}}(\text{FeS}) = 1.18 \Omega$ ), (e) long term CA measurement, (f) linear fits (derived by Figure S10) to obtain Cdl of the as prepared electrode and after CA measurement (e). . . . .	96
8.3. Electron microscopy of $\text{Cu}_2\text{FeSnS}_4$ after OER: (a) SEM image, the arrow indicates a particle of elemental sulfur, (b) SAED with crystallographic planes of FeOOH, (c) TEM image, the black circle indicates the area of the SAED, (d) HR-TEM image with the Fourier transformation of the selected area revealing fringes of the crystallographic plane (110) of FeOOH, the red circles indicate regions of uninterrupted ordered lattice fringes. . . . .	98
8.4. XPS analysis of $\text{Cu}_2\text{FeSnS}_4/\text{FTO}/\text{OER}$ ; a) Cu 2p spectrum with $\text{Cu}^{\text{II}}$ satellites marked with *; b) Fe 2p spectrum with $\text{Fe}^{\text{III}}$ satellites marked with +. . . . .	99
9.1. X-ray diffraction pattern of $\text{Cu}_2\text{MgSn}_3\text{S}_8$ with the results of the Rietveld refinement. . . . .	118
9.2. X-ray diffraction pattern of $\text{Ag}_2\text{MgSn}_3\text{S}_8$ with the results of the Rietveld refinement. . . . .	119

LIST OF FIGURES

---

9.3. X-ray diffraction patterns of milled (top) and annealed (middle) $\text{Cu}_2\text{MgSn}_3\text{S}_8$ samples, supplemented by a Table presenting the calculated crystallite sizes for selected reflections. . . . .	120
9.4. UV/Vis spectra of $\text{Cu}_2\text{MgSn}_3\text{S}_8$ (left) and $\text{Ag}_2\text{MgSn}_3\text{S}_8$ (right) with Tauc plot determination of the direct (top) and indirect (bottom) optical band gaps. . . . .	121
9.5. Temperature dependence of the magnetic susceptibility $\chi$ of $\text{Cu}_2\text{MgSn}_3\text{S}_8$ measured in ZFC mode with an applied magnetic field strength of 10 kOe.	122
9.6. Experimental (black dots) and simulated (red line) $^{119}\text{Sn}$ Mössbauer spectrum of $\text{Cu}_2\text{MgSn}_3\text{S}_8$ at 6 K. . . . .	123
A.1. X-ray diffraction pattern of synthesized CuS, covellite (space group $P6_3/mmc$ ). . . . .	144
A.2. X-ray diffraction pattern of synthesized CdS, greenockite (black, space group $P6_3mc$ ) with additional hawleyite (blue, space group $F\bar{4}3m$ ). . . . .	144
A.3. X-ray diffraction pattern of synthesized ZnS, sphalerite (black, space group $F\bar{4}3m$ ) with additional wurtzite (blue, space group $P6_3mc$ ). . . . .	145
A.4. X-ray diffraction pattern of synthesized SnS, herzenbergite (space group $Pnma$ ). . . . .	145
A.5. X-ray diffraction pattern of $\text{Ag}_2\text{S}$ , acanthite (space group $P2_1/m$ ). . . . .	146
A.6. X-ray diffraction pattern of $\text{FeS}_2$ , pyrite (space group $Pa\bar{3}$ ). . . . .	146
A.7. X-ray diffraction pattern of synthesized MgS (black, space group $Fm\bar{3}m$ ) with additional impurities of MgO (blue, space group $Fm\bar{3}m$ ). . . . .	147
A.8. X-ray diffraction pattern of $\text{Li}_2\text{S}$ (space group $Fm\bar{3}m$ ). . . . .	147
A.9. X-ray diffraction pattern of MnS, alabandite (space group $Fm\bar{3}m$ ). . . . .	148
A.10. X-ray diffraction pattern of synthesized NiS, millerite (black, space group $R\bar{3}m$ ) with additional NiS (blue, space group $P6_3/mmc$ ). . . . .	148
A.11. X-ray diffraction pattern of $\text{CoS}_2$ , cattierite (space group $Pa\bar{3}$ ). . . . .	149

## List of Tables

2.1.	Summarization of pronounced structure types derived from cubic/hexagonal diamond structure reaching $A_2^I B^II C^IV X_4^{VI}$ compounds. . . . .	11
5.1.	The four different structural models considered for the Rietveld refinements of the measured $Cu_2Cd_xZn_{1-x}SnS_4$ XRD patterns. The respective Wyckoff positions and isotropic Debye-Waller factors $B$ are also provided for each model. . . . .	48
5.2.	Elemental composition of the synthetic $Cu_2Cd_xZn_{1-x}SnS_4$ solid solution series, as determined by electron microprobe measurements. . . . .	53
5.3.	Refined lattice parameters and potential space groups for the synthetic $Cu_2Cd_xZn_{1-x}SnS_4$ samples with $x_{Cd} = 0, 0.25, 0.33, 0.37, 0.40, 0.50, 0.60, 0.75, 1$ . . . . .	54
5.4.	Direct optical band gaps $E_g$ of $Cu_2Cd_xZn_{1-x}SnS_4$ -samples with $x_{Cd} = 0, 0.25, 0.33, 0.37, 0.40, 0.50, 0.60, 0.75, 1$ , as determined from UV/VIS measurements (Figure 5.7). . . . .	60
9.1.	Phase composition of $Cu_2MgSn_3S_8$ and $Ag_2MgSn_3S_8$ calculated from EDX and elemental analysis. . . . .	116
9.2.	Results of the Rietveld refinements for $Cu_2MgSn_3S_8$ and $Ag_2MgSn_3S_8$ (standard deviations in parenthesis). . . . .	116
9.3.	Refined atomic parameters for $Cu_2MgSn_3S_8$ (standard deviations in parenthesis). . . . .	117
9.4.	Refined atomic parameters for $Ag_2MgSn_3S_8$ (standard deviations in parenthesis). . . . .	117
9.5.	Interatomic distances in $Cu_2MgSn_3S_8$ and $Ag_2MgSn_3S_8$ (standard deviations in parenthesis). . . . .	118
9.6.	Fitting parameters of the $^{119}Sn$ Mössbauer spectroscopic measurement on $Cu_2MgSn_3S_8$ at 6 K. $\delta$ = isomer shift, $\Delta E_Q$ = electric quadrupole splitting, $\Gamma$ = experimental line width. . . . .	123
A.1.	List of utilized chemicals. . . . .	143

LIST OF TABLES

---

A.2. List of utilized software. . . . . 149

## Bibliography

- [1] J. Bardeen, W. H. Brattain, *Phys. Rev.* **1948**, 74, 230–231.
- [2] I. M. Ross, *Proc. IEEE* **1998**, 86, 7–28.
- [3] R. H. Bube, *Photovoltaic materials*, vol. 1 of *Series on properties of semiconductor materials* (Imperial College Press, London, 1998).
- [4] J.-Y. Son, K. Ma, *Proc. IEEE* **2017**, 105, 2116–2131.
- [5] A. B. Murphy, P. R. F. Barnes, L. K. Randeniya, I. C. Plumb, I. E. Grey, M. D. Horne, J. A. Glasscock, *Int. J. Hydrogen Energ.* **2006**, 31, 1999–2017.
- [6] C. Goodman, *J. Phys. Chem. Solids* **1958**, 6, 305–314.
- [7] B. Pamplin, *J. Phys. Chem. Solids* **1964**, 25, 675–684.
- [8] S. Chen, X. Gao Gong, A. Walsh, S.-H. Wei, *APS Meeting Abstracts* **2009**, L21.013.
- [9] T. M. Friedlmeier, H. Dittrich, H.-W. Schock, *Inst. Phys. Conf. Ser.* **1998**, 152, 345–348.
- [10] K. Mertens, *Technologie und Praxis, Hanser, München* **2013**.
- [11] H. Katagiri, N. Sasaguchi, S. Hando, S. Hoshino, J. Ohashi, T. Yokota, *Sol. Energy Mater. Sol. Cells* **1997**, 49, 407–414.
- [12] J. J. Scragg, P. J. Dale, L. M. Peter, G. Zoppi, I. Forbes, *Phys. Stat. Sol. (b)* **2008**, 245, 1772–1778.
- [13] L. Piskach, O. Parasyuk, I. Olekseyuk, *J. Alloys Compd.* **1998**, 279, 142–152.
- [14] O. V. Parasyuk, I. D. Olekseyuk, L. V. Piskach, S. V. Volkov, V. I. Pekhnyo, *J. Alloys Compd.* **2005**, 399, 173–177.
- [15] M. Moroz, F. Tesfaye, P. Demchenko, M. Prokhorenko, D. Lindberg, O. Reshetnyak, L. Hupa, *J. Electron. Mater.* **2018**, 47, 5433–5442.

## BIBLIOGRAPHY

---

- [16] M. M. Thackeray, *J. Electrochem. Soc.* **1995**, 142, 2558.
- [17] G. T. Fey, J. R. Dahn, *US Patent 5518842* **1996**.
- [18] M. M. Thackeray, *J. Am. Ceram. Soc.* **1999**, 82, 3347–3354.
- [19] J. B. Goodenough, *J Solid State Electrochem.* **2012**, 16, 2019–2029.
- [20] A. Ritscher, J. Just, O. Dolotko, S. Schorr, M. Lerch, *J. Alloys Compd.* **2016**, 670, 289–296.
- [21] A. Ritscher, M. Schlosser, A. Pfitzner, M. Lerch, *Mater. Res. Bull.* **2016**, 84, 162–167.
- [22] A. Ritscher, A. Franz, S. Schorr, M. Lerch, *J. Alloys Compd.* **2016**, 689, 271–277.
- [23] B. Pamplin, *Prog. Cryst. Growth & Charact.* **1980**, 3, 179–192.
- [24] E. Parthé, *Z. Kristallogr. - Cryst. Mater.* **1964**, 119, 204–225.
- [25] E. Parthé, *Crystal Chemistry of Tetrahedral Structures* (Gordon and Breach Science Publishers Inc., New York, 1964).
- [26] H. G. Grimm, A. Sommerfeld, *Z. Physik* **1926**, 36, 36–59.
- [27] E. Mooser, W. B. Pearson, *Acta Cryst.* **1959**, 12, 1015–1022.
- [28] E. Mooser, W. B. Pearson, *J. Chem. Phys.* **1957**, 26, 893–899.
- [29] W. Schäfer, R. Nitsche, *Mater. Res. Bull.* **1974**, 9, 645–654.
- [30] A. R. West, *Z. Kristallogr. - Cryst. Mater.* **1975**, 141, 422–436.
- [31] H. Hahn, H. Schulze, *Sci. Nat.* **1965**, 52, 426.
- [32] T. Hirai, K. Kurata, Y. Takeda, *Solid State Electron.* **1967**, 10, 975–981.
- [33] H. Haeuseler, F. W. Ohrendorf, M. Himmrich, *Z. Naturforsch. B* **1991**, 46, 1049–1052.
- [34] C. L. Teske, *Z. Naturforsch. B* **1979**, 34, 544–547.
- [35] J. A. Aitken, P. Larson, S. D. Mahanti, M. G. Kanatzidis, *Chem. Mater.* **2001**, 13, 4714–4721.
- [36] E. Parthé, K. Yvon, R. H. Deitch, *Acta Crystallogr. B Struct. Sci.* **1969**, 25, 1164–1174.

BIBLIOGRAPHY

---

- [37] L. O. Brockway, *Z. Kristallogr. - Cryst. Mater.* **1934**, 89.
- [38] V. V. Ivanov, Y. A. Pyatenko, *Zap Vses Mineral Obshch* **1959**, 88, 165–168.
- [39] A. F. Moodie, H. J. Whitfield, *Acta Crystallogr. B Struct. Sci.* **1986**, 42, 236–247.
- [40] B.-W. Liu, M.-J. Zhang, Z.-Y. Zhao, H.-Y. Zeng, F.-K. Zheng, G.-C. Guo, J.-S. Huang, *J. Solid State Chem.* **2013**, 204, 251–256.
- [41] I. D. Olekseyuk, O. V. Marchuk, L. D. Gulay, O. Zhibankov, *J. Alloys Compd.* **2005**, 398, 80–84.
- [42] H. Katagiri, K. Saitoh, T. Washio, H. Shinohara, T. Kurumadani, S. Miyajima, *Sol. Energy Mater. Sol. Cells* **2001**, 65, 141–148.
- [43] J. S. Seol, S. Y. Lee, J. C. Lee, H. D. Nam, K. H. Kim, *Sol. Energy Mater. Sol. Cells* **2003**, 75, 155–162.
- [44] S. Schorr, H.-J. Hoebler, M. Tovar, *Eur. J. Mineral.* **2007**, 19, 65–73.
- [45] R. Caye, Y. Laurent, P. Picot, R. Pierrot, C. Lévy, *Bulletin de Minéralogie* **1968**, 91, 383–387.
- [46] Z. Johan, P. Picot, *Bulletin de Minéralogie* **1982**, 105, 229–235.
- [47] H. Haeuseler, M. Himmrich, *Z. Naturforsch. B* **1989**, 44, 1035–1036.
- [48] J. Lekse, *Dissertation* **2009**, Duquesne University.
- [49] S. Greil, *Dissertation* **2015**, Universität Regensburg.
- [50] C. D. Brunetta, B. Karuppanan, K. A. Rosmus, J. A. Aitken, *J. Alloys Compd.* **2012**, 516, 65–72.
- [51] C. D. Brunetta, J. A. Brant, K. A. Rosmus, K. M. Henline, E. Karey, J. H. MacNeil, J. A. Aitken, *J. Alloys Compd.* **2013**, 574, 495–503.
- [52] C. L. Teske, *Z. Anorg. Allg. Chem.* **1978**, 445, 193–201.
- [53] M. S. Devi, K. Vidyasagar, *J. Chem. Soc. Dalton Trans.* **2002**, 2092–2096.
- [54] J. W. Lekse, B. M. Leverett, C. H. Lake, J. A. Aitken, *J. Solid State Chem.* **2008**, 181, 3217–3222.
- [55] J. W. Lekse, M. A. Moreau, K. L. McNerny, J. Yeon, P. S. Halasyamani, J. A. Aitken, *Inorg. Chem.* **2009**, 48, 7516–7518.

## BIBLIOGRAPHY

- [56] K. P. Devlin, A. J. Glaid, J. A. Brant, J.-H. Zhang, M. N. Srnec, D. J. Clark, Y. Soo Kim, J. I. Jang, K. R. Daley, M. A. Moreau, J. D. Madura, J. A. Aitken, *J. Solid State Chem.* **2015**, 231, 256–266.
- [57] J. A. Brant, D. J. Clark, Y. S. Kim, J. I. Jang, A. Weiland, J. A. Aitken, *Inorg. Chem.* **2015**, 54, 2809–2819.
- [58] J. A. Brant, K. P. Devlin, C. Bischoff, D. Watson, S. W. Martin, M. D. Gross, J. A. Aitken, *Solid State Ion.* **2015**, 278, 268–274.
- [59] K. Wu, B. Zhang, Z. Yang, S. Pan, *J. Am. Chem. Soc.* **2017**, 139, 14885–14888.
- [60] G. Li, Y. Chu, Z. Zhou, *Chem. Mater.* **2018**, 30, 602–606.
- [61] G. Li, Y. Chu, J. Li, Z. Zhou, *Dalton Trans.* **2020**, 49, 1975–1980.
- [62] J. He, Y. Guo, W. Huang, X. Zhang, J. Yao, T. Zhai, F. Huang, *Inorg. Chem.* **2018**, 57, 9918–9924.
- [63] K. Wu, Z. Yang, S. Pan, *Angew. Chem. Int. Ed.* **2016**, 55, 6713–6715.
- [64] M. Auernhammer, H. Effenberger, E. Irran, F. Pertlik, J. Rosenstingl, *J. Solid State Chem.* **1993**, 106, 421–426.
- [65] P. Jackson, R. Wuerz, D. Hariskos, E. Lotter, W. Witte, M. Powalla, *Phys. Status Solidi RRL* **2016**, 10, 583–586.
- [66] W. Wang, M. T. Winkler, O. Gunawan, T. Gokmen, T. K. Todorov, Y. Zhu, D. B. Mitzi, *Adv. Energy Mater.* **2014**, 4, 1301465.
- [67] S. K. Deb, *AIP Conference Proceedings* **1997**, 401, 325–336.
- [68] A. Goetzberger, C. Hebling, H.-W. Schock, *Mat. Sci. Eng. R* **2003**, 40, 1–46.
- [69] P. A. Franken, A. E. Hill, C. W. Peters, G. Weinreich, *Phys. Rev. Lett.* **1961**, 7, 118–119.
- [70] D. S. Chemla, P. J. Kupecek, D. S. Robertson, R. C. Smith, *Opt. Commun.* **1971**, 3, 29–31.
- [71] G. C. Bhar, R. C. Smith, *Phys. Stat. Sol. (a)* **1972**, 13, 157–168.
- [72] W. Ruderman, J. Maffetone, D. E. Zelman, D. M. Poirier, *MRS Proc.* **1997**, 484.
- [73] A. G. Jackson, M. C. Ohmer, S. R. LeClair, *Infrared Phys. Techn.* **1997**, 38, 233–244.

BIBLIOGRAPHY

---

- [74] K. Kato, *IEEE J. Quantum Electron.* **1991**, 27, 1137–1140.
- [75] R. C. Miller, W. A. Nordland, *Phys. Rev. B* **1970**, 2, 4896–4902.
- [76] S. Brosnan, R. Byer, *IEEE J. Quantum Electron.* **1979**, 15, 415–431.
- [77] H. Schmid, *Ferroelectrics* **1994**, 162, 317–338.
- [78] G. Nénert, T. T. M. Palstra, *J. Phys.: Condens. Matter* **2009**, 21, 176002.
- [79] I. Tsuji, H. Kato, A. Kudo, *Angew. Chem. Int. Ed.* **2005**, 44, 3565–3568.
- [80] I. Tsuji, H. Kato, A. Kudo, *Chem. Mater.* **2006**, 18, 1969–1975.
- [81] I. Tsuji, Y. Shimodaira, H. Kato, H. Kobayashi, A. Kudo, *Chem. Mater.* **2010**, 22, 1402–1409.
- [82] B. Pamplin, *Nature* **1960**, 188, 136–137.
- [83] W. H. Bragg, W. L. Bragg, *Proc. R. Soc. Lond. A* **1913**, 89, 277–291.
- [84] S. R. Hall, J. T. Szymanski, J. M. Stewart, *Can. Mineral.* **1978**, 16, 131–137.
- [85] F. Gao, S. Yamazoe, T. Maeda, K. Nakanishi, T. Wada, *Jpn. J. Appl. Phys.* **2012**, 51, 10NC29.
- [86] S. Chen, J.-H. Yang, X. G. Gong, A. Walsh, S.-H. Wei, *Phys. Rev. B* **2010**, 81, 245204–1–245204–10.
- [87] A. Nagoya, R. Asahi, R. Wahl, G. Kresse, *Phys. Rev. B* **2010**, 81, 113202–1–113202–4.
- [88] F. P. Bundy, J. S. Kasper, *J. Chem. Phys.* **1967**, 46, 3437–3446.
- [89] H. He, T. Sekine, T. Kobayashi, *Appl. Phys. Lett.* **2002**, 81, 610–612.
- [90] E. I. du Pont de Nemours and Company, *Netherlands Patent Release No 6506395* **1965**.
- [91] F. Ulrich, W. Zachariasen, *Z. Kristallogr. - Cryst. Mater.* **1925**, 62, 260–273.
- [92] J. Y. Huang, L.-C. Tang, M. H. Lee, *J. Phys.: Condens. Matter* **2001**, 13, 10417–10431.
- [93] S. Chen, A. Walsh, Y. Luo, J.-H. Yang, X. G. Gong, S.-H. Wei, *Phys. Rev. B* **2010**, 82, 195203–1–195203–8.

BIBLIOGRAPHY

---

- [94] S. Chen, A. Walsh, Y. Luo, J.-H. Yang, X. G. Gong, S.-H. Wei, *Phys. Rev. B* **2011**, 83, 159904–1.
- [95] K. A. Rosmus, C. D. Brunetta, M. N. Srncic, B. Karuppappan, J. A. Aitken, *Z. Anorg. Allg. Chem.* **2012**, 638, 2578–2584.
- [96] T. Hom, W. Kiszczek, B. Post, *J. Appl. Crystallogr.* **1975**, 8, 457–458.
- [97] B. K. Agrawal, P. S. Yadav, S. Agrawal, *Phys. Rev. B Condens. Matter* **1994**, 50, 14881–14887.
- [98] L. Pauling, L. O. Brockway, *Z. Kristallogr. - Cryst. Mater.* **1932**, 82, 188–194.
- [99] H. Bärnighausen, *MATCH, Communications in Mathematical Chemistry* **1980**, 9, 139–175.
- [100] U. Müller, *Z. Anorg. Allg. Chem.* **2004**, 630, 1519–1537.
- [101] G. Surucu, K. Colakoglu, E. Deligoz, N. Korozlu, Y. O. Ciftci, *Solid State Commun.* **2010**, 150, 1413–1418.
- [102] H. Pfister, *Acta Cryst.* **1958**, 11, 221–224.
- [103] U. Müller, *Anorganische Strukturchemie: 6. Auflage* (Vieweg+Teubner, Wiesbaden, 2008).
- [104] L. Néel, *Ann. Phys.* **1948**, 3, 137–198.
- [105] T. Bitoh, T. Hagino, Y. Seki, S. Chikazawa, S. Nagata, *J. Phys. Soc. Jpn.* **1992**, 61, 3011–3012.
- [106] G. Cao, H. Kitazawa, H. Suzuki, T. Furubayashi, K. Hirata, T. Matsumoto, *Physica C Supercond.* **2000**, 341-348, 735–736.
- [107] J. B. Goodenough, *Solid State Commun.* **1967**, 5, 577–580.
- [108] R. J. Bouchard, P. A. Russo, A. Wold, *Inorg. Chem.* **1965**, 4, 685–688.
- [109] T. Furubayashi, H. Suzuki, T. Matsumoto, S. Nagata, *Solid State Commun.* **2003**, 126, 617–621.
- [110] G. Catalan, J. F. Scott, *Nature* **2007**, 448, E4–E5.
- [111] J. Hemberger, P. Lunkenheimer, R. Fichtl, S. Weber, V. Tsurkan, A. Loidl, *Phase Transit.* **2006**, 79, 1065–1082.

BIBLIOGRAPHY

---

- [112] F. K. Lotgering, *Philips Res. Rep.* **1956**, 11, 218–249.
- [113] N. Menyuk, K. Dwight, A. Wold, *J. Appl. Phys.* **1965**, 36, 1088–1089.
- [114] J. C. Jumas, E. Philippot, M. Maurin, *Acta Crystallogr. B Struct. Sci.* **1979**, 35, 2195–2197.
- [115] P. Lavela, J. L. Tirado, J. Morales, J. Olivier-Fourcade, J.-C. Jumas, *J. Mater. Chem.* **1996**, 6, 41–47.
- [116] M. A. Cochez, J. C. Jumas, P. Lavela, J. Morales, J. Olivier-Fourcade, J. L. Tirado, *J. Power Sources* **1996**, 62, 101–105.
- [117] S. Chykhrij, L. Sysa, O. Parasyuk, L. Piskach, *J. Alloys Compd.* **2000**, 307, 124–126.
- [118] C. Branci, M. Womes, P. E. Lippens, J. Olivier-Fourcade, J. C. Jumas, *J. Solid State Chem.* **2000**, 150, 363–370.
- [119] G. Garg, S. Bobev, A. Roy, J. Ghose, D. Das, A. K. Ganguli, *Mater. Res. Bull.* **2001**, 36, 2429–2435.
- [120] G. Garg, *Solid State Ion.* **2002**, 146, 195–198.
- [121] V. P. Sachanyuk, A. O. Fedorchuk, I. D. Olekseyuk, O. V. Parasyuk, *Mater. Res. Bull.* **2007**, 42, 143–148.
- [122] Z. Kormosh, A. Fedorchuk, K. Wojciechowski, N. Tataryn, O. Parasyuk, *Mat. Sci. Eng. C* **2011**, 31, 540–544.
- [123] J. Yajima, E. Ohta, Y. Kanazawa, *Mineral. J.* **1991**, 15, 222–232.
- [124] G. Garg, K. V. Ramanujachary, S. E. Lofland, M. V. Lobanov, M. Greenblatt, T. Maddanimath, K. Vijayamohanan, A. K. Ganguli, *J. Solid State Chem.* **2003**, 174, 229–232.
- [125] M. A. Keane, *Interfacial Applications in Environmental Engineering*, vol. v. 108 of *Surfactant Science* (CRC Press, Baton Rouge, 2002).
- [126] M. M. Thackeray, W. David, P. G. Bruce, J. B. Goodenough, *Mater. Res. Bull.* **1983**, 18, 461–472.
- [127] M. Liu, Z. Rong, R. Malik, P. Canepa, A. Jain, G. Ceder, K. A. Persson, *Energy Environ. Sci.* **2015**, 8, 964–974.

BIBLIOGRAPHY

---

- [128] C. Branci, J. Sarradin, J. Olivier-Fourcade, J. Jumas, *J. Power Sources* **1999**, 81-82, 282–285.
- [129] C. Daniel, D. Mohanty, J. Li, D. L. Wood, *AIP Conf. Proc.* **2014**, 1597, 26–43.
- [130] W. H. Bragg, *London Edinburgh Philos. Mag. J. Sci. London, Edinburgh Dublin Philos. Mag. J. Sci.* **1915**, 30, 305–315.
- [131] S. Nishikawa, *Proceedings of the Tokyo Mathematico-Physical Society. 2nd Series* **1915**, 8, 199–209\_1.
- [132] L. Passerini, *Gazz. Chim. Ital.* **1930**, 60, 389–399.
- [133] H. St. C. O’Neill, H. Annersten, D. Virgo, *Am. Mineral.* **1992**, 77, 725–740.
- [134] W. D. Derbyshire, H. J. Yearian, *Phys. Rev.* **1958**, 112, 1603–1607.
- [135] L. Passerini, *Gazz. Chim. Ital.* **1930**, 60, 389–399.
- [136] E. W. Gorter, *Philips Res. Rep.* **1954**, 9, 295–365.
- [137] R. B. von Dreele, A. Navrotsky, A. L. Bowman, *Acta Crystallogr. B Struct. Sci.* **1977**, 33, 2287–2288.
- [138] T. F. W. Barth, E. Posnjak, *Z. Kristallogr. - Cryst. Mater.* **1932**, 82.
- [139] A. Navrotsky, *Am. Mineral.* **1986**, 71, 1160–1169.
- [140] J. D. Dunitz, L. E. Orgel, *J. Phys. Chem. Solids* **1957**, 3, 20–29.
- [141] P. Holba, M. Nevřiva, E. Pollert, *Mater. Res. Bull.* **1975**, 10, 853–860.
- [142] W. A. Dollase, H. C. St. O’Neill, *Acta Crystallogr. C Cryst. Struct. Commun.* **1997**, 53, 657–659.
- [143] S. Holgersson, *Lunds universitets årsskrift. NF Avd* **1927**, 2, 1–9.
- [144] W. C. Hamilton, *Phys. Rev.* **1958**, 110, 1050–1057.
- [145] A. Mosbah, A. Verbaere, M. Tournoux, *Mater. Res. Bull.* **1983**, 18, 1375–1381.
- [146] A. Yamada, M. Tanaka, *Mater. Res. Bull.* **1995**, 30, 715–721.
- [147] K. Oikawa, *Solid State Ion.* **1998**, 109, 35–41.
- [148] M. Schieber, *J. Inorg. Nucl. Chem* **1964**, 26, 1363–1367.

BIBLIOGRAPHY

---

- [149] B. Reuter, R. Aust, C. Colsmann, Neuwald. C., *Z. Anorg. Allg. Chem.* **1983**, 500, 188–198.
- [150] K.-i. Matsuno, T. Katsufuji, S. Mori, Y. Moritomo, A. Machida, E. Nishibori, M. Takata, M. Sakata, N. Yamamoto, H. Takagi, *J. Phys. Soc. Jpn.* **2001**, 70, 1456–1459.
- [151] N. Soheilnia, K. M. Kleinke, E. Dashjav, H. L. Cuthbert, J. E. Greedan, H. Kleinke, *Inorg. Chem.* **2004**, 43, 6473–6478.
- [152] C. Haas, *J. Phys. Chem. Solids* **1965**, 26, 1225–1232.
- [153] J. S. Benjamin, T. E. Volin, *Met. Trans.* **1974**, 5, 1929–1934.
- [154] C. Suryanarayana, *Prog. Mater. Sci.* **2001**, 46, 1–184.
- [155] J. S. Benjamin, *Sci. Am.* **1976**, 234, 40–49.
- [156] P. S. Gilman, J. S. Benjamin, *Annu. Rev. Mater. Sci.* **1983**, 13, 279–300.
- [157] C. F. Burmeister, A. Kwade, *Chem. Soc. Rev.* **2013**, 42, 7660–7667.
- [158] T. Friščić, *J. Mater. Chem.* **2010**, 20, 7599.
- [159] T. K. Achar, A. Bose, P. Mal, *Beilstein J. Org. Chem* **2017**, 13, 1907–1931.
- [160] J. L. Howard, Q. Cao, D. L. Browne, *Chem. Sci.* **2018**, 9, 3080–3094.
- [161] W. C. Röntgen, *Ann. d. Phys. u. Chem.* **1898**, 64.
- [162] H. M. Rietveld, *J. Appl. Crystallogr.* **1969**, 2, 65–71.
- [163] H. M. Rietveld, *Phys. Scr.* **2014**, 89, 098002.
- [164] W. I. F. David, *J. Res. Natl. Inst. Stand. Technol.* **2004**, 109, 107–123.
- [165] B. H. Toby, *Powder Diffr.* **2006**, 21, 67–70.
- [166] J. Rodriguez-Carvajal, *Abstracts of the Satellite Meeting on Powder Diffraction of the XV. Congress of the IUCr* **1990**, 127.
- [167] P. Debye, P. Scherrer, *Nachrichten von der Gesellschaft der Wissenschaften zu Goettingen, Mathematisch-Physikalische Klasse* **1918**, 101–120.
- [168] C. V. Raman, *Transactions of the Faraday Society* **1929**, 25, 781–792.
- [169] J. Tauc, R. Grigorovici, A. Vanacu, *Phys. Stat. Sol. (b)* **1966**, 15, 627–637.

## BIBLIOGRAPHY

---

- [170] J. Tauc, *Mater. Res. Bull.* **1968**, 3, 37–46.
- [171] V. F. Sears, *Neutron News* **1992**, 3, 26–37.
- [172] I. Tsuji, Y. Shimodaira, H. Kato, H. Kobayashi, A. Kudo, *Chem. Mater.* **2010**, 22, 1402–1409.
- [173] X. Yu, X. An, A. Genç, M. Ibáñez, J. Arbiol, Y. Zhang, A. Cabot, *J. Phys. Chem. C* **2015**, 119, 21882–21888.
- [174] F. Ozel, E. Aslan, B. Istanbulu, O. Akay, I. Hatay Patir, *Appl. Catal. B Environ.* **2016**, 198, 67–73.
- [175] R. V. Digraskar, B. B. Mulik, P. S. Walke, A. V. Ghule, B. R. Sathe, *Appl. Surf. Sci.* **2017**, 412, 475–481.
- [176] P. Kush, K. Deori, A. Kumar, S. Deka, *J. Mater. Chem. A* **2015**, 3, 8098–8106.
- [177] I. Efthimiopoulos, T. Küllmey, S. Speziale, A. S. Pakhomova, M. Quennet, B. Paulus, A. Ritscher, M. Lerch, M. Koch-Müller, *J. Appl. Phys.* **2018**, 124, 085905–1–085905–10.